Technische Universität München

Physik-Department, Lehrstuhl E21

Forschungs-Neutronenquelle Heinz Maier-Leibnitz (FRM II)

Vortex Matter of the Intertype Superconductor Niobium

Studied by Neutron Imaging, Neutron Diffraction and Molecular Dynamics Simulations

Alexander Backs

Vollständiger Abdruck der von der
Fakultät für Physik der Technischen Universität München
zur Erlangung des akademischen Grades eines

Doktors der Naturwissenschaften (Dr. rer. nat.)

genehmigten Dissertation.

Vorsitzender:		Prof. Dr. Michael Knap
Prüfer der Dissertation:	1.	Prof. Dr. Peter Böni
	2.	Prof. Dr. Elizabeth Blackburn

Diese Dissertation wurde am 29.01.2021 bei der Technischen Universität München eingereicht und durch die Fakultät für Physik am 19.04.2021 angenommen.

Abstract

Conventionally, superconductors are separated into type-I and type-II materials, corresponding to the (in)stability of magnetic vortices. Recently, a transitional regime labeled intertype superconductivity has been explored theoretically using an extended Ginzburg-Landau (EGL) formalism. In the intertype regime, interactions between vortices are found to be non-monotonous, which enables unconventional vortex matter states. A well-known example is the intermediate mixed state (IMS), a two phase domain structure consisting of ordered vortex lattice domains and vortex-free Meissner state domains, which can now be considered in the new context of the intertype regime.

The IMS has been routinely studied in the elemental superconductor niobium, which we have readdressed in an extensive study consisting of two complementary parts: experimental work with a focus on neutron scattering techniques and simulations using a two dimensional molecular dynamics (MD) approach. Both approaches focus on the transition of a homogeneous vortex lattice into the domain structure of the IMS upon cooldown. The experimental work revolves around the hierarchical structure of the IMS, which features a vortex lattice on a submicrometer scale, a domain structure on a low micrometer scale, and a distribution of domains on the millimeter scale of the sample. This hierarchy is reflected in the employed experimental techniques, each of which focuses on the properties of the IMS on a different length scale. In our predominantly field cooled measurements, we find a microscopic rearrangement of vortices from a homogeneous vortex lattice into the domain structure of the IMS. In this process, the vortices form lattice clusters with a temperature dependent vortex spacing which is uniquely defined for each sample. Remarkably, the IMS transition takes place in samples of strongly different quality and pinning properties, including samples undergoing a flux freezing transition. Furthermore, the transition is reversible and homogeneous on a macroscopic scale.

The MD simulations augment our experimental results with the means to access the microscopic arrangement of vortices. In a novel approach, we have used the results of the EGL formalism for the interaction between vortices in intertype superconductors. In close relation to our experiments, the simulations were designed to resemble the field cooled measurements of niobium. Overall, the experiments and simulations have delivered consistent results. Again, a primary concern was the dependence of the IMS on different pinning properties, which we could address over several orders of magnitude of the pinning strength and pinning density. We found that the IMS domains persist over an extensive range of pinning parameters with very similar morphologies.

Zusammenfassung

Herkömmlich werden Supraleiter in Typ-I- und Typ-II-Materialien unterteilt, abhängig von der (In-) Stabilität magnetischer Vortices. Im Rahmen einer erweiterten Ginzburg-Landau (EGL) -Theorie wurde neuerdings zusätzlich ein Übergangsbereich untersucht, der sogenannte Intertype. In Intertype-Supraleitern können Vortices eine nicht-monotone Wechselwirkung aufzeigen, welche zu neuartigen Vortex Matter-Zuständen führen kann. Ein bekanntes Beispiel, das nun im Kontext des Intertypes verstanden werden kann, ist der Intermediate Mixed State (IMS), ein zwei-Phasen-Gemisch, bestehend aus Vortex-Gitter-Domänen und flussfreien Domänen im Meissner-Zustand.

Das Auftreten des IMS in Niob, einem elementaren Supraleiter, ist bereits gut etabliert. Wir griffen dieses Phänomen mit einer umfassenden Studie erneut auf, indem wir zwei komplementäre Ansätze kombinierten: experimentelle Methoden, die primär auf Neutronenstreuung basieren, sowie zweidimensionale Molekulardynamik (MD) -Simulationen. Mit beiden Ansätzen untersuchten wir den Übergang beim Abkühlen eines homogenen, hexagonalen Vortex-Gitters in die Domänenstruktur des IMS. Schwerpunkt der experimentellen Arbeit war die hierarchische Struktur des IMS, wobei das Vortex-Gitter eine Submikrometerskala aufweist, wogegen die Strukturgröße der Domänen im Bereich weniger Mikrometer liegt und die Verteilung der Domänen auf der Skala der Probe im Millimeterbereich variieren kann. Diese Hierarchie spiegelt sich in den verwendeten Methoden wieder, die jeweils auf eine der Größenordnungen angepasst sind. Unsere mehrheitlich feldgekühlten Experimente zeigen eine mikroskopische Umordnung der Vortices von einem homogenen Gitter in die Domänen-Struktur des IMS. Die dabei entstehenden Vortex-Gitter-Inseln besitzen einen temperaturabhängigen Gitterabstand, welcher eine spezifische Eigenschaft der jeweiligen Probe darstellt. Bemerkenswerterweise tritt der Übergang in den IMS in Proben mit stark unterschiedlichen Pinning-Eigenschafen auf. Die Bildung von Domänen im IMS wurde sowohl in Koexistenz mit dem Meissner-Effekt, als auch mit einem Flux-Freezing-Übergang beobachtet. Zusätzlich ist der IMS-Übergang reversibel und auf der makroskopischen Skala der Probe homogen.

Die MD-Simulationen ermöglichen es uns, zusätzlich die mikroskopische Verteilung der Vortices zu betrachten. In einem neuartigen Ansatz verwendeten wir die Ergebnisse des EGL-Formalismus, um die Wechselwirkung von Vortices in Intertype-Supraleitern zu beschreiben. In Anlehnung an unsere Experimente wurden die Simulationen derart gestaltet, dass sie eine feldgekühlte Messung an Niob repräsentieren. Zusammenfassend reproduzierten die Simulationen unsere experimentellen Ergebnisse. Eine Kernfrage der Simulationen war die Abhängigkeit des IMS von der Qualität des Supraleiters, die wir über mehrere Größenordnungen in zwei Simulationsparametern, der Stärke und Konzentration von Störstellen, untersuchten. Dabei konnten wir feststellen, dass der IMS über einen außergewöhnlich großen Bereich dieser Parameter auftritt, wobei seine Morphologie nur geringfügig beeinflusst wird.

Contents

List of Abbreviations

BCS	Bardeen-Cooper-Schrieffer
CCD	charge coupled device
CP	collective pinning
DFI	dark field image
EGL	extended Ginzburg-Landau
FC	field cooled
FH	field heated
FT	Fourier transform
FWHM	full width at half maximum
GL	Ginzburg-Landau
HP	high purity
IMS	intermediate mixed state
IP	individual pinning
IS	intermediate State
LP	low purity
MDS	molecular dynamics simulation
MLZ	Heinz Maier-Leibnitz Zentrum
MP	medium purity
MuSR	muon spin rotation
NGI	neutron grating interferometry
NIST	national institute of standards and technology
NP	no pinning
RRR	residual resistivity ratio
SANS	small angle neutron scattering
VL	vortex lattice
VSANS	very small angle neutron scattering
VSM	vibrating sample magnetometer
ZFC	zero field cooled

1 Introduction

Superconductivity is found in a large variety of compounds with different microscopic and phenomenological properties. There are different ways to classify the wealth of superconducting materials: A microscopic approach to their classification is along the coupling mechanism of cooper pairs. This leads to the distinction between conventional and unconventional superconductors [1]. From the phenomenological side, superconductors are divided into type-I and type-II by the Ginzburg-Landau parameter κ [2]. This classification mainly concerns magnetic properties, in particular, the stability of vortices. Parallel to the distinction of superconducting materials, the rich variety of vortex properties calls for a classification of their own [3]. Depending on the interaction of vortices between themselves and with their host superconductor, a range of vortex matter states can form.

The intermediate mixed state (IMS) in the model intertype superconductor niobium [4, 5], which is the main concern of this work, occupies a special place in the systematics of superconductors. Microscopically, niobium is a conventional superconductor [6, 7]. Phenomenologically, however, it does not fit in the classical Ginzburg-Landau classification. Vortices are stable in niobium, but they feature an atypical interaction with an attractive and repulsive contribution. In the IMS, a phase mixture of vortex matter domains and vortex-free Meissner state domains forms [8]. Although known for several decades now, the IMS is still not understood in full detail and an ongoing field of research [9–14].

In this chapter, we briefly review the rich variety of superconductivity in terms of coupling mechanisms and Ginzburg-Landau parameter (section (1.1)). Additionally, an overview of the vortex matter found in conventional superconductors will be given (section (1.2)). In section (1.3) we introduce prominent examples of inhomogeneous vortex matter states and finally discuss the intermediate mixed state in section (1.4). The chapter closes with an overview of this thesis (section (1.5)).

1.1 Classification of superconductors & vortex matter

The following chapter is meant to give a brief introduction into the wealth of superconducting materials and phenomena by discussing their classification. We note that especially the microscopic properties of many classes of superconductors are still being studied and a detailed overview of the various theories is by far too extensive for this work. For further reading on this subject we refer to the review articles by Pfleiderer [15] and Stewart [1].

Microscopic coupling mechanism: Conventional and unconventional superconductivity

The microscopic coupling mechanism of Cooper pairs, which enables superconductivity, is known in detail only for the group of conventional superconductors. In this case, the electrons interact via virtual phonons, as described by BCS theory [16] or extensions thereof. So far, all elemental superconductors and many of the simpler compounds fall into this category [17]. In BCS theory, the interaction is assumed to be weak, which is reflected in the low critical temperatures T_c. Furthermore, Cooper pairs form a spin singlet state with an isotropic s-wave spatial symmetry. Due to the pairing symmetry, the order parameter and the superconducting gap are isotropic and without nodes.

Any superconductors not covered by BCS theory are summarized under the umbrella term unconventional. Hence, unconventional superconductivity covers a large variety of materials and the coupling mechanism is not restricted to a specific type. Promising candidates include interactions via magnons [18, 19], spin or charge density waves [20–22] and spin or quantum fluctuations [1, 23, 24]. The interaction strength, and therefore T_c, is not necessarily higher in unconventional superconductors. Several materials from the cuprate family of unconventional superconductors have a $T_c > 100\,\mathrm{K}$ [25], while other compounds such as Sr_2RuO_4 [26] or $CeCu_2Si_2$ [27] have a low critical temperature of $T_c \approx 0.9\,\mathrm{K}$ and $T_c \approx 0.5\,\mathrm{K}$ respectively. Likewise, the cooper pair symmetry may take a number of non-isotropic forms. In these cases, the order parameter contains nodes or nodal lines where the superconducting gap vanishes. Candidates for, e.g., d-wave spatial symmetry are the cuprate [28] and iron pnictide [29] superconductors. Exemplarily, figure (1.1) shows the superconducting phases with different gap symmetry found in UPt_3, along with the corresponding vortex matter states. An additional feature found in unconventional superconductors is spin triplet coupling of the Cooper pairs, similar to the coupling of ^3He [30]. The tendency of parallel spin alignment in this state allows a close proximity or even coexistence of the superconductivity and a magnetically ordered state [23, 31, 32]. Spin triplets are found in Sr_2RuO_4 [33] and are considered for some organic superconductors [34] and materials with non-centrosymmetric crystal structure [35].

Unconventional superconductivity can also result from unusual electronic properties of the normal conducting state. In materials featuring two or one dimensional structures, the electronic density of states is greatly affected. Some examples of such compounds include cuprates [36], layered nitrides [37, 38], cobalt oxides [39, 40] and organic superconductors [41]. Similarly, heavy fermion materials are not compatible with BCS theory [42]. Due to the large effective electron mass ($\approx 100\,m_e$), the energy scales of the system are inverted with the Debye energy above the Fermi energy.

While they are not strictly considered unconventional, it is worth mentioning multi-band superconductors. If more than one valence band contributes significantly to the Cooper pairs, multiple superconducting states may compete in a single compound. Depending on the interaction of the different bands, the superconductor might sill be described by one effective band and exhibit purely conventional behavior. A prominent example is MgB_2, which coined the term of type-1.5 superconductivity [43, 44]. In this compound, a magnetic state similar to the IMS is found.

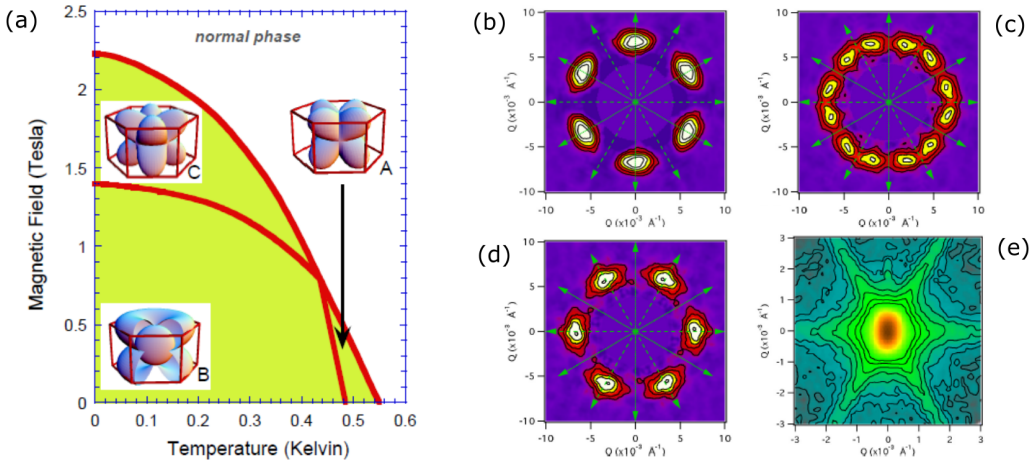

Figure 1.1: (a) Superconducting phases in UPt_3. The three phases A, B and C have distinct symmetries of the superconducting gap. These are shown in the corresponding inlays, including the hexagonal lattice structure of UPt_3. (b-e) Small angle scattering data of the vortex lattice after different temperature-field histories. (b) is measured after zero field cooling into the B-phase and (c) after zero field cooling into the A-phase. In contrast, (d) was field cooled and obtained the symmetry of the material structure shown in (e). Reprinted with permission from [45]. Copyright (2002) by Springer Nature.

Ginzburg-Landau parameter: Type-I / type-II dichotomy

Preceding BCS theory and a microscopic understanding of superconductivity, the phenomenological Ginzburg-Landau (GL) theory already allowed a meaningful classification [2]. GL theory is part of any standard textbook on superconductivity and we refer to, e.g., [3] for further details. Superconductivity is modeled as a second order phase transition with a newly introduced order parameter Ψ_{GL}. The Ginzburg-Landau parameter, which is used for the classification, is defined as $\kappa = \xi_{\mathrm{GL}}/\lambda_{\mathrm{L}}$. The London penetration depth λ_{L} characterizes a length scale on which magnetic field can enter a superconductor. Similarly, the Ginzburg-Landau coherence length ξ_{GL} defines a length scale for the superconducting order parameter Ψ_{GL}. κ characterizes the interface energy between the superconducting and a normal conducting state, which is directly corresponding to the stability of magnetic vortices.

For a critical value $\kappa_0 = 1/\sqrt{2}$, the interface energy vanishes, which divides two types of superconducting classes. In type-I materials, which are defined by $\kappa < \kappa_0$, interfaces cost energy and vortices are unstable. In contrast, vortices may form due to a negative interface energy in type-II superconductors with $\kappa > \kappa_0$. Due to their inability to form vortices, type-I materials only exist in the Meissner state, where the bulk of the material is free of magnetic flux. The Meissner state is stable up to a critical magnetic field H_{c}, where superconductivity breaks down. In type-II materials an additional state exists at magnetic fields above the Meissner state, called the Shubnikov state or mixed state [46]. In the Shubnikov state, a large number of vortices is present in the superconductor which can form a variety of vortex matter states (cf. section (1.2)).

Problems with the GL classification arise close to the type-I type-II transition [9, 10, 47]. At the critical value κ_0, vortices contribute no energy to the system [48, 49]. Any vortex configuration is energetically equal, which causes a high degeneracy of the superconducting state. Due to the approximations made in GL theory, this is only true at T_c. At lower temperatures, the degeneracy is lifted which leads to novel vortex properties and the coexistence of type-I and type-II characteristics [13]. Initially, this regime was labeled type-II/1, in distinction from the original type-II behavior [50]. A prominent example is the intermediate mixed state (IMS) found in niobium [51] and vanadium [52]. In the IMS, a partial attraction leads to the clustering of the vortices into domains, resulting in a phase mixture of vortex lattice and Meissner domains [14].

In chapter (2.1), we will discuss the vortex properties in superconductors with $\kappa \approx \kappa_0$, using an extended Ginzburg-Landau (EGL) formalism. In between the original type-I and type-II, EGL introduces a whole transitional area called the intertype regime (cf. figure (1.2)). Intertype superconductivity includes the type-II/1 and intermediate mixed state, alongside other unconventional vortex interactions and configurations.

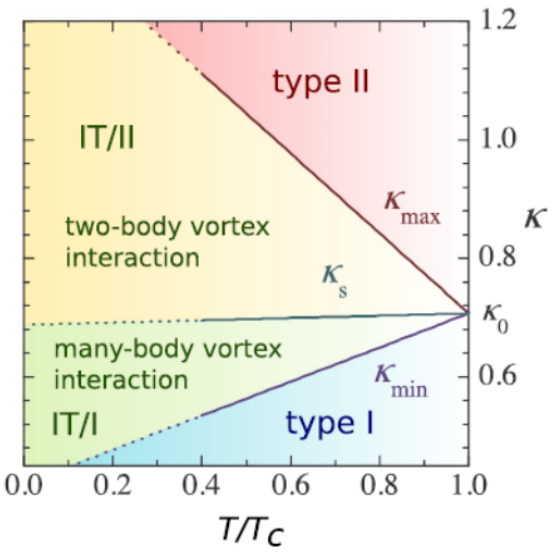

Figure 1.2: κ-T phase diagram of the intertype regime. The classical type-I and type-II dichotomy is valid exactly at T_c. At lower temperatures, the critical point at T_c, κ_0 opens up into the extended intertype regime. This is broadly divided into two regimes which favor single vortices (IT/II) and multi-vortex configurations (IT/I) respectively. The historically defined type-II/1 and the IMS loosely correspond to the IT/II phase. Reprinted with permission from [53]. Copyright (2017) by the American Physical Society.

1.2 Vortex matter in superconductors

The magnetic properties of a superconductor are tightly bound to the properties of the magnetic vortices [54]. Beside the variety of superconducting materials, vortices form a diverse set of vortex matter states (cf. figure (1.3)). This leads to a further classification of superconducting states, parallel to the distinction of materials. A detailed account on the properties of vortex matter is given in the book by Hübner [3].

Vortices are topological defects in the superconducting state, which grants them particle-like stability and properties. In distinction from atoms and molecules, vortices are elongated, string-like objects with elastic properties. They are subject to a variety of interactions, which affect the vortex matter state they form. Vortices imprint a variation of the order parameter, magnetic field and supercurrent onto the superconducting state, which results in an interaction between vortices. Additionally, they interact with material impurities and defects in the crystal lattice, where the superconductor is perturbed as well. Due to their magnetic properties, vortices are also affected by electrical currents via the Lorenz force. The close relation of vortices and the external magnetic field also makes them susceptible to demagnetization effects. In addition, they are affected by thermal fluctuations. The different vortex interactions are of similar magnitude and range and often change significantly over the superconducting phase.

The most well known vortex matter state is the Abrikosov vortex lattice [55]. The vortices align along an external field and arrange in a two dimensional lattice, due to their repulsive interaction. Depending on the symmetry of the order parameter and the material crystal structure, the lattice commonly has a hexagonal, scalene or rectangular structure [45, 56]. In the presence of disorder, mostly due to lattice defects or impurities in the superconducting material, the vortices form an amorphous or glassy state [55, 57]. A hybrid state, called a Bragg glass, has been found as well, which features a short range crystalline structure, but lacks any long range correlations [58, 59]. Close to the transition into the normal state, the length scales λ_{L} and ξ_{GL} diverge, which increases the vortex size and interaction range. In addition, thermal fluctuations increase. Under these conditions, the melting of solid vortex matter into a liquid state is possible [60]. In contrast to the solid states, vortices are typically entangled in a liquid. The intermediate mixed state is a special form of vortex matter, where only part of the superconductor contains vortices. Flux-free Meissner state regions and vortex lattice regions form a domain structure. The special properties of the IMS are caused by a non-monotonous vortex interaction [11, 13]. Figure (1.3)(a) shows a phase diagram of superconducting vanadium, where three distinct vortex matter states are found: the Bragg glass, true vortex glass and a depinned liquid state. In panel (b), results from computations using GL theory depict the three dimensional structure of different vortex states.

Generally, the vortex matter in superconductors is also interacting with the underlying material, especially the close correlation of the crystal lattice and electronic Fermi surface with the symmetry of the superconducting order parameter and gap. The effects of this interaction can be observed, e.g., in the symmetry of the vortex lattice,

which can even undergo structural transitions in the same material [56]. In addition to the importance of vortex matter for the superconducting properties, it also provides a model system for the properties of condensed matter. The various states of vortex matter can usually be easily manipulated by experimental parameters, such as magnetic field, temperature or pressure, which gives them an advantage over their conventional counterparts. Additionally, the vortex matter is always confined to the superconducting sample, which simplifies the handling, especially for liquid phases.

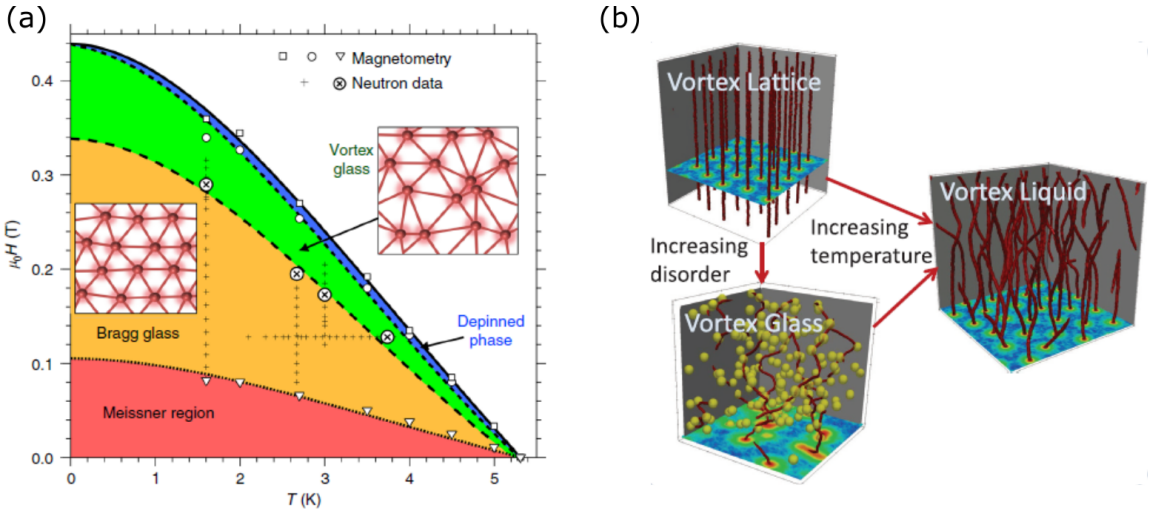

Figure 1.3: (a) Phase diagram of the different vortex matter states in vanadium based on magnetometry and neutron experiments. At low fields, the superconductor is in the Meissner state (red) and free of vortices. For higher fields, a vortex Bragg glass (orange) forms in the largest part of the superconducting phase. Close to the critical field, the vortices transition into a disordered state (green) and finally melt into a liquid (blue). (b) Visualizations of different vortex states computed using a time dependent GL theory. In a lattice, the vortices are straight and aligned to the magnetic field. They form an effectively two dimensional structure. A vortex glass is created by sufficient disorder in the material. The vortex lines jump randomly between the defects and pinning centers (yellow dots). With sufficient temperature, the vortices are strongly fluctuating and entangled with each other. Panel (a) is reprinted with permission from [59]. Copyright (2018) by Springer Nature. Panel (b) is reprinted with permission from [61]. Copyright (2016) by IOP Publishing.

1.3 Magnetic domains in superconductors

In the previous section, the various properties of superconductors have been treated primarily as homogeneous. However, like any other form of matter, the properties of a superconductor may be very inhomogeneous. Here, we present three very distinct inhomogeneous magnetic states which occur in superconductors. The selected examples illustrate the various length scales on which inhomogeneities may appear, ranging from a few micrometers to the macroscopic size of a sample. This broad bandwidth is due to the several interactions playing a role for the magnetic state of a superconductor.

The **critical state** in a type-II superconductor is shown in figure (1.4)(a) in a magneto-optical image. The image shows the average flux density in a circular sample of approximately 2 mm diameter, which is equivalent to the local vortex density. Light regions, such as the sample edge, indicate a high vortex density, while the dark region at the sample center is effectively flux-free. Concisely, this inhomogeneous flux distribution is due to two reasons. First, the vortex mobility is reduced due to strong pinning of vortices, e.g., at material impurities. Second, the sample geometry is cause for demagnetization effects affecting the external magnetic field. Since vortices are topological defects, they cannot be formed inside the superconductor, but have to enter and exit at the sample edges. As a result, the penetration and expulsion of vortices, as well as their redistribution inside the superconducting sample, are strongly restricted. Depending on the temperature and field history of a measurement, complex vortex distributions can be created in the sample [62]. The critical state will be discussed in detail in section (2.2).

The **intermediate state** (IS) is a microscopic phase separation found in type-I superconductors [63–65]. The IS is shown in figure (1.4)(b) in a magneto-optical image on the scale of some 100 μm. Here, the light regions correspond to areas in the flux-free Meissner state, while the dark areas are normal conducting and carry magnetic flux. Similar to the critical state, a nonzero demagnetization factor is essential for the IS to form. Due to the field enhancement at the sample surface, the superconducting state breaks down at a reduced external field, below the thermodynamic critical field [3]. Since this is a local effect, the superconductivity is not suppressed in the whole sample. Instead, the domain structure of the IS, consisting of normal and superconducting regions, emerges [66]. Energetically, the IS originates from an intricate balance between the domain interfaces, the bending of magnetic flux and the condensation energy of the superconducting state [67, 68].

The **intermediate mixed state** (IMS) is found in type-II superconductors with low GL parameter κ. It is similar to the IS in being a microscopic phase mixture, although on an even smaller scale of approximately 10 μm. However, the IMS consists of Meissner state and Shubnikov state domains and is therefore completely superconducting. Shown in figure (1.4)(c) are two Bitter decoration images, where the dark dots each represent the position of a single vortex. In these examples, the IMS has a bubble structure, with large flux-free Meissner state domains (light) separated by a mesh of vortex lattice domains (dark). In contrast to the critical state and the IS, the origin of the IMS lies in the microscopic properties of the superconductor, especially the vortex interaction. Due to a partial attraction, vortices tend to cluster together. Still, in order to observe a domain structure, as shown in the image, secondary effects such as demagnetization or pinning are necessary.

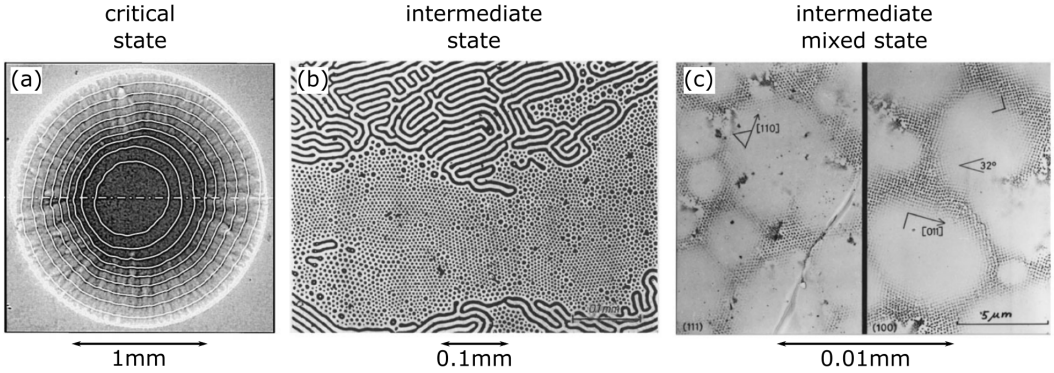

Figure 1.4: Optical images of inhomogeneous magnetic states in superconductors. (a) Magneto-optical image of the critical state in a YBaCuO disc (type-II, diameter $2\,\mathrm{mm}$, thickness $290\,\mathrm{nm}$). Lighter regions have a higher flux density. (b) Magneto-optical image of the intermediate state in a tantalum disc (type-I, diameter $5\,\mathrm{mm}$, thickness $33\,\mu\mathrm{m}$). The normal conducting domains are dark. (c) Decoration image of the intermediate mixed state in a niobium disc (intertype, diameter $4\,\mathrm{mm}$, thickness $1\,\mathrm{mm}$). Dark spots present single vortices. Panel (a) reprinted with permission from [69]. Copyright (1998) by Elsevier. Panels (b,c) reprinted with permission from [8]. Copyright (1987) by John Wiley and Sons.

1.4 The intermediate mixed state

The unusual properties of the intermediate mixed state (IMS) have been an ongoing research topic since its original discovery using the Bitter decoration technique [4, 5], both theoretically [8, 11, 13, 70] as well as experimentally [9, 10, 14, 47, 71–74]. Historically, the term type-II/1 superconductivity was coined for materials exhibiting the IMS [50], as an addition to the Ginzburg-Landau typology (cf. section (1.1)). As an explanation for the domain formation in the IMS, a partially attractive vortex interaction was postulated, which originates from an energetically favorable partial overlap of the vortices [11]. GL theory was, however, found to be unable to explain the behavior of superconductors with $\kappa \approx \kappa_0$.

An important **theoretical advancement** concerning the IMS poses the extended Ginzburg-Landau formalism (EGL) introduced by Vagov et al. [13], which will be discussed in detail in section (2.1). In essence, EGL is an expansion of BCS theory around the critical point at T_c and κ_0, also known as the Bogomolnyi point. In contrast to classical GL theory, EGL is therefore able to describe the phase region where the IMS occurs accurately. Moreover, it opens up a much more general phase space called intertype superconductivity, which is located in between the classical type-I and type-II (cf. figure (1.2)). In the intertype regime, we find a phase space corresponding to the former type-II/1, which features the vortex interaction required for the IMS with a long range attraction and short range repulsion. Ab initio calculations [13, 53] and Monte Carlo simulations [75] (cf. figure (2.2)) have shown that this non-monotonous interaction results in a domain structure characteristic for the IMS. In addition, the intertype regime includes further unusual vortex matter phases such as multi-quantum vortices and vortex liquid droplets.

While the IMS is an ongoing research topic, interest in magnetic domain structures in superconductors and vortex matter has been renewed by similar phenomena found in multi-band superconductors. The most prominent materials are MgB_2 [43, 76] and recently ZrB_{12} [44, 77] which are usually referred to as type-1.5 superconductors. Recent applications of EGL to multi-band superconductors with competing type-I and type-II properties have confirmed a very similar behavior to the intertype regime [13]. A thorough theoretical understanding of the experimental results is still limited due to the numerous secondary effects intervening in the IMS transition, such as described in section (2.2). Geometric effects like demagnetization create an inhomogeneous magnetic field distribution and therefore a global variation in the superconducting state. Pinning, on the other hand, affects the vortices on a microscopic scale.

Experimental studies of the IMS are, however, limited as well. Surface sensitive techniques, such as scanning tunneling microscopy [78], magnetic force microscopy [79] or magneto-optical imaging [80], allow to view the distribution of vortices and the domain structure directly. However, the properties observed at the sample surface may not be representative of the bulk due to surface defects and vortex branching. The bulk properties have been primarily investigated using neutron scattering techniques, since neutrons are sensitive to the magnetic structure and can penetrate a bulk sample [10, 14, 73]. In addition, muon spin rotation [81] can be used for bulk measurements. These techniques, however, do not allow to resolve the microscopic domain structure.

Reimann et al. started to approach the properties of magnetic domains in superconductors with a combination of techniques [14, 74]. These were selected to cover the different scales and properties of the domain structures. In the IMS in niobium single crystals, the vortex lattice crystallography was studied using small angle neutron scattering (SANS). The morphology of the larger domain structure was measured using very small angle neutron scattering (VSANS). In addition, the relatively novel technique of neutron grating interferometry (NGI) was used to observe the spatial distribution of domains on a millimeter scale. The neutron measurements were completed by global magnetization measurements using a vibrating sample magnetometer (VSM).

The hallmarks of the IMS in these experiments were a field independent vortex lattice constant coinciding with a domain scattering signal in VSANS and NGI. These features were found in two niobium single crystals with distinct pinning characteristics. In a sample of exceptional quality, the IMS was found to be inhomogeneous, depending on the magnetic state created by demagnetization. A sample of lower quality, undergoing a flux freezing transition, showed an inhomogeneous IMS as well. It is remarkable that the domain structure of the IMS was observed despite the very different pinning characteristics and vortex mobility. In the high pinning sample, the IMS domains were on the length scale of $1 - 10\,\mu$m. The domain size was increasing with higher fields and mostly constant over temperature. Especially the last point motivated a consideration of a domain formation process reminiscent of spinodal decomposition, instead of a nucleation and growth scenario.

1.5 Outline & main results

In this work, we continue the approach of using multiscale neutron techniques to further our understanding of the IMS in niobium as a prominent example of intertype superconductivity. We study the IMS transition in three sets of niobium single crystals with different levels of quality (chapter (4)). Our primary focus is the quantitative comparison of the vortex matter state in dependence on temperature, magnetic field and the pinning properties. Complementary to our measurements, we have used molecular dynamics type simulations (MDS) (chapter (6)). In a novel approach, the vortex interactions were implemented using EGL theory. Using MDS, the microscopic vortex positions and the IMS domain structure are directly accessible. Naturally, the simulations rely heavily on a multitude of parameters, which cannot be determined unambiguously. Therefore, we have performed several systematic parameter studies and used the results from our experiments to determine physically reasonable simulations. As in the experiments, the influence of pinning on the IMS was a focus point of the simulations.

Our **main results** highlight the universality of the intermediate mixed state, especially with respect to the pinning properties. In our field cooled experiments and simulations, the IMS was observed as a continuous rearrangement of vortices from a homogeneous lattice into increasingly dense VL domains. Thereby, a homogeneously distributed domain structure emerges. Experimentally, all our samples of distinct quality showed the IMS transition, albeit at different temperatures. The hallmark of the IMS is defined by a unique vortex separation, which shows the same temperature dependence in all samples. Outstandingly, the IMS occurs even below a global flux freezing transition. Conforming results were found in our simulations. Pinning, which has been varied both in strength and density of the pinning sites, could be observed to affect the IMS transition over several orders of magnitude in both parameters, without inhibiting the formation of domains.

This **thesis is organized** in the following way: In chapter (2) we will discuss the interaction between vortices in intertype superconductors, based on the extended Ginzburg-Landau formalism. Additionally, the impact on extrinsic properties, such as the sample geometry and material impurities, will be addressed. The following two chapters concern our experimental work. Chapter (3) starts with a summary of general neutron scattering theory which is then elaborated with respect to the specific experimental techniques we used: SANS, VSANS and NGI. Each section contains an elaboration on the respective scattering properties and a short summary of the instrumentation. In chapter (4), the experimental results will be presented and discussed, again separated by the experimental techniques. The chapter closes with a summary of our experimental findings. Chapters (5) and (6) cover our work with molecular dynamics simulations. Again, the fundamentals of the simulations are addressed first in chapter (5). This starts with an introduction to our algorithm and its adaption to vortex matter, which is followed by a definition of the experimental procedure we use for our simulations. Additionally, we discuss our evaluation methods using an exemplary simulation. The results of our simulations are presented in chapter (6). They are structured into multiple systematic

studies, each concerning a different set of parameters used to define the simulations. The first block concerns parameters which are related to the simulation procedure itself, while the second block addresses parameters representing sample properties. Again, the chapter is closed with a summary of our findings. Finally, we recap the results of this thesis in chapter (7), where we also address the interplay of our experimental and simulation work.

2 Vortex matter in superconductors

In chapter (1) we have discussed the wide variety of superconducting properties, classified either by their microscopic interaction properties or using the Ginzburg Landau (GL) parameter κ. The former is used to separate conventional from unconventional superconductors, which is by design a very crude distinction. In essence, it only describes, which materials are understood in the framework of BCS theory and which are not. This approach in itself reflects our limited understanding of the microscopic properties of superconductivity. In contrast, the distinction of type-I and type-II superconductors by using GL theory leaves no space for additional options. Later on, the deficiency of this approach has been acknowledged by the subdivision of type-II into the types II/1 and II/2, which are, however, not precisely defined. The limitation of GL theory is natural as it is strictly valid only at the superconducting critical temperature T_c. The recent theoretical works of Vagov et al. use an extended Ginzburg-Landau formalism to review the original distinction made with the GL parameter [13, 53, 75, 82]. Their result is a new, well defined intertype regime, which opens up between type-I and type-II below T_c. Figure (1.2) shows this region which its further subdivided into two intertype regimes.

Intertype superconductors are primarily defined by the inter-vortex interaction. In type-I and type-II, vortices are either purely attractive or purely repulsive, respectively. In contrast, the interaction found in the intertype regime can be non-monotonous. Additionally, multi-quantum vortices or multi-vortex droplets can be favored over the isolated single quantum vortices which define the original Shubnikov state in type-II materials. The unusual properties found in the intermediate mixed state (IMS), which is a major example of vortex matter outside the type-I/type-II dichotomy, can be readily explained using the novel vortex interactions found in the scope of EGL. In the IMS, vortices tend to stick together and form clusters. This behavior is straightforward, if the vortex interaction is non-monotonous, featuring a short range expulsion and a long range attraction.

In this chapter, we will introduce the EGL formalism, with a focus on the inter-vortex interaction, and discuss the resulting possibilities found in the intertype regime. As a main result, we will obtain an expression for the vortex-vortex interaction in dependence on κ and T. The different interactions found in the the intertype regime will be discussed with a special focus on the former type-II/1 regime where the IMS is found. In addition to this intrinsic vortex interactions, extrinsic influences on the vortex properties, such as pinning and geometric effects from the sample, will be addressed. As a whole, the chapter is designed to understand the features of vortex matter we encounter in our experiments (chapter (4)) and in our simulations (chapter (6)) of the intermediate mixed state.

2.1 Extended Ginzburg-Landau theory: Intertype superconductivity

In Ginzburg Landau (GL) theory, superconductivity is described as a second order phase transition in linear approximation in temperature. Strictly speaking, GL theory is only valid precisely at the superconducting critical temperature T_c. Therefore, the strict separation of type-I and type-II at $\kappa_0 = 1/\sqrt{2}$ is correct at T_c. However, at the critical point of GL theory at T_c and $\kappa_0 = 1/\sqrt{2}$, also known as the Bogomolnyi point [48, 49], the vortex matter in a superconductor is not well defined. Vortices do not interact with each other, which renders any vortex configuration energetically equal [48, 49] and causes an energetic degeneracy. At lower temperatures this degeneracy is lifted, which is however not included in GL theory. If treated correctly, the Bogomolnyi point opens up into an extended transitional region between type-I and type-II which is called the intertype regime [13, 83, 84].

Ginzburg Landau theory is included in BCS theory as an approximate case at T_c [85]. The extended Ginzburg Landau formalism takes the same approach as conventional GL theory, but includes higher order terms to extend its validity to lower temperatures. Since their EGL approach is especially aimed at treating the intertype regime, the approximation is based on the Bogomolnyi point. The expansion is then performed with respect to two parameters, $\tau = 1 - T/T_c$ for the temperature and $\delta\kappa = \kappa - \kappa_0$ for the GL parameter.

We note that the extended Ginzburg Landau theory developed by the group of Vagov et al. is controversially discussed [86]. To our knowledge, the criticism primarily concerns the extension to multi-band superconductors and the description of type-1.5 superconductivity. At the current time, we do not see any problems concerning the applicability of EGL theory to the conventional single band material niobium.

2.1.1 Introduction to the EGL formalism

The derivation of the extended Ginzburg-Landau (EGL) theory included in this section is primarily meant to introduce the basic approach of EGL theory. Furthermore, it focuses on the steps needed to calculate the vortex interaction. A full derivation and discussion of EGL theory can be found in [13].

Our aim is to calculate the energy of a vortex configuration as the Gibbs free energy $\mathfrak{G}$ of a superconductor. Since we are interested in the IMS, where vortices are straight lines along the magnetic field, Abrikosov vortices are assumed. Effectively, this reduces the formalism to the two dimensions perpendicular to the field direction. Accordingly, energies and related quantities will be expressed as length densities.

As a starting point of the EGL formalism, the Gibbs free energy density $\mathfrak{g}$ is divided into three terms, according to the two expansion parameters τ and $\delta\kappa$. Furthermore, the energy difference between the normal and superconducting state is considered.

$$\delta\mathfrak{g} = \mathfrak{g}_{\mathrm{SC}} - \mathfrak{g}_{\mathrm{NC}} = \mathfrak{g}_{\mathrm{GL}} + \mathfrak{g}_{\kappa}\delta\kappa + \mathfrak{g}_{\tau}\tau \tag{2.1}$$

Here, $\mathfrak{g}_{\mathrm{GL}}$ is the original Ginzburg-Landau contribution, while $\mathfrak{g}_{\kappa}$ and $\mathfrak{g}_{\tau}$ contain all terms linear in the corresponding expansion parameters. All terms of higher or mixed order are neglected as very small. The three leading contributions can be expressed as follows:

$$\mathfrak{g}_{\mathrm{GL}} = \frac{1}{2}(B-1)^2 + |\mathbf{D}\Psi|^2 - |\Psi|^2 + \frac{1}{2}|\Psi|^4 \tag{2.2}$$

$$\mathfrak{g}_{\kappa} = -\sqrt{2}B(B-1) - 2\sqrt{2}|\mathbf{D}\Psi|^2 \tag{2.3}$$

$$\begin{aligned}\mathfrak{g}_{\tau} =& (B-1)\left(\frac{1}{2}+c\right) - \frac{1}{2}|\Psi|^2 + 2|\mathbf{D}\Psi|^2 + |\Psi|^4 \\ &+ Q\left[\left|\mathbf{D}^2\Psi\right|^2 + \frac{1}{3}(\mathrm{rot}\mathbf{B}\cdot\mathbf{j}) + B^2|\Psi|^2\right] \\ =& \frac{L}{2}\left\{8|\Psi|^2|\mathbf{D}\Psi|^2 + \left[\Psi^2(\mathbf{D}^*\Psi^*)^2 + c.c.\right]\right\} + c|\Psi|^6\end{aligned} \tag{2.4}$$

$\mathbf{D} = \nabla + \imath\,\mathbf{A}$ is the gauge invariant gradient and $\mathbf{j} = 2Im[\Psi\mathbf{D}^*\Psi^*]$ is the supercurrent density. c, L and Q are scalar model parameters representing a class of isotropic s-wave superconductors in the clean limit.

For the calculation of δg, the order parameter Ψ of the configuration is needed, which is formally expanded in τ as well $\Psi = (\Psi_{\mathrm{GL}} + \tau\Psi_1 + ...)$. However, for the calculation of the Gibbs energy, all but the leading term of this expansion lead to higher order contributions in τ and $\delta\kappa$, which are neglected. Hence it is sufficient to directly use the original Ginzburg-Landau order parameter Ψ_{GL} in this context, which can be obtained using the original GL equations. For the task of calculating the energy of arbitrary vortex configurations, consisting of N vortices, Ψ_N is constructed from the single vortex order parameter Ψ_{v} as:

$$\Psi_N(\mathbf{r}) = e^{-\theta}\prod_i^N n^2\Psi_{\mathrm{v},i}\ ,\ \Psi_{\mathrm{v},i} = \Psi_{\mathrm{v}}(\mathbf{r}-\mathbf{r_i}) \tag{2.5}$$

where $\mathbf{r_i}$ are the vortex positions, and the newly introduced phase θ has to be obtained from solving the GL equations with this ansatz for a self consistent solution.

The total energy $\mathfrak{G}$ is then calculated by substituting Ψ_N into the Gibbs free energy density $\mathfrak{g}$ (equation (2.1)) and integrating over the volume of the sample. After lengthy rearrangements, $\mathfrak{G}$ can be expressed as:

$$
\begin{aligned}
\mathfrak{G} &\propto \left[\left\{\sqrt{2}\delta\kappa + \tau\,(1 - c + 2\,Q)\right\}\,\mathscr{I} + \tau\left\{2\,L - c - \frac{5}{3}Q\right\}\,\mathscr{J}\right] \\
\mathscr{I} &= \int |\Psi_{\mathrm{GL}}|^2\,\left(1 - |\Psi_{\mathrm{GL}}|^2\right)\,dV \\
\mathscr{J} &= \int |\Psi_{\mathrm{GL}}|^4\,\left(1 - |\Psi_{\mathrm{GL}}|^2\right)\,dV
\end{aligned}
\tag{2.6}
$$

With this expression of the Gibbs free energy, arbitrary vortex configurations can be evaluated in dependence of temperature and GL parameter. Thereby, the behavior of superconductors in the intertype regime can be thoroughly evaluated, e.g., in Monte Carlo type simulations. This approach, however, is quite extensive, and a much simpler alternative is to regard the two-vortex interaction instead and neglect possible many-body interactions. In the following section, results for the vortex-vortex interaction will be presented and discussed.

2.1.2 Vortex interactions of intertype superconductors

Starting from equation (2.5), the vortex-vortex interaction can be calculated as the total energy of a two-vortex system, which is denoted with the subscript vv. Since every vortex separation has to be treated separately, the result is limited to a finite set of vortex distances. However, the integrals $\mathscr{I}$ and $\mathscr{J}$ given in equations (2.6) can be expressed in a normalized way without explicit dependence on κ and T. They are shown in figure (2.1)(a). Here we only show the final result of the two-vortex potential V_{vv}, which uses the normalized integrals:

$$
\begin{aligned}
V_{\mathrm{vv}}(r) = \hat{V}\tau \Bigg[&\left\{1 - \sqrt{2}\kappa + \tau\,(1 - c + 2\,Q)\right\}\,\mathscr{I}_{\mathrm{vv}}\left(\frac{r\sqrt{\tau}}{\lambda_0}\right) \\
&+ \tau\left\{2\,L - c - \frac{5}{3}Q\right\}\,\mathscr{J}_{\mathrm{vv}}\left(\frac{r\sqrt{\tau}}{\lambda_0}\right)\Bigg] \\
\hat{V} = &\frac{\mu_0 H_{\mathrm{c},0}^2 \lambda_0^2}{2\pi}\kappa
\end{aligned}
\tag{2.7}
$$

The scaling factor $\hat{V}$ has units of energy per meter and makes use of the GL temperature scaling of λ_{L} and the thermodynamic critical field H_{c}. c, L and Q are again the parameters describing a class of isotropic s-wave superconductors in the clean limit. T_{c}, κ and $\lambda_{\mathrm{L}}(T)$ are used to define a specific model superconductor.

Figure (2.1)(b) shows examples of the two-vortex interaction V_{vv} at different κ at the reduced temperature $\tau = 0.5$. All curves tend to zero for large vortex separations and have a plateau at low distances. For sufficiently large positive $\delta\kappa$, the potential is decreasing monotonously with increasing separation. This corresponds to a purely repulsive interaction, as expected from type-II superconductors. In contrast, for large negative $\delta\kappa$, the potential is increasing monotonously. This purely attractive interaction results in a merging of vortices, which corresponds to the instability of single vortices in

a type-I superconductor. For $\delta\kappa \approx 0$, the interaction energy is non-monotonous. The observed curves can be broadly divided into three regimes. Close to type-II behavior ($\delta\kappa = 0.1$), the interaction remains positive at low separations, meaning single vortices are still preferred. However, the potential has a global negative minimum at low separations, which results in a preferred finite vortex separation. For lower values ($\delta\kappa = 0.05$), overlapping vortices become energetically favorable, with a negative potential at low separations. Still, the curve features a global negative minimum at larger separations. At $\delta\kappa = 0.0$, the low separation plateau and the global minimum merge into an extended region of constant energy. In this regime, single vortices become unstable. We note that with decreasing $\delta\kappa$, towards classical type-I behavior, many-body interactions become more important, which are not included in the two-vortex potential.

Figure (2.2)(a) shows a phase diagram of an intertype superconductor, where the different regimes are separated by κ_1^* and κ_s^*. The regime above κ_1^* contains the former type-II/1 and the IMS. The main feature of the vortex interaction here is a short range repulsion and long range attraction, which results in a preferred vortex separation. Typically, the vortices form a vortex lattice in this regime whose lattice constant is determined by the interaction minimum. In situations, where the average vortex density in a superconductor is lower than that preferred by the interaction, vortices may cluster into domains. The result is the phase mixture of vortex lattice and Meissner phase known as the intermediate mixed state. Below κ_1^*, the superconductor has a tendency of forming multi-quantum vortices. In the small regime down to κ_s^*, isolated multi-vortices are stable. Below this threshold, extended vortex liquid droplets are the usual configuration.

The results of an extensive Monte Carlo simulation series using EGL are shown in figure (2.2)(b), where the different regimes are well visible. The simulations were performed at various $\delta\kappa$ between -0.3 and $+0.3$, and for several flux densities B/B_c, up to the critical field B_c. Coded by color is the Cooper pair density which is 0 (blue) in the normal conducting state, and increases up to 1 (red) in the superconducting state. A large region at high κ and B is in the type-II phase and shows a mostly ordered vortex lattice. Above $0.8\,B_c$, the vortex matter melts into a liquid, preceding the breakdown of superconductivity. Towards lower κ and B, the type-II vortex lattice develops into a domain structure as known from the IMS. At $\delta\kappa < 0$, giant vortices and vortex liquid droplets are observed. Finally, the superconductor transitions to classical type-I behavior, where the normal and superconducting regions are separated and without individual vortices.

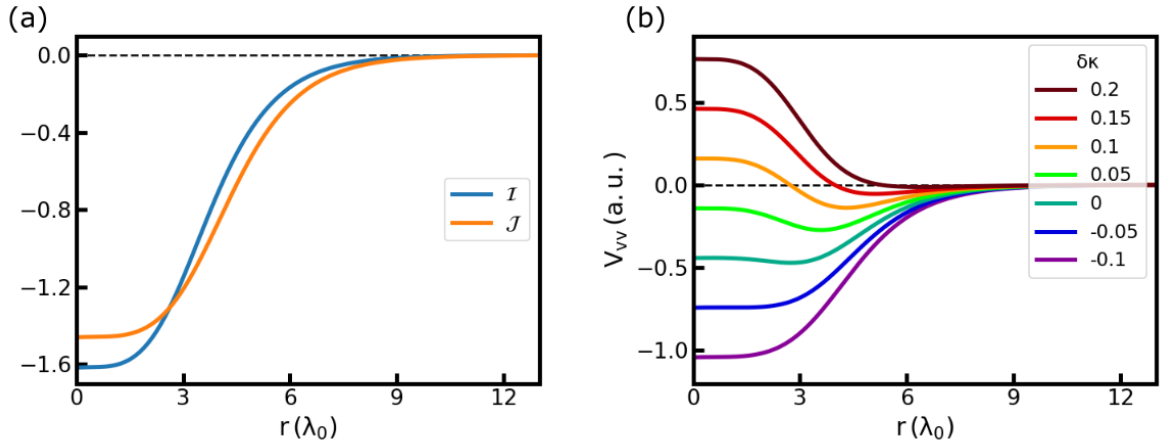

Figure 2.1: (a) Numerical results for $\mathfrak{I}_{vv}$ and $\mathfrak{J}_{vv}$ as defined in equation (2.6). Both integrals are independent of κ and T in EGL. (b) Vortex interaction V_{vv} (equation (2.7)) for several values of $\delta\kappa$ close to zero. For all curves, λ_0 is identical and $\tau = 0.5$. The character of the interaction changes from type-I ($\delta\kappa = -0.1$) to type-II ($\delta\kappa = +0.2$). The intertype regime is characterized by a global interaction minimum at finite distance r.

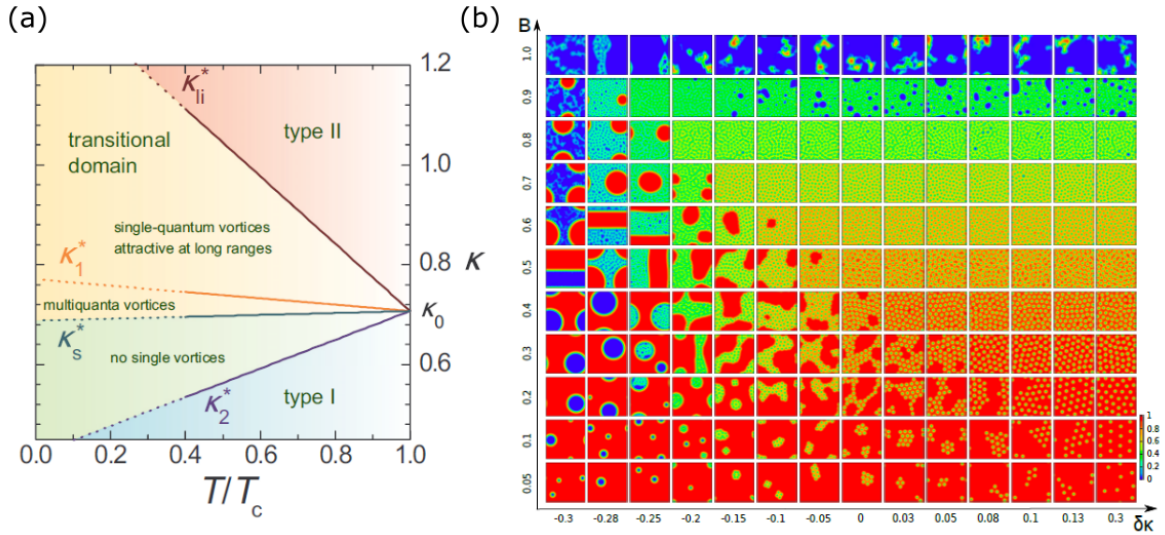

Figure 2.2: (a) Phase map of the intertype regime. Below T_c, the Bogomolnyi point opens up into an extended region between the classical type-I and type-II. The intertype region is further subdivided by the prominent vortex properties: single vortices are stable above κ_1^*, individual multi-vortices are stable between κ_1^* and κ_s^*, and below κ_s^* vortices merge into liquid droplets. (b) results of an extensive Monte Carlo simulation for various flux densities B and values of $\delta\kappa$. The color scale indicates the cooper pair density from zero (blue) to one (red). In the simulations, several vortex states are visible, including the ordered vortex lattice, the Meissner state, vortex lattice domains, a disordered state and a vortex liquid. Panel (a) reprinted with permission from [13]. Copyright (2016) by the American Physical Society. Panel (b) reprinted with permission from [75]. Copyright (2020) by Springer Nature.

2.2 Extrinsic influences on vortex properties

The properties of vortex matter are not only determined by the vortex-vortex interaction. Additionally, properties of the superconducting material, such as impurities and the sample shape, affect the vortex matter state. In an experiment, these effects may further depend on the measurement history which changes the observed properties significantly. In this following section, we give a summary of the most common effects encountered in experiment, which determine the magnetic properties of a superconductor.

Pinning

Pinning sites are material inhomogeneities, which exert an attractive interaction towards vortices. Examples are crystal lattice defects or grain boundaries [87], impurities [88] and surface defects [89] which locally reduce the superconducting order parameter. A similar situation is found at the core of a vortex, where the order parameter is suppressed completely. Placing a vortex on top of a such a defect reduces the overall loss of condensation energy. Effectively, this effect creates a short range attraction between vortex and pinning site. The range of interaction is of the order of the coherence length ξ_{GL}, while its strength is associated with the condensation energy [90]. A model for this interaction will be introduced (chapter (5)) and used (chapter (6)) with our molecular dynamics simulations.

Two extreme cases, individual pinning [3] and collective pinning [91], illustrate the different pinning mechanisms which can be encountered. In the first case, the pinning sites have a density much lower than the vortices and a relatively strong attractive potential. Single vortices are captured at the pinned sites, while most vortices are rather affected by the immobility of the few pinned vortices than by the pinning sites themselves. In contrast, the collective pinning features a much larger density of weak pinning centers. The interaction is too weak to trap a single vortex, but it introduces an inhomogeneous background potential which interacts with the vortex matter collectively. In either case, the vortex mobility is reduced by pinning.

If the pinning effects are strong enough, they can affect the ability of vortices to enter or leave a sample. In a changing magnetic field, these effects are described by the critical state model, which will be discussed in the following section (cf. figure (2.3)). A special case of the altered magnetic properties of a superconductor due to pinning is the flux freezing transition. Cooling a sample in an applied magnetic field usually leads to the expulsion of flux due to the Meissner-Ochsenfeld effect. If, however, vortices are sufficiently pinned, the flux expulsion is limited and typically inhibited completely below the critical temperature T_{f}.

Flux penetration in the critical state model

The entrance and expulsion of flux into a type-II superconductor in the presence of strong pinning is described by the critical state model [92]. In a clean sample, vortices entering the sample from the edges move to its center to reduce their line tension [93] (cf. figure (2.4)(a)). If pinning is strong enough to prevent the free movement of vortices,

magnetic flux accumulates at the sample edges instead (cf. figure (2.3)(a)). Generally, the diamagnetism of a superconductor is upheld by circular supercurrents around the sample edge. The current density has a maximum value j_c, which is determined by the cooper pair properties and is connected to the upper critical field H_{c2}. In the critical state model, however, the maximum current density j_{pin} is determined by the pinning strength of the vortices. If j_{pin} is exceeded, trapped vortices are unpinned by the Lorentz force acting on them, and they can penetrate further into the sample. Due to the changing flux distribution, the supercurrents decrease and a new steady state is reached where the vortices are pinned again. This situation is known as the critical state, because the current density is either at its critical value j_{pin} or zero. The flux density in a cylindrical sample is shown in figure (2.3)(b) for different points in a field loop.

A widespread application of the critical state model is the Bean model, where the critical current density j_{pin} is assumed to be field independent [94]. While the Bean model illustrates the principles of the critical state, it is only of limited use for real samples, especially at high magnetic fields. Therefore, additional models for the field dependence of j_{pin} were used [62, 95]. Exemplary magnetization loops for different field dependencies are shown in (2.3)(c), where the uppermost panel corresponds to the Bean model.

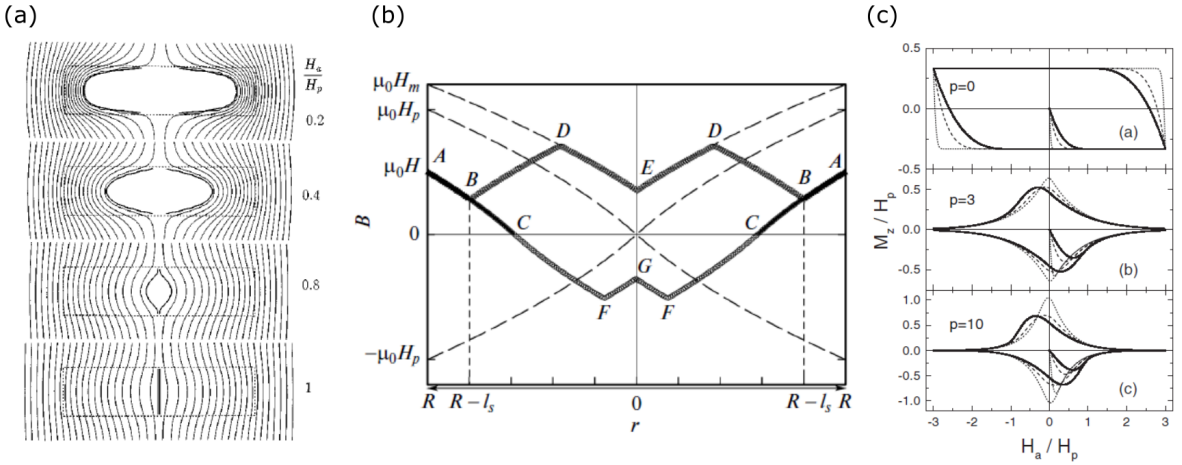

Figure 2.3: (a) Flux penetration into a cylindrical superconductor with strong pinning. The sample geometry leads to a strong bending of the individual vortices. (b) Internal flux density of a superconductor in the critical state model during a field loop. Path (ABC) corresponds to the initial flux entry. (ABDE) is a state in the decreasing branch after full penetration at the positive maximum field and (ABCFG) the state after reaching the negative maximum field. (c) Magnetization loops in the critical state for different models of the critical current ($p = 0$,3,10) and different sample shapes (solid, broken and dotted lines). In any case, the hysteresis curve is antisymmetric. Panel (a) reprinted with permission from [96]. Copyright (1998) by the American Physical Society. Panel (b) reprinted with permission from [62]. Copyright (2014) by Springer Nature. Panel (c) reprinted with permission from [95]. Copyright (2001) by IOP Publishing.

Geometric effects

Due to the diamagnetic properties of superconductors, the geometric shape of a sample leads to demagnetization effects [3]. The resulting enhancement of the magnetic field at the sample surface affects the field dependence of the equilibrium phase transitions. In type-I superconductors, demagnetization effects can lead to the formation of a magnetic domain structure, which is known as the intermediate state (IS) [63] (cf. section (1.3)). The IS is a transitional phase between the Meissner and the normal state in which normal and superconducting domains coexist on a micrometer scale. The properties of the IS are determined by a delicate interplay of multiple energetic contributions. Beside the condensation energy of the superconducting state, the interface energy between the domains and the line tension of the magnetic flux has to be taken into account. In type-II superconductors with low κ (also known as type-II/1, cf. section (1.1)) a similar reasoning is used to explain the intermediate mixed state (IMS) [97, 98]. However, in this case the domains consist of Meissner state and Shubnikov state regions. It is important to note that the vortex attraction, which enables the IMS, is not depending on the demagnetization effects, but a fundamental property of intertype superconductors (cf. section (2.1.2)). A further geometric effect are surface barriers, which cause an aggravated flux entrance into a sample [50]. For elliptical samples, a vortex line can penetrate the superconductor homogeneously over its full length. In any other geometry, the penetration initiates at the most exposed points [99] (cf. figure (2.4)(a)). This partial entrance is associated with additional deformations of the vortex line which is energetically unfavorable. Effectively, the flux entrance is delayed, which broadens the transition from Meissner to Shubnikov state and may increase the Meissner state above the equilibrium critical field. Since the expulsion of flux is not affected by geometric barriers, this effect creates an asymmetric behavior which is typically observed in hysteresis loops. Exemplary magnetization loops for samples with different aspect ratio are shown in figure (2.4)(b).

Summary

In an ideal type-II superconductor, the Meissner and Shubnikov state are well defined thermodynamic phases, defined by the critical fields $H_{c1}(T)$ and $H_{c2}(T)$, respectively. Ideal, in this case, refers to the absence of extrinsic effects such as the examples discussed in this section. Irrespective of the measurement history, an ideal superconductor will be in the identical state at any point of the phase diagram. However, due to effects such as pinning, the critical state and geometric influences, the magnetic state of a superconductor is heavily depending on the experimental procedure, especially the temperature and magnetic field history. In experiments, this usually results in inhomogeneous magnetic states and vortex distributions in a superconducting sample.

In a real sample, the ability of vortices to enter and exit the sample is greatly affected by the sample properties. The magnetization curves shown in figure (2.4)(b) illustrate the interplay of demagnetization and geometric barriers. The macroscopic magnetic state of the superconductor deviates strongly from the ideal case and is additionally

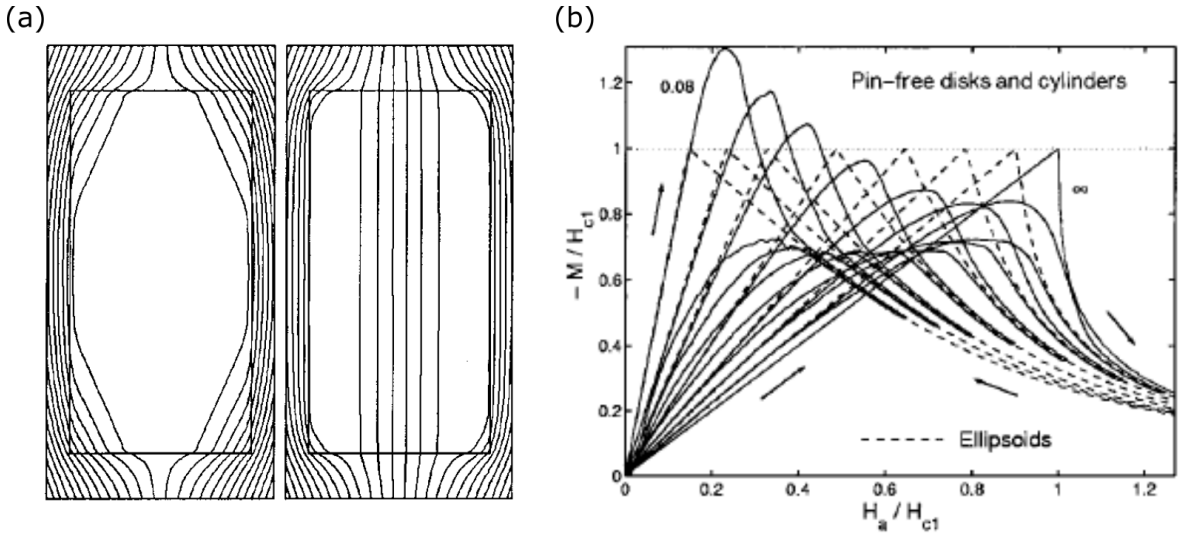

Figure 2.4: (a) Flux penetration into a pinning-free cylindrical superconductor. In the left image, the partial penetration of vortices due to geometrical barriers at the sample edges is visible. After fully entering the material, vortices move to the center of the sample where they accumulate. (b) Magnetization of a pinning-free superconductor with geometrical barriers (solid lines) with increasing and decreasing field (see arrows). Broken lines correspond to the magnetization of an elliptical sample. From left to right, the aspect ratio of the cylindrical samples (L/R) increases from 0.08 to ∞. Images taken from (a) [100], (b) [93]. Panel (a) reprinted with permission from [100]. Copyright (1999) by the American Physical Society. Panel (b) reprinted with permission from [93]. Copyright (2001) by AIP Publishing.

asymmetric regarding increasing and decreasing field. Similarly, measurements with increasing or decreasing temperature behave differently, because flux is either entering or leaving the sample.

In samples with pronounced pinning, the limited mobility of vortices leads to the inhomogeneous flux distribution described by the critical state. As shown in figure (2.3)(b), Meissner and Shubnikov state can even coexist in a sample. In such a case, a transition between the states, as defined by the critical fields, is no longer meaningful.

3 Experimental methods

In the following chapter, we introduce the experimental methods used to investigate the vortex matter in the in intertype superconductor niobium. In the intermediate mixed state (IMS) (cf. sections (1.3) and (2.1.2)), the vortex matter has a hierarchical structure on three length scales. On the smallest scale, the vortices form a regular vortex lattice with a lattice constant of approximately 200 nm. The domain structure found in the IMS, consisting of VL and Meissner state domains, has a typical length scale of a few μm. Additionally, inhomogeneities of the vortex matter on the mm scale of the sample may be present.

In order to obtain a complete picture of the IMS, we have chosen a set of experimental techniques which cover the range of different length scales in the IMS. The crystallographic properties of the vortex lattice (VL) have been studied using small angle neutron scattering (SANS). Similarly, the morphology of the larger IMS domains has been measured with very small angle neutron scattering (VSANS). Both techniques are closely related, but due to the different experimental setups and investigated structures we discuss them separately. On the sample scale, the real space distribution of IMS domains has been analyzed using neutron grating interferometry (NGI). Additionally, the global magnetic properties of the sample have been studied with a vibrating sample magnetometer (VSM).

In this following sections, the experimental techniques VSANS (section (3.3)), NGI (section (3.4)) and SANS (section (3.5)) will be presented. We start with a short introduction to scattering theory (section (3.1)) and a discussion of the neutron coherence volume (section (3.2)). Afterwards, each technique will be addressed separately, with a focus on the data acquired in the IMS. Additionally, the experimental setup will be presented. At the end of the chapter, the neutron techniques are summarized in table (3.1). The magnetization measurements using VSM will not be further discussed in this chapter. A description of this technique is available in [101] and references therein.

3.1 Neutron scattering

In the next section, we give a brief overview of the most important quantities used in scattering theory which are relevant for the discussion of the neutron techniques. A detailed derivation is omitted, since the topic of neutron scattering is treated in many textbooks. For an introductory approach to neutron scattering we recommend the book by Sivia [102], while an in-depth discussion can be found in the book by Squires [103].

Commonly, scattering is introduced via the interaction of neutrons with single atoms, or, more precisely, their nuclei via the strong nuclear force. The scattering strength is quantified by the scattering length b which depends on the isotope and the spin of the neutron. For nuclear scattering with thermal to cold neutrons, the neutron wavelength λ_N is much larger (typically a few Å) than the nuclei and the associated interaction range (approximately 10^{-4} Å). Therefore, the interaction can be described as point-like and isotropic. Simultaneously, λ_N is of the same order as the atomic separations in a crystal lattice. This leads to the well known interference effect of scattered neutrons observed in nuclear diffraction experiments. In addition, neutrons carry a magnetic moment μ_N, which allows an interaction with the magnetic moment of the atoms. The atomic magnetization field $\mathbf{M}(\mathbf{r})$ is due to the nucleus and the electron shell and is therefore on the length scale of an Å. Due to the size and shape of $\mathbf{M}(\mathbf{r})$, the magnetic interaction is neither point-like, nor isotropic.

On a scale of $\approx 10\,\mathrm{nm}$ and above, the individual atomic positions loose relevance. The scattering properties of a material, both nuclear and magnetic, can be described by a continuous scattering length density $\rho(r)$. This is used, e.g., for nanoparticles, magnetic domains in metals or superconducting vortex matter. In the experiments presented in this work, the superconducting vortices and vortex matter domains are on a scale much larger ($\approx 100\,\mathrm{nm}$ and $\approx 10\,\mu\mathrm{m}$, respectively) than atomic separations and the neutron wavelength. The interaction of neutrons with the vortex matter depends fundamentally on the Zeeman interaction, and the scattering length density can be expressed using the local flux density $B(\mathbf{r})$:

$$\rho\left(\mathbf{r}\right) = \frac{g_\mathrm{N}\, B\left(\mathbf{r}\right)}{4\,\Phi_0} \tag{3.1}$$

Here, $g_\mathrm{N} \approx -3.826$ is the g-factor of a neutron and $\Phi_0 = \hbar/2e$ is the magnetic flux quantum. The vortex matter in a superconductor is not correlated with the material structure, such as crystallites, so that only magnetic scattering is observed. This is not generally the case, as, e.g., in magnetic nanoparticles or ferromagnetic domains, the magnetic and material structure are usually identical or coupled [104].

In the Born approximation, a scattered neutron is modeled as a spherical wave originating at the point $\mathbf{r}$ with the amplitude given by $\rho(\mathbf{r})$ [103]. Scattered neutrons from all points of a sample interfere and result in a measurable intensity, which is in this way directly linked to the scattering length density. In the far field, the interference pattern under a specific scattering angle θ can be calculated by the Fourier transform of $\rho(\mathbf{r})$.

$$f\left(\mathbf{q}\right) = \int \rho\left(\mathbf{r}\right) \exp\left(\imath\, \mathbf{r}\cdot\mathbf{q}\right) d\mathbf{r} \tag{3.2}$$

$f(\mathbf{q})$ is called the scattering function, which contains the amplitude and phase of the interference pattern. $\mathbf{q} = \mathbf{k}_\mathrm{f} - \mathbf{k}_\mathrm{i}$ is the wave vector transfer of a scattered neutron, where $\mathbf{k}_\mathrm{i}$ is the initial, and $\mathbf{k}_\mathrm{f}$ the final value. For elastic scattering, i.e. no energy transfer between sample and neutron, $\mathbf{q}$ is related to the scattering angle θ as $|\mathbf{q}| = 4\pi \sin(\theta)/\lambda_N$.

In an experiment, only the scattering intensity can be measured. This is expressed as the differential scattering cross section, which describes the probability of a neutron to be scattered into a specific direction, indicated by the solid angle Ω:

$$\frac{d\sigma}{d\Omega}(\mathbf{q}) = |f(\mathbf{q})|^2 \tag{3.3}$$

Due to this experimental limitation, $\rho(\mathbf{r})$ cannot be determined from the measured signal. However, analogue to the scattering function f, the scattering cross section can be related to the autocorrelation function $\gamma(\mathbf{r})$ via Fourier transform.

$$\frac{d\sigma}{d\Omega}(\mathbf{q}) = \int \gamma(\mathbf{r}) \exp(\imath\, \mathbf{r} \cdot \mathbf{q})\, d\mathbf{r} \tag{3.4}$$

γ is connected to the scattering length density as:

$$\gamma(\mathbf{r}) = \int \Delta\rho(\mathbf{r}) \cdot \Delta\rho(\mathbf{r} + \mathbf{R})\, d\mathbf{R} \tag{3.5}$$

where we use the scattering length density contrast $\Delta\rho(\mathbf{r}) = \rho(\mathbf{r}) - \overline{\rho}$, with the mean value $\overline{\rho}$ of a sample.

A depiction of the autocorrelation function is shown in figure (3.1) on the example of an individual spherical particle. Geometrically, $\gamma(\mathbf{r})$ is defined by the overlap of the particle with a copy of itself, which is displaced by the vector $\mathbf{r}$. Consequentially, $\gamma(0)$ is always the maximum value of the correlation function. Additionally, for displacements larger than the particle diameter, the correlation is zero. $\gamma(r)$ and the differential scattering cross section defined by it are shown in panels (b) and (c) of the figure, respectively.

Due to the small scattering angles in SANS and VSANS, the wave vector transfer in direction of the neutron bean (z direction) q_z is typically negligible. Therefore, the scattering cross section is restricted to $q_z = 0$, and only the structural information perpendicular to the neutron beam is accessible. Corresponding to this simplification, a further definition of the correlation function denoted G is commonly used:

$$G(x,y) = \int \gamma(x,y,z)\, dz = \int \frac{d\sigma}{d\Omega}(q_x,q_y,0) \exp(\imath\, (q_x\, x + q_y\, y))\, dq_x\, dq_y \tag{3.6}$$

It is worth noting that the integrated scattering probability σ_{int} is connected to the auto correlation function G as:

$$\int \frac{d\sigma}{d\Omega}(q_x,q_y,0)\, d\Omega = \sigma_{\text{int}} = \lambda_{\text{N}}^2\, G(0,0) \tag{3.7}$$

We emphasize that the scattering cross section obtained in an experiment only measures the scattering intensity, not the complex scattering amplitude. Therefore, only the autocorrelation function can be determined, from which $\rho(\mathbf{r})$ cannot be uniquely inferred.

In practice, the scattering cross section is often divided into two multiplicative contributions: the form factor F and the structure factor S. This is possible, if the scattering system is made up from a number of individual sections, such as molecules, nanoparticles or vortices. The form factor describes the scattering pattern caused by a single section. In contrast, the structure factor contains the distribution of parts in the whole system and describes the interference effect of scattering from separate sections. For our experiments on superconducting vortex matter, the form factor and the structure factor are very different in the cases of the IMS domains and of the vortex lattice. Therefore we will discuss the usage of these terms in the respective sections on VSANS (section (3.3)) and SANS (section (3.5)), separately.

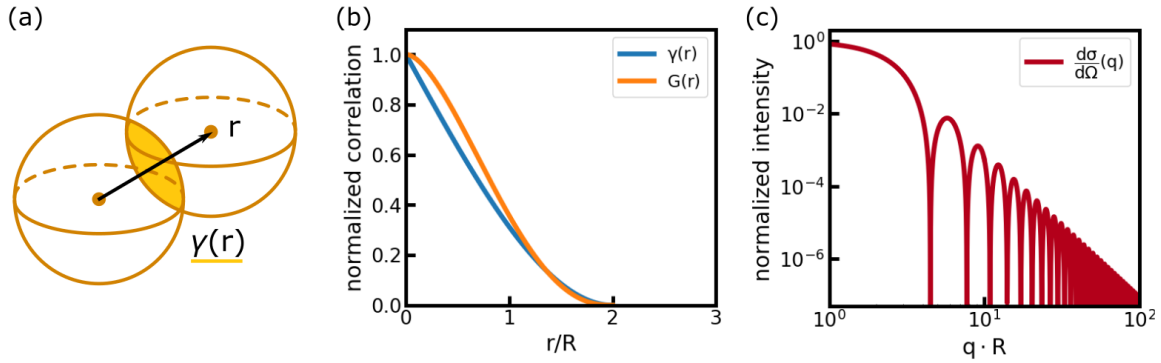

Figure 3.1: (a) Visualization of the correlation function γ on the example of a spherical particle with homogeneous scattering length density. $\gamma(\mathbf{r})$ corresponds to the overlap of the particle with itself when it is displaced by the vector $\mathbf{r}$. (b) Corresponding result of $\gamma(r)$ and $G(r)$. Since the particle is isotropic in this example, the correlation functions are independent from the direction of $\mathbf{r}$. (c) differential scattering cross section for the spherical particle.

3.2 Neutron coherence volume

In terms of neutron instrumentation, the structures present in superconducting vortex matter are very large. In the studies performed in this work, the vortex lattice has a lattice constant of $a_{\mathrm{VL}} \approx 0.2\,\mu$m, and the IMS domains are in the range of a few microns. While structures of these length scales can be measured, they approach the resolution limit of the instruments we used. In this case, the resolution is not merely a smearing effect, which decreases the accuracy of our results. Instead, the measurements may be distorted and give entirely wrong answers. Therefore, it is necessary to discuss in detail, what information can be obtained with our experiments.

The intensity measured in an experiment is given by the scattering cross section (equation (3.4)), which is equivalent to the correlation function (equation(3.5)). Both equations are derived under the assumption that incoming neutrons are perfect plane waves with a well defined phase relation at any point in the sample. In a real experiment, this is not the case, and the plane wave approximation only holds true over a small coherence volume. The limitation of neutron coherence is mainly due to two effects: First, the origin of a neutron is not precisely defined. Usually, a pinhole defines the effective size of the neutron source. Second is the wavelength of a neutron, which has an uncertainty due to the wavelength spread of the employed velocity selector or monochromator. Figure (3.2)(a) can be understood as the progressing plane wave character of a neutron originating from a pinhole.

The scattering observed in an experiment is actually an average of signals originating from any point in the sample. At each point, the coherent scattering is restricted to the structure contained in the coherence volume. This situation is shown in figure (3.4)(b) for one exemplary scattering position. Only the fraction of the sample (yellow) in the coherence volume (blue) contributes to the coherent signal observed at the detector (green arrows). In contrast, the whole sample contributes to the incoherent scattering background (green and red arrows).

If the coherence volume is sufficiently larger than the typical size of the scattering structure, the effects of the limited neutron coherence reduce to a smearing effect. In this case, a higher correlation volume yields a higher resolution of the measured signal. However, if the scattering structure is on a similar or larger scale than the coherence volume, the signal obtained in a measurement is strongly distorted. Any long range correlations of a structure, which are beyond the coherence volume, do not contribute to the measurable signal. Only local features, such as the edges of large particles or domains, are still visible in the coherent scattering. The information obtained in this case is comparable to the well-known Porod regime, which is routinely evaluated in scattering experiments [102].

In figure (3.2)(a) the emerging coherence from an incoherent source is shown, using a depiction of the Cittert-Zernike theorem [105, 106]. Thereby, the interference pattern created by the pinhole is representative of the emerging coherence. The growing white spaces along the beam direction can be understood as the coherence volume of a neutron, where the phase relation is well defined. For the coherence volume, an ellipsoid shape can be assumed, which is asymmetric in beam direction (z) and perpendicular to it (x,y) in most cases. The diameters along its main axes are referred to as coherence length $\zeta_{x,y,z}$ in the appropriate direction.

Perpendicular to the beam, the coherence length has been derived as [107]:

$$\zeta_{x,y} = \frac{L_{\mathrm{col}}\,\lambda_{\mathrm{N}}}{\pi\,d_{\mathrm{pin}}} \tag{3.8}$$

λ_N is the neutron wavelength, d_{pin} is the diameter of the pinhole or more generally the neutron source, and L_{col} is the collimation length between pinhole and sample. $\zeta_{x,y}$ is primarily defined by the instrument geometry, particularly the beam collimation L_{col}/d_{pin}. It is furthermore changing along the traveling path of the neutron. Note that, if the pinhole is asymmetric, the coherence volume is anisotropic as well.

In direction of the beam, ζ_z depends primarily on the wavelength spread of the neutrons $\Delta\lambda_N$ [107]:

$$\zeta_z = \frac{\lambda_N^2}{\Delta\lambda_n} \tag{3.9}$$

ζ_z is constant over the neutron flight path and is typically significantly lower than $\zeta_{x,y}$.

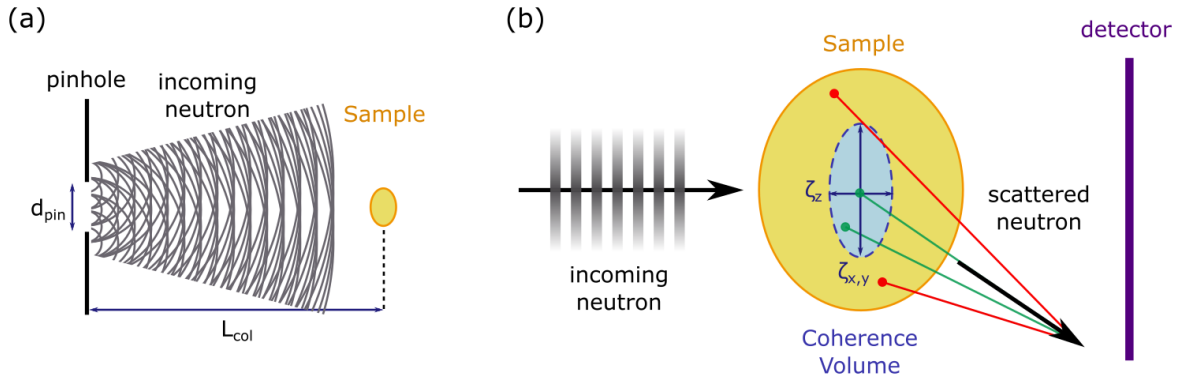

Figure 3.2: (a) Visualization of the increasing beam coherence from an incoherent source (pinhole) to the sample. We use the Cittert-Zernike theorem [105, 106], which states that the beam correlation corresponds to the interference pattern from point sources focused on the sample position. The interference is depicted using the Huygens principle (referring to figure 1 of [107]). (b) The incoming neutron can locally be modeled by a plane wave with a limited coherence volume which is characterized by the coherence length in beam direction ζz and perpendicular to the beam $\zeta_{x,y}$. Scattered waves can only interfere coherently, if they originate from within the coherence volume (green arrows). However, the whole sample does contribute to incoherent scattering (green and red arrows).

3.3 Very small angle scattering of magnetic microstructures

The typical size of the IMS domains lies in the low micrometer range, which corresponds to scattering angles of cold neutrons in the order of 0.01°. We refer to this regime as very small angle scattering (VSANS). In this work, VSANS measurements were used to investigate the morphology of the magnetic IMS domains.

Diffuse scattering from magnetic domains

In order to interpret the data obtained with VSANS, we need a model describing the IMS domain structure. The morphology, however, can be, e.g., insular or laminar [108] and is not known a priori. For examples of possible domain structures refer to section (1.3). In this case of an unknown domain structure, it is not possible to define a form factor for the single domains and a structure factor for the domain distribution separately. Especially in laminar structures, both contributions are difficult to separate. Furthermore, the domains may be anisotropic and varying strongly in size and orientation. Consequentially, it is difficult to determine the scattering cross section (equation (3.4), or the correlation function (equation (3.5)) of the system a priori. However, the general structure of the scattering signal is well reflected in the phenomenological model function [109]:

$$\frac{d\sigma\left(|\mathbf{q}|\right)}{d\Omega} = I_{\max}\frac{\left(1+\frac{\beta}{2}\right)\left(\frac{q}{q_{\max}}\right)^{2}}{\frac{\beta}{2}+\left(\frac{q}{q_{\max}}\right)^{2+\beta}} \tag{3.10}$$

The equation was originally derived to describe the two-phase mixtures emerging in the context of spinodal decomposition, but has since been successfully used for the IMS [14]. While the actual domain structure cannot be determined using this model, it allows us to analyze some general properties.

The main features of equation (3.10) are a peak at $q_{\max}$ and a power law decay at high q. $q_{\max}$ characterizes the correlation length of the domain morphology:

$$\xi_{\mathrm{IMS}} = \frac{2\,\pi}{q_{\max}} \tag{3.11}$$

For the IMS domains we expect values of $\xi_{\mathrm{IMS}} \approx 10\,\mu\mathrm{m}$ and $q_{\max} \approx 10^{-4}/\text{Å}$. The domain correlation corresponds to the typical distance between domains of the same phase. Especially for anisotropic domains, such as a laminar structure, ξ_{IMS} represents a mean value which is rather defining a scale than a definite value. The exponent β is determined by the dimensionality d of the domains, with two distinct cases. If the two phases are separated by smooth boundaries, $\beta = d+1$. For rough and entangled boundaries, $\beta = 2d$. Therefore, we expect $\beta = 3$ to 4 for strictly two dimensional IMS domains.

Magnetic domain scattering contrast

Not included in the model function (equation (3.10)) is the intensity of the scattering signal. For the correct normalization we use the macroscopic scattering cross section $\Sigma = \sigma_{\mathrm{int}}/V$. Σ has been derived for arbitrary two phase systems as [110]:

$$\begin{aligned} \Sigma &= \left(\lambda_{\mathrm{N}}\,\Delta\rho\right)^{2}\,\nu\,(1-\nu)\,L_z \\ L_z &= G(0)/\gamma(0) \end{aligned} \tag{3.12}$$

where ν is the volume fraction of one of the two phases and L_z characterizes the correlation of the system in beam direction.

The scattering length contrast $\Delta\rho$ can be deduced from the magnetic properties of the domains. We assume that the vortex matter domains are sufficiently larger than the vortex separation. In this case, we neglect the magnetic field profile of the individual vortices and instead work with an average magnetic flux density B_{IMS}. The Meissner state domains are assumed to be perfectly free of magnetic flux. Using equation (3.1), we calculate the scattering length density ρ, which is zero in the Meissner domains and finite in the vortex domains. The scattering length contrast is then given by:

$$\Delta\rho = \frac{g_{\mathrm{N}}\, B_{\mathrm{IMS}}}{4\,\Phi_0} \tag{3.13}$$

The fraction of the vortex domains is given as $\nu_{\mathrm{VL}} = \overline{B}/B_{\mathrm{IMS}}$, with the average flux density in the sample $\overline{B}$. Using these results, we can express the macroscopic scattering cross section as:

$$\Sigma = \left(\frac{g_{\mathrm{N}}\,\lambda_{\mathrm{N}}}{4\,\Phi_0}\right)^2 \overline{B}\,\left(B_{\mathrm{IMS}} - \overline{B}\right)\,L_z \tag{3.14}$$

Instrumental setup

The VSANS experiments shown in this work were performed at the beamline KWS-3 at MLZ [111]. The instrument is illustrated schematically in figure (3.3). It is located at the end of a focusing neutron guide and has a cold spectrum with maximum flux at 12.8 Å. A velocity selector is used for monochromatation. Instead of a collimation approach, the neutron beam is projected from a pinhole onto the detector using a torodial mirror. This way, the size of the direct beam on the detector is reduced which makes lower scattering angles discernible.

For all data presented in this work, a neutron wavelength of $\lambda_{\mathrm{N}} = 12.8\,\text{Å}$ was used with a spread of 20 %. The source aperture has a size of $1.5 \times 1.5\,\mathrm{mm}^2$, and the sample is placed 10 m in front of the detector. The resolution was determined from the direct beam as $5 \cdot 10^{-5}/\text{Å}$.

The coherence lengths of the instrument are $\zeta_{x,y} = 4\,\mu\mathrm{m}$ and $\zeta_z = 7\,\mathrm{nm}$ (equations (3.8) and (3.9)). In these calculations, a possible influence of the neutron mirror of KWS-3 is neglected. Since the domain size is expected to be in the low micrometer range, $\zeta_{x,y}$ and ξ_{IMS}, are probably similar and the domain morphology may not be fully resolved. This has primarily two effects: The position of the correlation peak described by the model function (equation (3.10)) is shifted to a higher value of q, corresponding to a smaller correlation length. In addition, the scattering intensity is reduced. In an experiment, it is difficult to tell if the full correlation is measured, and if an increasing signal is due to a changing domain size or a change of the scattering contrast. The coherence in beam direction ζ_z is certainly much lower than the domain size and correlation in this direction. However, since our measurements do not access this information, this poses no further obstacle.

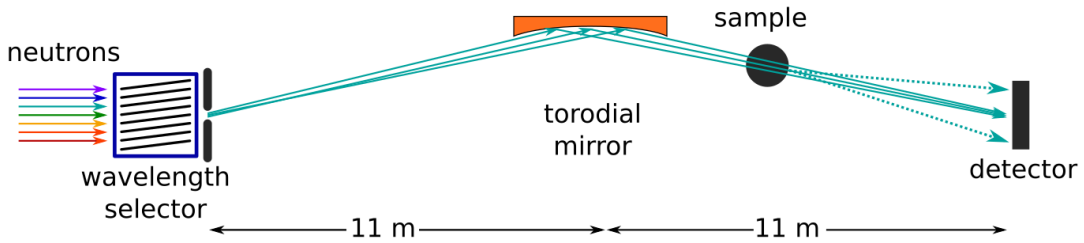

Figure 3.3: Schematic setup of the VSANS instrument KWS-3. The instrument is situated at the end of a focusing neutron beam, where the incident neurons are monochromatized by a velocity selector. From a pinhole, the divergent beam is projected onto the detector via a torodial mirror. The sample can be placed between the mirror and detector to adjust the resolution.

VSANS data

Exemplary data of the VSANS measurements is shown in figure (3.4). The reference data was taken above the superconducting phase at 12 K and zero magnetic field. It is shown in linear (a) and logarithmic (b) color scale. The direct beam has a slightly asymmetric shape and is wider along the q_x direction by $\approx 25\%$. Panel (c) shows data measured in the IMS, after field cooling in $\mu_0 H_{\text{ext}} = 40\,\text{mT}$ to 4 K, again on a logarithmic scale. From the raw data images, the scattering in the IMS is not obvious, although $\approx 14\%$ of incident neutrons are scattered. The radial averages of the reference and data measurement are shown in panel (d) on a double logarithmic scale. A difference is in the low-q intensity and the curve shape above $q \approx 10^{-4}/\text{Å}$.

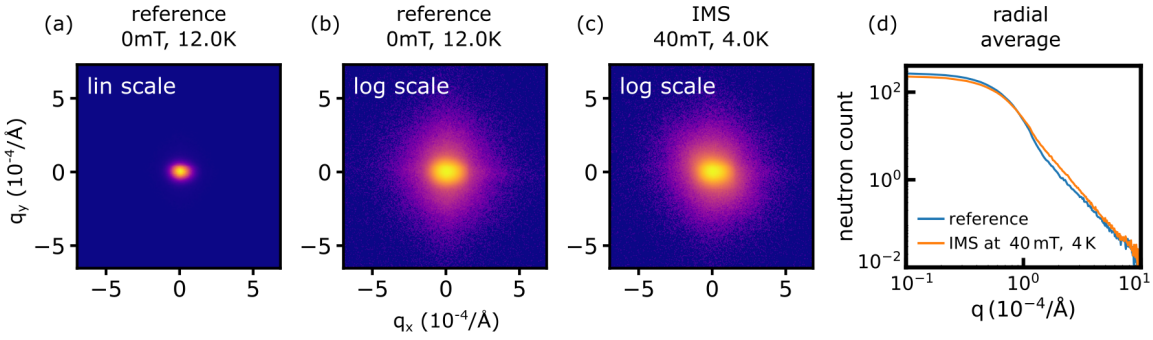

Figure 3.4: Exemplary raw data of VSANS measurements. The reference image was taken in the normal conducting state and is shown on a linear (a) and logarithmic (b) color scale. It shows a slight anisotropy of the direct beam by $\approx 25\%$. The data image taken in the IMS was field cooled in 40 mT to 4 K and is shown on a logarithmic scale (c). A difference between reference and data image is not visible in the raw data despite a scattering rate of $\approx 14\%$. Panel (d) shows radial averages of reference and IMS data on a double logarithmic scale. The additional magnetic scattering due to the IMS domains is visible above $q \approx 10^{-4}/\text{Å}$.

3.4 Neutron grating interferometry of magnetic microstructures

NGI is an imaging technique, which measures the transmission, refraction and scattering of neutrons simultaneously. A detailed description of the method can be found in [112]. Here, we focus on the scattering signal, which is used to investigate the spatial variation of the IMS domain morphology.

The dark field image

NGI is based on the Talbot-Lau interference effect, which is introduced by a linear phase grating G_1 [113, 114]. For the practical application, typically two additional absorption gratings are required (G_0 and G_2), whose functions are discussed further below (cf. figure (3.5)). At the detector position, this produces an intensity oscillation with the periodicity of the grating. Placing a scattering sample in the neutron beam reduces the interference effect. The process is sketched in figure (3.6). The interference pattern is quantified by the visibility V, which is the ratio of the amplitude to the mean of the intensity oscillation.

Experimentally, scattering is measured in the dark field image (DFI). The value of the DFI is defined via the visibility of the interference pattern with sample V_s and without sample V_0.

$$\mathrm{DFI} = \frac{V_\mathrm{s}}{V_0} \tag{3.15}$$

From a theoretical side, the DFI has been derived as [112] :

$$\mathrm{DFI} = \exp\left(\Sigma\, t\left(\frac{G\left(\xi_\mathrm{NGI},0\right)}{G\left(0,0\right)} - 1\right)\right) \tag{3.16}$$

which accounts for multiple scattering. Σ is the macroscopic scattering cross section, as defined in equation (3.14) for VSANS, and t is the thickness of the sample. The correlation function G (equation (3.6)) describes the effectiveness of a scattering system to destroy the interference pattern. Due to the line gratings used in NGI, $G(x,y=0)$ can only be evaluated perpendicular to the grating lines.

ξ_NGI determines the range of sensitivity of the experimental setup. It translates roughly to the length scale of structures which can be observed.

$$\xi_\mathrm{NGI} = \frac{\lambda_\mathrm{N} L_\mathrm{s}^\mathrm{eff}}{p}\ ,\ L_\mathrm{s}^\mathrm{eff} = \begin{cases} (L+d-L_\mathrm{s})\frac{d}{L} & \text{for } L_\mathrm{s} > d \\ L_\mathrm{s} & \text{for } L_\mathrm{s} < d \end{cases} \tag{3.17}$$

Here, p is the periodicity of the interference pattern and λ_N is the neutron wavelength. $L_\mathrm{s}^\mathrm{eff}$ is the effective distance between sample and detector, which is depending on the placement of the sample on either side of the phase grating. L_s is the actual sample-detector distance, L is the length from the source to the phase grating, and d is the separation between phase grating and detector.

NGI stepping scan

In principle, only one grating (G_1) is needed for the operation of an NGI. However, for practical reasons, two additional gratings are introduced into the beamline (cf. figure (3.5)). G_1 is the phase grating which generates the Talbot-Lau interference effect. The gratings G_0 and G_2 are additional absorption gratings. The source grating G_0 ensures the spatial coherence of the neutron beam. Each grating line creates a mutually incoherent line source, whose interference patterns overlap at the detector position. While a sufficiently small pinhole could be used instead, the neutron intensity would be decreased to an impractical level. G_2 is required to analyze the interference pattern, which has a sub-pixel periodicity. This analyzer grating has a periodicity matched to the interference pattern. As a result, it blocks a certain part of the intensity oscillations, e.g., all maxima. The whole Talbot pattern can be measured by shifting G_2 over one period in small steps and thereby measuring the full pattern. This approach is known as a stepping scan. In fact, any of the three gratings can be used for stepping with identical results. The positioning and periodicities of all gratings have to fulfill a set of geometric conditions for optimal performance, which are described in [115].

Instrumental setup

The NGI experiments shown in this work were performed at the beamline ANTARES at MLZ [115, 116]. ANTARES is an imaging instrument and is shown schematically in figure (3.5). The neutron spectrum used at ANTARES is a mixture of thermal and cold neutrons with a peak intensity at 1.8 Å. For collimation, a pinhole with a diameter between 2 and 36 mm can be selected. Afterwards, the beam can be monochromatized with a velocity selector or a double crystal monochromator. For the detection, combinations of different scintillation screens and CCD cameras are available.

For the data presented in this work, a neutron wavelength of $\lambda_\mathrm{L} = 4\,\text{Å}$ was used, which is the optimal wavelength of the setup. We used the velocity selector, which has a spread of 10 %. For collimating the beam, the pinhole with 35.68 mm diameter was used, which corresponds to $L/d = 250$. Due to the cryomagnetic sample environment, the sample-detector distance is large at $L_\mathrm{s} = 0.2\,\mathrm{m}$. Therefore, the spatial resolution is limited to $\approx 500\,\mu\mathrm{m}$. The correlation length of the NGI was calculated as $\xi_\mathrm{NGI} = 1.9\,\mu\mathrm{m}$.

The coherence lengths of the NGI are calculated as $\zeta_{x,y} = 2\,\mu\mathrm{m}$ and $\zeta_z = 4\,\mathrm{nm}$ (equations (3.8) and (3.9)). Similar to the VSANS measurements at KWS-3, $\zeta_{x,y}$ is probably lower than the IMS domain correlation ξ_IMS. Therefore, the correlation function $G(\xi_\mathrm{IMS})$ and the scattering cross section Σ cannot be expected to include the full domain morphology. Measured values of the the DFI are unreliable. However, the main application of NGI concerns the spatial homogeneity of the IMS domains on the millimeter scale of the sample. Therefore, the absolute value of the DFI is not as important as the quantitative results of the VSANS measurements. For ζ_z, again the reasoning for VSANS measurements apply. The coherence in beam direction is much lower than the domain correlation in this direction. However, since this information is not studied, this limitation does not affect the experiments.

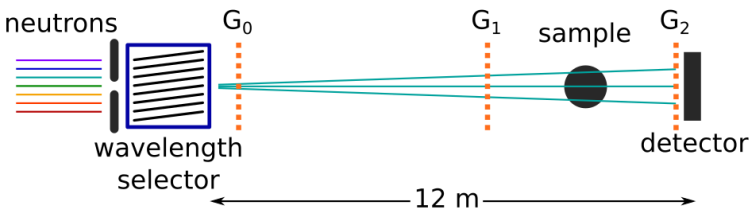

Figure 3.5: Schematic setup of the NGI instrument at ANTARES. The incident neutron beam first passes a pinhole for collimation. Afterwards, it is monochromatized by a velocity selector. The three gratings of the interferometer are placed between the selector and the detector. G_0 is the source grating, generating virtual coherent line sources. G_1 is the phase grating which induces the Talbot-Lau interference pattern. G_2 is the analyzer grating which is needed to resolve the sub-pixel interference pattern. Finally, the detector is a scintillation screen which is recorded with a CCD camera.

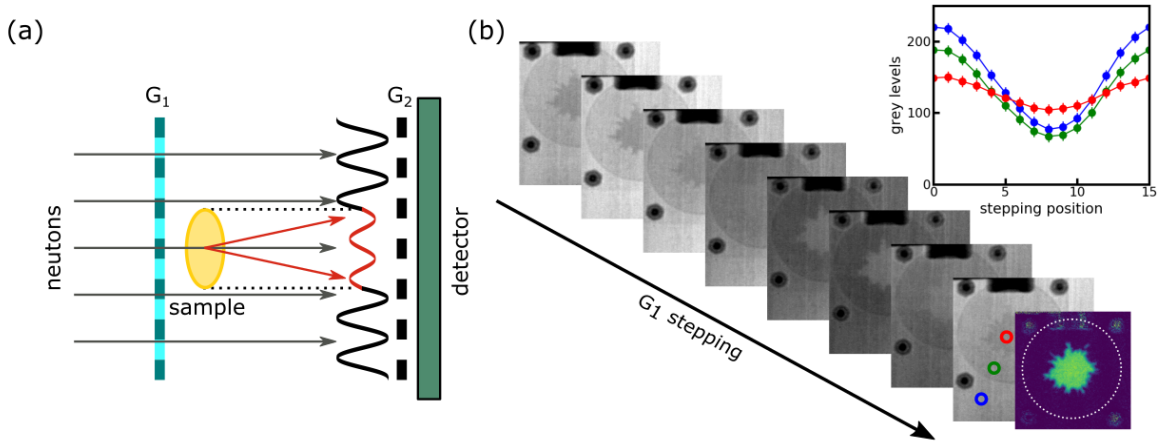

Figure 3.6: (a) Schematic depiction of a DFI measurement. The phase grating G_1 creates a modulated intensity pattern (black sine wave) at the position of the absorption grating G_2. Behind the sample (yellow), scattered neutrons reduce the intensity oscillation (red). G_2 has the same periodicity as the interference pattern and is used to block a specific part of the oscillation. With stepping either of the gratings, the intensity pattern is scanned over a full period. (b) Exemplary raw data of a NGI stepping scan. Shown are 8 out of 16 raw images of a full scan (gray scale). The evaluated DFI image is shown in color. The disk shaped sample shows two region, the outer in the Shubnikov state, the inner in the IMS. In the raw images, both sample regions and the background change differently over the stepping scan. The corresponding values are plotted in the inset. In the DFI image, only the center region in the IMS has a value lower than one (shown green).

NGI data

Exemplary data of the NGI measurements is shown in figure (3.6)(b). The images show part of a stepping scan (8 out of 16 images). The sample is a disc of 25 mm diameter. In the sample, two different regions are visible, the outer part is in the Shubnikov state, while the inner part is in the IMS. The intensity in the two sample regions and in the background change differently during the stepping scan. This is the effect of the sample on the interference pattern, which can be analyzed to obtain the DFI value using equation (3.15).

3.5 Small angle neutron scattering of the vortex lattice

The vortex lattice in niobium has a lattice constant of a few 100 nm. Compared to the larger domains, the scattering angles of cold neutrons are therefore larger, between approximately 0.1° and 1°. Scattering in this regime is denoted small angle neutron scattering (SANS). The major difference between the domain scattering, described in section (3.3), and the vortex lattice signal is, however, not the scale of both systems, but the different structure. Essentially, the vortex lattice is a two dimensional Bravais lattice, comparable to the case of atomic lattices only on a much larger scale. Consequentially, we use SANS as a diffraction experiment, in contrast to the diffuse scattering of the IMS domains seen with VSANS.

Vortex lattice Bragg scattering

In order to describe the scattering signal of the vortex lattice, we start by dividing the scattering length density into two separate contributions. This separation is retained in the differential scattering cross section, which simplifies the description of the scattering properties. In a vortex lattice, vortices are positioned at the lattice points $\mathbf{r}_i$, which can be expressed as $L(\mathbf{r}) = \sum \delta(\mathbf{r} - \mathbf{r}_i)$. At each lattice point, a vortex contributes the single vortex magnetic profile $B_\mathrm{v}(\mathbf{r})$. The total magnetic flux distribution and hence the scattering length density (equation (3.1)) is the convolution of both parts.

$$\rho(\mathbf{r}) = \frac{g_\mathrm{N}}{4\,\Phi_0} L(\mathbf{r}) \otimes B_\mathrm{v}(\mathbf{r}) \tag{3.18}$$

Calculating the differential scattering cross section (3.4), we can use the convolution theorem to transform the convolution into a simple product.

$$\begin{aligned} f(\mathbf{q}) &= FT(\rho) = FT(L(\mathbf{r}) \times B_\mathrm{v}(\mathbf{r})) = FT(L(\mathbf{r})) \cdot FT(B_\mathrm{v}(\mathbf{r})) \\ \frac{d\sigma}{d\Omega}(\mathbf{q}) &= |f(\mathbf{q})|^2 = |FT(L(\mathbf{r}))|^2 \cdot |FT(B_\mathrm{v}(\mathbf{r}))|^2 = F(\mathbf{q}) \cdot S(\mathbf{q}) \end{aligned} \tag{3.19}$$

Here, we used FT as shorthand for a Fourier transform. The two contributions to the scattering cross section are referred to as the form factor $F(\mathbf{q})$ and the structure factor $S(\mathbf{q})$ [117].

In the ideal case of an infinite lattice, $S(\mathbf{q}) = \sum \delta(\mathbf{q} - \mathbf{g}_i)$ has the same structure as the vortex distribution $P(R)$. It defines the reciprocal lattice, with the lattice points $\mathbf{g}_i$. The peaks of the differential scattering cross section at the reciprocal lattice points are referred to as Bragg peaks. In the case of a two dimensional hexagonal VL, the reciprocal lattice is again hexagonal, rotated by 90°. For a hexagonal lattice, the lattice constant of the real space vortex lattice a_{VL} and of the reciprocal lattice g_{VL} are connected via:

$$g_{\mathrm{VL}} = \frac{4\pi}{\sqrt{3}\, a_{\mathrm{VL}}} = \sqrt{\frac{8\pi^2 B_{\mathrm{VL}}}{\sqrt{3}\Phi_0}} \tag{3.20}$$

B_{VL} is the average flux density of the vortex lattice and Φ_0 is the flux quantum.

Rocking scans

In a diffraction experiment, not all Bragg peaks can be observed simultaneously. This problem is illustrated in figure (3.7) using the Ewald construction for Bragg scattering. The constraints for elastic scattering imply, that $\mathbf{q}$ cannot be perpendicular to the incident beam. Therefore, the sample has to be rotated slightly, to fulfill the scattering condition. The necessary rotation is different for every reciprocal lattice point. Experimentally, the problem is averted by performing a rocking scan in which the sample is rotated around one or two axes perpendicular to the beam. The measured Bragg peak intensity is then integrated over all angles. Normalized to the incident neutron flux, the intensity has been derived as [10]:

$$I(\mathbf{g}) = \left(\frac{g_{\mathrm{N}}}{4\Phi_0}\right)^2 \frac{2\pi\lambda_{\mathrm{N}}}{|\mathbf{g}|} |F(\mathbf{g})|^2 V \nu_{\mathrm{VL}} \tag{3.21}$$

where V is the volume of the sample and ν_{VL} is the volume fraction of the vortex lattice.

The vortex lattice correlation length : disorder in the lattice plane

Via $L(\mathbf{r})$ and $S(\mathbf{q})$, we have described the vortex and reciprocal lattice as infinite. However, in an experiment only a part of the lattice contributes to the coherent scattering. This limitation can be due to several effects, such as an actual finite lattice size, as in the IMS domains, or a finite order of the lattice due to lattice defects. Irrespective of the actual case, the effective size of the lattice is described with the lattice correlation length ξ_{VL}. The positions $\mathbf{g}_i$ of the reciprocal lattice points are not affected by such a spatial restriction. Instead, the assumption of $S(\mathbf{q})$ as a sum of delta function is no longer valid, and the Bragg peaks gain a finite width. We define the lattice correlation by the full width at half maximum (FWHM) of the first order Bragg peaks:

$$\xi_{\mathrm{Vl}} = \frac{2\pi}{\mathrm{FWHM}} \tag{3.22}$$

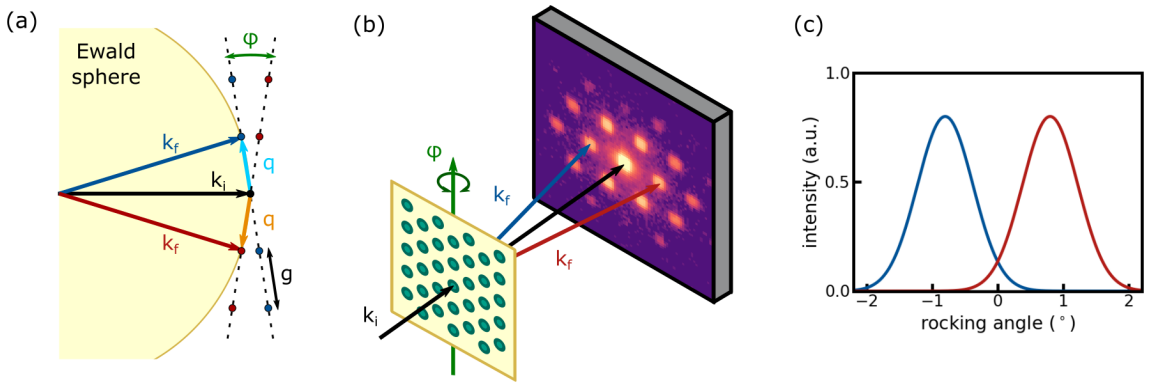

Figure 3.7: Illustration of the vortex lattice diffraction in reciprocal space (a) and real space (b). (a) Due to the elastic scattering condition, the initial and final wave vectors of a neutron have to be equally long, which is reflected in the Ewald construction. For Bragg scattering, the Ewald sphere has to intersect two lattice points. This is only possible, if the sample and with it the reciprocal lattice is rotated by an angle φ around an axis perpendicular to the beam (green). Two possible scattering configurations are shown in red and blue. (b) In the experimental setup, the vortex lines (teal) are parallel to the magnetic field and the neutron beam. The hexagonal vortex lattice leads to Bragg scattering in a hexagonal pattern rotated by $90°$ on the detector. Each Bragg peak is only visible under a small range of rocking angles φ. The scattering image included in (b) shows the sum over a whole rocking scan, while (c) depicts the angle dependence of the left (blue) and right (red) first order Bragg peaks.

The limited coherence of neutrons perpendicular to the beam $\zeta_{x,y}$(equation (3.8)) has a similar effect. Even, if the lattice is infinite and perfectly ordered, the neutron only interacts with a small part of it, which leads to a broadening of the Bragg peaks. Usually, this effect is synonymous to the finite resolution of an experiment, and $\zeta_{x,y}$ can be determined from the width of the direct beam. In an experiment, the finite size effects from the coherence length/resolution and from the actual lattice properties are superimposed. Mathematically, this can be treated as a convolution of the two broadening effects and the contributions add up as:

$$\mathrm{FWHM} = 2\pi \sqrt{\left(\frac{1}{\zeta_{x,y}}\right)^2 + \left(\frac{1}{\xi_{\mathrm{Vl}}}\right)^2} \tag{3.23}$$

The vortex correlation length : disorder along the field

In a similar approach, the correlation of the vortices along the beam direction can be measured. The FWHM of the Bragg peaks in q_z direction δ_z is measured in the rocking scan in units of radians. The correlation length is defined as [118]:

$$\xi_{\mathrm{vortex}} = \frac{2\pi}{\mathrm{FWHM}_z} = \frac{2\pi}{q_{\mathrm{Bragg}} \sin(\delta_z)} \tag{3.24}$$

where q_{Bragg} is the position of the Bragg peak. Again, the coherence length ζ_z contributes to the measured rocking width of the Bragg peak. However, due to the special structure of the vortex lattice, equation (3.9) cannot be used. The lattice structure results in a highly increased coherence length of the neutrons which has been estimated as [118]:

$$\zeta_z \leq \left(\frac{\lambda_{\mathrm{N}}}{\Delta\lambda_{\mathrm{N}}}\right)\frac{d_{\mathrm{VL}}^2}{\lambda_{\mathrm{N}}} \tag{3.25}$$

$d_{\mathrm{VL}} = a_{\mathrm{VL}}\sqrt{3}/2$ is the interplane distance in a hexagonal lattice. The correlation length ζ_z in a diffraction experiment is usually higher than the value calculated for diffuse scattering by several orders of magnitude.

SANS data

Exemplary data of the SANS measurements is shown in figure (3.8). The data for each sample was taken after field cooling in an external field of $\mu_0 H_{\mathrm{ext}} = 60\,\mathrm{mT}$ in the Shubnikov state. The temperature varies to meet the different sample properties. All data was acquired as rocking scans and summed up for presentation. Bragg peaks are visible in all samples. For the high purity and low purity measurements, the hexagonal pattern of the Bragg peaks is obvious. The medium purity sample shows the superposition of two hexagonal patterns rotated by 90°. Higher order Bragg peaks are clearly visible only for the high purity sample.

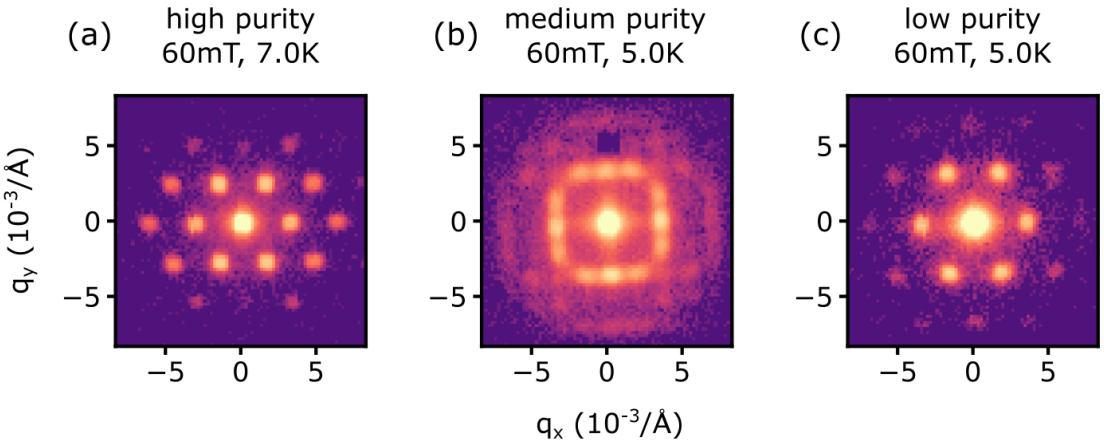

Figure 3.8: Exemplary raw data of SANS measurements. Shown are the sums of rocking scans on a logarithmic scale. All measurements were performed at 60 mT, at the indicated temperature, in the Shubnikov state. In all samples, the Bragg peaks form a hexagonal pattern, which is in a single orientation in the HP and LP sample and a twofold orientation in the MP sample. Note that the color scale is different for all samples, due to different scattering intensities. Deviating from the illustration, the center peak of the direct beam has the same width in all measurements.

Instrumental setup

The SANS experiments shown in this work were performed at the SANS-1 instrument at Maier-Leibnitz-Zentrum (MLZ) [119]. SANS-1 is a typical pinhole instrument and is shown schematically in figure (3.9). It is positioned at the end of a beam guide with a cold neutron spectrum, where the neutrons are monochromatized by a neutron velocity selector. The neutrons are collimated in a 20 m long collimation tube, which can be loaded with a variety of pinholes and collimation guides. The detector is a $1\,\mathrm{m}^2$ array of 128×128 ^3He detection tubes. It can be placed between 1.2 and 20 m behind the sample, in a 20 m long evacuated detector tube. Further information can be found in [119].

For all data presented in this work, a neutron wavelength of $\lambda_N = 12.0\,\text{Å}$ was used with a spread of 6 %. The neutron beam was collimated over the length of 20 m, using a source aperture with 20 mm diameter and a sample aperture with 7 mm diameter. The instrument resolution was measured as $7.5\,10^{-4}/\text{Å}$.

For SANS-1, the coherence length perpendicular to the beam is $\zeta_{x,y} = 0.4\,\mu\mathrm{m}$ (equation (3.8)). With a typical lattice constant of $0.2\,\mu\mathrm{m}$, the coherence is sufficient to measure the periodic structure of the vortex lattice. However, long range correlations are not resolvable with this coherence.

For diffuse scattering, the correlation in beam direction is $\zeta_z = 20\,nm$ (equation (3.9)). In the case of diffraction at the vortex lattice, this value is increased to $\zeta_z \leq 0.5\,mm$ (equation (3.25)). In comparison to our typical sample thickness of a few mm, this coherence length is expected to be sufficiently high to measure the real correlation length of the vortex lines.

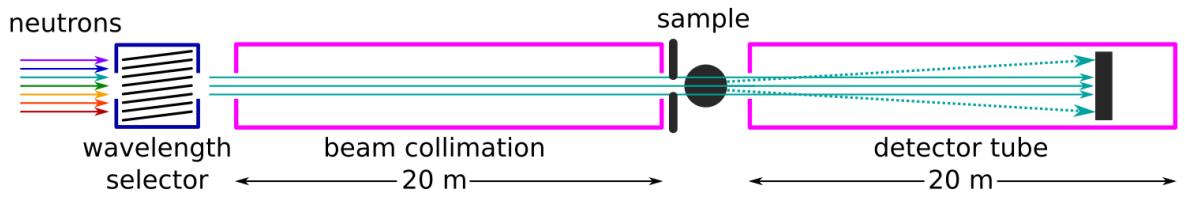

Figure 3.9: Schematic setup of the SANS instrument SANS-1. First, the incident neutron bean is monochromatized by a velocity selector. Next, it is collimated in the collimation tube, which can be fitted with various segments of collimators or pinholes. The detector can be moved inside an evacuated chamber up to 20 m behind the sample.

Very small angle neutron scattering (VSANS) @ KWS-3		
IMS domain morphology • domain correlation peak $q_{\max}$ & correlation length ξ_{IMS} • integrated scattering intensity I	Instrument resolution • spatial: 10 mm • reciprocal: $5 \cdot 10^{-5}$ /Å • coherence volume: $\zeta_{x,y} = 4\,\mu$m, $\zeta_z = 7$ nm	The primary feature obtained from the diffuse scattering signal of the IMS domain structure is a correlation peak at $q_{\max}$ (eq. (3.10)), which defines the domain correlation length ξ_{IMS} (eq. (3.11)). The intensity is primarily defined by the average flux density in the vortex domains and the Meissner state regions (eq. (3.14)). The scattering shape at high q is connected to the dimensionality of the domains via the exponent of a power law decay (eq. (3.10)).
Neutron grating interferometry (NGI) @ ANTARES		
IMS domain distribution • correlation function $G(\xi_{\mathrm{NGI}})$ • macroscopic scattering cross section Σ	Instrument resolution • macroscopic: 0.5 mm • microscopic: $\xi_{\mathrm{NGI}} = 1.9\,\mu$m • coherence volume: $\zeta_{x,y} = 2\,\mu$m, $\zeta_z = 4$ nm	The DFI value measured with the NGI depends on the IMS domain correlation function at the specific distance ξ_{NGI} and the macroscopic scattering cross section (eq. (3.16)). Detailed insight from a single measurement on these quantities is limited. The main advantage of NGI is to obtain a spatial variation of the scattering DFI. A changing DFI can indicate a change of the domain size, shape or scattering contrast. The scattering contrast is defined by the average flux density in the vortex domains and the Meissner state regions (eq. (3.14)).
Small angle neutron scattering (SANS) @ SANS-1		
Vortex lattice crystallography • vortex lattice constant a_{VL} • Bragg peak intensity I • VL correlation length ξ_{VL} • vortex correlation length ξ_{vortex}	Instrument resolution • spatial: 5 mm • reciprocal: $7.5 \cdot 10^{-4}$ /Å • coherence volume: $\zeta_{x,y} = 0.4\,\mu$m, $\zeta_z = 1$ mm	Scattering from the well ordered vortex lattice takes the form of Bragg peaks (diffraction). From the Bragg peak position, the lattice constant a_{VL} is obtained (eq. (3.20)). The scattering intensity depends on the several factors including the field distribution of a single vortex, the Bragg peak position and the temperature (eq. (3.21)). In the IMS, the reduced volume fraction of the vortex lattice domains decreases the observed intensity. The width of the Bragg peaks in direction of q is used to determine the lattice correlation length ξ_{VL}, which is reduced in the IMS domain structure (eq. (3.22)). Similarly, the rocking width defines a correlation length of the vortices along the field direction ξ_{vortex} (eq. (3.24)).

Table 3.1: Summary of the neutron scattering techniques. For detailed descriptions see sections (3.3) for VSANS, (3.4) for NGI and (3.5) for SANS.

4 Experimental results

With the techniques presented in chapter (3), we have investigated the intermediate mixed state (IMS) in the intertype superconductor niobium. The focus of our study was the transition of vortex matter from a homogeneous lattice in the Shubnikov state into the domain structure of the IMS. In this work, the experiments are restricted primarily to field cooled procedures. We have used a set of experimental techniques which allows us to probe the vortex matter on different length scales. Using SANS, we can measure the properties of the vortex lattice on a scale of approximately 200 nm. The IMS domain with a characteristic length scale of a few micrometers is covered by VSANS and NGI. Here, VSANS was used to measure the domain morphology, while NGI allows us to see the domain distribution on the mm scale of the sample. Finally, the global magnetic properties of the superconductor were measured with VSM. The combination of techniques allows us to obtain a comprehensive picture of the IMS transition. In the experiments, the dependence of the IMS on the external field and on the sample purity was addressed.

In this chapter, we present our experimental studies, starting with an overview over the used samples (section (4.1)), followed by the results of the different experimental techniques in the order: VSM (section (4.2)), SANS (section (4.3)), VSANS (section (4.4)) and NGI (section (4.5)). In each section, the general findings and differences of the distinct sample purities will be addressed. The chapter closes with a summary and discussion of the complete experimental results.

4.1 Sample overview

In our study of the IMS we have used niobium single crystals of three purities: high (HP), medium (MP) and low (LP). Samples of the same purity were cut from the same single crystal. All details about the samples are summarized in table (4.1), including their shape, dimension, demagnetization factor and the corresponding experimental techniques. The high purity sample is a custom grown crystal with exceptional quality, which was specifically oxidized to improve the surface quality. It has been previously used in neutron scattering experiments [56, 74, 120] and showed no signs of surface pinning or flux trapping. The sample is cylindrical, with a crystalline (110) axis corresponding to the cylinder axis.

The medium purity samples were cut from a large polycrystalline disc, which was originally manufactured by Heraeus for the use in microwave cavities [121]. Individual grains have a diameter up to $\approx 10\,\mathrm{cm}$. All MP samples were cut from the same grain, which has a crystalline (100) axis nearly perpendicular to the surface, with a deviation

of $\approx 2°$. All low purity samples were cut from a single crystal obtained from Matek. They have been previously used in a neutron scattering study [14]. The disc shaped samples have a crystallographic (110) axis perpendicular to their surface. Medium purity and low purity samples have been prepared by spark erosion, diamond wire cutting, grinding, polishing and etching in fluoric acid. We do not elaborate on the different combinations of polishing and etching, as they had no visible impact on the measurements.

The assignment of different purities is based on measurements of the residual resistivity ration (RRR) and impurity determination by neutron activation analysis [122]. HP-1 exhibits a $RRR > 10000$ and contains 20 ppm Ta as primary impurity. The MP samples were specified with $RRR > 300$ and 150 ppm Ta. For the LP samples, a $RRR \approx 100$ and 200 ppm Ta and 350 ppm W were measured.

Sample	RRR	Impurities	Shape	Dimensions [mm]	D	Experiment
HP-1	>10k	20 ppm Ta	rod	$d = 5.5$, $t = 19.7$	0.14 ($\parallel$)	VSM
					0.43 ($\perp$)	SANS
MP-1	>300	150 ppm Ta	disc	$d = 25$, $t = 1.3$	0.90	SANS, NGI
MP-2			disc	$d = 10$, $t = 1.3$	0.79	SANS
MP-3			disc	$d = 5$, $t = 0.3$	0.89	VSM
MP-4			strip	$20 \times 2 \times 0.2$	0.87	VSANS
MP-5			cuboid	$4.0 \times 3.8 \times 1.9$	0.24	VSM
LP-1	≈100	200 ppm Ta	disc	$d = 20$, $t = 0.6$	0.94	SANS
LP-2		350 ppm W	cuboid	$4.0 \times 3.7 \times 1.9$	0.24	VSM

Table 4.1: Single crystal niobium samples (HP: high purity, MP: medium purity, LP: low purity). All MP and LP samples were cut from the same crystal, respectively. Dimensions are given either as diameter (d) and thickness (t) for a cylindric shape or as the three edge lengths for cuboid shape. Demagnetization factors (D) were calculated for all discs with the magnetic field perpendicular to the surface, for the cuboids with the field parallel to the longest edge, and for the rod shaped HP-1 two values are given with the field parallel ($\parallel$) and perpendicular ($\perp$) to the cylinder axis.

4.2 VSM: Bulk magnetic properties

The magnetization was measured with a vibrating sample magnetometer (VSM), equipped with a helium flow cryostat. Due to practical limitations, the experimental arrangement of the samples is not identical to the neutron experiments. The high purity sample HP-1 was measured with the field applied parallel to the cylinder axis. For the lower purities, the cuboid samples MP-5 and LP-2 were used with the field applied along the longest axis. Additionally, the disc shaped sample MP-3 was measured with the field perpendicular to the sample face.

Results

Comparative data of the different sample purities is shown in figure (4.1)(a,b). Magnetization loops were recorded in the range of $-0.5\,\mathrm{T} \leq \mu_0 H_{\mathrm{ext}} \leq 0.5\,\mathrm{T}$. Panel (b) shows the data at 4 K after zero field cooling (ZFC). MP-5 and LP-2 display similar broad hysteresis loops, which are characteristic for strong vortex pinning. After ZFC, the initial branch of both samples has the same slope, according to their identical demagnetization factor. Both curves deviate from the linear behavior at $\mu_0 H_{\mathrm{ext}} \approx 100\,\mathrm{mT}$, after which they cross over to the hysteresis loop. The turning point of MP-2 is significantly higher, at $\mu_0 H_{\mathrm{ext}} \approx 157\,\mathrm{mT}$, than for LP-1, at $\mu_0 H_{\mathrm{ext}} \approx 129\,\mathrm{mT}$. Generally, MP-5 displays a broader and more asymmetric hysteresis than LP-2. The shape of the HP data is distinct from the other two curves. The initial branch of the magnetization has a different slope due to the lower demagnetization factor. The sample stays in the Meissner phase up to $\mu_0 H_{\mathrm{ext}} = 122\,\mathrm{mT}$, where the magnetization drops steeply by $\approx 80\,\mathrm{mT}$. Above 140 mT, the magnetization is perfectly reversible. Between 130 mT and 70 mT on the decreasing branch, the magnetization is linear and parallel to the initial branch, approximately 50 mT lower. After changing sign with the external field, the initial branch of the magnetization after ZFC is almost immediately reproduced.

The temperature dependence of the magnetization was measured field heated after zero field cooling (FH) and field cooled (FC). Panel (a) shows the data at $\mu_0 H_{\mathrm{ext}} = 40\,\mathrm{mT}$, which is corrected for the demagnetization factor of the samples. After zero field cooling, all samples are in the Meissner state and have a magnetization equal to the external field. For LP-2, magnetic flux starts to enter the sample above $\approx 7.0\,\mathrm{K}$. For MP-5, the transition is slightly delayed to $\approx 7.4\,\mathrm{K}$. In contrast, HP-1 stays in the Meissner phase up to $\approx 8.3\,\mathrm{K}$, where we see a slight peak. For all samples, the magnetization is practically zero above 8.7 K. The field cooled data is qualitatively similar to FH, but shows very different saturation magnetizations at low temperatures. Additionally, the transition temperature in slightly decreased for MP and LP. They reach their saturation at 8.1 K and 7.6 K, with a magnetization of $-1.0\,\mathrm{mT}$ and $-3.3\,\mathrm{mT}$, respectively. The transition of HP-1 is instead slightly increased and it reaches saturation very fast at 8.4 K with a value of $-27\,\mathrm{mT}$.

Panels (c,d) show magnetization data of the sample MP-3, which has a shape and demagnetization factor comparable to the MP and LP samples used for SANS and NGI. The field heated data is comparable to the example shown for MP-5, but with a much broader transition region. In the field cooled case, the saturation magnetization is below 1 mT for all fields.

Discussion

In the magnetization measurements, the different purities of the samples are obvious, with a stark contrast between HP and MP/LP. MP-5 and LP-2 have similar qualitative properties. The broad, asymmetric hysteresis loop is caused by flux trapping due to impurities and surface defects, as well as edge barriers which hamper the flux entrance.

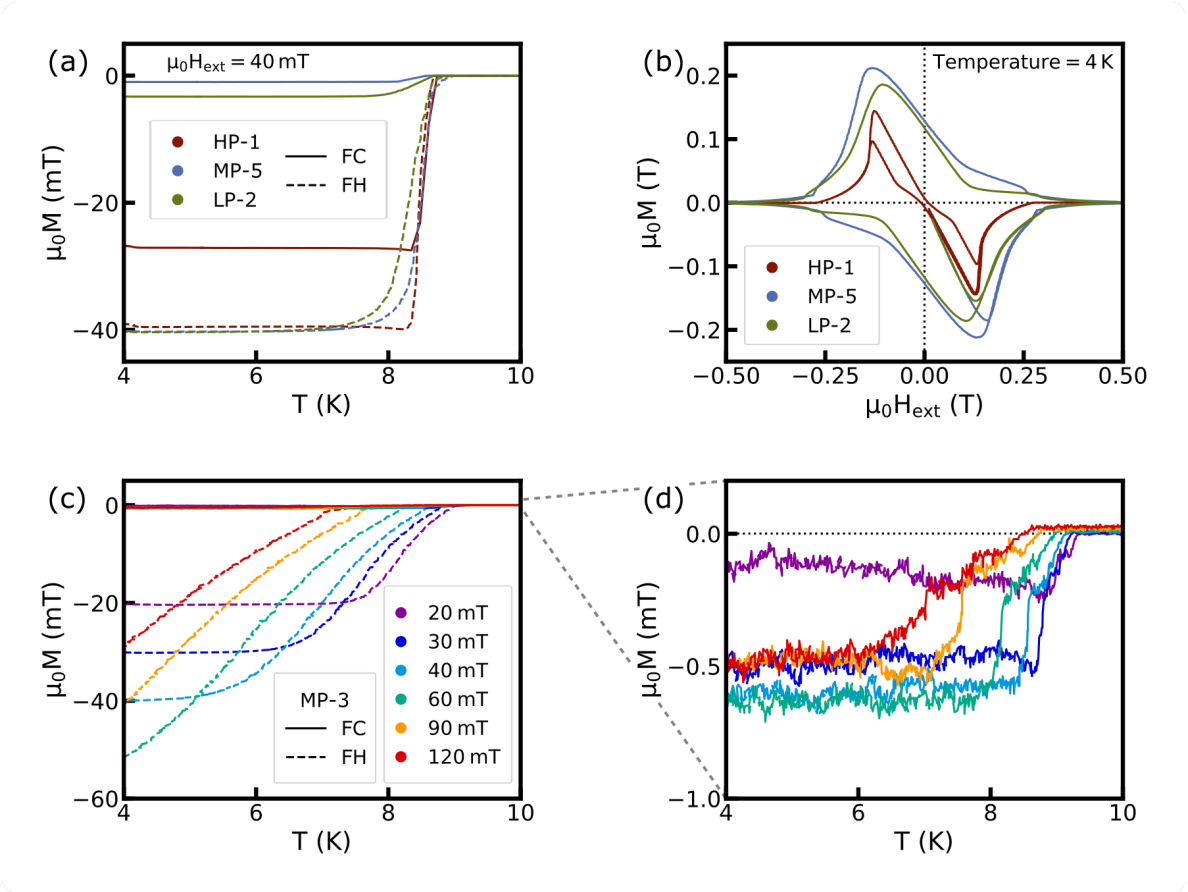

Figure 4.1: Magnetization measurements of all three different sample purities. (a) Temperature dependent magnetization in $40\,\mathrm{mT}$ for the samples HP-1, MP-5 and LP-2 in field cooled (FC, solid lines) and field heated (FH, dashed lines) measurements. The field heated data shows the perfect diamagnetism of the Meissner effect, while the FC data reveals a strong flux freezing in MP-5 and LP-2 and a possible signature of the IMS in HP-1. The transition between normal and superconducting state is different for each sample. (b) Field dependent measurements at $4\,\mathrm{K}$ for the same samples as in (a). The hysteresis loops visible for MP-5 and LP-2 are indicative of strong pinning and geometric effects. HP-1 is, again distinct, with a hysteresis only at small fields, which is likely related to the IMS. (c,d) show temperature dependent data measured on MP-3 in a comparable geometry to the neutron measurements. It reveals a nearly perfect flux freezing transition in field cooled measurements.

In the FC measurements, we observe a flux freezing transition due to pinning. In the temperature dependent data, the transition to the normal state starts at a lower temperature for LP-1 than for MP-2. Additionally, the extent of the Meissner state in the initial branch of the field loops is lower for LP-2. Both features are in accordance with the level of purity defined by the samples *RRR* and impurity content. In contrast, the field cooled saturation magnetization is lower for MP-5 and its hysteresis loop is larger compared to LP-2. Both features can be attributed to the overall sample quality or to surface effects. A conclusive quality hierarchy is not obtained from magnetization alone. In the medium and low purity sample, no indication of the IMS is visible.

In contrast, the HP data is not indicative of bulk or surface pinning. The reversibility of the high field magnetic loop, as well as the sharp superconducting transition in the temperature dependence underline the high quality of the sample. The hysteretic part of the magnetization loop is most likely connected to the IMS. In the IMS, a specific vortex lattice constant is preferred, which corresponds to a mean flux density B_{IMS}. In the initial branch, geometrical barriers hinder the entrance of magnetic flux into the sample, which preserves the Meissner state. On the decreasing branch, however, the internal flux density decreases to a finite value, which is connected to B_{IMS}. The internal flux stays constant over a range of $\approx 60\,\mathrm{mT}$ at $4\,\mathrm{K}$, until the Meissner effect dominates the low energy state of the IMS. Similarly, the reduced saturation magnetization observed in FC measurements is likely connected to B_{IMS}, and is not a sign of a partial flux freezing.

The data taken with MP-3 further illustrates the circumstances in the neutron experiments on MP and LP samples. All neutron data is recorded in field cooled measurements, where flux freezing is close to perfect. Hence, the internal magnetic flux can always be assumed to be constant, and demagnetization effects can be neglected. With the similarity between MP-5 and LP-2 in mind, the flux freezing in a disc shaped LP sample is also assumed to be close to perfect. For HP-1 it was not possible to measure the magnetization in a setup which resembles the neutron measurements. However, with the magnetic field perpendicular to the sample's cylinder axis, demagnetization effects are expected to be significantly larger. Furthermore, a spatially inhomogeneous magnetic state in the sample has already been reported [74].

4.3 SANS: Vortex lattice crystallography

Using small angle neutron scattering (SANS), the properties of the vortex lattice were investigated. The measurements were performed on the samples HP-1 with the field perpendicular to the cylinder axis and on MP-2 and LP-1 with the field perpendicular to the sample face. Demagnetization effects only apply to HP-1, since MP-2 and LP-1 undergo a flux freezing transition. All data was acquired in the form of rocking scans with respect to one or two axes perpendicular to the neutron beam. For HP-1, the rocking was performed over $\pm 1^\circ$ on the vertical axis in 41 steps, with a total exposure time of 410 s. The MP samples were rocked over the horizontal and vertical axis, each in the range of $\pm 1^\circ$ over 25 steps, with a total exposure of 500 s. LP-1 was rocked over the range of $\pm 1.2^\circ$ of the vertical axis in 25 steps, with a total exposure of 250 s.

The neutron beam was monochromatized with a velocity selector at 12.0 Å with a spread of 6 %. The collimation length and sample-detector distance were both 20 m. The resolution determined from the center beam was measured as FWHM $= 0.65 \cdot 10^{-3}$/Å. This corresponds to a resolvable structure size of $2\pi/\mathrm{FWHM} \approx 1000\,\mathrm{nm}$, which is in reasonable agreement with the correlation length $\zeta_{x,y} = 400\,\mathrm{nm}$ (equation (3.8)).

Results

Exemplary raw data of the SANS images were shown in figure (3.8) in chapter (3.5). The pattern of Bragg peaks corresponds to a hexagonal vortex lattice in all samples. This hexagonal pattern was found at all fields and temperatures where a VL was observed. Deviations from the perfect angles of 60° are below 2°.

The **lattice constant** a_{VL}, determined from the first order Bragg peak positions (cf. equation (3.20)), is shown in figure (4.2)(a,b,c) for the samples HP-1, MP-2 and LP-1. In the data, two regimes can be identified for all samples. At high temperatures and fields we find the Shubnikov state. Starting at high temperature, a_{VL} depends on the applied magnetic field $\mu_0 H_{\mathrm{ext}}$. In the MP and LP samples, the lattice constant is temperature independent. The mean flux density of the lattice corresponds to the external field $\mu_0 H_{\mathrm{ext}}$, which is indicated on the right side of each plot. For HP-1, a_{VL} increases with decreasing temperature. The second regime is the intermediate mixed state, where we find a unique temperature dependence in each sample with no dependence on the external field. With decreasing temperature, the lattice constant decreases in all samples. The curves describing the second regime are included in all graphs to indicate the hierarchy of the different sample purities. Using the lattice constant, we define the transition temperature from Shubnikov state to the IMS T_{IMS}, which is marked in all graphs. For HP-1, the IMS is observed up to 90 mT, for MP-2 up to 60 mT and for LP-1 up to 30 mT.

The **integrated intensity** of the first order Bragg peaks is shown in figure (4.2)(d,e,f). In the Shubnikov state, the intensity increases linearly with decreasing temperature to a maximum at T_{IMS} in all samples. In the IMS, we see a decreasing intensity. For HP-1, the decrease is linear and strongest. In the measured temperature range, the intensity reduces to zero for fields up to 75 mT. In MP-2 and LP-1, the intensity decreases much less in the IMS. In MP-2, a stagnation is observed for 20 mT and 40 mT, which cannot be seen for LP-1 due to the lower transition temperatures.

For selected fields, field heated measurements were performed subsequent to the field cooling. These are marked with open circles in the plots of figure (4.2). In all cases, field cooled and field heated measurements yield identical lattice parameters. In the intensity slight differences are present, but the general behavior is well reproduced. Additionally, field dependent measurements were performed on HP-1 after zero field cooling. The lattice parameter obtained in these measurements is included in panel (a) as black diamonds and matches the other measurements perfectly.

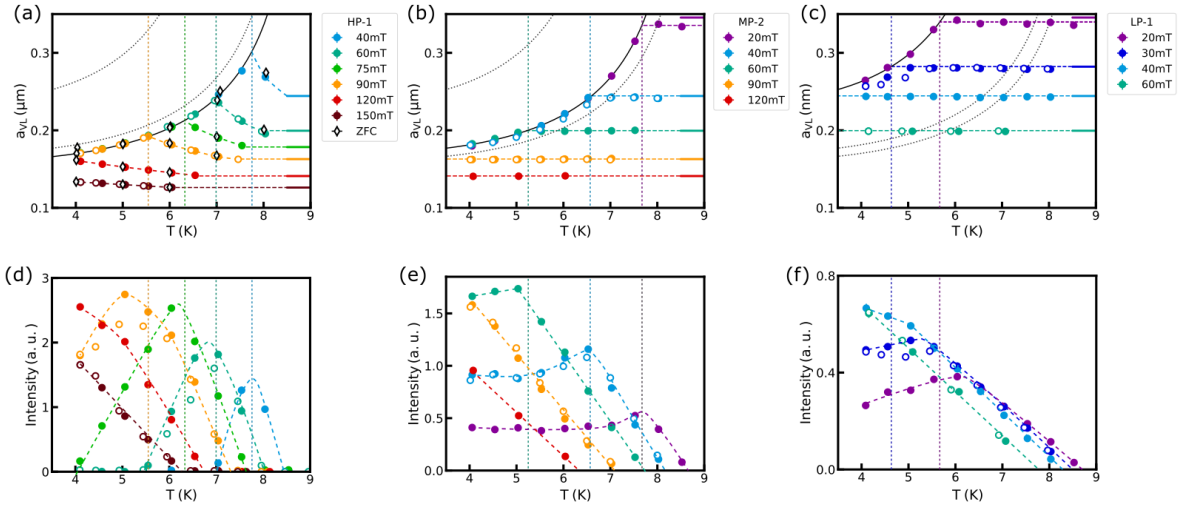

Figure 4.2: (a,b,c) The lattice constant a_{VL} of the vortex lattice has been calculated from the position of the first order Bragg peaks (equation (3.20)). All samples show two distinct regimes. In the Shubnikov state (high temperatures and fields) a_{VL} is either increasing (HP-1) or constant (MP-2, LP-1). In the intermediate mixed state (low temperatures and fields), a_{VL} decreases on a unique line. The IMS line orders with the sample purity. (d,e,f) Integrated intensity of the first order Bragg peaks. In the Shubnikov state, the intensity increases linearly due to the temperature dependent vortex shape. In the IMS, the intensity decreases due to the reduced VL filling factor. In HP-1 the decrease is enhanced by the Meissner effect.

The **width of the first order Bragg peaks** FWHM_q in radial q direction is shown in figure (4.3)(a,b,c). Included in the images is the FWHM of the center beam (black broken line) which determines the resolution limit at $0.65 \cdot 10^{-3}/\text{Å}$. In the Shubnikov state, the Bragg peaks have a FWHM_q of $0.7 - 0.8 \cdot 10^{-3}/\text{Å}$ close to the resolution limit, which has only a weak temperature dependence. Below the IMS transition the width increases significantly, up to $\approx 1.0 \cdot 10^{-3}/\text{Å}$ in HP-1 and $\approx 1.3 \cdot 10^{-3}/\text{Å}$ in MP-2 and LP-1. Panels (d,e,f) show the corresponding correlation length ξ_{VL} of the vortex lattice (cf. equation (3.22)). The results are presented in units of the measured lattice constant $a_{\mathrm{VL}}(T)$. In the Shubnikov state, the correlation is $\approx 15\, a_{\mathrm{VL}}$ in HP-1 and $\approx 8\, a_{\mathrm{VL}}$ in MP-2 and LP-1. In the IMS, all samples have a notably reduced correlation length of $3 - 4\, a_{\mathrm{VL}}$ which is mostly temperature independent. These values correspond to a correlation length of $\approx 1.8\,\mu$m in the Shubnikov state and $0.9\,\mu$m in the IMS. We note that the calculated values are quite uncertain due to their closeness to the resolution limit. Error bars have been omitted in the graphs for better visibility of the data.

Rocking curves for selected measurements are shown in figure (4.4). The scans were performed in $0.1°$ steps for the medium and low purity samples and in $0.05°$ steps for the high purity sample. The data shown in panels (a,b,c) are in the Shubnikov state at all temperatures, in an external field of 120 mT (HP-1), 90 mT (MP-2) and 60mT (LP-1), respectively. For HP-1, the peak position shifts with temperature, due to the shifting q position of the Bragg peak. The rocking peaks of MP-2 and LP-1 remain at

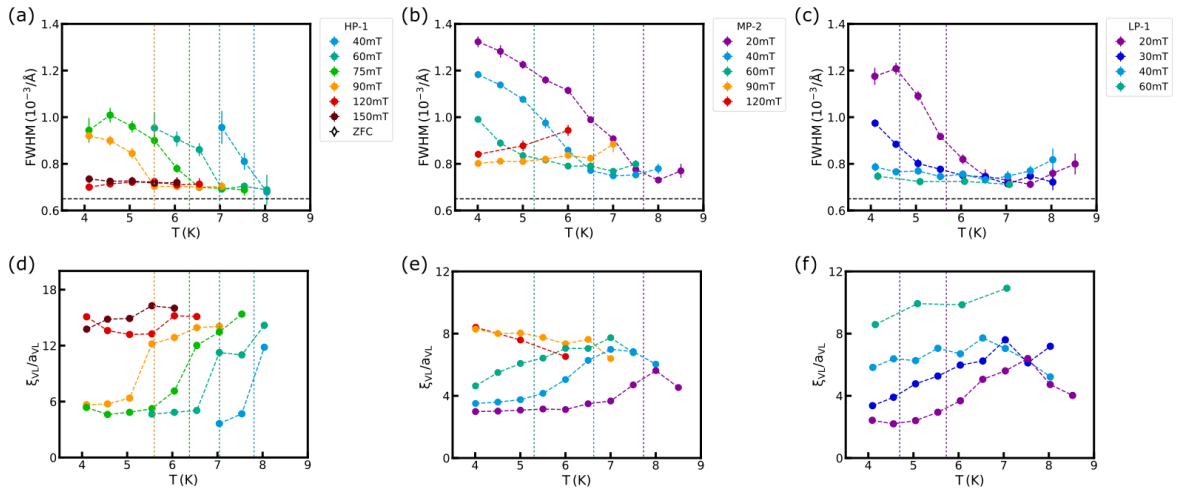

Figure 4.3: (a,b,c) FWHM of the first order Bragg peaks in radial q direction. The width of the center beam is included as black line and represents the resolution limit. In the Shubnikov state, the width is close to the resolution limit and nearly temperature independent. In the IMS, the width is increasing with decreasing temperature. (d,e,f) Lattice correlation length calculated from FWHM_q in units of the lattice parameter $a_{\mathrm{VL}}(T)$. Due to the closeness to the resolution limit, the values have a relatively large error, especially in the Shubnikov state. The error bars were omitted for better visibility.

the same angle. The shape and width of the rocking peaks is only slightly changing with temperature. Panels (d,e,f) show measurements at 75 mT (HP-1), 40 mT (MP-2) and 30mT (LP-1), respectively, where the IMS transition is observed. Below T_{IMS}, the rocking peaks broaden significantly.

The full width at half maximum $\mathrm{FWHM}_{\mathrm{rock}}$ of all peaks is shown in figure (4.5)(a). In the Shubnikov state $\mathrm{FWHM}_{\mathrm{rock}}$ is in the range of $0.1° - 0.3°$ in all samples and therefore close to the resolution limit of the instrument $\approx 0.05°$. In the IMS, the rocking width increases with decreasing temperature. Similar to the lattice correlation, a vortex correlation ξ_{vortex} in direction of the field can be determined from the rocking width. The calculated values are shown in figure (4.5)(b). In HP-1, the maximum correlation is in the order of 100 μm and decreases drastically in both measurements. In the lower purity samples, the correlation in the Shubnikov state is $\approx 30 - 40\,\mu$m and decreases in the IMS to values around 10 μm. Again, the close proximity to the resolution limit renders the calculated correlation lengths prone to errors.

Coinciding with the IMS transition, we have measured a broadening of the direct beam in all samples. Due to the resolution limit, this effect was not further evaluated. However, we identify this effect with the IMS domain scattering, which is the subject of our VSANS measurements.

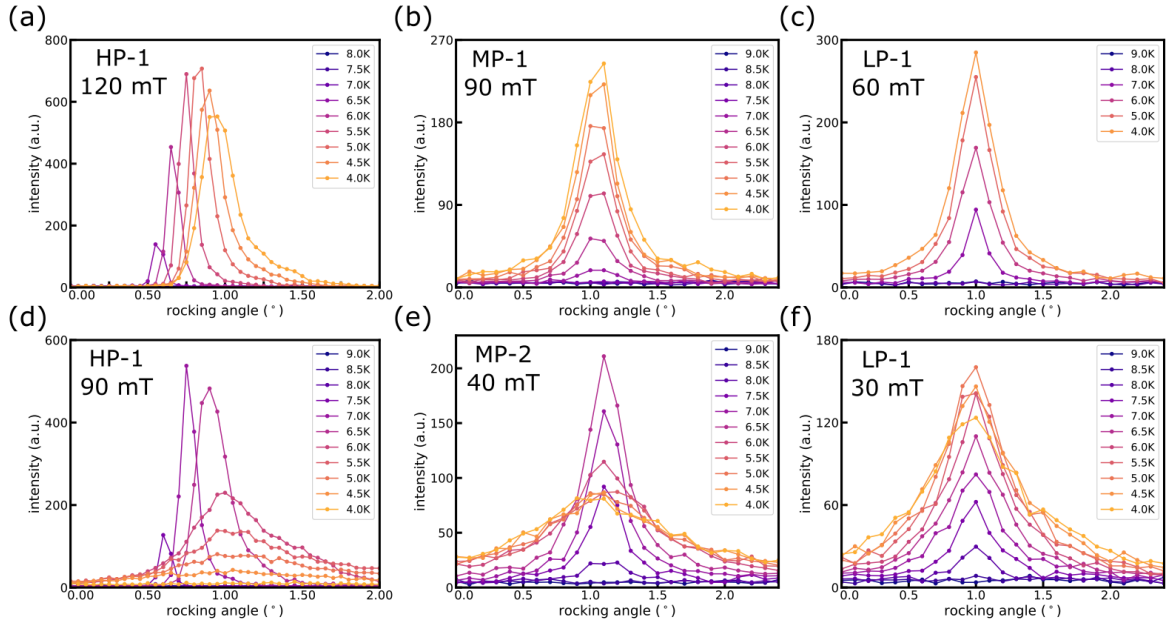

Figure 4.4: Rocking curves of the intensity of one Bragg peak, for representative magnetic fields. (a,b,c) At the chosen higher fields, the samples are in the Shubnikov state at all temperatures. In all cases, the shape and width of the rocking peak remain similar at all temperatures. The changing center angle observed in HP-1 is due to the changing Bragg peak position. (d,e,f) At the chosen lower fields, the samples undergo the IMS transition. Below the IMS, the rocking peaks become notably broader.

Discussion

While all samples were measured in the same geometry and in field cooled procedures, we have observed a clear discrepancy between HP-1 and the lower purity samples MP-2 and LP-1. Due to the high quality of HP-1, the Meissner effect is visible in the measurements, which is not the case for the other samples. Most directly, this is observed as an increasing lattice parameter a_{VL} in the Shubnikov state. Figure (4.6) shows the corresponding flux density of the vortex lattice B_{VL}. At all external fields, B_{VL} decreases linearly with the temperature. The dotted lines give an estimate at which temperature the vortex lattice is completely excluded from the sample. This transition into the Meissner state is observed in our measurement range up to 75 mT, which fits reasonably well with the extrapolations of B_{VL}. Note that, while B_{VL} increases in the IMS, the flux expulsion is simultaneously taking place. In contrast, the constant lattice parameter seen in the Shubnikov state of MP-2 and LP-1 is indicative of a strong flux freezing transition. Therefore, the internal and external flux density are identical at all fields and temperatures, irrespective of Shubnikov state or intermediate mixed state.

The **lattice constant** a_{VL} constitutes the clearest signature of the transition from the Shubnikov state into the IMS. We note, however, that the transition is clearly visible in all quantities extracted from the SANS measurements. In the IMS, the lattice parameter is decreasing with temperature in all samples. The lattice parameter in the IMS has the

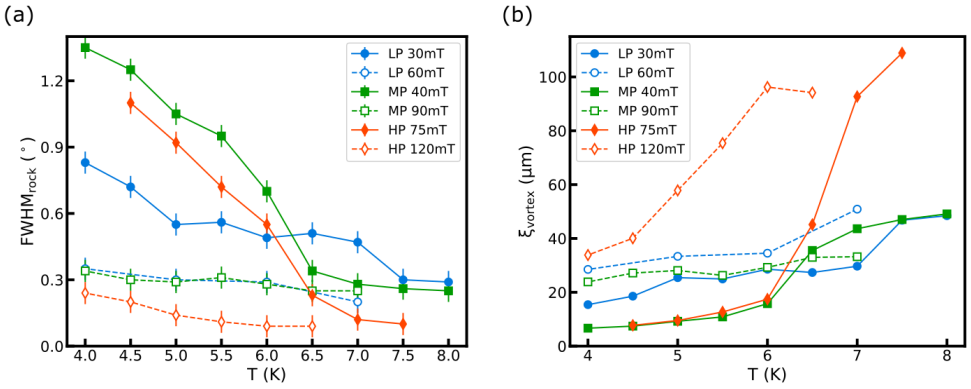

Figure 4.5: (a) Width of the rocking curves $\mathrm{FWHM}_{\mathrm{rock}}$ of the curves shown in figure (4.4). In the Shubnikov state, the width stays mostly constant at a low value of $0.1 - 0.3°$. Below the IMS transition, the width increases notably. (b) Correlation of the vortices in field direction ξ_{vortex} calculated from the rocking width.

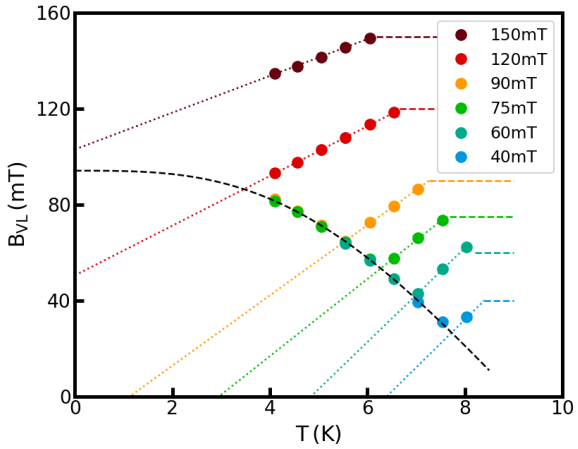

Figure 4.6: Magnetic flux density B_{VL} of the vortex lattice in HP-1, calculated from the Bragg peak positions. The unique line of the IMS is included in the image (black dashed line). In the Shubnikov state (temperatures and fields above the IMS line), the flux density of the VL is linearily decreasing. The colored dashed lines on the right side mark the value of the external magnetic field. Colored dotted lines are showing the extrapolation of the linear decrease.

same temperature dependence in all samples which can be expressed as:

$$a_{\mathrm{IMS}} = a_{\mathrm{IMS},\,0}\left(1 - t^{3-t}\right)^{-\frac{1}{2}} \quad , \text{with } t = \frac{T}{T_{\mathrm{c,\,IMS}}} \tag{4.1}$$

This formula phenomenologically describes the temperature dependence of the London penetration depth λ_{L} [123] and has been used in a previous study [73]. All fit parameters ($a_{\mathrm{IMS},\,0}$ and $T_{\mathrm{c,\,IMS}}$) are listed in table (4.2). The critical temperature $T_{\mathrm{c,\,IMS}}$ is below the actual transition of the superconducting state at zero field 9.2 K and decreasing

from HP-1 to MP-2 to LP-1. The zero temperature parameter $a_{\mathrm{IMS},\,0}$ is increasing with decreasing sample purity. Overall, the difference between HP and MP is relatively small, while the low purity curve is strongly shifted towards lower temperature and larger lattice constants. The sample purity has two effects, which are likely responsible for the different curves. First, the London penetration depth and the GL correlation length are increased in impure superconductors, due to the decreased electron mean free path [124]. Both parameters factor into the range of the vortex-vortex interaction. Second, the increased pinning in the lower purity samples may have an effect on the IMS transition, e.g., by restricting the vortex mobility.

It is noteworthy that HP-1 and MP-2 have a very similar transition line a_{IMS}, although the macroscopic magnetic properties are quite different. Especially the presence of a flux freezing transition in the medium purity sample is a stark contrast to the flux expulsion and demagnetization effects present in HP-1. In contrast, the transition line is very different between MP-2 and LP-1, despite their very similar magnetic properties. A possible explanation is, that flux freezing and the changing IMS transition are caused by different effects.

The **Bragg peak intensity** is given by equation (3.21), which depends on the vortex form factor, the reciprocal lattice vector and the filling factor of the vortex lattice. In the Shubnikov state, we observe a mostly linear increase of the intensity in all samples. This increase is primarily due to the changing form factor of the vortices. With decreasing temperature, the size of a vortex decreases and its magnetic flux density increases accordingly. Therefore, the magnetic scattering contrast increases, which is seen in the scattering intensity. In MP-2 and LP-1 this is the only factor, since the Bragg peak position $\mathbf{g}$ and the filling factor of the vortex lattice ν_{VL} are constant due to the flux freezing. In HP-1, ν_{VL} can be assumed to stay constant as well, while $\mathbf{g}$ decreases due to the flux expulsion. In the IMS, the reciprocal lattice vector increases in all samples, which reduces the scattering intensity. Furthermore, the filling factor of the vortex lattice decreases due to the domain structure of the IMS. In the medium and low purity samples, $\nu_{\mathrm{VL}} = B_{\mathrm{ext}}/B_{\mathrm{IMS}}$ is restricted due to the flux freezing, which leads to the roughly constant scattering intensity deep in the IMS (see sample MP-1, 20 mT and 30 mT). In contrast, in HP-1 the Meissner effect reduces ν_{VL} down to zero in the IMS, along with the scattering intensity.

The **correlation lengths** of the vortex lattice ξ_{VL} and the vortices themselves ξ_{vortex}, which are extracted from the widths of the Bragg peaks, are a further indication of the IMS transition. Concerning the vortex lattice, the quantities measured in q direction, FWHM_q and ξ_{VL}, are at the resolution limit of $0.65 \cdot 10^{-3}/\text{Å}$ and 1 μm, respectively, in

	HP-1	MP-2	LP-1
$T_{\mathrm{c,\,IMS}}$ (K)	9.02	8.80	7.55
$a_{\mathrm{IMS},\,0}$ (nm)	159.3	168.7	234.0

Table 4.2: Fit parameters of the IMS transition line using equation (4.1)

the Shubnikov state. Due to the relatively large lattice constants ($0.1 - 0.3\,\mu$m) this means that only a small part of the lattice can actually contribute to the coherent Bragg scattering. In the IMS, the Bragg peak width notably increases, which has two likely reasons. First, due to the rearrangement of vortices into a denser lattice, the degree of order in the lattice can decrease. Second, due to the break up of the lattice into domains, the measurable correlation is limited by the edges of VL domains. It is noteworthy that the correlation length in units of the lattice constant is approximately constant $\xi_{\mathrm{VL}} \approx 3 - 4\,a_{\mathrm{VL}}$ in the IMS and similar for all fields. In absolute units, the lattice correlation in the IMS is between $0.5 - 1.0\,\mu$m.

In direction of the field, a similar broadening of the Bragg peaks is observed in the IMS (see figure (4.5)). In field direction, the broadening does not correspond to the order of the vortex lattice, which is a two dimensional structure. Instead, it corresponds to a bending of the flux lines. In the Shubnikov state, the vortices are straight over a length of approximately ξ_{vortex} which is in the order of $30\,\mu$m. Due to the limited resolution, this is rather a lower boundary, and the actual value might be higher.

In the IMS, ξ_{vortex} reduces to $\approx 10\,\mu$m. This gives an estimate of the length in field direction, over which the IMS domains are well defined. We have two primary scenarios which are likely for the domain morphology in z direction. They are shown schematically in figure (4.7). A domain might be consisting of a fixed set of vortices (panel (a)). These may be bent over the scale of the coherence length, but the domain fundamentally stays intact. Alternatively, the domains might be truly confined in field direction (panel (b)). The vortices making up a domain split up and rearrange into several new domains along the field direction. Additionally, the vortex coherence can be limited by pinning centers. In the broken vortex lattice of the IMS, pinning sites may distort vortices more strongly than in the homogeneous Shubnikov state, especially at the domain boundaries where restricting vortex interactions are missing.

In summary, the IMS is observed in every quantity evaluated from the SANS measurements. Below the transition temperature T_{IMS}, the vortex lattice constant decreases, while the initial hexagonal structure is retained throughout the whole temperature range. Accompanying the agglomeration of the VL is a loss of correlation perpendicular to the field as well as in field direction. We interpret the limited correlation as a domain structure consisting of well ordered VL domains and flux-free Meissner state domains. The VL domains have a typical length scale of $3 - 4$ vortices, which corresponds to $0.5 - 1.0\,\mu$m. Note that, depending on the actual shape of these domains, the correlation might be very anisotropic, e.g., in elongated stripes with a width of ≈ 4 vortices. In field direction, the correlation reflects a bending of the vortex lines, rather than an actual finite size. With $\approx 10\,\mu$m in the IMS, ξ_{vortex} is notably larger than ξ_{VL}.

We want to emphasize two points: First, the IMS transition is observed in samples with very different magnetic properties. In HP-1, flux can move freely and leave the sample as can be seen in the Meissner effect. In contrast, MP-2 and LP-1 are undergoing a flux freezing transition. Despite the differences, all samples show an IMS transition with a

very similar transition line $a_{\mathrm{IMS}}(T)$. Second, the IMS transition is reversible. The results from field cooled and subsequent field heated measurements yielded nearly identical results, as well as the field scans performed on HP-1. Both observations imply that the IMS is a well defined state. Especially the vortex lattice constant reflects fundamental properties of the superconductor, which are manifest in the vortex interaction.

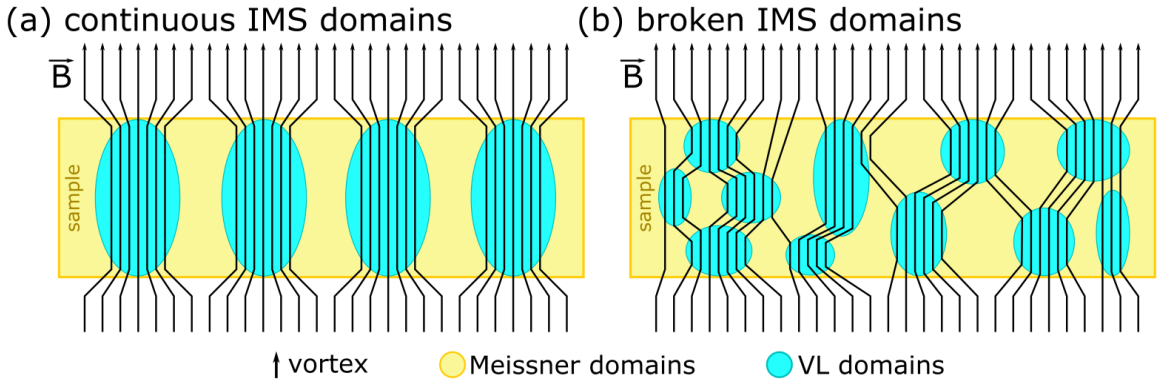

Figure 4.7: Schematic morphology of IMS domains in direction of the magnetic field and the neutron beam. (a) Continuous domains, which consist of the same set of vortices throughout the whole sample. (b) Broken domains, where vortices contribute to several different domains throughout the sample thickness. In both cases, pinning centers may introduce flaws in the individual domains, which reduces the correlation of vortices in field direction.

4.4 VSANS: IMS domain morphology

The morphology of the vortex matter domains in the IMS was measured using very small angle neutron scattering. The measurements were performed on the medium purity sample MP-5. A thinner sample was necessary to reduce the multiple scattering rates. The shape and demagnetization factor of MP-5 is different to the samples used with SANS and NGI. However, due to the flux freezing transition, this has a negligible effect. The exposure time for each data point was 3 h for measurements at 40 mT and 60 mT and 2 h at 90 mT. The neutron beam was monochromatized with a velocity selector at 12.8 Å with a spread of 20 %. The resolution was determined from the center beam as $10.5 \cdot 10^{-5}$/Å, which corresponds to a structure size of 6 μm. The coherence volume of the neutron depends on the focusing geometry of the instrument. Neglecting this effect, we calculate $\zeta_{x,y} \approx 4\,\mu$m and $\zeta_z \approx 6.5$ nm.

Results

Figure (4.8) shows field cooled VSANS data of MP-5 at three different external fields: 40 mT, 60 mT and 90 mT. Depicted are the radial averages of the two dimensional intensity. For raw data examples, see figure (4.8) in chapter (3).

The **full intensity** as measured is shown in panels (a). At 90 mT, the signal has no temperature dependence and does not change between normal and superconducting state. This background intensity has a Gaussian shape at low q with FWHM $= 10.5 \cdot 10^{-5}$/Å. At $q \approx 1.3 \cdot 10^{-4}$/Å, it changes to a power law with exponent 2.8 ± 0.1. At 60 mT and 40 mT, the signal changes below 5 K and 6.5 K, respectively. Primarily, we observe additional scattering in the region above $q = 1 \cdot 10^{-4}$/Å. At both fields, the scattering intensity increases with decreasing temperature.

The **magnetic scattering signal** at 40 mT and 60 mT is shown in panels (b). We have subtracted the high-temperature signal, normalized by the intensity at $\mathbf{q} = 0$. At both fields, a slight peak at $q \approx 0.7 \cdot 10^{4}$/Å is visible. This is, however, very close to the resolution limit of the instrument. At large q, the data follows a power law with exponent 3.5 ± 0.5 The shape of the scattering signal is not changing with temperature.

The **integrated scattering probability** S is shown in panel (c). It is defined as the fraction of the magnetic scattering signal (shown in panels (b)) to the total signal (shown in panels (a)). For 3.5 K it increases up to $S = 13.8\,\%$ and $S = 9.6\,\%$ for 40 mT and 60 mT, respectively. The black dashed lines included in the plot indicate the expected temperature dependence, based on the changing scattering cross section in the IMS (cf. equation (3.14)).

Discussion

The scattering signal observed in the VSANS measurements emerges precisely at the IMS transition temperature observed in SANS for 40 mT and 60 mT. Additionally, the data at 90 mT confirms no signal in the Shubnikov state at all measured temperatures. Therefore, we attribute the signal to the magnetic domain structure of the IMS. The curves of the magnetic signal show a correlation peak, however, since the peak is very close to the direct beam, an exact determination of its position cannot be expected. For 40 mT and 60 mT, at temperatures below 6 K and 5 K respectively, the peak position is at $q \approx 0.7 \pm 0.05 \cdot 10^{-4}$/Å. This corresponds to a correlation length of $\xi_{\mathrm{IMS}} \approx 10\,\mu$m.

The **correlation peak** of the magnetic scattering signal is close to the resolution limit of the instrument ($\approx 6\mu$m) and the neuron coherence length ($\zeta_{x,y} \approx 4\mu$m). Therefore, we do not measure the real correlation of the domain structure, but rather a lower boundary. The behavior at high q, however, contains information about the interface between the domains, which are at a smaller scale and therefore still resolvable. We observe a power law with an exponent of 3.5 ± 0.5. With reference to the model function describing a two phase domain structure in spinodal decomposition (cf. equation (3.10)), this corresponds to a two or three dimensional domain structure with smooth interface, where the expected value is 3.0 and 4.0, respectively. While the exponential behavior is therefore reasonable, the data does not yield a clear insight into the domain morphology.

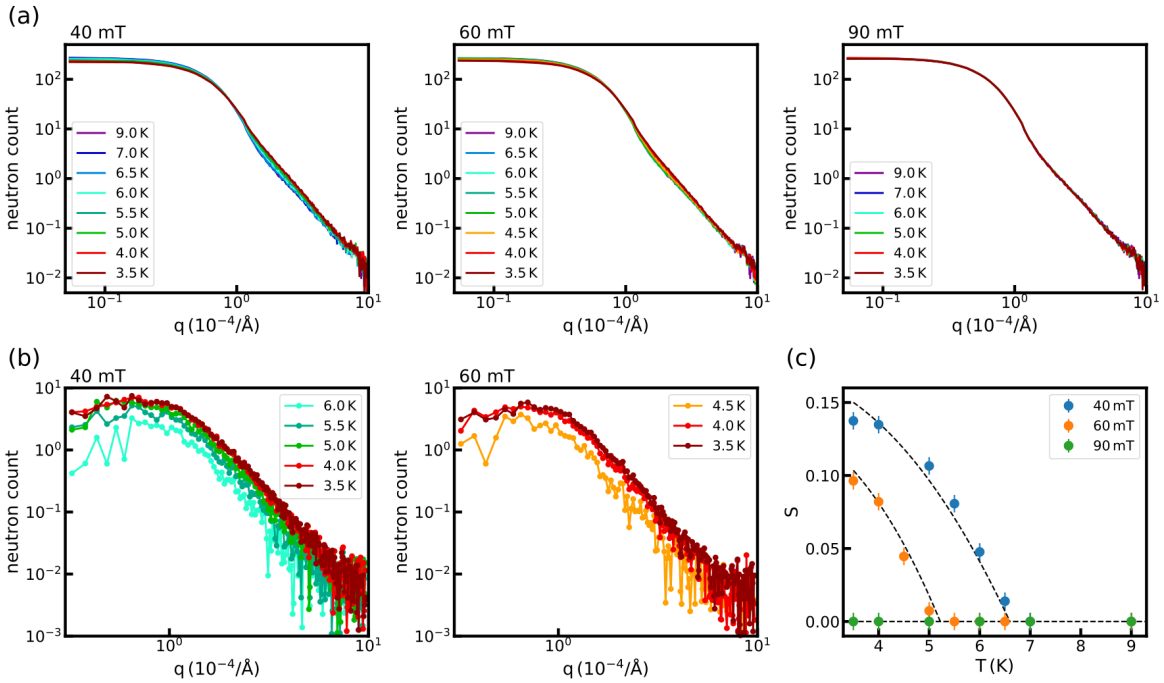

Figure 4.8: Radially averaged VSANS signal at several temperatures during field cooling in 40 mT, 60 mT and 90 mT. (a) Raw scattering data as measured. At 90 mT the signal does not change with temperature and is identical to the signal in the normal conducting state. At the lower fields, scattering changes below a critical temperature. (b) Magnetic scattering signal. Shown are only the temperatures where additional scattering was observed. The signal shows a slight peak at $q \approx 0.7 \cdot 10^4/\text{Å}$. With decreasing temperature the scattering intensity increases, but the signal shape does not change significantly. (c) Integrated scattering probability of the magnetic contribution shown in (b). The broken lines show the expectation for a constant domain size.

The **scattering probability** at 3.5 K is relatively high with $S = 13.8\,\%$ and $S = 9.6\,\%$ at 40 mT and 60 mT, respectively. Roughly 10 % of the scattered neutrons can be expected to scatter multiple times which leads to a further smearing of the obtained signal. We have modeled the temperature dependence of the scattering probability $S = 1 - \exp(-\Sigma\, t)$ using equation (3.14) and the sample thickness $t = 0.2\,\text{mm}$. For this, we have used the internal flux density of the IMS domains B_{IMS} determined by the SANS experiments. The domain structure was assumed to be constant. Fitting curves are included in figure (4.8)(c), which describe the data very well. The fitting parameters include a correlation length in beam direction L_z, which was $L_z(40\,\text{mT}) = 1.7\,\mu\text{m}$ and $L_z(60\,\text{mT}) = 1.9\,\mu\text{m}$. Due to the low neutron correlation length ($\zeta_z = 6.5\,\text{nm}$) and generally measuring in the resolution limit, these values are not further interpreted.

For **low purity samples** (including LP-1), measurements using a Bonse-Hart camera were performed at the BT-5 beamline at NIST in a previous study [14]. The results revealed a correlation peak at $q \leq 4 \cdot 10^{-4}/\text{Å}$ which decreased down to zero for increasing external fields. Accordingly, the domain correlation length is in the low micrometer

range with a minimum measured value of 1.5 μm. For the high purity sample, no domain scattering experiments could be performed due to its thickness and the resulting multiple scattering.

In summary, the VSANS measurements prove that the decreasing vortex lattice constant a_{VL} observed with SANS is in fact a hallmark of an emerging magnetic micrometer structure in the IMS. We obtain a characteristic length scale of this domain structure exceeding 10 μm, whereas a definite value is obscured by the instrument resolution. The shape of the scattering signal and the associated domain size do not change with temperature, which indicates a constant morphology. Additionally, the scattering probability resembles the expected temperature dependence for a constant domain morphology with a changing vortex density in the VL domains matching the SANS measurements. This result, which is in accordance with a previous study by Reimann et al. [14], indicates a gradual unmixing of the magnetic domains. This scenario is comparable to spinodal decomposition, from which we have adapted the fitting function for the VSANS signal.

4.5 NGI: IMS domain distribution

With neutron grating interferometry (NGI) the real space distribution of the IMS vortex matter domains in sample MP-1 was studied. NGI measurements were performed as stepping scans with 16 positions and three images each. The total exposure time per stepping scan was 960 s. The neutron beam was monochromatized with a velocity selector at 4 Å with a spread of 10 %. A collimation of L/D = 250 was used and the sample placed 20 cm before the scintillator. The spatial resolution was ≈ 0.5 mm. The correlation length of the interferometer was $\xi_{\mathrm{NGI}} = 1.9\,\mu$m. The neutron coherence lengths for the experiment were $\zeta_{x,y} \approx 2\,\mu$m and $\zeta_z \approx 4$ nm. In all images, the sample position has been marked by a white circle. Additional features, visible in the corners and at the top of the images, stem from brass screws used in the sample holder.

Results

The **temperature dependence** of a field cooled measurement sequence in an external field of 40 mT is shown in figure (4.9)(a). The data has been normalized to a measurement at 9.5 K in the normal state. At high temperatures above 7 K, the DFI = 1, which means no scattering is present. Below 7 K, the DFI value decreases with decreasing temperature, which corresponds to an increasing scattering signal. Most notably, the DFI is homogeneous in the whole sample. The average DFI is plotted in panel (b). A theory curve is included, which corresponds to a constant domain size and will be discussed in detail later on. T_{IMS} marks the transition temperature of the IMS at 40 mT.

A **field dependent** measurement sequence is shown in figure (4.10)(a). Each image shows the DFI after separately field cooling from the normal state to 4 K. Each image has been normalized to a measurement at 12 K in the normal state at the respective external field. Again, the DFI signal is homogeneous throughout the whole sample at all fields. The average DFI is shown in panel (b). Between 0 mT and

80 mT, the DFI shows a broad dip with its minimum (DFI = 0.36) at 40 mT. Above 80 mT, the DFI is slowly increasing from 0.95 to ≈ 1. The graph contains a theoretical curve assuming a constant domain size, which will be discussed later on. B_{IMS} is the internal field of the IMS domains at 4 K and marks the upper boundary of the IMS.

A **field scan** at 4 K subsequent to the field cooling in 40 mT is shown in figure (4.11). The data has been normalized to a zero field cooled measurement at 4 K. After ZFC, the sample shows a homogeneous DFI (cf. figure (4.9)(a)). With increasing external field, the signal remains unchanged at DFI ≈ 0.36 up to $\mu_0 H = 80$ mT. Above 80 mT, the edge of the sample ceases to scatter and shows a DFI = 1. The edge region grows inwards with increasing field, until the scattering is suppressed in the whole sample at ≈ 230 mT. At fields between 80 mT and 230 mT, the scattering center region is approximately circular, with a frayed edge. Throughout the measurement series, the DFI value of the scattering region does not change. The mean radius of the center region is shown in panel (b). From 80 mT to 230 mT, it is decreasing almost linearly.

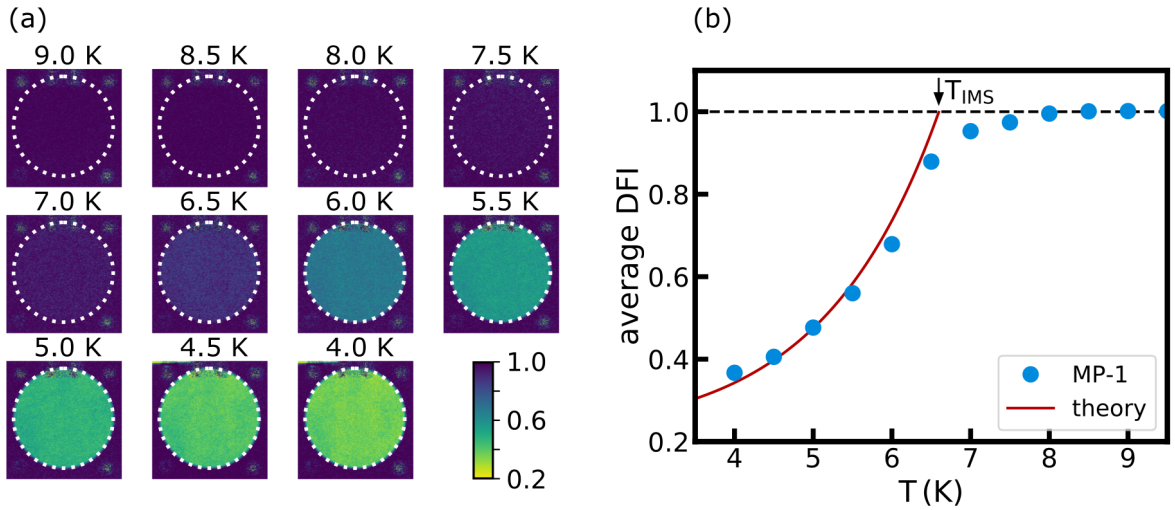

Figure 4.9: Temperature dependence of the DFI in a field cooled measurement at 40 mT. (a) shows the DFI images, normalized to a reference measurement at 9.5 K. A signal below 1 appears below 7 K and indicates the onset of scattering from the IMS domains. At all temperatures, the signal is homogeneous throughout the sample. (b) contains the average DFI in the sample area, which decreases in the range between 7 K and 4 K. T_{IMS} is the transition temperature of the IMS at 40 mT. The red curve is a theoretical fit, assuming a constant domain size.

Discussion

First, we discuss the identification of the DFI signal with the IMS. Due to the lack of q resolution, its origin is less conclusive than SANS or VSANS. In our data, the DFI signal is below one only deep in the superconducting phase. Therefore, we can exclude the material itself and the vortex lattice in the Shubnikov state as its origin. Additionally,

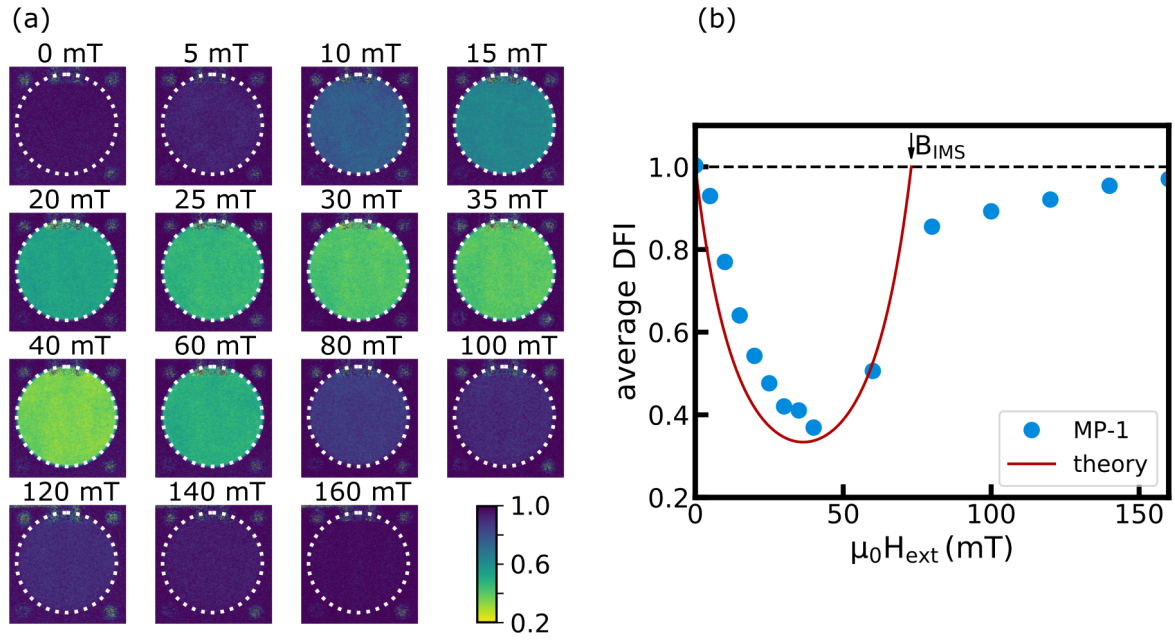

Figure 4.10: Magnetic field dependence of the DFI at 4 K after separately field cooling in $\mu_0 H$. (a) shows the DFI images, normalized to reference measurements at 12 K. A signal below 1 indicates scattering from the IMS domains. At all fields, the signal is homogeneous throughout the sample. (b) contains the average DFI in the sample area, which is strongly changing in the range between 0 mT and 80 mT. B_{IMS} is the flux density of the IMS VL domains at 4 K and marks the upper boundary of the IMS. The red curve is a theoretical line, assuming a constant domain size. It uses the same parameters as in figure (4.9)(b).

the onset of scattering in the DFI and the IMS hallmarks seen in SANS and VSANS, coincide very well. In conclusion, we find it justified to attribute the DFI directly to the IMS domain structure.

The **resolution limit** of the NGI is below the domain structure size, similar to the situation in VSANS. With $\xi_{\mathrm{NGI}} \approx \zeta_{x,y} \approx 2\,\mu$m, the resolution is still below the $\approx 6\,\mu$m of VSANS. Since all measurements were performed at the same correlation length ξ_{NGI}, the effects of this limitation are not as obvious as in the VSANS measurements. Primarily, we observe a reduced scattering intensity and the measurements not as sensitive to a changing domain morphology, because mainly the domain interfaces contribute to the signal. For the **temperature series** shown in figures (4.9) and (4.10), the most prominent feature is the homogeneous DFI. This means that the transition from the Shubnikov state to the IMS is taking place simultaneously in the whole sample. The possibility of a transition front, e.g., from the sample edges inward, is ruled out, as well as macroscopically distributed centers of condensation. Furthermore, the IMS morphology is identical in the whole sample. While we are not able to resolve the complete domain structure, a variation would still be seen due to a change in the total scattering intensity.

In section (3.4), we introduced the formulas to calculate the DFI of the IMS domains (equations (3.16) and (3.14)). We can use the flux density of the VL domains $B_{\mathrm{IMS}}(T)$,

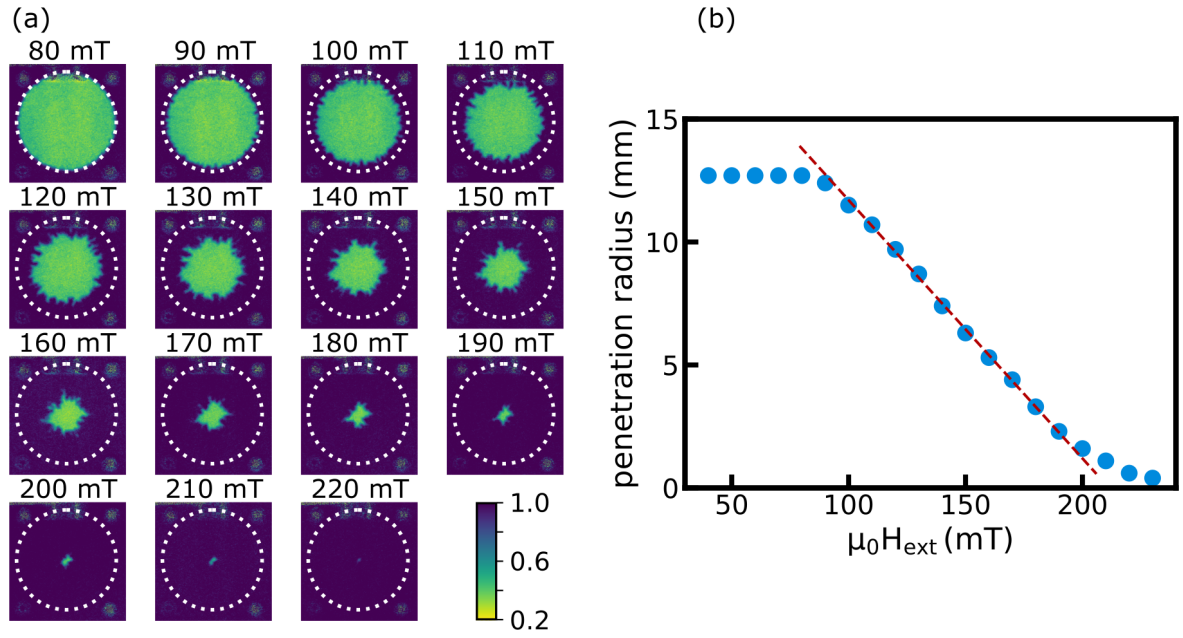

Figure 4.11: Magnetic field dependence of the DFI at 4 K after field cooling at 40 mT. (a) shows the DFI images, normalized to a reference measurement at 4 K after zero field cooling. A signal below 1 appears indicates scattering from the IMS domains. The DFI imaged are unchanged up to a field of 80 mT. At higher fields, the scattering disappears, starting from the edge of the sample. (b) contains the average radius of the scattering center region, which decreases linearly in the range between 80 mT and 230 mT. The red line is a guide to the eye.

determined in the SANS experiments, to calculate $\Delta\rho$ and ν_{VL}. The remaining unknown factors in the DFI are L_z and the value of the correlation function, which we combine into a single fitting parameter:

$$\alpha = L_z \left(\frac{G\left(\xi_{\mathrm{NGI}}\right)}{G\left(0\right)} - 1 \right) \tag{4.2}$$

With the assumption of a constant domain size over temperature, which is prompted by the VSANS results, α is temperature independent. A fitting curve with $\alpha = 18.5\,\mu$m is included in figure (4.9)(b) and shows a very good agreement. For the setup with $\xi_{\mathrm{NGI}} \approx \zeta_{x,y} \approx 2\,\mu$m we can assume that $G(\xi_{\mathrm{NGI}}) = 0$, since we measure at the resolution limit. Therefore, α is an estimate for the domain correlation in field direction. It should be regarded carefully due to the limited resolution.

For the **field dependent** data shown in figure (4.10), the assumption of a field independent domain size is almost certainly not justified. Since we do not have sufficient data to rectify this, panel (b) includes a model curve with $\alpha = 18.5\,\mu$m. While the general trend is quite well described, there are obvious deviations from the data. With the available data, the field dependence of the domain size cannot be further specified. We note that

above $B_{\mathrm{IMS}} = 73\,\mathrm{mT}$ no scattering signal should be present from the IMS. Currently, the origin of the DFI signal at high fields is not known.

The **magnetic field sequence** shown in figure (4.11) illustrates the penetration of magnetic flux into the sample according to the critical state model. After field cooling, the sample is homogeneously in the IMS. When increasing the external field, no additional flux can enter the sample due to the pinning properties and the geometrical barriers of the sample. The IMS remains intact even at external fields above $B_{\mathrm{IMS}} = 73\,\mathrm{mT}$. Additional magnetic flux in the form of vortices can enter the sample, if the maximal screening current is reached. The new vortices fill up the Meissner state domains, starting at the edge of the sample. This creates a homogeneous VL state which shows no scattering in the range visible by NGI. With increasing field, the front between Shubnikov state and IMS penetrates further into the sample until the IMS is entirely suppressed.

In **previous studies** by Reimann et al., NGI was used with low purity samples including LP-1 [14] and the high purity sample HP-1 [74]. In contrast to our measurements, the low purity samples revealed a spatial inhomogeneity in the form of concentric rings. The origin of this pattern was, however, not determined. For HP-1, primarily the field dependence was examined. In this case, the DFI signal was inhomogeneous as well, which could be attributed to the inhomogeneous magnetic field due to demagnetization effects.

In summary, the NGI measurements have shown, that the IMS transition in MP-1 is spatially homogeneous in field cooled measurements. Due to the prominent flux freezing in this sample, the total amount of vortices does not change throughout the cooling procedure. The homogeneous DFI contrast reveals that the IMS domains have the same morphology in the whole sample. This also requires that the initial vortex distribution in the Shubnikov state has to be homogeneous. Apparently, the IMS transition does not rely on any global inhomogeneities but is determined by the microscopic properties of the sample. The temperature dependence of the DFI shown in figure (4.9)(b) additionally supports the result from VSANS measurements that the domain morphology is constant over temperature and only the scattering contrast of the domain changes according to $a_{\mathrm{VL}}(T)$.

4.6 Summary

In the previous sections, we have presented a comprehensive study of the intermediate mixed state (IMS) in superconducting niobium of three distinct quality levels. We have used a combination of four experimental techniques, each focusing on a distinct length scale of the vortex matter found in the IMS. Magnetometry was used to determine the bulk magnetic properties (VSM). Neutron scattering was used in three different techniques to obtain information about the vortex lattice crystallography (SANS), the IMS domain morphology (VSANS) and the IMS domain distribution (NGI).

Our experiments were performed predominantly in a field cooled manner, where the IMS transition could be observed as a microscopic rearrangement of vortices into micrometer sized domains. The process is apparent in all three neutron techniques, with the most prominent hallmarks visible with SANS as decreasing vortex lattice constant a_{VL} and correlation length ξ_{VL}. Simultaneously, a scattering signal from the IMS domain structure emerges in VSANS and NGI measurements. During the transition, the initial lattice structure is retained in the vortex domains. With decreasing temperature, the VL becomes denser and the vortex domains decrease in size, accordingly. Meanwhile, the characteristic length scale of the domain morphology ξ_{IMS} appears to be temperature independent. In contrast to the neutron scattering techniques, the bulk magnetization measurements show no indication of the IMS domain structure.

A key feature of our experiments is the vortex lattice constant in the IMS $a_{\mathrm{VL}}^{\mathrm{IMS}}(T)$. For each sample, this defines a unique line which is independent of the external magnetic field. In fact, the lattice constant poses the most reliable and accessible parameter to determine the transition into the IMS. Remarkably, $a_{\mathrm{VL}}^{\mathrm{IMS}}(T)$ has the same temperature dependence in each of our samples, which is reminiscent of the temperature dependence of the fundamental superconducting parameters λ_{L} and ξ_{GL}. However, the IMS transition line is shifted for the different samples. We find a clear hierarchy where $a_{\mathrm{VL}}^{\mathrm{IMS}}(T)$ tends to higher temperatures and lower lattice constant with increasing sample quality. The impact of the sample purity on the IMS is, however, not straightforward. On the one hand, the high purity and medium purity samples differ significantly in their bulk magnetic properties, which is most prominent in the observation of the Meissner effect in contrast to a flux freezing transition, respectively. Concerning the IMS transition, however, both samples reveal very similar results. On the other hand, both, the medium purity and low purity sample, exhibit flux freezing and are comparable in their magnetic bulk properties. However, the IMS transition is significantly reduced for the low purity samples.

In fact, the coexistence of a flux freezing transition and the IMS is noteworthy in its own right. Despite the global pinning of vortices in the MP and LP samples observed in the magnetization measurements, a microscopic rearrangement is still possible in the IMS. Furthermore, the IMS transition is fully reversible in all samples.

5 MDS of vortex matter

Complementary to experiments, vortex matter in superconductors is routinely studied by simulations, either based on Monte Carlo [125–129] or molecular dynamics [130–134] methods. Similarly, ab initio calculations [13, 53, 135] are performed, which are, however, typically restricted to much smaller systems, due to the increased computational complexity. The molecular dynamics simulations presented in this chapter study the intermediate mixed state (IMS) transition and domain morphology. In analogy to the experiments presented in chapter (4), a model superconductor resembling niobium is used, and the simulations follow a similar field cooling procedure. In the experiments, we have observed the transition from a homogeneous vortex lattice (VL) into VL domains in the IMS. The most important hallmarks of the IMS were a temperature dependent lattice constant a_{VL} in combination with a temperature independent domain morphology. In contrast to these microscopic parameters, the IMS was not accompanied by a unique bulk signature. Measurements on three different niobium single crystals showed a dependence of the hallmarks on the sample purity. Especially noteworthy was the observation of the domain formation even in the presence of a macroscopic flux freezing transition. The absence of a hysteresis in field cooled and subsequent field heated measurements underlined the intrinsic character of the IMS properties. Inaccessible with experiments, however, was the microscopic shape of the IMS domain structure. An advantage of simulations is the direct access to the microscopic picture. Additionally, all quantities obtained in experiment can be evaluated in the simulations as well, which allows a comparison of the two methods.

In the first part (section (5.1)) of this chapter, the simulation algorithm will be discussed. The section starts with a general introduction to MD simulations, followed by a detailed presentation of the algorithm especially adapted for superconducting vortex matter. Afterwards, the specific details for our simulations of the IMS in intertype superconductors will be covered in section (5.2). These include the model parameters used to emulate superconducting niobium and the explicit forms of all relevant interactions. In section (5.3), the evaluation methods developed to quantitatively analyze our MD simulations are introduced along an exemplary simulation. Systematic MD studies using the techniques presented in this chapter will be presented in chapter (6).

5.1 Molecular dynamics simulations

5.1.1 Introduction

Molecular dynamics simulations (MDS) are a computational method typically employed to investigate complex many-body systems. Examples for recent studies can be found in

[136–139]. Their primary application are cases where the physics of individual particles can be described mathematically, while the collective behavior is too complex for an analytical approach. An important example is the simulation of large molecules and their dynamical behavior (e.g. [136]). Interactions between single atoms can be derived quantum mechanically, which is, however, not feasible for the whole molecule. In the MDS approach, the collective behavior is explored, as it emerges from the single particle properties. Inherently, this neglects alterations of the single atom interactions due to many-body effects. The fundamentals of MDS can be found in many standard textbooks, e.g., by Frenkel [140] or Leach [141].

In MD simulations of a many-particle system, it is evolved over time in discrete steps. In each step, the forces acting on each particle are calculated, and the particles are accelerated accordingly. Based on the acceleration, the motion of the particles is calculated for a small time interval. In the next step, the procedure is repeated using the new particle configuration. Over time, the system propagates into a state of minimized forces, which corresponds to an energetic minimum. It is important to keep in mind that the stepwise movement is only an approximation to the real motion of particles. Depending on the specific simulation, a multitude of algorithms have been developed to optimize this approximation [140, 141].

This section introduces the Euler method, which is a simple MD algorithm we use to illustrate the fundamentals of the simulations. Afterwards, we present our algorithm adapted for vortex matter in intertype superconductors. The Euler method is based on Newtons equations, which give a simple equation of motion for each particle i:

$$\begin{aligned} r_i\left(t+\Delta t\right) &= r_i\left(t\right) + v_i\left(t\right)\,\Delta t \\ v_i\left(t\right) &= v_i\left(t\right) + \frac{F_i\left(t\right)}{m_i}\,\Delta t \end{aligned} \tag{5.1}$$

Here, r_i, v_i and m_i are the position, velocity and mass of each particle i, respectively, and F_i is the total force acting on it. Δt is the small time interval defining the length of a simulation step. Over the duration of one step, F_i is assumed to be constant, which results in a deviation from the correct differential equation of motion. F_i includes all forces acting on a particle, most importantly the pairwise interaction with all other particles. Additionally, friction, thermal effects or additional forces due to the experimental setup may be considered. Naturally, the choice of interactions included in F_i is crucial for the results of a simulation.

While F_i defines the physical properties of a simulated system, some methodical parameters of the computation may also have a strong impact on the result. As already mentioned, the time steps introduce an error to the simulation, which is purely methodical. This error can be reduced by choosing a smaller Δt. However, with decreasing Δt, the number of simulation steps rises which results in a trade-off between accuracy and simulation time. A similarly important parameter is the size of a simulation. Here, size refers to the particle number and the spatial volume. Basically, the simulation has

to be appropriately large to portray the physics of a system. Points of consideration for the size include the structure size of a domain system or the range of interactions, which both have to fit the simulation volume. The particle number has to be sufficiently large to allow collective phenomena to emerge, such as a well ordered crystal lattice. Additionally, higher particle numbers increase the statistical significance of a simulation. It is important to be aware that the volume and particle number determine the particle density, which can be a highly relevant physical property of the simulation. Typical numbers of particles lie between $10^3 - 10^4$, depending on the system, the available computational power and the complexity of interactions. In addition to the size of a simulation, its shape and boundary conditions have to be considered. The shape may be used to introduce, or avoid, spatial anisotropies. The boundary conditions are defining whether the system is, e.g., isolated (hard boundaries or no boundaries) or represents bulk material (periodic boundaries). In all cases, an inadequate choice of boundaries, which is not representative of the simulated system, may introduce artefacts in the results.

In practice, it is important to distinguish parameters representing a real physical property of a system and parameters which determine the simulation procedure. Both affect the outcome of a simulation, often in similar ways, and one has to be aware of their influences. At the end of this section, we summarize all important parameters and divide them into three categories. Methodical parameters define the simulation procedure and have no, or no clearly identifiable physical meaning. The physics of the simulation are determined by the experimental and material parameters, which define the fundamental properties of the simulated system. In chapter (6), systematical studies on methodical parameters (section (6.1)) and experimental parameters (section (6.2)) are presented separately, while the material parameters (cf. section (5.2.2)) are fixed for all simulations.

5.1.2 Vortex matter simulations

A common approach of vortex matter in superconductors are two dimensional MD simulations based on a Langevin equation of motion [130, 132, 133, 142]. This is mainly due to the complexity of three dimensional vortices and the quasiparticle properties of vortices (cf. the discussion on vortex matter in section (1.2)). In this section, we present our algorithm adapted for the simulation of superconducting vortices, which is especially designed for the study of the IMS transition in intertype superconductors.

Reduction to two dimensions

In MD simulations, atoms are point-like, described by a single position and the two particle interaction. In contrast, vortices extend along the magnetic field and possess string-like elastic properties [50]. Simulating a freely movable vortex requires to divide it into small sections and treat each of them as individual particle [131, 134, 143]. The interaction between parts of the same vortex and the interaction of parts from different vortices has to be treated differently. As a result, the system becomes more complex, and each vortex requires many subsections, which both increases the computation time.

However, in a large part of the superconducting phase, the line tension of a vortex is high enough to prevent significant bending [144]. Only close to the upper critical field H_{c2}, vortices are in a liquid state (cf. figure (1.3)). For pure niobium, the liquid phase has not been observed experimentally [145, 146]. This means that vortices are very strictly oriented along an externally applied magnetic field. The individual elastic properties are replaced by a collective elasticity of the vortex matter, which, in our simulations, is important only in the context of thermal fluctuations. In this scenario, the vortex positions of the system are only changing slowly in the direction of the field. This allows to consider only a two dimensional cut through the vortex system, perpendicular to the vortex line direction. Larger elastic deformations are assumed to be on a scale surpassing the interaction range and are neglected. In the reduced 2D vortex system, each vortex is described as single point-like particle with an interaction potential in two dimensions. This greatly reduces the complexity of the simulation and the number of required particles. For simulating the IMS transition, this is a great benefit, as large systems ($> 10^3$ vortices) have to be studied in order to observe the vortex domains. We note that in a 2D simulation quantities like interaction potentials, forces and associated parameters have to be normalized per unit length.

We want to emphasize that several effects are systematically neglected in this reduced two dimensional approach. This includes small scale deformations, e.g., due to strong pinning centers [61], or branching [147, 148] and pinning [149, 150] at the sample surface. Effects, such as melting of the vortex matter and liquid-like behavior, where vortices can be significantly bent, are out of the scope of the 2D approximation per design. However, the region of interest in this work is in the high κ region of the intertype (above κ_1^* in figure (2.2)(a)), where the IMS transition is sufficiently below T_c. In addition, the magnetic fields regarded in our simulations are in an intermediate range, where the vortices are well aligned to the field direction. The presented two dimensional approach is therefore viable in our case. Fluctuations due to the elastic nature of vortices are very small (cf. section (5.2.5)), and larger deformations are not expected. Like our neutron experiments, the simulations focus on the bulk properties, which makes surface branching a lesser concern. Surface pinning, however, might be of importance, especially in very high purity samples. The implementation of this effect remains for further work.

Equation of motion

The Euler scheme is based on Newtons equations, which applies to the motion of particles with a well defined mass m_i and moderate damping. In contrast, the motion of vortices is not usually described in terms of an effective vortex mass (for an extensive article on the effective mass of vortices see [151]). Additionally, vortex motion in superconductors is highly dissipative [152, 153]. This is caused by the movement of the electrons inside the normal conducting core of vortices [154]. Hence, the Newtonian description is replaced by the overdamped Langevin equation [155–157]. Here, the friction coefficient η is taking the place of the particle mass. Instead of accelerating the particles, the acting forces result in a constant momentary velocity $v_{i\,,\mathrm{cm}}$ of the vortices.

$$\begin{aligned} r_i\,(t+\Delta t) &= r_i\,(t) + v_{i\,,\mathrm{cm}}\,(t)\;\Delta t \\ v_{i\,,\mathrm{cm}}\,(t) &= \frac{F_i\,(t)}{\eta} \\ \eta &= \frac{\Phi_0^2}{2\pi\xi_{\mathrm{GL}\,,0}^2\rho_{\mathrm{res}}} \end{aligned} \tag{5.2}$$

For η, the Bardeen-Stephen expression [154] was chosen, with the zero temperature Ginzburg-Landau correlation length $\xi_{\mathrm{GL}\,,0}$ and the residual resistivity of the normal conducting state ρ_{res}. The overdamped Langevin equation corresponds to the prompt relaxation of the system. We have expanded the equation by a term which allows a short exponential relaxation of the motion instead:

$$\begin{aligned} r_i\,(t+\Delta t) &= r_i\,(t) + v_i\,(t)\;\Delta t \\ v_i\,(t) &= v_{i\,,\mathrm{cm}}\,(t) + exp\left(\frac{-1}{\gamma}\right) v_i(t-\Delta t) \end{aligned} \tag{5.3}$$

Here, γ is a relaxation constant, which is measured in simulation steps. In the absence of forces F_i, the motion of a vortex will relax exponentially over γ steps. Otherwise, a corresponding fraction of the velocities is carried over to the next step and added to the new momentary velocity. The correspondence between γ and the physical properties of a real superconductor are difficult to quantify. Instead, γ should be understood primarily as a way to optimize the convergence of the simulations. The maximally damped case ($\gamma = 0$) has a tendency of moving towards a local optimum of the vortex configuration. Slower relaxation increases the tendency of finding a state closer to the global optimum, but may require longer simulation times to achieve a steady state. Generally, γ is a useful tool to assess the impact of changing vortex dynamics on the simulation result.

Thermal fluctuations

A further adaption for the simulation of vortex matter concerns the implementation of thermal effects. Typically, a statistic thermal force is added to the total force F_i (examples can be found in [130, 158, 159]). This approach is also especially useful for thin film superconductors, where the vortices are small and the thermal force acts on the whole vortex identically. In solid vortex matter in a bulk superconductor, thermal effects rather locally bend the vortices, on a scale depending on the collective elastic properties [144]. For our simulations in two dimensions, we have included the local deformations of the vortices as a small correction δr_{th} of the vortex positions.

$$r\,(t+\Delta t) = r\,(t) + v\,(t)\;\Delta t + \delta r_{\mathrm{th}}\,(t) \tag{5.4}$$

The expression for δr_{th} we use has been derived in linear elastic theory [144, 160, 161]. In this derivation, a non-monotonic vortex-vortex interaction was assumed, which is different from the expression from EGL theory we use, but which is qualitatively similar. Since δr_{th} is very small in our simulations, we estimate the errors due to the exact

interaction potential negligible. δr_{th} follows a Gaussian distribution with the standard deviation σ_{th}:

$$\sigma_{\mathrm{th}} = \frac{k_B T \mu_0 \lambda \kappa}{\phi_0 B} \sqrt{\frac{2b}{(1-b)^3}} \tag{5.5}$$

Here, k_B is the Boltzmann constant, ϕ_0 is the magnetic flux quantum and $b = B/B_{\mathrm{c2}}(T)$ is the reduced flux density with critical upper field B_{c2}.

Time steps

The classical approach to MD simulations is to use equidistant time steps with fixed Δt. Instead, we have decided to restrict the maximal motion of vortices per step and adapt Δt accordingly. The motivation lies in the field cooling procedure of the simulations. With decreasing temperature, the vortex-vortex interaction changes in range and magnitude (cf. section (5.2.3)). In the IMS, the proximity of vortices increases with decreasing temperature which results in larger inter-vortex forces. With fixed time steps, the vortex movement would increase and the simulation would eventually become prone to errors. The dynamical adaption of Δt ensures the proper functionality of the simulations at all temperatures. In each step, we determine the maximum vortex displacement and compare it to an upper limit r_{max} and a lower limit $0.1\, r_{\mathrm{max}}$. Any time one of the limits is crossed, Δt is set to a new value to prevent this. r_{max} was chosen as a fraction $\tau = 0.1$ of the expected vortex separation. This is either the lattice constant of a hexagonal vortex lattice $a_{\mathrm{VL}}(B_{\mathrm{sim}})$ or the minimum position of the vortex interaction potential $r_{\mathrm{VL}}^{\mathrm{min}}(T)$, whichever is smaller. While r_{max} ensures the simulation accuracy, the lower boundary keeps the simulation from stalling. As both these boundaries are linked to the vortex with highest velocity, the average displacement of vortices is always lower. A potential downside of this approach is that the absolute duration of each simulation (regarding the physical system, not the computation time) is different and not known beforehand.

Simulation shape and boundaries

The simulations are designed to study the vortex matter in a bulk superconductor. To represent this, periodic boundary conditions have been chosen. Since the interaction between vortices is of long range order, a hard or missing border would lead to strong distortions of the vortex arrangement near the edge of the simulation. For the same reason, the area of the simulations A_{sim} was chosen to perfectly fit a homogeneous hexagonal lattice. The simulations are performed in rectangular areas with an aspect ratio of $1 : \sqrt{3}/2$, which accommodate a lattice consisting of n rows with n vortices each. Due to the periodic boundaries, a vortex sees multiple copies of another vortex via the different boundaries (e.g., the original vortex and one copy to the left or right). In order to reduce errors in the vortex lattice, at most one instance of any vortex should contribute appreciably to F_i. Therefore, the simulation should be larger than the inter-vortex interaction range. The domains in the IMS, however, may be large enough to stretch over the whole simulation area.

5.1.3 Interactions

In the following part, the interactions used for the simulations will be presented. For the behavior of vortex matter in the IMS, the most relevant forces are the pairwise vortex interaction F_{vv} and the interaction between a vortex and a pinning center F_{vp}. These are the only contributions to the force term F_i of the equation of motion (equation (5.2)). The additional influence of temperature through position fluctuations has already been discussed. Dissipation effects, which are usually included as an explicit term, are an integral component of Langevin type equations of motion and will not be discussed in this section.

Vortex-vortex interaction

The force F_{vv} acting between vortices is based on the pairwise vortex interaction V_{vv} derived from extended Ginzburg-Landau (EGL) theory in chapter (2) (cf. equation (2.7)):

$$\begin{aligned} F_{\mathrm{vv}}(r) = \frac{\partial}{\partial r} V_{\mathrm{vv}} = \hat{F}\tau^{3/2} \quad & \left[\left\{ 1 - \sqrt{2}\kappa + \tau\left(1 - c + 2\,Q\right) \right\} \dot{\mathscr{I}}_{\mathrm{vv}}\left(\frac{r\sqrt{\tau}}{\lambda_0} \right) \right. \\ & \left. + \tau \left\{ 2\,L - c - \frac{5}{3} Q \right\} \dot{\mathscr{J}}_{\mathrm{vv}}\left(\frac{r\sqrt{\tau}}{\lambda_0} \right) \right] \\ \hat{F} = \frac{\mu_0 H_{\mathrm{c},0}^2 \lambda_0}{2\pi} & \end{aligned} \tag{5.6}$$

c, Q and L are fixed model parameters of EGL theory and $\tau = 1 - T/T_{\mathrm{c}}$ is the reduced temperature, with T_{c} being the critical temperature of the superconductor. $\dot{\mathscr{I}}_{\mathrm{vv}}$ and $\dot{\mathscr{J}}_{\mathrm{vv}}$ are the derivatives of the respective integrals introduced in equation (2.6). For the computation of the simulations, the integrals $\mathscr{I}_{\mathrm{vv}}$ and $\mathscr{J}_{\mathrm{vv}}$ were calculated numerically and approximated by a fitting function. Since they are independent of material parameters, they can be rescaled and used for any set of simulation parameters. The scaling $\hat{F}$ has units of N/m due to the two dimensional simulation.

Most superconductors exhibit a spatial anisotropy of the vortex lattice, which is primarily observed as a finite number of vortex lattice orientations [56, 162, 163]. This effect may occur due to the incommensurability of the vortex lattice symmetry and the superconducting state. Vortex interactions may be anisotropic, due to the underlying crystal lattice, Fermi topology or the topology of the superconducting order parameter and gap [45, 56, 162]. In the simple example of a hexagonal vortex lattice on top of a fourfold superconductor, two equivalent alignments of the VL exist. This phenomenon is not included in the EGL vortex interaction potential and is therefore not part of the simulations. A simple way to include the effects of the crystal symmetry is to introduce an according anisotropy to the interaction potential V_{vv} in the form of a prefactor $S_{\mathrm{aniso}}(\theta)$:

$$S_{\mathrm{aniso}}(\theta) = \left(1 + \alpha \cos\left(\frac{2\pi}{n} \theta \right) \right) \tag{5.7}$$

The parameter n in the cosine determines the symmetry of the potential. For a hexagonal VL, it may be chosen, e.g., as $n = 6$ to match the lattice symmetry and lock the VL in a single orientation, or as $n = 4$ to model a cubic crystal lattice. The parameter α is used to control the strength of anisotropy.

Vortex-pinning interaction

The pinning force F_{vp} is based on the widely used model of a Gaussian potential well for the pinning center [90, 164]. In the vicinity of pinning sites, the superconducting state is at least partially suppressed. This makes an overlap with the likewise normal conducting vortex core energetically preferable. The maximum energy that can be gained by the overlap with a pinning center is the superconducting condensation energy lost in the vortex core. Therefore, the depth of the interaction potential well is a fraction ν_{p} of this energy. At the pinning site, the superconducting order parameter changes on a length scale of the GL coherence length ξ_{GL}. The range of the pinning interaction is defined by this length scale as well by choosing the standard deviation of the potential well as $\sigma_{\mathrm{vp}}(T) = \xi_{\mathrm{GL}}(T)$.

$$F_{\mathrm{pv}}(r) = \frac{\partial}{\partial r} V_{\mathrm{vv}}(r) = \nu_{\mathrm{p}} \frac{\pi}{2\mu_0 \kappa^2} B_{\mathrm{c2}}^2 \left(1 - \frac{B}{B_{\mathrm{c2}}}\right) r \exp\left(-\left(\frac{r}{\xi_{\mathrm{GL}}}\right)^2\right) \tag{5.8}$$

5.1.4 Parameter overview

For a better overview, all simulation parameters are listed below with a short comment on their function. They are divided into methodical parameters, which concern the performance of the algorithm, and experimental parameters, which define the properties of the simulated vortex matter.

Methodical parameters:

- Δt
  Each step of a simulation has the duration of a small time Δt. Typically, this time is identical for all steps and is chosen small enough to avoid errors in the calculation. Instead, we have linked Δt to the maximum movement of the vortices in each step. The time interval is changed every time the maximum movement would cross an upper or lower boundary (r_{max} or r_{min}), to prevent this. We have chosen r_{max} as 10 % and r_{min} as 1 % of the expected vortex separation.

- N_{v}, A_{sim}
  The size of a simulation is determined by two parameters; the number of vortices N_{v} and the area A_{sim} in which these vortices are located. Both size parameters limit the physical phenomena which can be simulated. For the observation of a vortex lattice, the simulation has to be large compared to the long range interaction

of vortices. Otherwise, vortices may interact with each other over multiple paths by using the periodic boundary conditions. For the simulations of this work, the long-range interaction has a range of $\approx 10 \times a_{\mathrm{VL}}$ (cf. section (5.2.3)). In the IMS, the simulation has to be large enough to contain several vortex domains. With reference to the neutron experiments, a simulation area of $A_{\mathrm{sim}} > 10 \times 10\,\mu\mathrm{m}^2$ is desirable. The number of vortices is typically chosen according to the available computational time, which increases quadratically with N_{v}. The large number of performed simulations restricted us to durations between 6 h and 12 h and a standard number of vortices $N_{\mathrm{v}} = 2450$. Instead of using higher numbers of vortices, it was more practical to repeat a simulation several times. Both size parameters are depending on each other through the magnetic flux density B_{sim} of a simulation, which is an important physical parameter of the system.

- S_{T}
  The number of steps performed throughout a simulation determines the accuracy of the final result. However, the duration of a simulation increases linearly with the number of steps. Since all simulations in this work are divided into several temperature steps, we define the number of steps per temperature S_{T} instead of a total step number.

- ΔT
  The simulations performed in this work emulate a field cooled experiment. The temperature is reduced in intervals of ΔT, at which a number of S_{T} simulation steps is performed. Each temperature change equals to a small quench of the vortex system. Hence, smaller ΔT are usually preferred.

- γ
  The simulation algorithm is based on the overdamped Langevin equation, which corresponds to an instantaneous relaxation of the vortex movement. The equations were adapted to reintroduce a finite exponential relaxation over a small number γ of simulation steps. With increasing gamma, the vortex system becomes more dynamic, as the vortices acquire and lose velocity over a few steps. Due to the increased mobility of vortices with higher γ, the tendency of the simulation to find lower energy states is increased.

Experimental parameters:

- B_{sim}
  The density of vortices in a simulation is synonymous to a mean magnetic flux density $B_{\mathrm{sim}} = N_{\mathrm{v}}\,\Phi_0/A_{\mathrm{sim}}$. In each simulation, the number of vortices and the area of the simulation are kept constant, which corresponds to a fixed B_{sim}. This corresponds to the case of an experiment with perfect flux freezing in an external magnetic field $H_{\mathrm{ext}} = B_{\mathrm{sim}}/\mu_0$. In the simulations, B_{sim} is used to define the external field and therefore the vortex density. With B_{sim}, the transition temperature into the IMS T_{IMS} and the transitional behavior of the vortex matter changes. Additionally, for a fixed density of pinning sites, the number ratio of vortices to pinning sites changes with the field.

- N_p, ν_p
  The pinning characteristic of the simulated superconductor is defined by two parameters; the number of pinning sites N_p and the relative strength of the pinning potential ν_p. For the number of pinning centers, it is often more helpful to consider the relative number of pins to vortices $N_\mathrm{p}/N_\mathrm{v}$ or the density of pinning centers $\rho_\mathrm{p} = N_\mathrm{p}/A_\mathrm{sim}$. With both parameters, different pinning cases can be realized, e.g., few strong pinning sites or many weak pinning centers.

- T_init, T_final
  All simulations are initiated at a temperature T_init slightly above the expected IMS transition, where the system is in the Shubnikov state. A field cooling procedure in temperature steps of ΔT is performed down to a minimal temperature T_final. The temperature range is mostly dictated by the simulation field B_sim, which determines the IMS transition temperature.

Material parameters:

- T_c, λ_0, ξ_0, κ, $\delta\kappa$, $B_{\mathrm{c2},0}$, ρ_{res}
  The superconducting model system investigated in the simulations is defined by a set of material parameters. T_c is the superconducting transition temperature, λ_L is the London penetration depth and ξ_GL is the Ginzburg-Landau correlation length. κ is the GL parameter and $\delta\kappa$ its deviation from $\kappa_0 = 1/\sqrt{2}$. $B_{\mathrm{c2},0}$ is the zero temperature upper critical magnetic field. Finally, ρ_res is the residual electric resistivity of the normal conducting state. These parameters are identical for all simulations performed in this work and will be introduced in detail in the following section.

5.2 Simulation details

The simulations performed in this work were designed in close semblance to the experiments presented in chapter (4). In the following section, we will describe the experimental procedure of the simulations and the model superconductor used for them.

5.2.1 Simulation procedure

Analogous to the neutron experiments, the simulations follow a field cooling procedure. They are initiated at a temperature T_{init} slightly above the expected IMS transition. Initially, the vortices are arranged in a perfect hexagonal lattice with N rows containing N vortices each. The simulation area A_{sim} fits this lattice perfectly, assuring that the periodic boundaries create a seamless infinite lattice. In contrast, pinning sites were distributed completely randomly in each individual simulation. During the simulation, the temperature is decreased in steps of ΔT down to the final temperature T_{fin}. At each temperature, a number of S_{T} simulation steps is performed. With decreasing temperature, the vortex interactions and some of the material parameters change, which will be addressed in detail throughout this section.

The number of vortices N_{v}, the number of pinning centers N_{p} and the simulation area A_{sim} are fixed throughout each simulation. A_{sim} is rectangular with an aspect ratio of $1 : \sqrt{3}/2$ and periodic boundaries. The average magnetic flux density is given by $B_{\text{sim}} = \phi_0 N_{\text{v}}/A_{\text{sim}}$ and is constant as well. B_{sim} corresponds to the external magnetic field in an experiment. The setup of the simulation corresponds to the case of perfect flux freezing, which was observed in the low purity and medium purity samples. Flux expulsion due to the Meissner-Ochsenfeld effect, which was present in the high purity sample, is not included in the simulations.

The parameters S_{T}, ΔT and γ define the cooldown procedure, which may have a strong impact on the IMS transition. This dependence on these methodical parameters will be systematically explored in section (6.1). In contrast, N_{p}, ν_{p} and B_{sim} are experimental properties which define the sample and experimental conditions. Their impact on the IMS will be examined in detail in section (6.2).

5.2.2 Model superconductor

For the model superconductor, we chose parameters representing clean niobium. The full list is given in table (5.1). For the London penetration depth $\lambda_{\text{L}}(T)$ and the Ginzburg-Landau (GL) correlation length $\xi_{\text{GL}}(T)$, the Ginzburg-Landau temperature dependence was assumed $\propto 1/\sqrt{1-t}$, where $t = T/T_{\text{c}}$ is the reduced temperature. A possible dependence on the magnetic field was neglected. Accordingly, the Ginzburg-Landau parameter $\kappa = \lambda_L/\xi_{\text{GL}}$ is independent from temperature and magnetic field. For the upper critical magnetic field $B_{\text{c2}}(T)$, we used the Gorter-Casimier dependence $B_{\text{c2}}(T) = B_{\text{c2},0}(1-t^2)$. Two different temperature dependencies were used, because λ_{L} and ξ_{GL} were present in the EGL expressions which already contained the GL dependence.

B_{c2}, on the other hand, was based on our own experiments, where the GT dependence was more appropriate. However, for high temperatures, both temperature dependencies are very similar. In the simulations, the temperature range is restricted to $T/T_c > 0.66$, which makes the discrepancies negligible. The sample quality was defined by the low temperature residual resistivity ρ_{res} which was chosen in accordance with the residual resistivity ratio RRR of one of our real samples. We have used the same values in all simulations, irrespective of the pinning parameters, despite their obvious correlation.

T_c	λ_0	ξ_0	κ	$\delta\kappa$	$B_{c2,0}$	ρ_{res}	RRR
9.2 K	32 nm	39.7 nm	0.807	0.1	450 mT	$3 \cdot 10^{-10}\,\Omega$m	500

Table 5.1: List of parameters used for the superconducting model system. The values are chosen to resemble pure niobium. T_c is the zero magnetic field critical temperature of the superconductor. λ_0 and ξ_0 are the zero temperature London penetration length and Ginzburg-Landau correlation length, respectively. Their temperature dependence is given as $\propto 1/\sqrt{1-t}$. κ is the temperature independent GL parameter and $\delta\kappa = \kappa - \kappa_0$. B_{c2} is the upper critical field of a type-II superconductor at zero Kelvin. It has a temperature dependence $\propto (1-t^2)$. ρ_{res} is the low-temperature residual resistivity of a sample with the residual resistivity ratio RRR.

5.2.3 Inter-vortex interaction

Vortex pairs

The two-vortex potential V_{vv} and corresponding force F_{vv} are shown in figure (5.1) for several temperatures. Temperatures below 4 K were omitted, as the EGL model is not valid there. The shape of the potential is characteristic for intertype superconductors and is seen best at low temperatures (cf. section (2.1)). It features a repulsive core region close to $r = 0$ with an approximate range of $\xi_{GL}(T)$. Outside the core, the potential drops to a negative minimum at r^{vv}_{min}, as indicated in the plot. Afterwards, the interaction approaches zero for large separations. With increasing temperature, the core region becomes larger. Simultaneously, the potential minimum gets shallower and broader. Above $T \approx 8$ K, the minimum is negligibly small. Still, the long range interaction of the vortices remains attractive at all temperatures, which is a stark contrast to type-II superconductors.

In panel (b), the vortex force F_{vv} is shown, where positive and negative values indicate a repulsive and attractive action, respectively. With decreasing temperature, the forces increase and shift towards lower r. F_{vv} is zero at r^{vv}_{min}, which marks the potential minimum and the preferred separation of vortices. Additionally, the interaction vanishes close to $r = 0$. Accordingly, perfectly overlapping vortices do not repel each other. Therefore, multi vortices are a stable solution in our model. We note that in EGL true multi-quantum vortices can be stable in some regions of the intertype and their interactions can be calculated. However, their shape, in terms of the order parameter

and magnetic flux density, and their interaction with other vortices differs from a simple superposition of several single-quantum vortices. In our simulation, the occurrance on multi-vortices was rare and mostly restricted to low temperatures, which were not regarded. Therefore, this phenomenon can be mostly neglected.

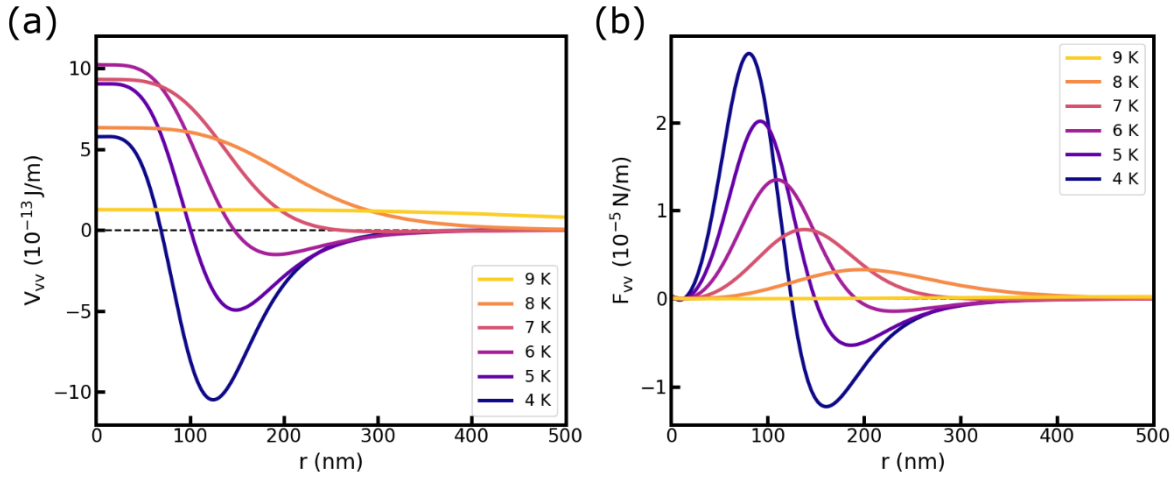

Figure 5.1: (a) Two-vortex potential $V_{vv}(r)$ and (b) force $F_{vv}(r)$ at several temperatures. With decreasing temperature the interaction changes from a repulsive behavior (positive values for V_{vv} and F_{vv}) to the mixed repulsive-attractive intertype behavior. The intertype is characterized by a low-r repulsive part followed by an attractive minimum at finite separation. The long range tail remains attractive. With decreasing temperature, both attraction and repulsion increase in strength. Simultaneously, the minimum position r_{vv}^{min} shifts towards lower separations. The depicted range is limited to temperatures above 4 K due to the range of validity of EGL theory.

Vortex lattice

For the calculation of vortex movement in the simulations, the two-vortex potential is correct. However, due to the long range interaction, the optimal vortex separation in a lattice is different from $r_{\mathrm{min}}^{\mathrm{vv}}$. We have calculated the energy of a vortex in a perfect hexagonal lattice in dependence of the lattice constant. For this, the interaction of all vortices up to a distance of $10\,a_{\mathrm{VL}}$ was taken into account, while vortices further away were neglected. The vortex-lattice interaction V_{VL} is shown in figure (5.2) on the same scale as the two-vortex interaction in figure (5.1). At high temperatures, V_{VL} is strongly repulsive at small a_{VL}. This is plausible, because at small lattice constants multiple repulsive vortex cores are pushed into each other. Below $\approx 7\,\mathrm{K}$, a visible negative potential minimum forms, which is comparable to the two-vortex case. As with the two-vortex potential, the minimum is present at all temperatures, but arbitrarily small. The minimum position $r_{\mathrm{min}}^{\mathrm{VL}}$ is located at a slightly larger separation than $r_{\mathrm{min}}^{\mathrm{vv}}$. A new behavior is observed below $\approx 6.1\,\mathrm{K}$, where a second minimum forms below $r_{\mathrm{min}}^{\mathrm{VL}}$.

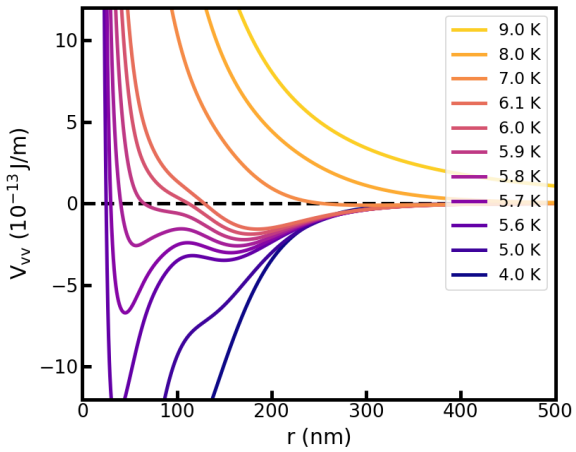

Figure 5.2: Interaction potential of a homogeneous hexagonal vortex lattice. At high temperatures $T > 7\,\mathrm{K}$, the lattice is purely repulsive. Below 7 K, first a single minimum appears in the potential, which is followed by a second minimum at lower temperatures and lower separations. With decreasing temperature, the second minimum deepens, and becomes the global minimum. Finally, the overall potential becomes purely attractive with its minimum at $r = 0\,\mathrm{nm}$, which we denote the vortex lattice instability. Note that temperature steps in the plot are not equidistant.

With the dominance of the second minimum at approximately 5.8 K, the initial assumption of a well ordered lattice is no longer sensible. We refer to this temperature as instability of the vortex lattice. Below the instability, other vortex configurations may become energetically favorable. In simulations below $T \approx 6\,\mathrm{K}$, we have observed the formation of multi-vortices, where a small number of vortices occupies the same position. They have typically formed regular arrangements with a well defined vortex-vortex separation close to $r_{\mathrm{min}}^{\mathrm{vv}}$. Such a solution does not represent the real case of multi-quantum vortices as derived in EGL theory, which have a different shape and interaction potential. However, this instability signifies a new regime in the vortex matter of an intertype superconductor, which is not sufficiently covered by our algorithm.

We note that the lattice potential depends on the size of the vortex lattice. For our calculations, we have considered a patch of 20 vortices diameter. Larger numbers of vortices yielded identical results for our purposes. However, a VL domain in the IMS might be smaller, which will result in a lattice interaction closer to the two-vortex interaction. Since this effect depends on the exact shape of the domain, we did not analyze this effect further.

IMS transition

The temperature dependence of the potential minimum positions $r_{\mathrm{vv}}^{\mathrm{min}}$ and $r_{\mathrm{VL}}^{\mathrm{min}}$ is depicted in figure (5.3)(a). The temperature range is again restricted to $T \geq 4\,\mathrm{K}$. The lattice spacings $a_{\mathrm{VL}}^{\mathrm{SS}}(B_{\mathrm{sim}})$ of hexagonal vortex lattices are shown as dashed lines for

selected flux densities B_{sim}. Close towards T_{c}, the potential minimum position increases very steeply and approaches infinity. For practical purposes, the interaction can be assumed to be purely repulsive above $T \approx 8\,\mathrm{K}$. With decreasing temperature, $r_{\mathrm{vv}}^{\mathrm{min}}$ and its slope decrease. $r_{\mathrm{VL}}^{\mathrm{min}}$ shows a similar behavior above 5.80 K, with slightly reduced values. The deviation increases with decreasing temperature. At 5.80 K, the vortex lattice becomes unstable. The lattice constant a_{VL} of a finite sized vortex lattice lies in between the two theoretical values $r_{\mathrm{vv}}^{\mathrm{min}}$ and $r_{\mathrm{VL}}^{\mathrm{min}}$.

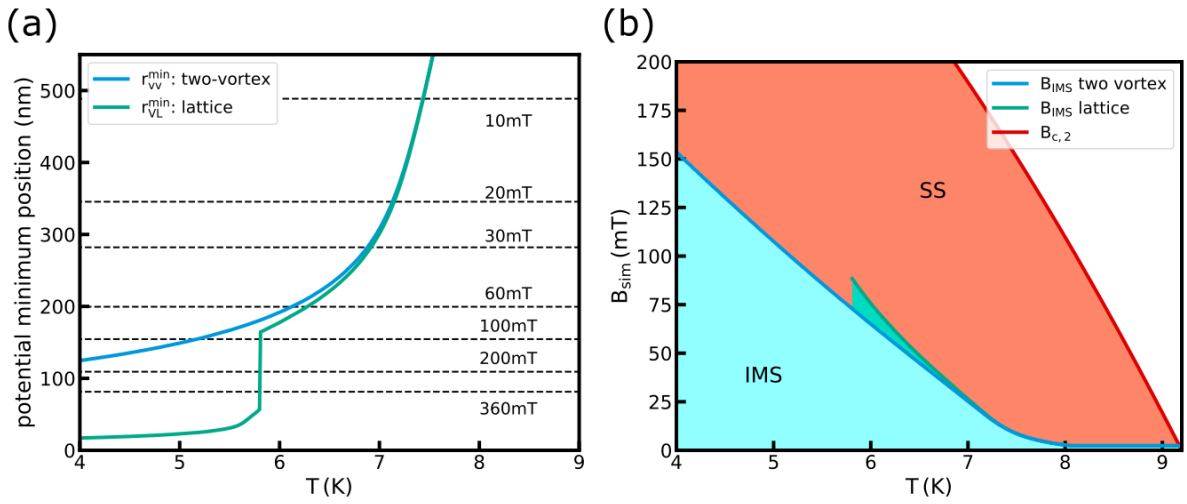

Figure 5.3: (a) Temperature dependence of the vortex potential minimum positions $r_{\mathrm{vv}}^{\mathrm{min}}$ (blue) and $r_{\mathrm{VL}}^{\mathrm{min}}$ (teal). The black dashed lines correspond to the lattice parameter $a_{\mathrm{VL}}(B)$ of hexagonal lattices with mean flux density B as indicated. In field cooled simulations, the transition to the IMS is expected at the intersection of the lines $a_{\mathrm{VL}}(B)$ and $r_{\mathrm{VL}}^{\mathrm{min}}$. (b) B-T-phase diagram for field cooled simulations based on the curves shown in panel (a). The blue and teal areas show the IMS according to the two-vortex potential and the vortex lattice potential, respectively. The Shubnikov state is colored red, defined by the upper critical field B_{c2}. In both panels, results based on the vortex lattice potential are meaningful only above the instability at 5.8 K.

In field cooled simulations, the lattice constant is limited by the magnetic field as $a_{\mathrm{VL}} = \sqrt{2\phi_0/\sqrt{3}B}$. At high temperatures, where $r_{\mathrm{VL}}^{\mathrm{min}} > a_{\mathrm{VL}}$, the lattice cannot expand to satisfy the lowest energy condition. However, at low temperatures where $r_{\mathrm{VL}}^{\mathrm{min}} < a_{\mathrm{VL}}$, the vortex lattice can contract and follow the changing $r_{\mathrm{VL}}^{\mathrm{min}}$. Since the number of vortices is fixed, this causes a domain structure of VL and flux-free regions, which we know as the IMS. Therefore, we define the theoretical IMS transition temperature $T_{\mathrm{IMS}}^{\mathrm{VL}}$ as the crossing point of the constant $a_{\mathrm{VL}}(B)$ lines with $r_{\mathrm{VL}}^{\mathrm{min}}$.

A B-T-phase diagram for field cooled simulations is shown in figure (5.3)(b). T_{IMS} separates the IMS phase space at low temperatures (blue and teal) from the Shubnikov state (red). Additionally, the upper critical field B_{c2} is included in the graphic, which defines the transition to the normal conducting state (white). The blue area is derived from the two-vortex potential, using $r_{\mathrm{vv}}^{\mathrm{min}}$. In the depicted temperature range, above

4 K, the IMS can occur up to a maximum flux density of 154 mT. The smaller teal area corresponds to the lattice interaction with $r_{\mathrm{VL}}^{\mathrm{min}}$ and is truncated at the lattice instability. An IMS transition is only well defined above 5.80 K and below 88 mT. Below 5.80 K, the vortex matter properties are expected to be dominated by the instability.

5.2.4 Pinning interaction

The pinning potential V_{vp} and corresponding force F_{vp} is depicted in figure (5.4) for selected temperatures. Because the interaction strength depends on the magnetic flux density, the plots are shown exemplarily for $B_{\mathrm{sim}} = 30\,\mathrm{mT}$. The interaction potential has the form of a Gaussian distribution with standard deviation $\sigma = \xi_{\mathrm{GL}}$. Therefore, the range of the interaction has the same temperature dependence and decreases with decreasing temperature. The depth of the well is linked to the upper critical field $B_{\mathrm{c2}}(T)$, which results in an increasing pinning strength with decreasing temperature. The pinning force F_{vp} has a maximum attraction at the radius $\xi_{\mathrm{GL}}(T)/\sqrt{2}$ and drops down to zero at $r = 0$. With decreasing temperature, the force maximum increases and shifts towards lower distances. In the temperature range of the simulations, the interaction maximum lies approximately between 50 nm and 60 nm. Because the pinning force is small at the pinning site, a pinned vortex can still move in a limited range. The scaling ν_{p} can be chosen freely to change the relative strength of vortex and pinning interactions.

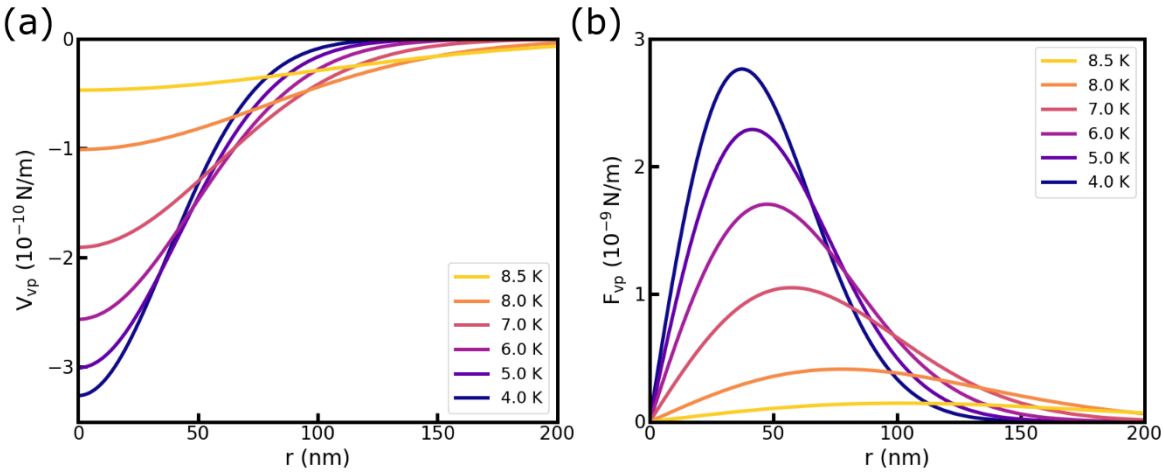

Figure 5.4: (a) Pinning potential $V_{\mathrm{vp}}(r)$ and (b) force $F_{\mathrm{vp}}(r)$ at several temperatures. With decreasing temperature, the potential well deepens and becomes narrower. Accordingly, the pinning force increases. The point of maximal force is located at a distance $r = \xi_{\mathrm{GL}}(T)/\sqrt{2}$, which decreases with temperature.

5.2.5 Thermal fluctuations

Figure (5.5) contains the mean displacement $\sigma_{\mathrm{th}}(T)$ of vortices caused by thermal fluctuations. Through the elastic properties of the vortex lines, σ_{th} depends on the

magnetic flux density and is depicted for $B_{\mathrm{sim}} = 30\,\mathrm{mT}$. At 30 mT, the superconducting transition is at $T_{SC} = 8.89\,\mathrm{K}$ and the expected IMS transition is at $T_{\mathrm{IMS}}^{\mathrm{VL}} = 6.88\,\mathrm{K}$. T_{SC} is derived from the upper critical field B_{c2}. At T_{SC}, the thermal fluctuations are diverging, but drop below 1 nm within 0.5 K. Close to and below T_{IMS}, σ_{th} is significantly smaller than the vortex core radius ($\approx \xi_{\mathrm{GL}} \approx 40\,\mathrm{nm}$), the vortex-vortex separation ($< 100\,\mathrm{nm}$), and the limiting step size of the simulations ($r_{\mathrm{max}} \approx 10\,\mathrm{nm}$). Therefore, it introduces a small randomness to the system to aid the transition from a perfect lattice into the IMS, while not being a significant contribution to the physics of the vortex system.

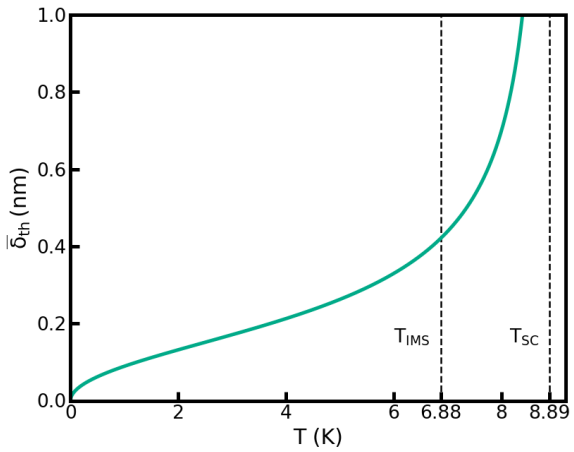

Figure 5.5: Temperature dependence of the average thermal displacement σ_{th} at 30 mT. Indicated are the superconducting transition temperature T_{SC} and the expected IMS transition temperature $T_{\mathsf{IMS}}^{\mathsf{VL}}$ at this field. For comparison, typical values used in the simulations are :$\lambda_{\mathsf{L}}(0\,K) = 32\,\mathsf{nm}$, $a_{\mathsf{VL}}(30\,\mathsf{mT}) = 285\,\mathsf{nm}$ and $r_{\mathsf{max}} \approx 20 - 30\,\mathsf{nm}$.

5.3 Data analysis

In the next section, the data visualization and analytic methods established for the MD simulation of vortex matter will be discussed on one exemplary simulation. In the first part of this section, the real space representation of the vortex arrangement will be discussed. The second part treats the data analysis via its Fourier transform. The data used in this section is a representative field cooled simulation at 30 mT with no pinning. In the simulation, the number of vortices and the simulation area remain constant, which corresponds to a perfect flux freezing transition. The temperature is decreased in steps of 0.1 K, which changes the acting forces and all associated parameters. All simulation parameters are listed in table (5.2). Additionally, the model superconductor parameters given in table (5.1) apply.

N_v	N_p	$B_\mathrm{sim}[mT]$	$T_\mathrm{IMS}^\mathrm{VL}$	$T_\mathrm{init}[K]$	$T_\mathrm{final}[K]$	$\Delta T[K]$	γ	S_T	S_tot
2450	–	30	6.88	7.0	6.1	0.01	0	40	3640

Table 5.2: List of simulation parameters used in the exemplary simulation.

The raw data obtained from a simulation consists of the vortex positions and velocities in each step. These can be used to visualize and analyze the simulation. For the methods presented in this chapter, only the position data is used to create real space images of the vortex distribution and to calculate approximative results of neutron experiments performed on the simulated vortex matter. Since the steady state of the vortex matter was of interest, the velocities were only used for monitoring purposes and not evaluated further.

5.3.1 Real space

A direct visualization of the simulation is depicted in figure (5.6). During the simulation, the temperature is decreased by 0.1 K after performing 40 simulation steps. The images show the final vortex arrangement of the specified temperatures. Each vortex is represented by a marker (blue circles), whose size corresponds to the vortex core region with radius $\xi_\mathrm{GL}(T)$. The simulation was initiated in a perfect hexagonal lattice, which is still intact at 6.7 K. Due to thermal fluctuations, the vortex positions slightly deviate from a perfect arrangement. However, this is not visible in the images due to the resolution of the plot. At $T = 6.6$ K and below, the lattice has broken apart into several domains. The vortex domains still contain a mostly ordered VL, but defects and grain boundaries are visible at several points. Additionally, the vortex lattice orientation changes slightly in some domains. White regions between the VL domains represent the flux-free Meissner state domains. From the images, it is clear that the vortex lattice parameter a_VL and the size of the vortex domains decrease with decreasing temperature. Complementary, the Meissner domains are growing. The overall domain morphology, however, appears to be relatively unaffected.

The rearrangement of vortices and the domain morphology can be visualized by taking the sum over all images presented in figure (5.6). The resulting image is shown in figure (5.7)(a). Darker blue regions present areas of low vortex movement. Areas with a higher change of the vortex positions are in lighter blue. The regions of initial break-up of the lattice appear as white. In the VL domains, special movement patterns can be distinguished. At some points, single isolated vortices in dark blue are visible. These vortices are stationary and present the center of a contracting domain. White stripes indicate a movement of vortices along the primary lattice axes.

In figure (5.7)(b), histograms of the vortex separation are shown. The range is limited to the distance between neighboring vortices. From this image, the vortex lattice parameter a_{VL} may be extracted from the peak positions of the histograms. The width and shape of the distributions also give a direct visualization of the state of order of the lattice.

5.3.2 Reciprocal space

With the real space representation of the simulations, the IMS transition can be easily analyzed in a qualitative way. However, the quantitative evaluation is challenging, especially with respect to the domain size. Instead, we have used the Fourier transform of the real space simulation data in order to extract quantitative results. This approach corresponds to the evaluation of scattering data in the neutron experiments. Consequently, the results of simulations and experiments are directly comparable.

The Fourier transform was calculated directly from the vortex position r_{v}.

$$FT(\mathbf{q}) = \Re\left\{\frac{1}{2\pi}\sum_{i}^{N} exp\left(-\imath\mathbf{q}\cdot\mathbf{r}_{\mathrm{v}}\right)\delta\left(\mathbf{r}-\mathbf{r}_{\mathrm{v}}\right)\right\} \tag{5.9}$$

The shape of the vortices, i.e. their magnetic flux distribution, was neglected for the transformation. Instead, the vortices were assumed as point-like and described with delta-distributions. Due to the limited size of the simulation, the shape of A_{sim} is also present in $FT(q)$ at low $q \approx 2\,\pi/\sqrt{A_{\mathrm{sim}}}$.

Vortex lattice

Figure (5.8) contains all 2D Fourier transforms corresponding to the vortex distributions shown in figure (5.6). The intensity is plotted on a logarithmic color scale. At 6.8 K and 6.7 K, sharp hexagonally ordered peaks are visible. This is the signal corresponding to the initial ordered vortex lattice. In correspondence to scattering theory, we will refer to these spots as Bragg peaks (cf. section (3.5)). The streaks visible around each peak are artefacts from the rectangular shape of the simulation area and the resolution of the image. The position of the first order peaks is marked in the image and at all other temperatures for comparison. With decreasing temperature, the position of the Bragg peaks increases, from initially $q_{\mathrm{Bragg}} = 2.56\cdot10^{-3}/\text{Å}$ above 6.6 K to $q_{\mathrm{Bragg}} = 3.86\cdot10^{-3}/\text{Å}$ at 6.1 K. At 6.6 K and below, the Bragg peaks are significantly broader. Additionally,

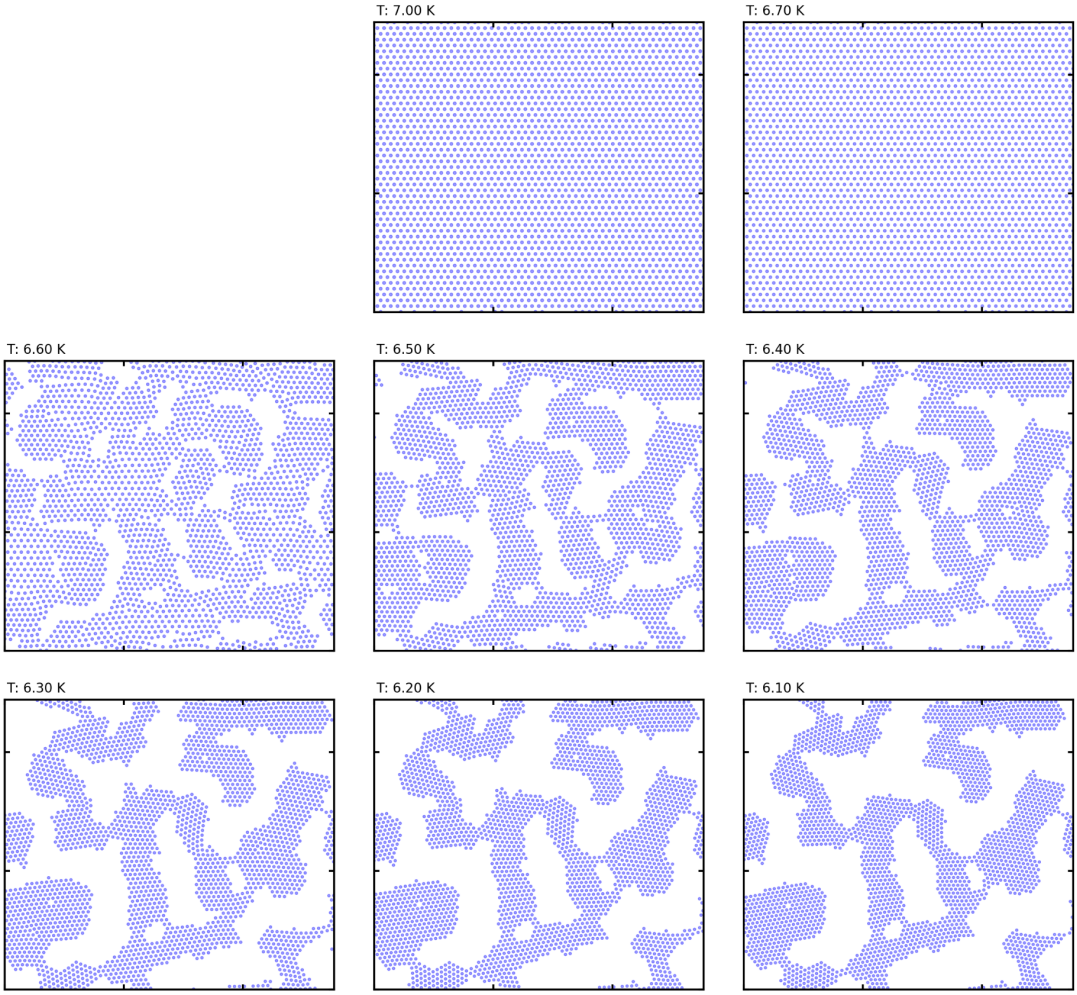

Figure 5.6: Real space visualization of the vortex position in temperature steps of $0.1\,\mathrm{K}$. The position of each vortex is represented by a blue circle with radius $\xi_{\mathrm{GL}}\,(T)$. Shown are the configurations at the final simulation step of each respective temperature. In the first two figures, the initial hexagonal lattice is still intact. At $6.6\,\mathrm{K}$ and below, domains of vortex lattice and of Meissner state are visible. With decreasing temperature, the lattice parameter a_{VL} and the VL domain size are visibly decreasing.

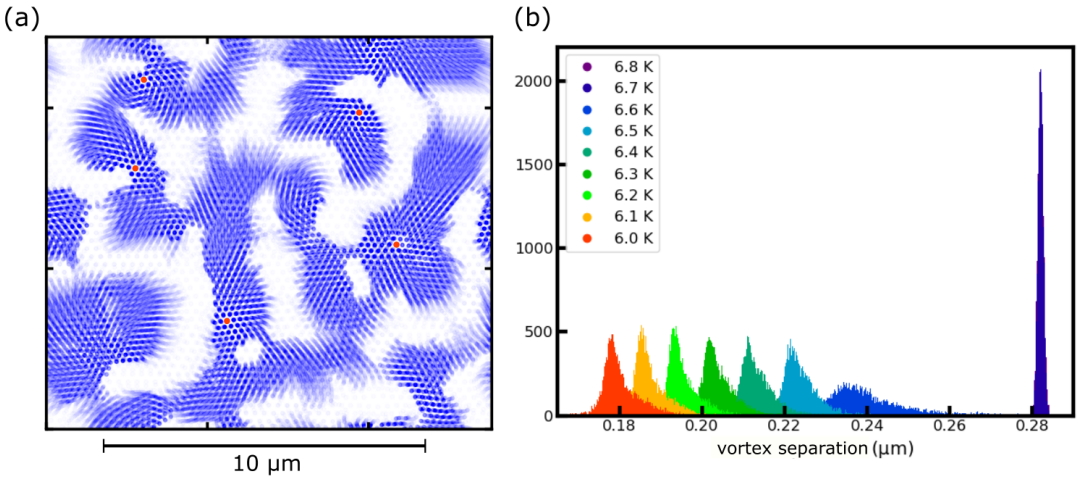

Figure 5.7: (a) Summed up images from figure (5.6). In the image, the votex rearrangement is further illustrated. Lighter colors correspond to areas with high vortex movement and darker colors to low vortex movement. Some stationary vortices are marked red. (b) Histograms of the vortex-vortex separation at different temperatures. The range is restricted to show only nearest neighbors. The peak position corresponds to the average vortex lattice parameter a_{VL}. The width and shape of the peaks correspond to the amount of order in the VL domains. Note that for 6.8 K and 6.7 K the vortex distribution is almost identical and the histograms are hardly distinguishable.

the initial hexagonal arrangement becomes smeared out and changes towards a circular pattern. The broadening is caused by the finite size of the domains. The circular pattern stems from the signal of domains with different alignment of the VL.

For the quantitative evaluation of the Bragg peaks, the 2D Fourier transforms were radially averaged around the center peak. The q-range containing the first order Bragg peaks is shown in figure (5.9)(a), for all images in figure (5.8). Close to $q = 0$, the center peak is also visible, which will be discussed later. At 6.8 K and 6.7 K, the curves are practically identical. Furthermore, the second order Bragg peak is also visible in the plot. In the radial averages, the changing position and width of the Bragg peaks are clearly visible. We have fitted the peaks to obtain the peak center position q_{Bragg} and its full width at half maximum (FWHM). Examples are shown in figure (5.9)(b) for a few temperatures. We have chosen a Lorenzian peak function for the fit, as it matches the simulation data sufficiently well. At the base of the peaks, deviations are common, but the center position and FWHM are precisely determined. To our knowledge, the Lorenzian peak shape does not reflect any mathematical or physical properties of the vortex system.

The radial integration and fitting of the Bragg peaks was performed automatically for each temperature of the simulation. The results are presented in figure (5.10) as lattice constant a_{VL} and correlation length ξ_{VL} of the vortex lattice. The average lattice

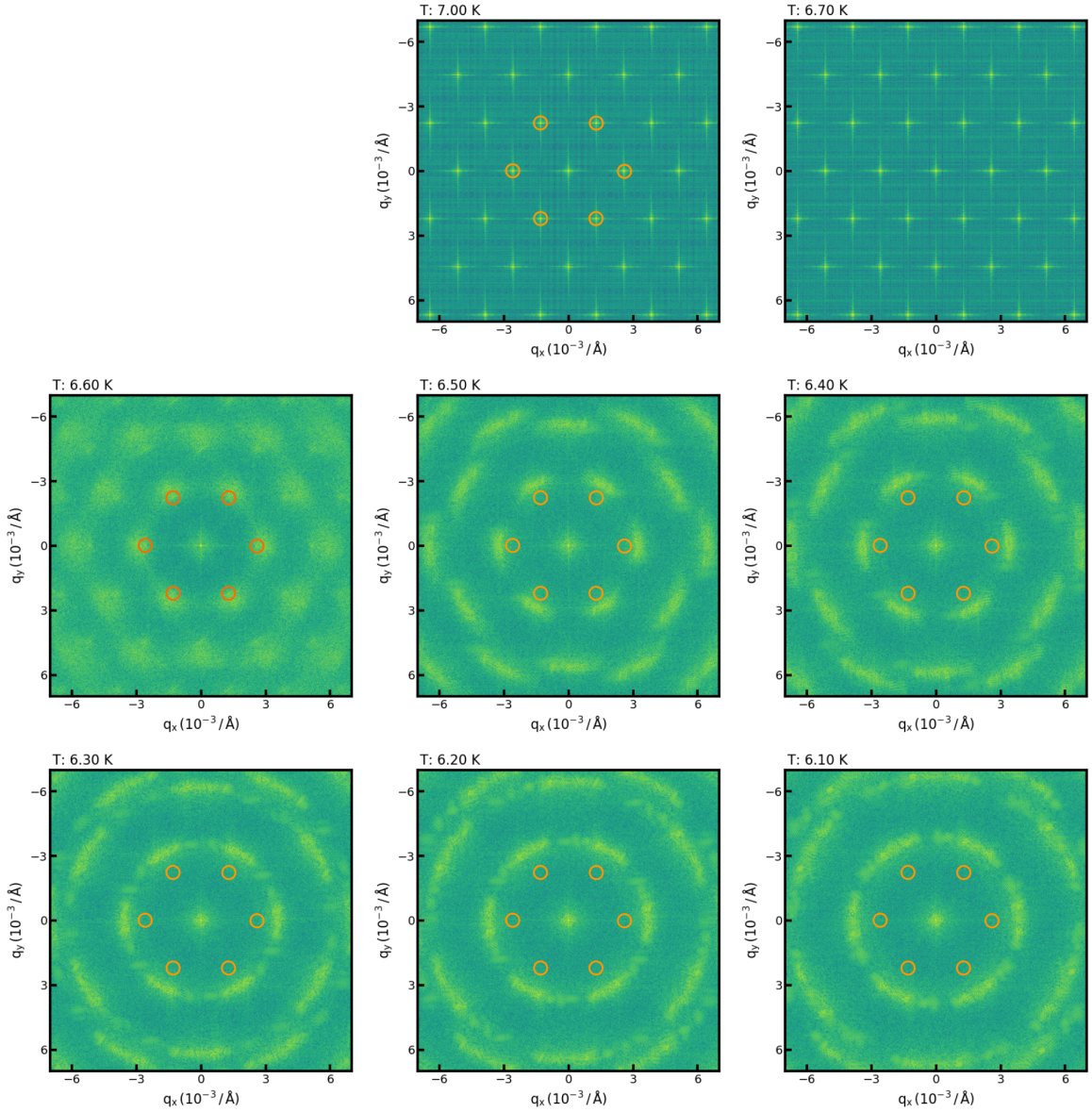

Figure 5.8: Fourier transforms / scattering images of the vortex configurations shown in figure (5.6). Visible in all images are the Bragg peaks stemming from the ordered vortex lattice. With reduced temperature, the peaks become broader and smear out into a ring, due to the loss of correlation between the single domains. The positions of the peaks in the initial ordered state are included in all images to illustrate the changing lattice constant. The intensity around the center peak includes the contribution from the domain structure, which is, however, not distinct in the presented q-range.

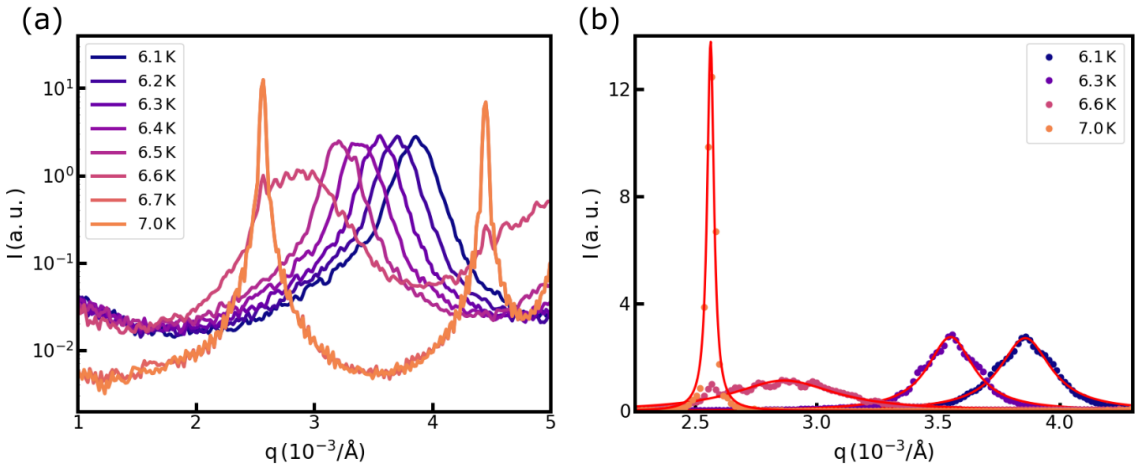

Figure 5.9: Radial averages of the scattering images shown in figure (5.8) in the range of the first Bragg peak. (a) At the highest temperatures, the simulation is still in the initial well-ordered lattice configuration, with identical very sharp peaks. With decreasing temperature, the peaks shift to higher q and broaden due to the finite domain sizes. (b) At selected temperatures, the fit of Bragg peaks with a Lorenzian function is shown, from which the peak position and width in q-direction are determined (cf. figure (5.10)). Note the different scales and ranges for (a) and (b).

constant corresponds to the Bragg peak center position via:

$$a_{\mathrm{VL}} = \frac{4\pi}{\sqrt{3}\, q_{\mathrm{Bragg}}} \tag{5.10}$$

The FWHM of the Bragg peaks in q-direction is a measure for the average lattice correlation length:

$$\xi_{\mathrm{VL}} = \frac{2\pi}{\mathrm{FWHM}} \tag{5.11}$$

ξ_{VL} is an approximate measure for the diameter of the vortex lattice domains. In the simulations, the lattice correlation is limited by the edges of the simulation area. However, this is a considerable problem only if the domains are large compared to A_{sim}. Since the validity of the simulations in such a case is doubtful, this restriction poses no further problems. Usually, we present ξ_{VL} in units of $a_{\mathrm{VL}}(T)$, which highlights a constant domain size in terms of the amount of vortices instead of absolute diameter. As a reference, the image also contains the expected lattice constant $r_{\mathrm{min}}^{\mathrm{vv}}$ and $r_{\mathrm{min}}^{\mathrm{VL}}$ (cf. section (5.2.3)). Between 7.5 K and 6.6 K, $a_{\mathrm{VL}} = 288$ nm, which is equivalent to a global flux density of 30 mT. In this temperature range, the superconductor is in the Shubnikov state. The deviation from the initial a_{VL} is identified as the IMS transition temperature $T_{\mathrm{IMS}} = 6.6$ K. In this example, a considerable undercooling effect is observed, which is present in most of our simulations. Compared to the theoretical transition temperature $T_{\mathrm{IMS}}^{\mathrm{VL}} = 6.88$ K given by the intersection of a_{VL} and $r_{\mathrm{min}}^{\mathrm{VL}}$, the observed T_{IMS} is lower by 0.18 K. In the IMS, the lattice constant is quickly approaching the theoretical curve

of $r_{\mathrm{min}}^{\mathrm{VL}}$. Above T_{IMS}, in the Shubnikov state, the lattice correlation is limited only by the simulation size and has a high constant value $\xi_{\mathrm{VL}} \approx 50\, a_{\mathrm{VL}}$. At the IMS transition, the correlation drops very steeply to a minimum value $\xi_{\mathrm{VL}} \approx 5\, a_{\mathrm{VL}}$. With decreasing temperature, a value around $\xi_{\mathrm{VL}} \approx 13\, a_{\mathrm{VL}}$ is recovered. This value stays constant below $T \approx 6.5\,\mathrm{K}$.

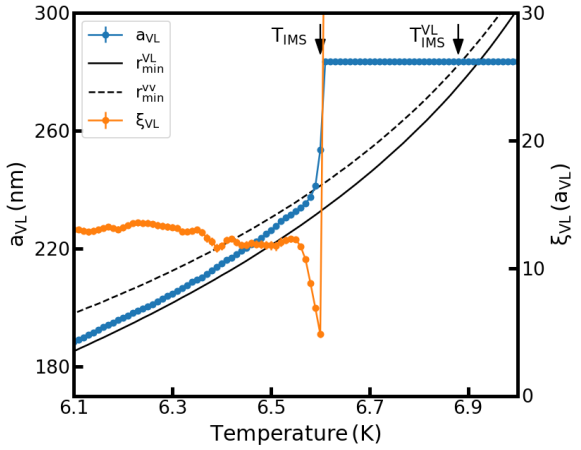

Figure 5.10: Vortex lattice parameters extracted from fits of the first Bragg peak, as shown in figure (5.9). The lattice parameter a_{VL} (blue) is calculated from the peak position (equation (5.10)) and the lattice correlation ξ_{VL} (orange) from its width (equation (5.11)). ξ_{VL} is given in units of $a_{\mathrm{VL}}(T)$. $r_{\mathrm{min}}^{\mathrm{VL}}$ and $r_{\mathrm{min}}^{\mathrm{vv}}$ are shown as solid and dashed black curves, respectively (cf. section (5.2.3)). The coinciding decrease of a_{VL} and ξ_{VL} marks the transition to the IMS at $T_{\mathrm{IMS}} = 6.6\,\mathrm{K}$.

Undercooling of vortex matter

The vortex lattice parameters (figure (5.10)) clearly show that the homogeneous vortex lattice is stable for a considerable range below the expected IMS transition temperature. A change of a_{VL} and ξ_{VL} is first observed at $T_{\mathrm{IMS}} = 6.60\,\mathrm{K}$ instead of $T_{\mathrm{IMS}}^{\mathrm{VL}} = 6.88\,\mathrm{K}$. This undercooling of the VL can be observed in most simulations shown in chapter (6). At $T_{\mathrm{IMS}}^{\mathrm{VL}}$, a_{VL} perfectly matches the energetic optimum of the vortex lattice. As a result, inter-vortex forces are close to zero. Additionally, for a rearrangement of the lattice into domains, the lattice has to split, which locally costs energy. The effect is analogous to the cleaving energy of solid matter [165]. In this exemplary simulation, the effect is enhanced because the vortex lattice is free of defects or grain boundaries by design. The eventual break-up of the VL is largely supported by the thermal fluctuations in combination with the increasing inter-vortex forces.

IMS domains

At small $q < 10^{-3}/\mathrm{Å}$, the Fourier transform contains information about the VL domains. In the 2D images shown in figure (5.8) this is visible as a broadening of the center

peak. Radial averages of this region are shown in figure (5.11). From each curve, the high-temperature signal has been subtracted as background. Below $T_{\mathrm{IMS}} = 6.6\,\mathrm{K}$, a correlation peak emerges which increases in intensity with decreasing temperature. On top of the peak, oscillations are visible. These present an artefact caused by the finite size of the simulation area with $q \approx 2\,\pi/\sqrt{A_{\mathrm{sim}}} \approx 0.04 \cdot 10^{-3}/\text{Å}$. In this example, the number of domains is low and the shape of the peak strongly depends on the individual shape of the domains. Throughout our simulations, we found that the correlation peak can be well described by the same function as used for the experimental data (cf. section (3.3)):

$$I\,(q) = I_{\mathrm{max}} \frac{\left(1 + \frac{\beta}{2}\right)\left(\frac{q}{q_{\mathrm{max}}}\right)^2}{\frac{\beta}{2} + \left(\frac{q}{q_{\mathrm{max}}}\right)^{2+\beta}} \tag{5.12}$$

This phenomenological function was originally derived in the context of domain formation in systems exhibiting spinodal decomposition. β describes the power law of the peak shape at high q and is connected to the dimensionality d of the domain structure. For smooth interfaces, $\beta = d+1$, while rough or entangled domain boundaries lead to $\beta = 2d$. Therefore, the exponent should yield $\beta = 3 - 4$ for our two dimensional simulations. Recently, the formula has also been used to describe the domain structure of the IMS in neutron scattering experiments. We use the peak position q_{max} to define a domain correlation length,

$$\xi_{\mathrm{IMS}} = 2\pi/q_{\mathrm{max}} \tag{5.13}$$

which is interpreted as the average periodicity of the domains, similar to the lattice correlation length ξ_{VL}. Fitting the curves shown in figure (5.11) yields a peak position of $q_{\mathrm{max}} = 0.15 - 0.2 \cdot 10^{-3}/\text{Å}$. q_{max} decreases with temperature, which is likely due to the changing relative intensity of the double peak. The peak position corresponds to a domain correlation length of $\xi_{\mathrm{IMS}} = 3 - 4\,\mu\mathrm{m}$, which fits the real space images well (figure (5.6)). β will not be further evaluated in this work, however, for the sake of completeness, it lies between 3.4 and 3.5 in this example. We deem this value sensible, since the domains have rather smooth interfaces, but the morphology is a complex interconnected structure.

5.3.3 Interaction energy

During the simulation, all calculations are based on the forces acting between vortices and pinning centers (if pinning is considered). However, the interaction energy can be calculated as well and used to evaluate the results. The total energy of the simulation E_{sim} includes all two-vortex interactions and vortex-pinning interactions, if there are any pinning sites. We use two values as reference for E_{sim}, which both assume a perfect hexagonal lattice with different lattice constants. The case $a_{\mathrm{VL}} = r_{\mathrm{min}}^{\mathrm{VL}}$ describes the desired ground state of the intertype superconductor. This ground state energy E_{GS} gives a lower boundary for the energy. However, due to the fixed number of vortices in

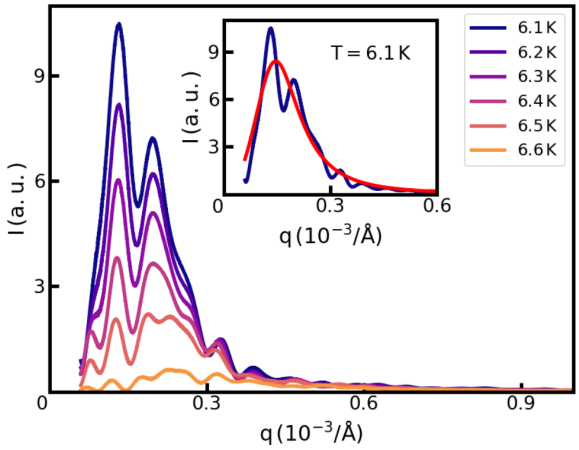

Figure 5.11: Radial averages of the scattering images shown in figure (5.8) in the range of the center peak. From all curves, the background of the initial configuration has been subtracted. The thermal evolution illustrates the increasing scattering signal from the domains, while the q-range of the signal does not shift. Due to the relatively small amount of domains in the simulation, the shape of the peak is rich in features, which have, however, no significant meaning for the further evaluation and are unique to each simulation. The inset shows a fit of the data at 6.1 K using equation 5.12.

the simulation, this homogeneous configuration cannot be achieved. An upper boundary for the energy is given by the energy of the initial vortex configuration, which we call the Shubnikov energy E_{Sh}. E_{Sh} describes the case that no rearrangement of the vortices occurs, despite the changing vortex interaction. The three energy terms are shown in figure (5.12) for the complete simulation. Except for a small region below $T_{\mathrm{IMS}}^{\mathrm{sim}}$, the energy change occurring during the simulation steps at a constant temperature is smaller than the line width. Between 7.5 K and 6.6 K, the simulation stays in the Shubnikov state and $E_{\mathrm{sim}} = E_{\mathrm{Sh}}$ to very good approximation. Close to the theoretical transition temperature $T_{\mathrm{IMS}}^{\mathrm{VL}}$, E_{sim} and E_{GS} touch, making the transition into the IMS possible. Below $T_{\mathrm{IMS}}^{\mathrm{sim}}$, E_{sim} and E_{GS} are almost parallel. The absolute difference between E_{sim} and E_{VL} is difficult to interpret, but can be used for the comparison of simulations.

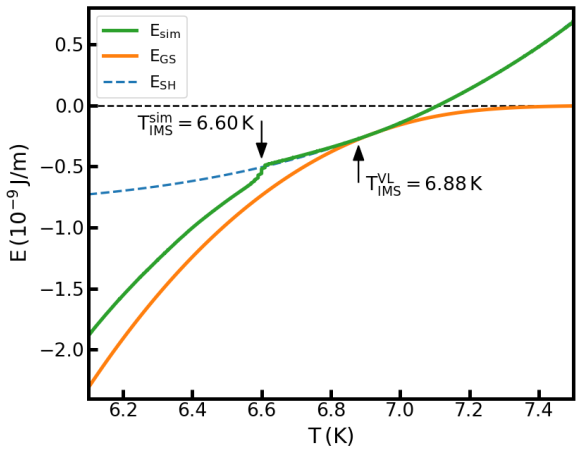

Figure 5.12: Energy of the vortex system over temperature. E_{sim} is the energy calculated from the vortex position. At each temperature, the energy of all steps is plotted. However, the change is smaller than the line width. E_{GS} is the theoretical ground state energy. It is calculated from the minimal energy of the vortex-lattice potential V_{VL} and the number of vortices N_{v}. E_{Sh} is the theoretical energy in the Shubnikov state. It assumes a perfect hexagonal lattice configuration. Down to the observed IMS transition at $T^{\mathsf{sim}}_{\mathsf{IMS}} = 6.6\,\mathrm{K}$, E_{sim} and E_{Sh} are identical. Below $T^{\mathsf{sim}}_{\mathsf{IMS}}$, the curves are almost parallel. In the simulation, the vortex system cannot reach the theoretical ground state due to the domain structure of the IMS. Theoretically, the IMS transition could happen below $T^{\mathsf{VL}}_{\mathsf{IMS}}$, where E_{sim} and E_{Sh} are equal.

6 Systematic MDS studies

In this chapter, simulations of vortex matter will be presented using the molecular dynamics simulation (MDS) algorithm discussed in chapter (5). The simulations are grouped in parameter studies to analyze their systematic effect. Due to the high number of simulation parameters, physically meaningful cases have to be selected from the results. Our main goal is to explore the various possibilities for the IMS transition and the resulting vortex morphology. Finally, the simulations will be compared to the experimental results of chapter (4).

We have divided the parameters into three categories (cf. section (5.1.4)). First, the parameters determining the superconductor model system were defined in section (5.2.2) to represent pure niobium. These values are fixed throughout all simulations. Second are the methodical parameters, which affect the cooldown procedure. In section (6.1), two studies will be presented on the cooling procedure and the relaxation behavior of the vortices. The primary goal of these studies is to evaluate the physical plausibility of the chosen parameters and select a parameter set for the further simulations. Third are the experimental parameters which correspond to the different samples and external fields in the neutron experiments. These will be presented in section (6.2) in two studies, which treat the pinning characteristics and the magnetic field dependence of the IMS.

6.1 Methodical studies

The first two systematic studies focus on the methodical parameters ΔT, S_T, and γ. ΔT and S_T define the duration and the cooling rate of the simulation, while γ affects the ability of the vortex system to follow the temperature change. In combination, these parameters regulate the relaxation towards a stable configuration.

6.1.1 Temperature step size

During the simulation, the system is repeatedly quenched due to the discrete temperature steps ΔT. After each temperature change, the system has S_T number of steps to relax into the new conditions. In the first study, we address the trade-off between smaller quenches or longer relaxation times, which may affect the simulation result differently. For this, a vortex system is cooled down into the IMS from 6.9 K to 6.1 K using different temperature step sizes ΔT in the range between 0.005 K and 0.1 K. With ΔT, the number of steps per temperature S_T is changed to have a constant average cooling rate $S_\mathrm{T}/\Delta T = 5000\mathrm{steps/K}$. This procedure ensures the comparability between simulations and is sketched in figure (6.1). All parameters are summarized in table (6.1).

N_v	N_p	$B_\mathrm{sim}\,(\mathrm{mT})$	$T_\mathrm{IMS}\,(\mathrm{K})$	$T_\mathrm{init}\,(\mathrm{K})$	$T_\mathrm{final}\,(\mathrm{K})$	$\Delta T\,(\mathrm{K})$	γ	S_T	$S_\mathrm{T}/\Delta T$
2450	–	30	6.92	6.9	6.1	*var*	0	*var*	5000

$\Delta T\,(\mathrm{K})$	0.005	0.01	0.02	0.05	0.1
S_T	25	50	100	250	500

Table 6.1: List of parameters used in the systematic study of ΔT.

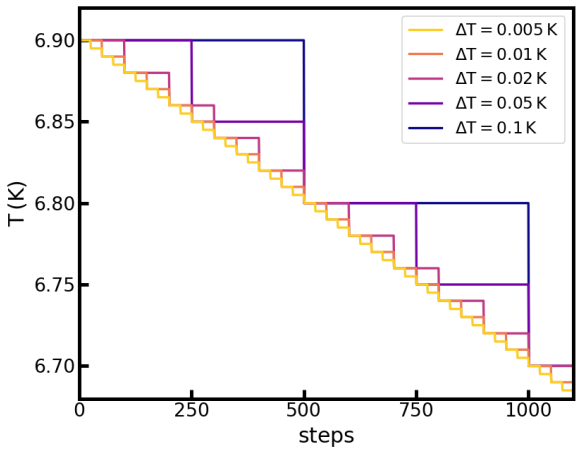

Figure 6.1: Schematic of the cooldown procedure for the different ΔT. Shown are the first 1100 steps. Note that the average cooling rate is the same for all temperature step sizes.

Results

The final vortex configurations of the simulations at 6.1 K are shown in figure (6.2). For the different values of ΔT, they are virtually identical. The domain structure in the IMS consists of a combination of elongated and roundish VL domains which are partially connected. The temperature dependence of a_VL and ξ_VL is shown in figure (6.3). Both parameters are visibly in excellent agreement for all simulations. Slight differences between the curves occur at the IMS transition, due to the different number of temperature steps. The initial VL is under-cooled below the theoretical transition temperature to $T_\mathrm{IMS} \approx 6.6\,\mathrm{K}$. Below this temperature, the lattice parameter a_VL rapidly drops towards the vortex lattice separation (black solid curve). At the same transition temperature, the lattice correlation ξ_VL breaks down from initially $\approx 130\,a_\mathrm{VL}$ to $\approx 5\,a_\mathrm{VL}$. Until the end of the simulation, the correlation recovers to $\xi_\mathrm{VL} \approx 10\,a_\mathrm{VL}$. Values for ξ_VL, a_VL, ξ_IMS and E_tot at $T_\mathrm{fin} = 6.1\,\mathrm{K}$ and T_IMS are listed in table (6.2). Considering the different temperature steps, $T_\mathrm{IMS} \approx 6.6\,\mathrm{K}$ is identical for all simulations. The total interaction energy of the vortex system E_tot shows a very slight decrease to larger ΔT. The numerical values of the lattice parameters show minor random variations. Errors indicated in brackets stem from the fitting process. The graphic presentation in figure (6.3) shows that fluctuations during the simulation are larger, especially for ξ_VL. Finally, the domain correlation length ξ_IMS has a large error, due to the small simulation system

size. Within the error margins, the domain size agrees very well for all ΔT.

ΔT (K)	0.005	0.01	0.02	0.05	0.1
T_{IMS} (K)	6.585(5)	6.58(1)	6.58(2)	6.60(5)	6.6(1)
E_{tot} (nJ/m)	−1.64	−1.69	−1.74	−1.81	−1.87
ξ_{IMS} (μm)	3.3(3)	3.6(3)	3.5(3)	3.2(3)	3.0(3)
ξ_{VL} (a_{VL})	5.8(1)	4.9(1)	5.5(1)	5.1(1)	5.4(1)
a_{VL} (nm)	188.96	189.60	188.55	189.36	188.41

Table 6.2: Results of the simulation analysis. E_{tot}, ξ_{IMS}, ξ_{VL} and a_{VL} are the values at $T_{\mathrm{fin}} = 6.1\,\mathrm{K}$. None of the results indicate a significant dependence of the IMS transition on the temperature step size ΔT.

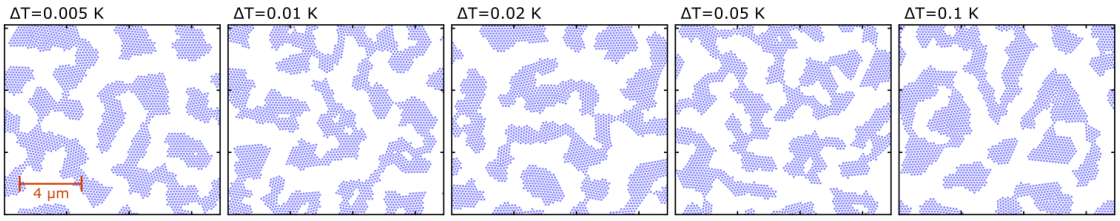

Figure 6.2: Real space images of the final vortex configuration for the systematic study of ΔT. For all other simulation parameters see table (6.1). In all images, the domain morphology is comparable, with a tendency towards elongated and partially connected VL domains. There is no indication of a major influence of ΔT.

Discussion

In the considered range of ΔT, the temperature steps do not show any impact on the IMS transition and the final domain morphology. At first glance, this is not expected. For larger values of ΔT, the vortex interactions are changing stronger from one temperature to the next. The discrete temperature steps can be understood as a repeated quenching of the vortex system. Accordingly, we expected a higher degree of disorder and smaller VL domains for large ΔT. However, this effect is most likely dominated by an intrinsic quenching of the simulation. The transition temperature, observed in the lattice parameters, $T_{\mathrm{IMS}} \approx 6.6$ is already below the theoretical temperature at 6.92 K. This undercooling of $\approx 0.3\,\mathrm{K}$ is more significant than the additional quenching due to $\Delta T \leq 0.1\,\mathrm{K}$.

As a consequence, a small $\Delta T = 0.01\,\mathrm{K}$ was chosen for all further simulations, as a slow change of temperature seemed to be beneficial in cases where the undercooling is not as strong. Additionally, the determination of T_{IMS} is more precise. A smaller value was avoided as it would lead to cases of $S_{\mathrm{T}} < \gamma$ in later studies.

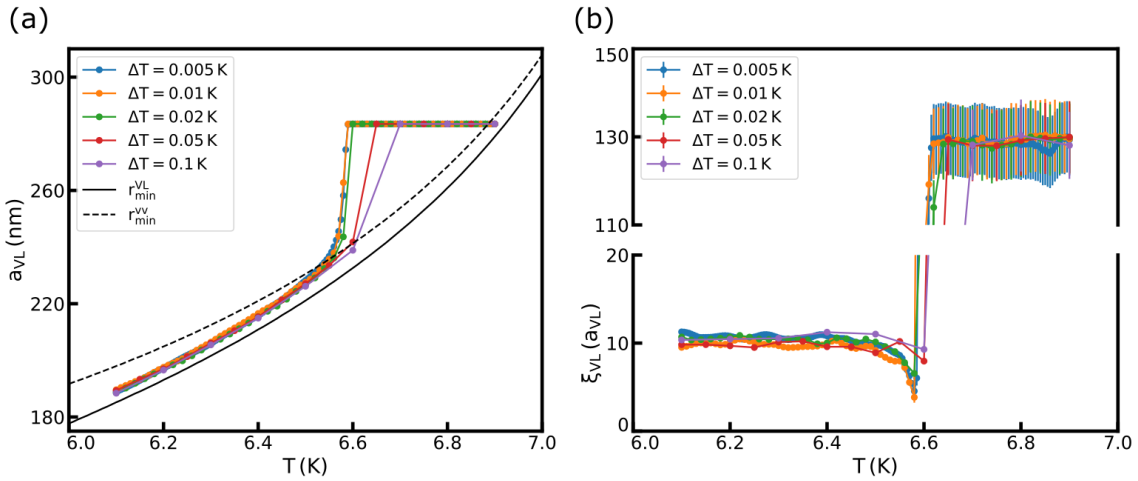

Figure 6.3: Temperature dependence of the lattice parameters for the systematic study of ΔT. For all other simulation parameters see table (6.1). (a) a_{VL} remains constant below the theoretical IMS transition at $6.92\,\mathrm{K}$. At $T_{\mathrm{IMS}} = 6.6\,\mathrm{K}$, the transition is observed as a rapid decrease of the lattice constant toward the optimal VL separation (solid black curve). The optimal two-vortex separation is included for reference (dashed black line). (b) ξ_{IMS} is at a very high level $\approx 130\,a_{\mathrm{VL}}$ above T_{IMS}. Below the IMS transition, it drops to a minimum of $5\,a_{\mathrm{VL}}$ and recovers to a constant value of $\approx 10\,a_{\mathrm{VL}}$ below $6.5\,\mathrm{K}$. Except for the different temperature step sizes, the curves of all simulations are in very good agreement. There is no indication of a major influence of ΔT.

6.1.2 System relaxation

The relaxation of the vortex system towards a stable ground state is mainly governed by the number of simulation steps per temperature S_{T} and the relaxation parameter γ. The interplay of both parameters was studied systematically with values of $\gamma = 0, 1, 2, 4, 8, 16$ for each $S_{\mathrm{T}} = 6, 13, 25, 50, 100$. All parameters of the simulations are summarized in table (6.3).

N_{v}	N_{p}	$B_{\mathrm{sim}}\,(\mathrm{mT})$	$T_{\mathrm{init}}\,(\mathrm{K})$	$T_{\mathrm{final}}\,(\mathrm{K})$	$\Delta T\,(\mathrm{K})$
2450	–	30	6.9	6.1	0.01 (K)

S_{T}	6	13	25	50	100
S_{tot}	486	1053	2025	4050	8100

Table 6.3: List of parameters used in the systematic study of γ and S_{T}.

Results

Real space images of the final vortex configuration of all combinations of γ and S_T are depicted in figure (6.4). The domain size clearly increases with both increasing γ and S_T. In simulations where both parameters are small, the domain size is relatively small as well. The morphology mostly shows isolated islands, partially elongated or connected. For combinations of high parameters, the domain structure is comparable to the simulation size. The VL domains are completely connected in these cases. For large domains, an influence of the periodic boundary conditions on the simulation outcome is probable. Since the overall dependence on γ and S_T is obvious, however, this effect was not further investigated.

Numerical results for a_VL, ξ_VL, T_IMS, E_tot and ξ_IMS are summarized in figure (6.5). The observed transition temperature T_IMS lies between 6.54 K and 6.62 K while the theoretical value is 6.92 K. The change of T_IMS is small, but shows a clear systematic increase with increasing γ and increasing S_T. The resulting undercooling of the vortex matter is $\approx 0.3 - 0.4\,\mathrm{K}$. a_VL and ξ_VL behave qualitatively identical in all simulations and are comparable to the example shown in figure (5.10). The lattice constant a_VL is smaller for larger domains and decreases with increasing γ and S_T. Values are between 194.5 nm and 187.0 nm. For comparison, $r_\mathrm{min}^\mathrm{vv} = 198.0\,\mathrm{nm}$ and $r_\mathrm{min}^\mathrm{VL} = 185.2\,\mathrm{nm}$. Note that the color scale of a_VL has been reversed for easier comparability. In correspondence to the behavior seen in the real space images, both correlation lengths increase with increasing γ and S_T. ξ_VL changes from $3.3\,a_\mathrm{VL}$ to $10.3\,a_\mathrm{VL}$ by a factor of ≈ 3.1. ξ_IMS ranges between $1.6\,\mu$m and $6.9\,\mu$m, and changes by a factor of ≈ 4.3 with almost identical systematics as ξ_IMS. Values above $\approx 6\,\mu$m should be taken cautiously due to the comparable size of the simulation. The total interaction energy E_tot of the vortex system is smallest for large domains with a minimal value $-1.99\,\mathrm{nJ/m}$ and a maximum of $-1.64\,\mathrm{nJ/m}$. The systematics is again comparable to the other parameters. As a comparative value, the energy of a perfect lattice configuration with $a_\mathrm{VL} = r_\mathrm{min}^\mathrm{VL}$ would be $-2.31\,\mathrm{nJ/m}$.

Discussion

The behavior seen in the variation of γ and S_T corresponds to the ability of the vortex system to adapt to changing interactions. Increasing S_T gives the vortices more time to adjust to a temperature change. Increasing γ effectively increases the mobility and inertia of the vortices, making it easier to adapt to a new temperature. As a result, the quenching due to discrete ΔT is weakened by increasing both parameters. In cases of low γ and S_T, the series of temperature changes is too fast for the system to follow. In essence, the vortex system behaves more rigid, if γ and S_T are low. At the IMS transition, the initial lattice fractures into more, smaller pieces and lacks the ability to reform larger domains in the remainder of the simulation. In contrast, high values of γ and S_T increase the ductility of the vortex matter, which allows the formation of larger domains.

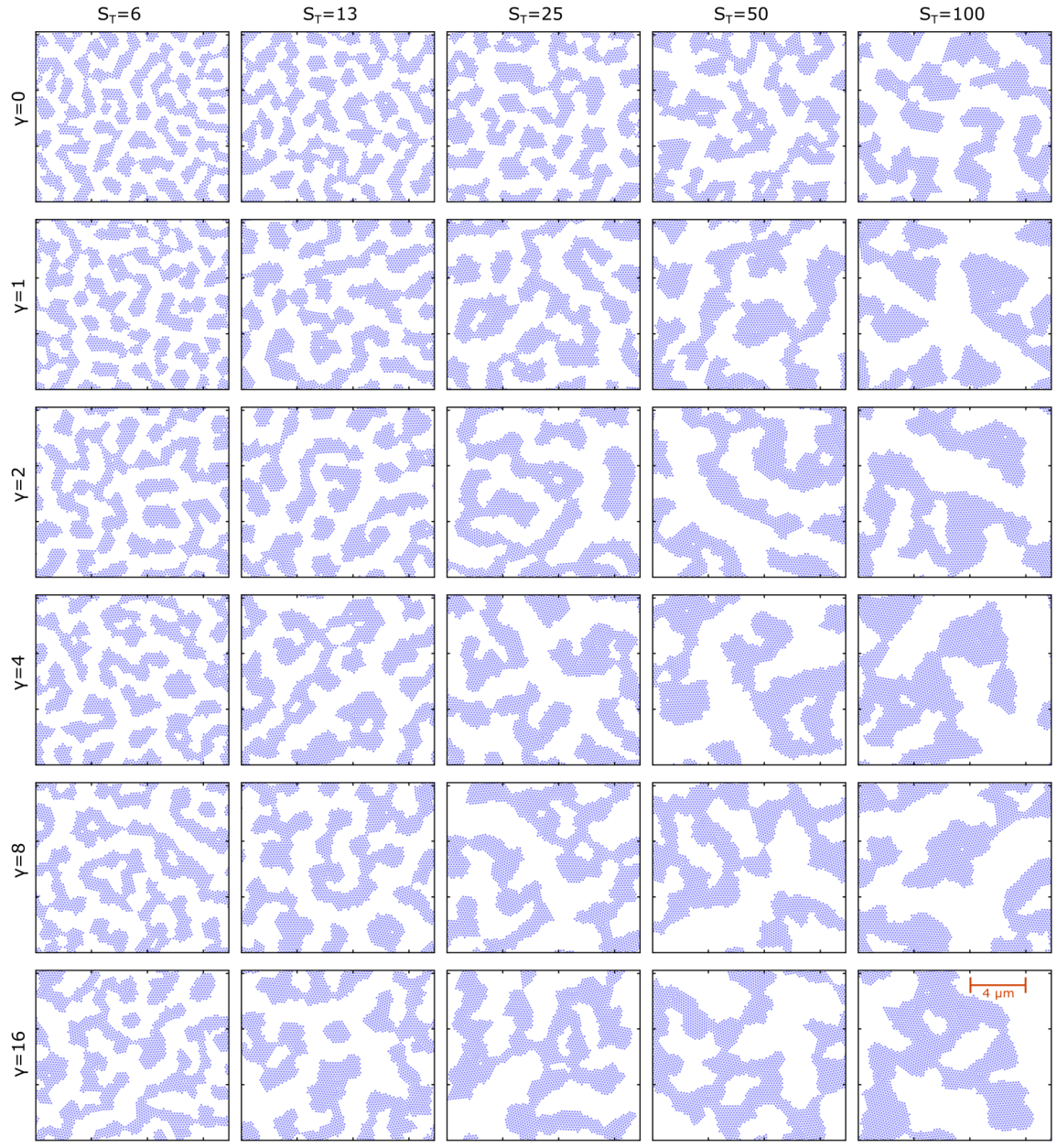

Figure 6.4: Real space images of the final vortex configuration for the systematic study of γ and S_T. For all other simulation parameters see table (6.3). With increasing γ and S_T the domain size is visibly increasing. Note that for large parameters, the domain size becomes comparable to the simulation area which might affect the results.

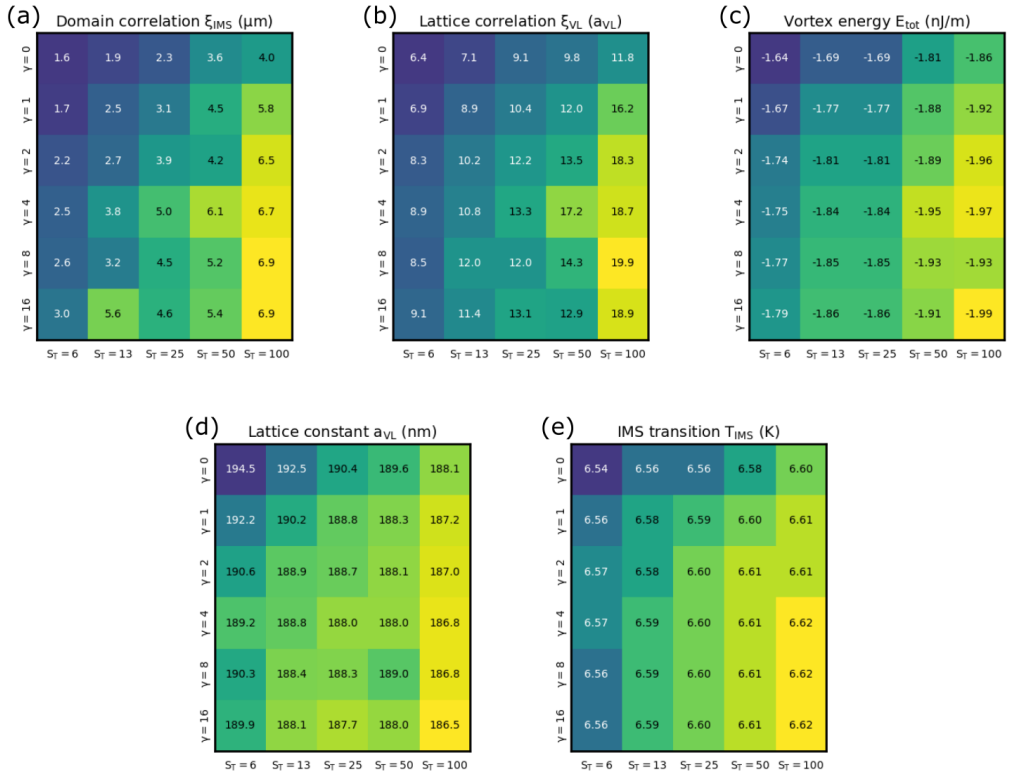

Figure 6.5: Results from the systematic study of γ and S_T evaluated at $T_\mathrm{fin} = 6.1\,\mathrm{K}$. (a) Correlation length of the VL domains ξIMS, (b) correlation length of the vortex lattice ξ_VL, (c) total interaction energy E_tot, (d) lattice constant a_VL and (e) IMS transition temperature T_IMS. All plots show the same systematic dependence. The correlation lengths (a, b) are particularly identical and show an increasing domain size with increasing γ and S_T. With increasing domains, E_tot, a_VL and T_IMS (c, d, e) decrease. However, the change in the three last parameters is much less pronounced compared to ξ_IMS and ξ_VL.

Obviously, the IMS morphology is strongly depending on the vortex dynamics defined by the parameters γ and S_T. It is therefore difficult to make a correct choice for further simulations. We have decided to use the combination $\gamma = 4$ and $S_\mathrm{T} = 25$ for the following reasons: First, we have considered the validity of the simulation results. For higher γ or S_T, the domain size becomes too close to the simulation size, which may introduce artefacts in the morphology. Second, the simulations ought to reflect the results from our neutron experiments. With $\xi_\mathrm{IMS} \approx 13\,a_\mathrm{VL}$, the lattice correlation is larger than measured for the high purity sample ($\xi_\mathrm{IMS} \approx 5\,a_\mathrm{VL}$). However, in simulations including pinning centers, a further decrease of ξ_IMS is expected. Choosing this higher value of the lattice correlation in the pinning-free case increases our margin to explore the pinning parameters, before destroying the lattice correlation altogether. Third, we had to consider the computational time. For the amount of simulations performed for this work, higher numbers of steps would still be feasible, however, we deemed it an unnecessary complication. Higher relaxation constants γ were avoided to stay close to the original Langevin equation of motion.

6.2 Experimental studies

The systematic studies of experimental parameters presented in the following sections are concerned with the pinning and magnetic field dependence of the IMS. First, the interplay of the number of pinning sites N_p and their relative interaction strength ν_p will be addressed at a fixed magnetic field. Second, the dependence of the IMS on B_sim will be analyzed for three different cases of pinning.

6.2.1 Pinning

The effect of pinning is a major concern for the vortex domain structure in the IMS. Our experiments have shown that the IMS transition temperature depends on the purity of the sample. In the simulations, two parameters are defining the pinning properties: the density of pinning centers $\rho_\mathrm{p} = N_\mathrm{p}/A_\mathrm{sim}$ and the relative strength ν_p of the pinning interaction. Due to the reduction of the simulation to 2 dimensions, it is difficult to relate the area density of pinning sites to a real three dimensional distribution. Furthermore, the pinning included in the simulations only comprises bulk pinning. Surface pinning is not included, but might play an important role, especially in clean samples. Through the systematic study of both pinning parameters, however, various pinning regimes will be identified, which may be related to experimental data. For this study, simulations were performed with $\rho_\mathrm{p} = 0.145, 1.45\,, 14.5\,, 145.0\,(1/\mu\mathrm{m}^2)$ for each $\nu_\mathrm{p} = 10^{-5}, 10^{-4}, 10^{-3}, 10^{-2}, 10^{-1}$. All simulation parameters are listed in table (6.4).

N_v	N_p	ν_p	$B_\mathrm{sim}\,(\mathrm{mT})$	$T_\mathrm{init}\,(\mathrm{K})$	$T_\mathrm{final}\,(\mathrm{K})$	$\Delta T\,(\mathrm{K})$	γ	S_T	S_tot
2450	*var*	*var*	30	6.9	6.1	0.01	4	25	2025

Table 6.4: List of parameters used for the systematic study of N_p and ν_p.

Results

Figure (6.6) shows the final vortex configurations of simulations at $T_\mathrm{final} = 6.1\,\mathrm{K}$. The pinning sites are randomly distributed for each simulation, but have been omitted in the images for graphical reasons. Vortex positions which appear in a darker blue indicate the occupation of multiple vortices. In the figure, three primary regimes can be identified. For high ρ_p and ν_p, the vortex system is disordered, showing neither a vortex lattice, nor a domain structure. In the opposing case of low ρ_p and ν_p, the system is effectively pinning-free and exhibits large domains of vortex lattice. In between, roughly on a diagonal with constant $\rho_\mathrm{p} \cdot \nu_\mathrm{p}$, smaller domains and single vortices are visible. Overall, the domain size decreases with increasing ρ_p and ν_p, developing from the unpinned IMS domain structure to a disordered state.

In figure (6.7), the lattice parameters a_VL (blue) and ξ_VL (orange) are shown. The changes seen in the temperature dependence of the lattice parameters are less systematic

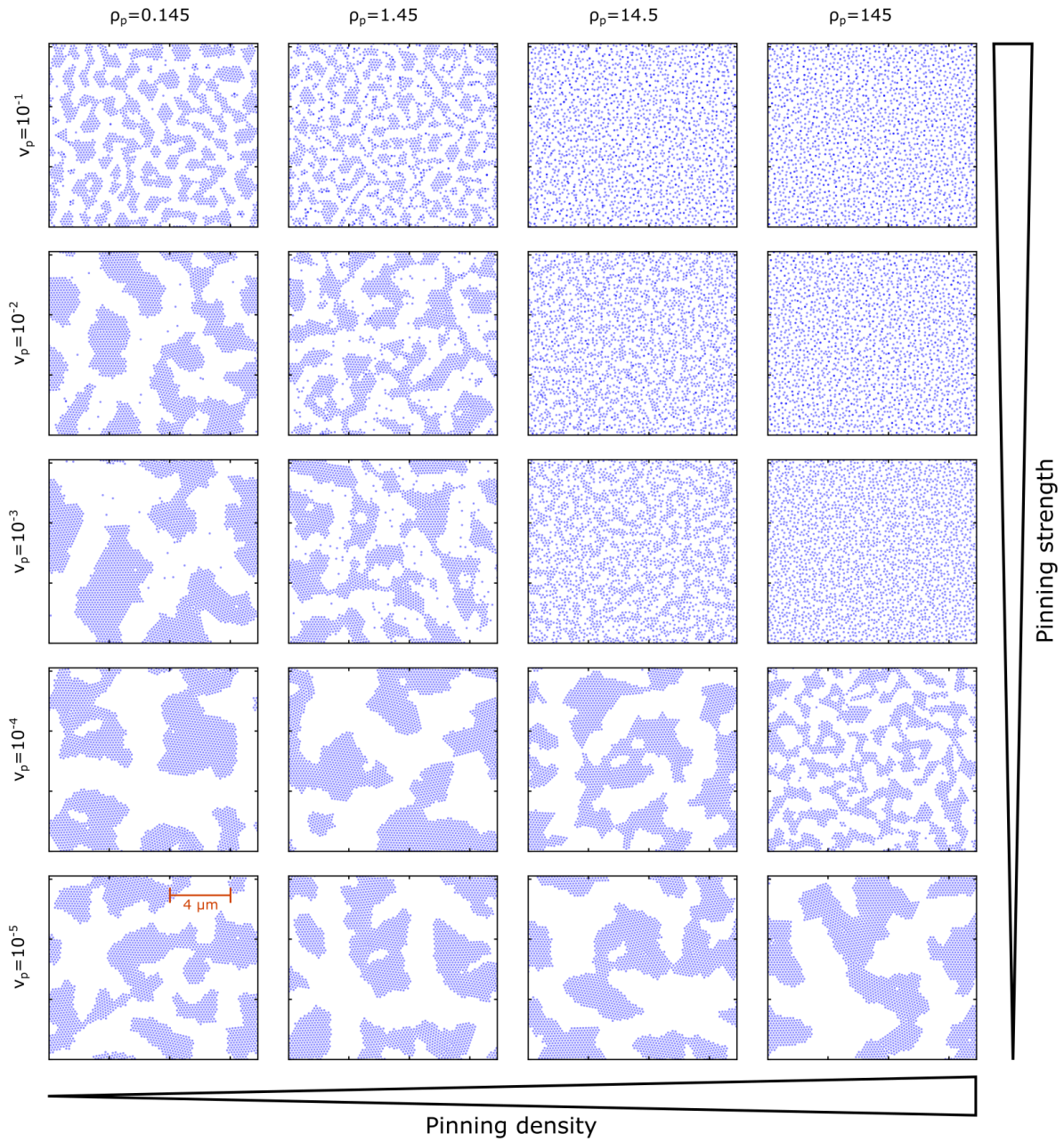

Figure 6.6: Real space vortex configurations for the systematic study of the pinning parameters ρ_p and ν_p. For all other simulation parameters see table (6.4). At the bottom left (low ρ_p and ν_p), the system is practically pinning-free with large domains. In contrast, at the top right (high ρ_p and ν_p) pinning is dominant and the vortices are in disorder. In between, the IMS domain size decreases with increasing pinning parameters. For low pinning densities, single isolated vortices are present in the Meissner regions. Note the logarithmic scale of both N_p and ν_p.

compared to the real space vortex configuration. Again, for low ρ_p and ν_p, the pinning-free behavior is seen. The hallmarks of this case are a sharp drop of a_VL and ξ_VL at the identical temperature, which were already seen in the simulations of section (6.1). For high ρ_p and ν_p, the disorder renders an evaluation of the lattice parameters meaningless. The plots are shown for the sake of completeness. A common feature in the presence of moderate pinning is a broadening of the IMS transition, which is seen in a_VL and ξ_IMS. At the same time, the transition temperature is increased in all cases, except for $\nu_\mathrm{p} = 10^{-1}$. In simulations where the domains are visibly smaller, ξ_VL is lower and the lattice constant a_VL tends towards the two-vortex separation $r_\mathrm{min}^\mathrm{vv}$ as opposed to the vortex lattice separation $r_\mathrm{min}^\mathrm{VL}$.

Numerical values for ξ_IMS, ξ_VL at $T_\mathrm{fin} = 6.1\,K$ and T_IMS are shown in figure (6.8). Both correlation lengths confirm the behavior seen in the real space data. ξ_IMS lies in the range between $1.0\,\mu$m and $9.2\,\mu$m and ξ_VL between $1.2\,a_\mathrm{VL}$ and $10.2\,a_\mathrm{VL}$. Both quantities are clearly correlated. The lowest values are found close to the disordered regime (blank spaces in the parameter maps). Close to the pinning-free region, with small ρ_p and ν_p, the domain size is probably limited by the simulation area. The lattice constant a_VL resembles the domain size, where smaller domains have a larger lattice constant. Values are between 205.8 nm and 187.2 nm. For comparison, $r_\mathrm{min}^\mathrm{vv} = 198.0\,\mathrm{nm}$ and $r_\mathrm{min}^\mathrm{VL} = 185.2\,\mathrm{nm}$. The transition temperature T_IMS lies between 6.48 K and 6.88 K. For comparison, the theoretical value is 6.92 K and the pinning-free value is 6.60 K. T_IMS is increasing with increasing pinning strength ν_p. The dependence on the pinning density seems to feature a maximum value for $\rho_\mathrm{p} \approx 10^{-3}$. The transition temperature does not seem to be correlated to the other parameters. For the pinning study, we have not analyzed the interaction energy E_tot, because the contribution from the pinning interaction is changing too much with the pinning parameters.

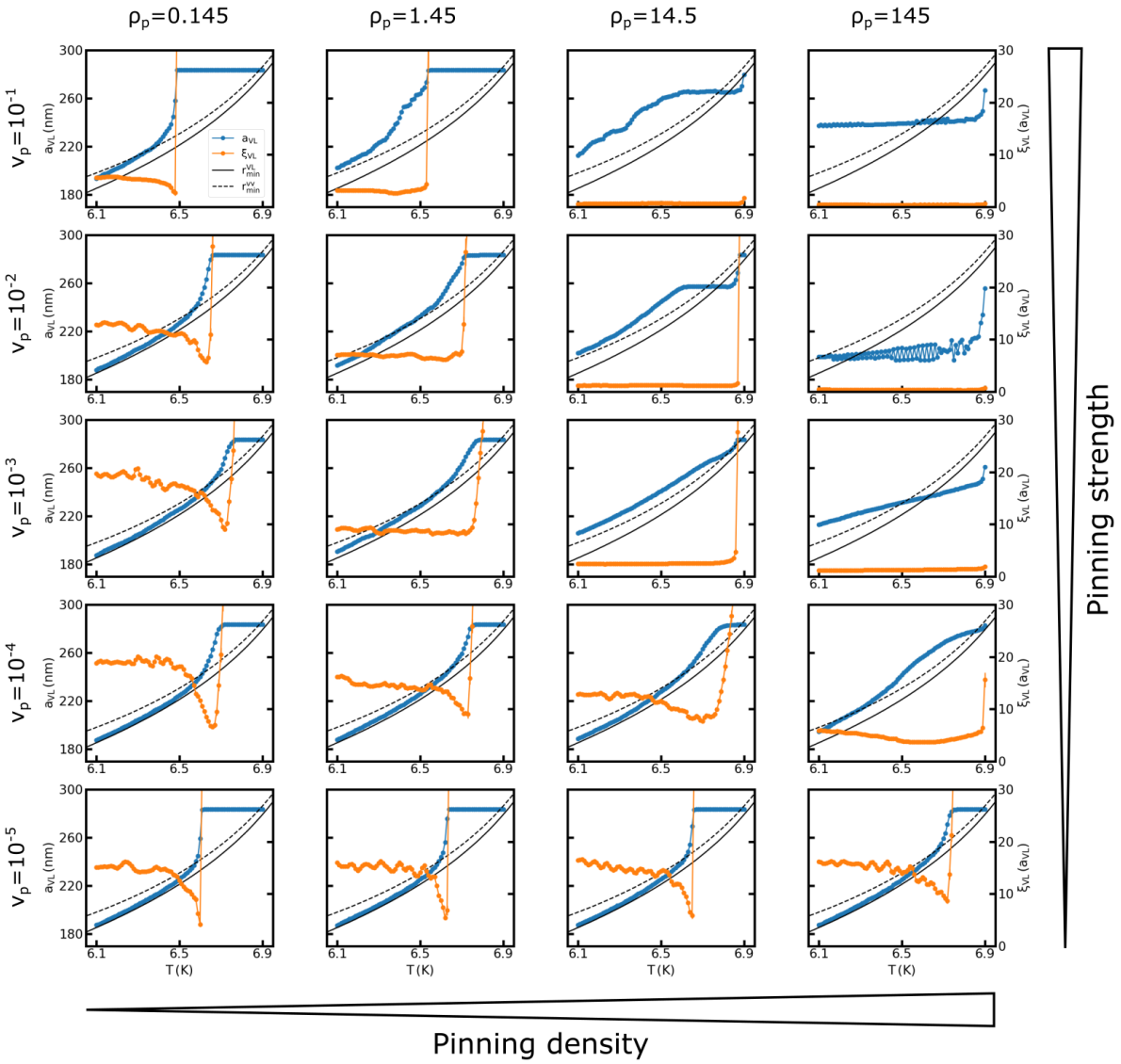

Figure 6.7: Temperature dependence of the lattice parameters a_{VL} (blue) and ξ_{VL} (orange) for the systematic study of the pinning parameters ρ_{p} and ν_{p}. For all other simulation parameters see table (6.4). At the bottom left (low ρ_{p} and ν_{p}), the system is practically pinning-free and shows a sharp transition into the IMS. In contrast, at the top right (high ρ_{p} and ν_{p}) pinning is dominant and the evaluation of the lattice parameters is not meaningful. The data is shown for completeness. In between, the transition is broadened in most cases. Simultaneously, pinning increases the transition temperature T_{IMS}. Note the logarithmic scale of both N_{p} and ν_{p}.

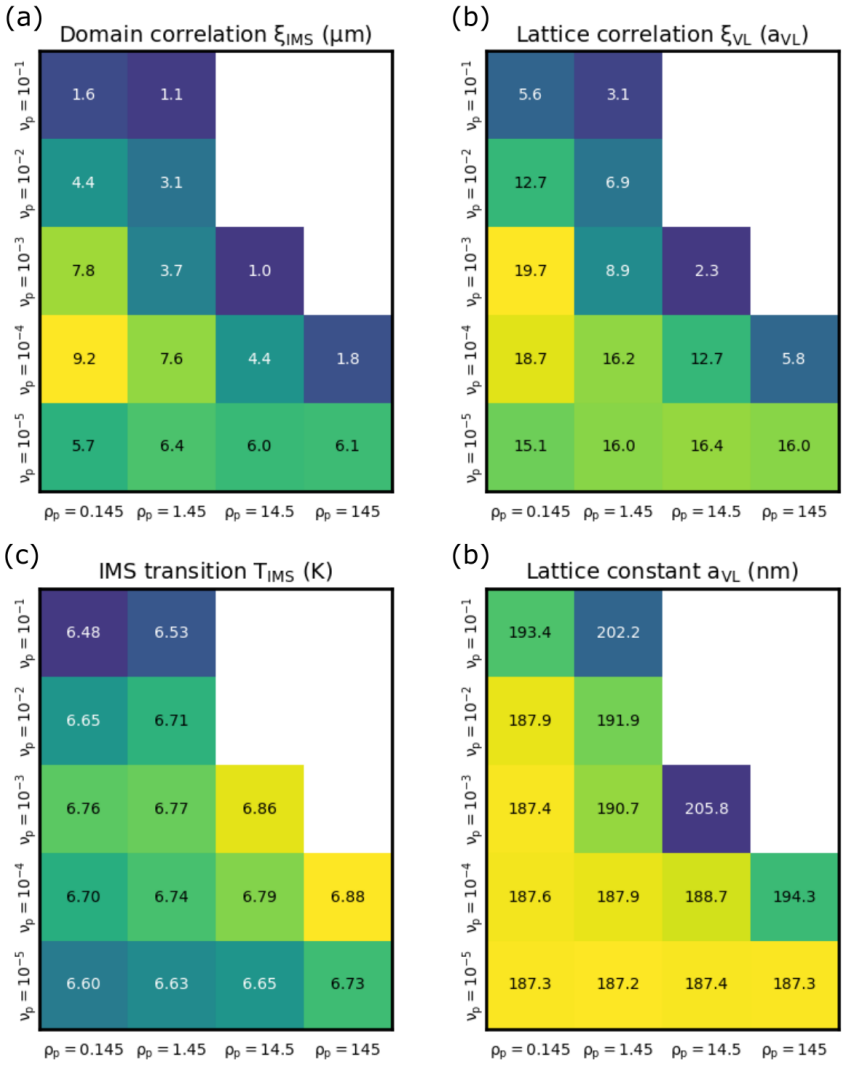

Figure 6.8: Results from the systematic study of the pinning parameters ρ_p and ν_p evaluated at $T_\mathrm{fin} = 6.1\,\mathrm{K}$. (a) Correlation length of the VL domains ξIMS, (b) correlation length of the vortex lattice ξ_VL, (c) IMS transition temperature T_IMS. (d) lattice constant a_VL. The correlation lengths (a, b) show an identical systematics. Generally, increasing ρ_p and ν_p, decreases the domain size, but deviations from this trend are visible around $\rho_\mathrm{p} = 0.145$ and $\nu_\mathrm{p} = 10^{-4}$. The lattice constant (d) resembles the domain size, with larger domains featuring smaller a_VL. T_IMS (c) increases with ν_p and has maximum values for $\rho_\mathrm{p} = 10^{-3}$.

Discussion

Over the considered range of pinning parameters, a multitude of characteristic parameters is changing, including the domains size and morphology, but also the IMS transition process and the qualitative temperature dependence of the lattice parameters. We have identified several pinning regimes, which will be discussed in the following. The values given for the pinning parameters are approximate, and an overview of the different regimes is shown in figure (6.9).

No pinning ($N_\mathrm{p} = 0.145, 1.45$ / $\nu_\mathrm{p} = 10^{-5}$)
In the case of few, weak pinning centers, pinning has no effect on the simulation. As has been shown previously, the resulting domain morphology mostly depends on the technical parameters of the algorithm. In the presented cases, the domains are very large and comparable to the simulation size. The transition into the IMS at T_IMS is clearly defined by a sharp drop of the lattice constant a_VL and the lattice correlation ξ_VL. With decreasing temperature, the former rapidly approaches the theoretical curve, while the latter recovers to a plateau.

Dominant pinning ($N_\mathrm{p} = 14.5, 145$ / $\nu_\mathrm{p} = 10^{-1}, 10^{-2}, 10^{-3}$)
Opposing the case of no pinning, dominant pinning describes situations where the pinning interactions are strong enough to override the vortex interaction. Almost initially in the simulations, the vortex lattice changes to a random, evenly distributed vortex configuration which is governed by the pinning positions. Depending on the pinning strength, multiple vortices might be trapped in the same pinning center. A lattice is no longer observed and the two-vortex separations are broadly distributed. Therefore, the usual evaluation of the lattice parameters is no longer meaningful. The temperature dependence of the vortex configuration is almost completely lost.

Individual pinning ($N_\mathrm{p} = 0.145, 1.45$ / $\nu_\mathrm{p} = 10^{-2}, 10^{-3}$)
For individual pinning, a relatively low number of vortices is trapped at the pinning sites where they remain throughout the simulation. Close to the pinning sites, lattice defects and distortions appear, while the overall VL remains coherent. At the IMS transition, the lattice breaks apart preferably at the pinning centers. More pinning sites and the related lattice defects result in more initial breaking points and smaller VL domains. In the IMS, many of the pinned vortices are located in the otherwise flux-free Meissner domains. Due to the defects at pinning sites, larger vortex lattice domains tend to consist of multiple grains, or exhibit a smooth variation of the lattice orientation. T_IMS is slightly increased, compared to the no pinning case. The qualitative picture of a_VL and ξ_VL is comparable to the pinning-free case, with the edge in both parameters slightly smoothed out.

Strong individual pinning ($N_\mathrm{p} = 0.145, 1.45$ / $\nu_\mathrm{p} = 10^{-1}$)
If ν_p is large enough, pinning centers are able to trap two or three vortices at the same position. The defects discussed for individual pinning are additionally accompanied by vacancies in the lattice. The rest of the VL further remains unaffected. The break-up of the lattice starts at the pinning sites, but the resulting domains fracture further

during cool-down. The domains are small, but often connected to each other. A large fraction of pinned vortices remains in the Meissner regions between larger domains. The transition temperature T_{IMS} is lower than in the non-pinning case. Otherwise, a_{VL} is not as smoothly and quickly decreasing and stays at higher values.

Weak individual pinning ($N_{\mathrm{p}} = 0.145, 1.45$ / $\nu_{\mathrm{p}} = 10^{-4}$)
Instead of inducing defects, the pinning centers introduce only slight deviations to the VL. In the cooldown, the IMS transition and final domain morphology are not distinguishable from the pinning-free case. However, the lattice breaks up first at the pinning sites and has an increased transition temperature. Contrary to the other individual pinning cases, no isolated vortices remain.

Collective pinning ($N_{\mathrm{p}} = 14.5, 145$ / $\nu_{\mathrm{p}} = 10^{-4}$)
In the case of collective pinning, instead of trapping single vortices, patches of the vortex lattice adapt to the underlying pinning structure and are pinned as a whole. This leads to an initial loss of coherence of the VL when different patches are slightly rotated and shifted. The domain morphologies are comparable to the individual pinning cases, but without featuring isolated vortices. During cooldown, the lattice breaks apart at the boundaries between different lattice patches. The transition to the IMS is less well defined in both VL-parameters. Still, the transition starts at higher temperatures compared to no pinning. In the IMS, isolated domains may regain better correlation when not connected to other patches.

Strong collective pinning ($N_{\mathrm{p}} = 14.5$ / $\nu_{\mathrm{p}} = 10^{-3}$)
If the pinning centers are strong enough, the lattice structure of vortices is suppressed. Vortices are mostly located on top of pinning centers, which is possible due to the comparable vortex and pinning densities. A transition to a domain structure is still observed, with vortices hopping between pinning sites. The vortex matter making up the domains is, however, closer to a glassy state than the VL observed in the IMS. a_{VL} changes gradually over the whole temperature range and ξ_{VL} is practically zero everywhere. A transition temperature is not well defined. The average vortex separation in this case is closer to the optimum defined by the two-vortex potential, instead of the lattice potential.

Weak collective pinning ($N_{\mathrm{p}} = 14.5, 145$ / $\nu_{\mathrm{p}} = 10^{-5}$)
Weak collective pinning is very similar to weak individual pinning in all regards, except for the underlying pinning parameters.

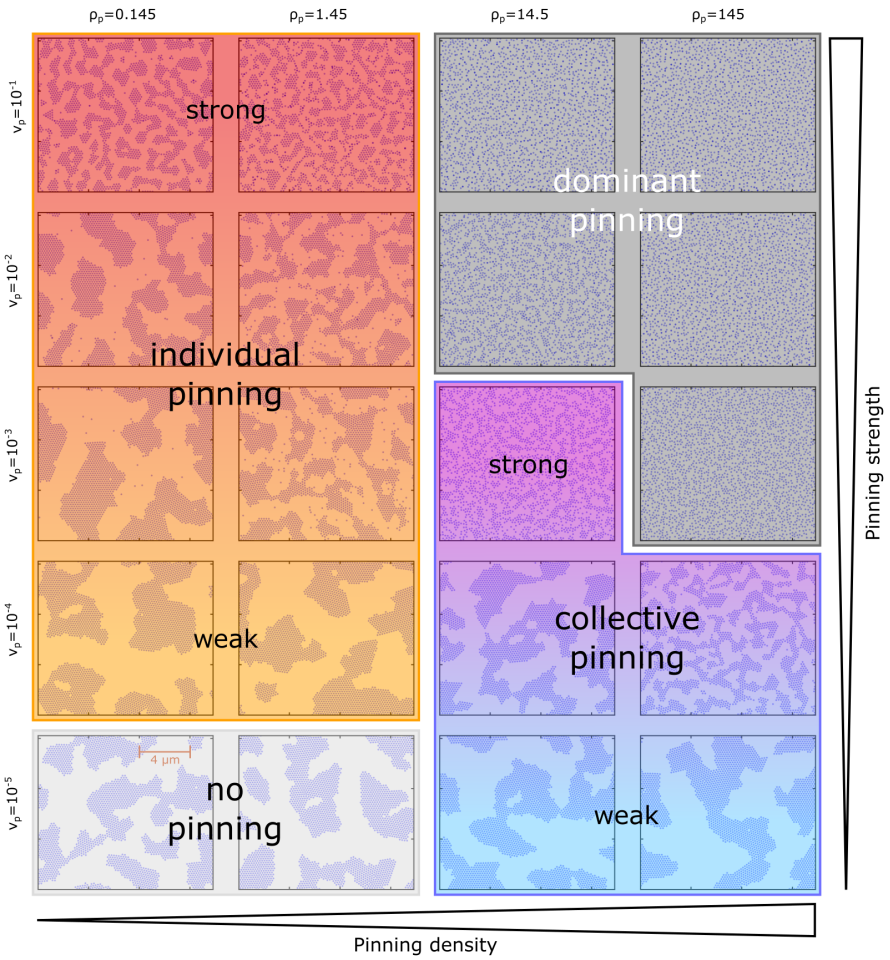

Figure 6.9: Graphic representation of the different pinning regimes found in our simulations. The colored areas are overlaid on top of the real space vortex configurations shown in figure (6.6).

6.2.2 Field dependence

In the following section, we explore the dependence of the IMS transition and the vortex domain morphology on the magnetic flux density B_{sim}. As shown in figure (5.3), the IMS transition temperature T_{IMS} is field dependent in the simulated case (field cooling and flux freezing). Since all interactions used in the simulation are temperature dependent, the critical point of the IMS transition at T_{IMS} has different properties under different fields. This concerns the absolute and relative strength of the forces as well as their rate of change with the temperature. Furthermore, the relative number of vortices and pinning centers is field dependent. While the pinning density is a property of the model superconductor and is independent of the magnetic field, the vortex density is directly corresponding to B_{sim} due to the flux freezing scenario.

In the following section, the dependence of the IMS on the magnetic field B_{sim} will be studied for three different cases of pinning:

- no pinning (NP) ($\rho_{\mathrm{p}} = 0$, $\nu_{\mathrm{p}} = 0$)
- individual pinning (IP) ($\rho_{\mathrm{p}} = 0.145\,/\mu\mathrm{m}^2$, $\nu_{\mathrm{p}} = 10^{-2}$)
- collective pinning (CP) ($\rho_{\mathrm{p}} = 14.5\,/\mu\mathrm{m}^2$, $\nu_{\mathrm{p}} = 10^{-4}$)

In all cases, the magnetic flux density was changed in the range of $B_{\mathrm{sim}} = 10$, 15, 20, 25, 30, 35, 40 mT. Higher magnetic flux densities could not be evaluated, due to the proximity of the IMS transition to the vortex lattice instability at $T \approx 5.5\,\mathrm{K}$ (cf. section (5.2.3)). All parameters of the simulations are given in table (6.5). For all combinations of B_{sim} and the pinning cases, four simulations were performed. Presented below are either representative results in the case of simulation images, or averages of the evaluated quantities of one set.

N_{v}	N_{p}	nu_{p}	$B_{\mathrm{sim}}\,(\mathrm{mT})$	$T_{\mathrm{init}}\,(\mathrm{K})$	$T_{\mathrm{final}}\,(\mathrm{K})$	$\Delta T\,(\mathrm{K})$	γ	S_{T}	S_{tot}
2450	*var*	*var*	*var*	7.5	6.1	0.01	4	25	3425

	$\rho_{\mathrm{p}}\,(1/\mu\mathrm{m}^2)$	B_{sim}	10 mT	15 mT	20 mT	25 mT	30 mT	35 mT	40 mT
NP	–	N_{p}	–	–	–	–	–	–	–
IP	0.145	N_{p}	74	49	37	29	25	21	18
CP	14.5	N_{p}	7350	4900	3675	2940	2450	2100	1838

Table 6.5: List of parameters used for the systematic study of B_{sim}.

No pinning (NP)

Results of the final real space vortex configurations in the pinning-free case are shown in figure (6.10). In all images, a $10 \times 10\mu\mathrm{m}^2$ area is indicated as a orange rectangle to highlight the change of A_{sim} with B_{sim}. At low fields $B_{\mathrm{sim}} = 10, 15\,\mathrm{mT}$, the vortex

domains have the shape of isolated islands, well separated by large areas of vortex-free Meissner domains. With increasing B_{sim}, elongated domains appear, and the VL domains become increasingly connected. Above 30 mT, the VL domains are fully connected. With increasing magnetic field, the area ratio of VL domains to Meissner domains increases. This is a result of the changing vortex density throughout the simulation, which is field dependent at T_{init} (in the Shubnikov state), but field independent at T_{final} (in the IMS). Below 25 mT, the Meissner domain is fully connected. At higher fields, isolated Meissner domains are present in small numbers. An insular structure of Meissner domains is not achieved in the presented field range. A visual comparison of the domain sizes is difficult due to the field dependent simulation size A_{sim} and the ratio of VL and Meissner domains. However, in all simulations a very low number of distinguishable domains is visible in the same area rectangles.

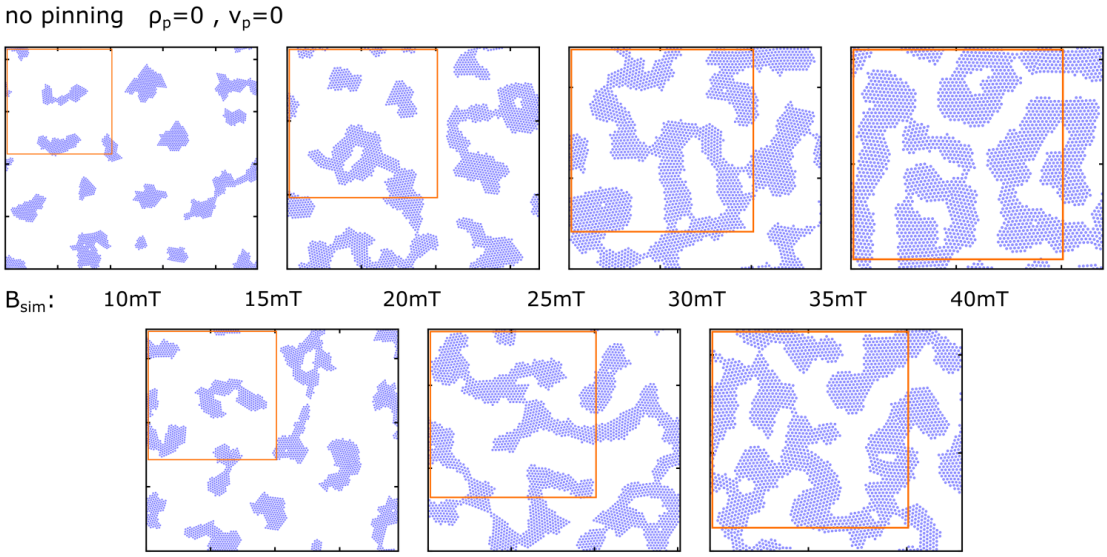

Figure 6.10: Real space vortex configuration from the systematic study of the external magnetic field dependence in the case of no pinning (NP). All images show the final simulation step at $T_{\mathrm{final}} = 6.1\,\mathrm{K}$. The orange box marks an area of $10\,\mu\mathrm{m} \times 10\,\mu\mathrm{m}$. Clearly visible is the increasing area fraction of VL domains with increasing field. Concurrently, the VL domains change from isolated islands to a highly interconnected morphology. Except for 10 mT, isolated Meissner state domains are present. The domain size cannot be easily assessed from the images.

Figure (6.11) contains the temperature dependent vortex lattice parameters. The qualitative behavior of a_{VL} and ξ_{VL} is independent of B_{sim}. The lattice constant a_{VL} is constant at high temperatures down to the IMS transition at T_{IMS}, where it sharply drops and converges to the theoretical value $r_{\mathrm{min}}^{\mathrm{VL}}$ within approximately 0.5 K. At all B_{sim}, the vortex lattice is cooled below the theoretical transition temperature by $0.1 - 0.4\,\mathrm{K}$. The lattice correlation length ξ_{VL} is very high ($> 50\,a_{\mathrm{VL}}$) above the IMS transition and drops down to a minimum precisely at T_{IMS}. With decreasing temperature, ξ_{VL} increases strongly in the span of about 0.1 K and keeps increasing slightly below. The

final value is similar for all fields with $\xi_{\mathrm{VL}}(6.1\,\mathrm{K}) \approx 11 - 13.5\,a_{\mathrm{VL}}$. For 35 mT and 40 mT the correlation length is less certain due to the smaller temperature span between T_{IMS} and T_{final}.

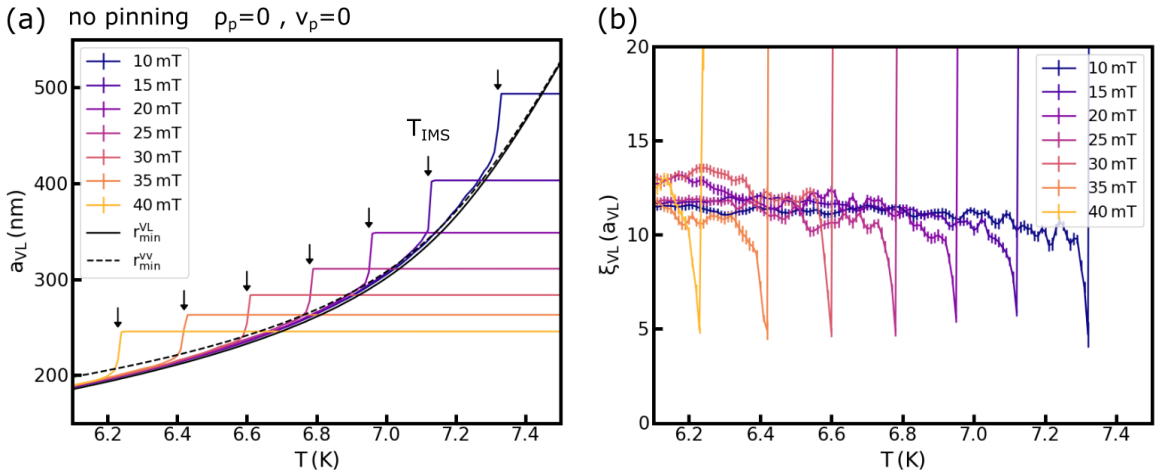

Figure 6.11: (a) Lattice constant a_{VL} and (b) lattice correlation length ξ_{VL} from the systematic study of the external magnetic field dependence in the case of no pinning (NP). At all fields, a sharp transition into the IMS is seen as a sudden drop of a_{VL} and ξ_{VL}. The lattice parameter reveals an undercooling of the VL which increases with increasing field. At low temperatures, a_{VL} is very close to the ideal vortex lattice separation $r^{\mathrm{VL}}_{\mathrm{min}}$. The lattice correlation recovers to a slightly increasing plateau at low temperatures. The final value of ξ_{VL} is only weakly depending on the external field.

The low-q range of radially averaged Fourier transforms is depicted in figure (6.12) for all fields at $T = 6.1\,\mathrm{K}$. The background from the initial perfect lattice has been subtracted from all plots. Instead of using bars, the error of the curves is given by the colored area, for graphical reasons. Large errors are mostly due to superimposed oscillations, which are a remaining artefact from the size and shape of A_{sim}. The curves have been fitted as described in section (5.3.2), in order to extract the domain correlation length ξ_{IMS}. With increasing field, the peak position at q_{max} is clearly increasing, indicating a decreasing size of the domain morphology from 6.1 μm to 2.7 μm.

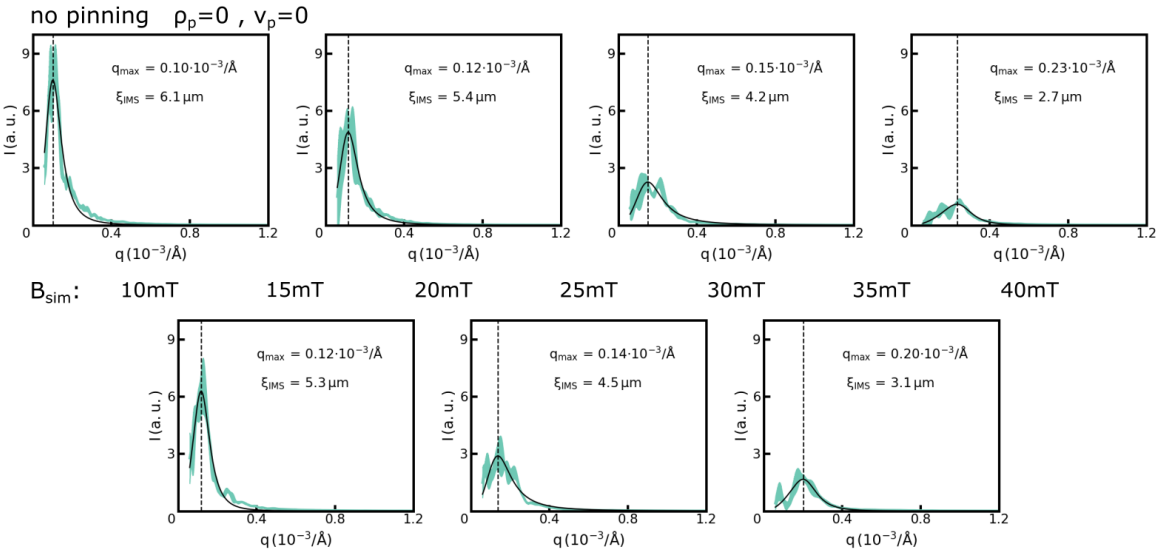

Figure 6.12: Radial averages of the Fourier transforms at low q from the systematic study of the external magnetic field dependence in the case of no pinning (NP). The thickness of the teal curve corresponds to the standard deviation due to the averaging. All curves show strong oscillations which stem from the small number of domains. The black curve shows the fit of the data according to equation (5.12). With increasing field, the peak position q_{max} increases by a factor of 2, and the corresponding domain correlation length ξ_{IMS} decreases. Coincidentally, the peak amplitude decreases.

Individual pinning (IP)

For the case of individual pinning, we have chosen the pinning strength as $\nu_\mathrm{p} = 10^{-2}$. Comparing the peak forces of the vortex-vortex and the vortex-pinning force, this value of ν_p is high enough to ensure a dominant pinning force at all temperatures of the simulations ($7.5\,\mathrm{K} > T > 6.1\,\mathrm{K}$). Still, it is low enough to avoid pinning of multiple vortices in most cases. The number of pinning sites is defined as a pinning density $\rho_\mathrm{p} = N_\mathrm{p}/A_\mathrm{sim} = 0.145\,/\,\mu\mathrm{m}^2$. Accordingly, N_p is field dependent in these simulations (cf. table (6.4)).

The real space vortex configurations at $T_\mathrm{fin} = 6.1\,\mathrm{K}$ are depicted in figure (6.13). The pinning sites have been omitted in the images. Due to the changing simulation size A_sim, a rectangle with $10 \times 10\,\mu\mathrm{m}^2$ has been marked in all images (orange). At all fields B_sim, isolated vortices are present in the regions between larger vortex lattice domains. At higher fields, instead of single vortices small clusters of vortices may be found, which are significantly smaller than the VL domains. In all cases, these isolated vortices are located on top of a pinning site. The domain size is visibly increasing with the magnetic field. At the lowest field $B_\mathrm{sim} = 10\,\mathrm{mT}$, the VL domains are isolated islands with varying size and shape, while the Meissner domain is fully connected. From 15 mT to 25 mT, many of the VL domains have an elongated shape, and the domains grow with increasing field. From 30 mT upwards, the vortex domains become increasingly connected and grow in size. The Meissner domains are shrinking with increasing B_sim, but still feature a connected laminar structure at 40 mT. Only very few instances of isolated Meissner domains are present in the simulations.

The temperature dependence of a_VL and ξ_VL is shown in figure (6.14). In general, the behavior of the lattice constant a_VL is similar to the pinning-free case. The drop of the lattice constant a_VL at T_IMS is slightly rounded, especially at higher fields, and the following convergence to the theoretical lattice parameter is prolonged. At temperatures above 6.6 K, a gap between the measured a_VL and the expected $r_\mathrm{min}^\mathrm{VL}$ is visible. For the lattice correlation length ξ_VL, the drop coinciding with T_IMS is slightly broadened. The recovery to a plateau value at low temperatures is slower than seen in the pinning-free case. Additionally, the increasing trend of ξ_VL with decreasing temperature is more pronounced. The value achieved at T_final is strongly depending on the magnetic field. For 10 mT to 30 mT, $\xi_\mathrm{VL}(6.1\,\mathrm{K})$ is increasing with the field from $4.55\,a_\mathrm{VL}$ to $13.8\,a_\mathrm{VL}$, but is almost stagnant above 30 mT. Compared to the pinning-free simulations, the transition temperature T_IMS is reduced for low fields and increased for high fields. Accordingly, the undercooling is stronger at low fields and less pronounced at high fields.

The Fourier transforms in the VSANS regime are shown in figure (6.15), including fitting curves. For individual pinning, the peak position decreases with increasing B_sim, corresponding to an increasing domain size from $2.0\,\mu\mathrm{m}$ to $6.3\,\mu\mathrm{m}$. At high fields above 30 mT, the domain size is comparable to the simulation area A_sim, which increases the uncertainty of the peak position.

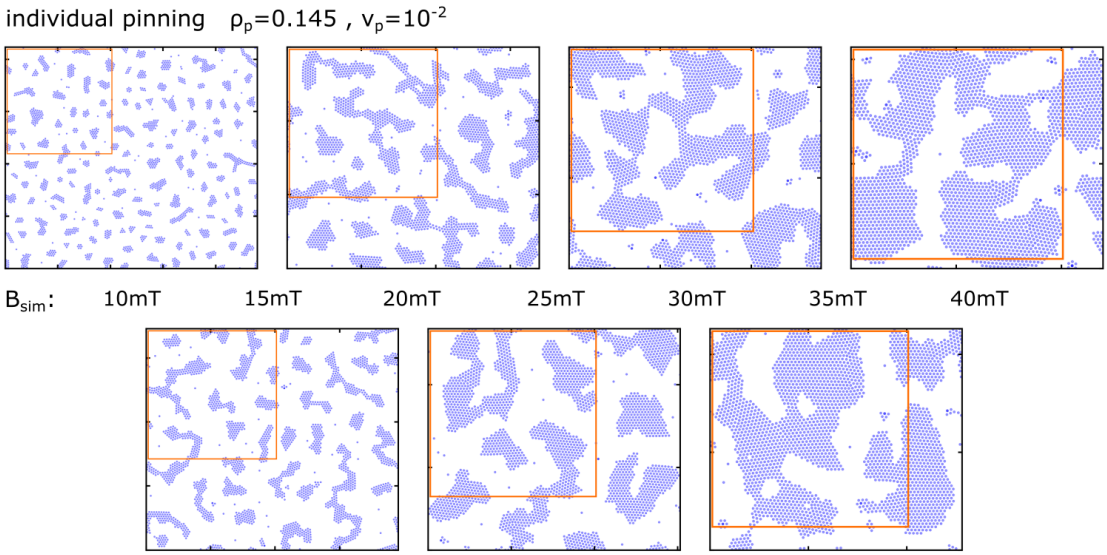

Figure 6.13: Real space vortex configuration from the systematic study of the external magnetic field dependence in the case of individual pinning (IP). All images show the final simulation step at $T_{\text{final}} = 6.1\,\text{K}$. The orange box marks an area of $10\,\mu\text{m} \times 10\,\mu\text{m}$. Clearly visible is the increasing size of VL domains with increasing field. Concurrently, the VL domains change from isolated islands to a highly interconnected morphology. At all fields, isolated vortices and small clusters (< 10 vortices) are present in between the larger domains. At 35 and $40\,\text{mT}$, isolated Meissner state domains are present.

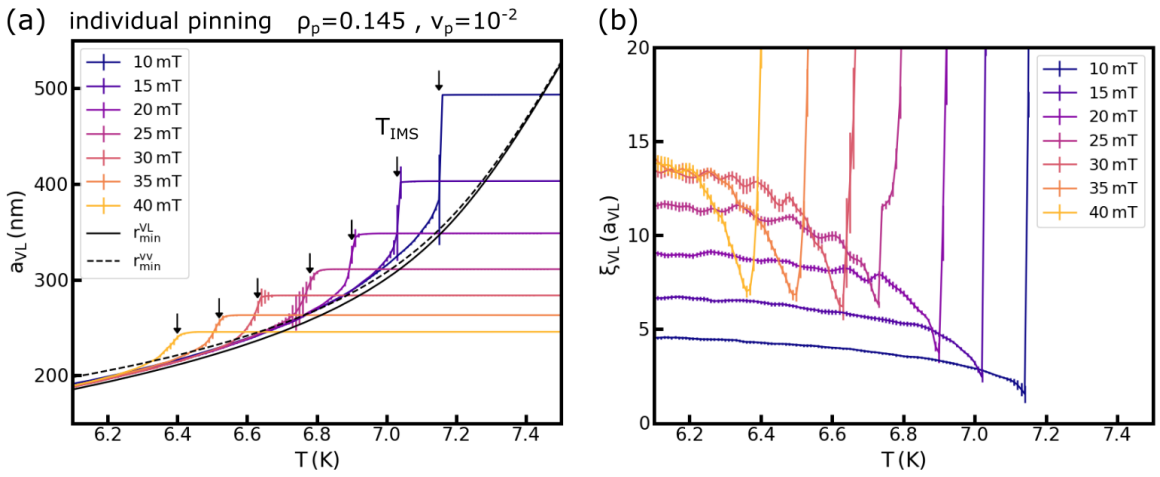

Figure 6.14: (a) Lattice constant a_{VL} and (b) lattice correlation length ξ_{VL} from the systematic study of the external magnetic field dependence in the case of individual pinning (IP). The transition into the IMS is seen as a drop of a_{VL} and ξ_{VL}. At small fields, these features are very sharp, but broaden with increasing field. The lattice parameter reveals an undercooling of the VL which comparable in all curves. At low temperatures, a_{VL} is very close to the ideal vortex lattice separation $r_{\text{min}}^{\text{VL}}$. The lattice correlation recovers to a slightly increasing plateau at low temperatures. The final value of ξ_{VL} is strongly increasing with the external field.

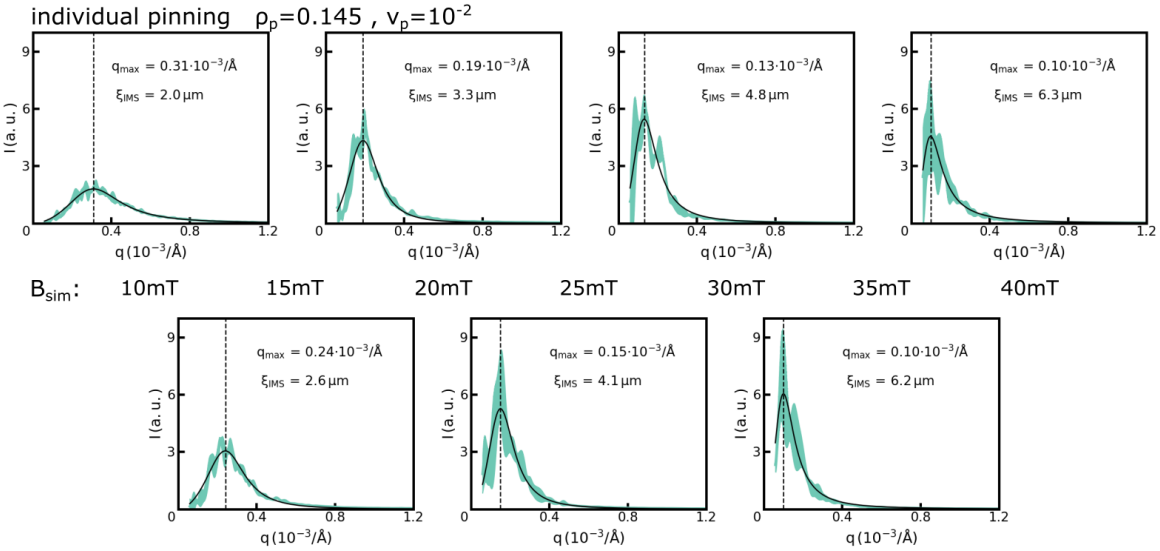

Figure 6.15: Radial averages of the Fourier transforms at low q from the systematic study of the external magnetic field dependence in the case of individual pinning (IP). The thickness of the teal curve corresponds to the standard deviation due to the averaging. All curves show strong oscillations which stem from the small number of domains. The black curve shows the fit of the data according to equation (5.12). With increasing field, the peak position q_{max} decreases by a factor of 3, and the corresponding domain correlation length ξ_{IMS} increases. Coincidentally, the peak amplitude decreases.

Collective pinning (CP)

For the case of collective pinning, we have chosen the pinning parameters $\nu_\mathrm{p} = 10^{-4}$ and $\rho_\mathrm{p} = 14.5/\mu\mathrm{m}^2$. Despite the fixed values, this case is not as well defined as the previous two. First, the pinning force is lower than, but comparable to the vortex interaction. Since both forces are temperature dependent, the IMS transition temperature T_IMS has a larger effect on the relative strength of F_vv and F_vp. Second, collective pinning is based on the interplay between several vortices and pinning sites. Therefore, the changing ratio of N_v and N_p at different fields affects the pinning characteristics as well.

In figure (6.16), the final vortex configurations at all fields B_sim are shown. Pinning sites have been omitted in the images. Orange rectangles mark an area of $10 \times 10\,\mu\mathrm{m}^2$ in each figure. The domain size and morphology have a clear and strong field dependence. At 10 mT, the vortex domains are very small, rarely consisting of more than 15 vortices. Between the small domains, many isolated vortices are present. From 15 mT to 25 mT, the domain size is growing. Their shape becomes more elongated, and larger connected vortex lattice regions start to form. Simultaneously, the number of isolated vortices decreases and vanishes at 35 mT. Above 30 mT, a single connected VL domain is observed. The Meissner domains at high fields still feature a mostly laminar structure, with few additional isolated islands.

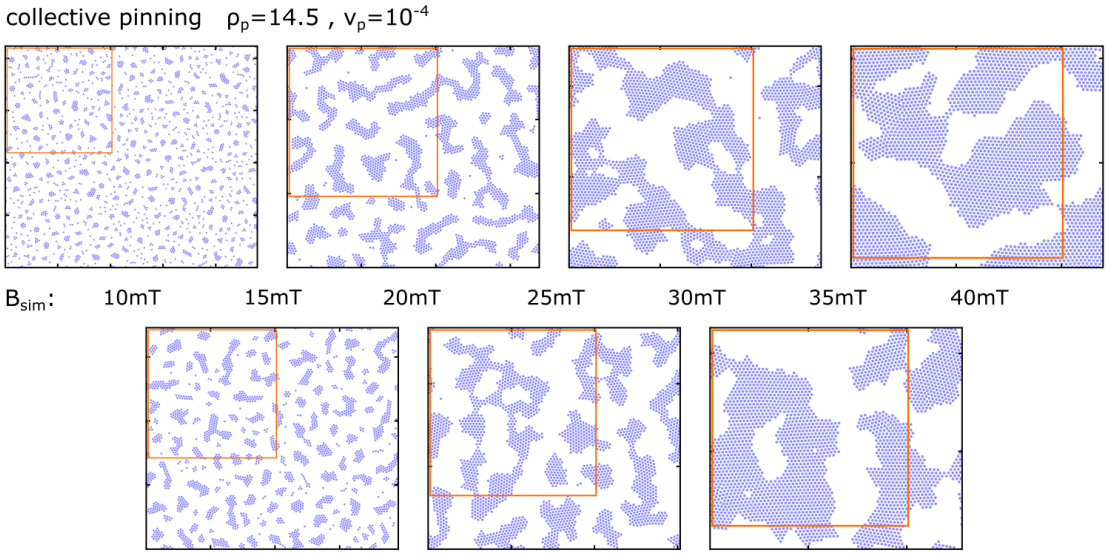

Figure 6.16: Real space vortex configuration from the systematic study of the external magnetic field dependence in the case of collective pinning (CP). All images show the final simulation step at $T_\mathrm{final} = 6.1\,\mathrm{K}$. The orange box marks an area of $10\,\mu\mathrm{m} \times 10\,\mu\mathrm{m}$. Clearly visible is the increasing size fraction of VL domains with increasing field. Concurrently, the VL domains change from isolated islands to elongated shapes and finally to a highly interconnected morphology. At low fields, a large number of isolated vortices and small clusters (< 10 vortices) is present, which decreases with increasing field and is practically zero at 25 mT. Above 25 mT, isolated Meissner state domains can be observed.

The lattice constant a_{VL} and correlation length ξ_{VL} are shown in figure (6.17). Both parameters show a very broadened shape, compared to the previous cases NP and IP. Especially for the lower fields, a clear drop of a_{VL} and ξ_{VL} corresponding to the IMS transition is not observed. Instead, the lattice constant decreases smoothly towards the trend of the theoretical value. Due to the smeared out transition, T_{IMS} could not be determined from the change in a_{VL}. Instead, the real space images of the simulations were used to determine a temperature, where the vortex configuration starts to redistribute into domains. While obviously less precise, this was the only viable method we found. For temperatures above 6.6 K, there is an obvious discrepancy between the measured a_{VL} and the predicted $r_{\mathrm{min}}^{\mathrm{VL}}$. Likewise, the correlation length features a smeared out drop at the IMS transition, followed by a very broad minimum, especially for low magnetic fields. The steep decrease of ξ_{VL}, observed at high temperatures for the lowest fields, is rather representing the adaption of the initial vortex lattice to the pinning centers than the IMS transition. Still, all simulations show an increasing correlation length towards low temperatures. The values at the final temperature 6.1 K are increasing over the complete field range from 2.39 a_{VL} to 14.9 a_{VL}. The highest two fields are reversed, likely due to the low transition temperature compared to T_{final}. In both lattice parameters, the qualitative shape changes towards the highest fields and assumes a behavior closer to the IP case.

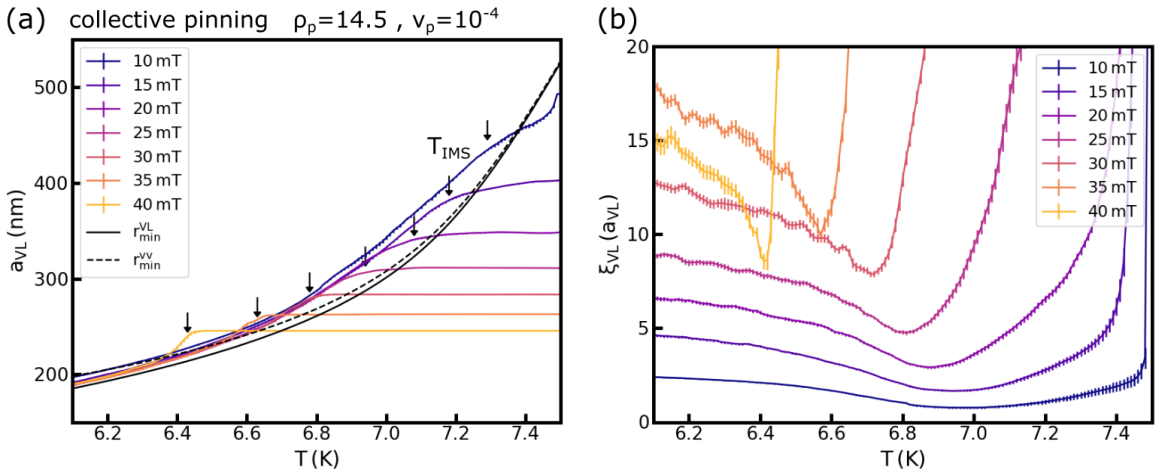

Figure 6.17: (a) Lattice constant a_{VL} and (b) lattice correlation length ξ_{VL} from the systematic study of the external magnetic field dependence in the case of collective pinning (CP). The hallmarks of the IMS transition, a sudden drop of a_{VL} and ξ_{VL}, are only visible for high fields. With decreasing field, both features become broader, rendering the distinction of a transition temperature imprecise. An undercooling is observed in the lattice parameter which seems to increase with increasing field. However, its extent at the lower fields is unclear, especially at 10 mT. Simulations at low fields tend to the optimal two-vortex separation $r_{\mathrm{min}}^{\mathrm{vv}}$ at low temperatures, while the higher fields tend to the lattice optimum $r_{\mathrm{min}}^{\mathrm{VL}}$. The lattice correlation recovers to a slightly increasing plateau at low temperatures. The final value of ξ_{VL} is only weakly depending on the external field.

Figure (6.18) depicts the Fourier transforms of the vortex domains along with their fitting curves. As expected from the real space images, the peak position at $q_{\max}$ decreases with the external field, and the domain correlation is increasing from 1.2 μm to 7.7 μm. As in the previous cases, the domain size becomes comparable to the simulation size at fields above 30 mT.

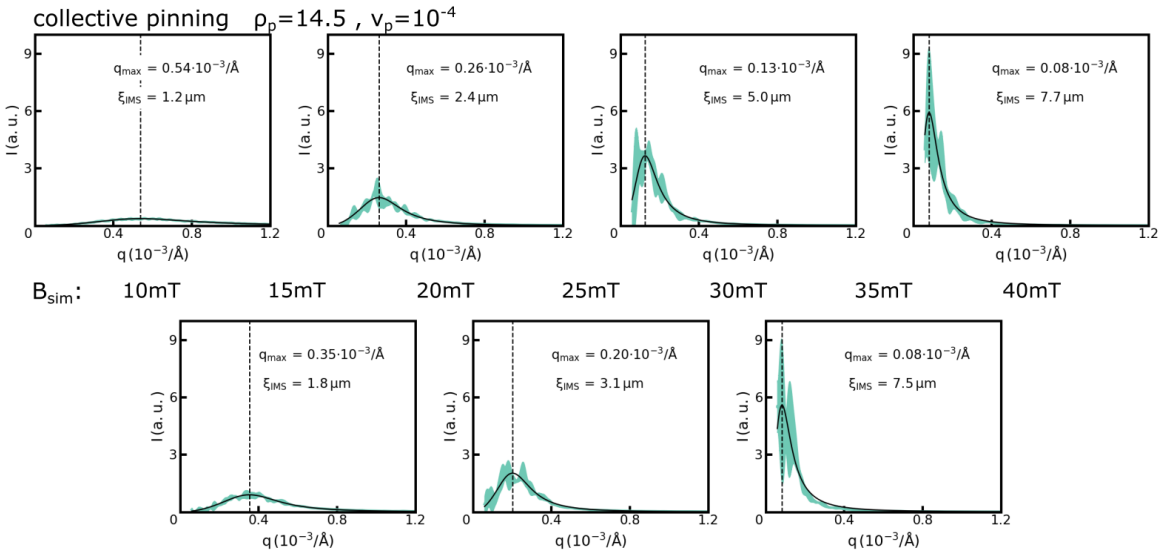

Figure 6.18: Radial averages of the Fourier transforms at low q from the systematic study of the external magnetic field dependence in the case of collective pinning (CP). The thickness of the teal curve corresponds to the standard deviation due to the averaging. All curves show strong oscillations which stem from the small number of domains. The black curve shows the fit of the data according to equation (5.12). With increasing field, the peak position $q_{\max}$ decreases by a factor of 7, and the corresponding domain correlation length ξ_{IMS} increases. Coincidentally, the peak amplitude increases.

Discussion

The results from the three presented scenarios, no pinning (NP), individual pinning (IP) and collective pinning (CP), have illustrated that the field dependence of the IMS transition is strongly depending on the pinning characteristics. As primary hallmarks, we compare the IMS transition temperature T_{IMS} and the correlation lengths of the vortex lattice ξ_{VL} and of the IMS domains ξ_{VL} in the final state of the simulations.

The IMS transition temperature is shown in figure (6.19)(a) for all cases, along with the theoretical value $T_{\mathrm{IMS}}^{\mathrm{VL}}$. First of all, all simulations resulted in an undercooling of the vortex lattice. The difference $\Delta T_{\mathrm{uc}} = T_{\mathrm{IMS}}^{\mathrm{VL}} - T_{\mathrm{IMS}}$ is shown in panel (b). For NP and IP, T_{IMS} is linear in the external field, with a steeper slope for NP. In contrast, T_{IMS} has a curved form for CP. The different behaviors are more pronounced in ΔT_{uc}. The undercooling increases strongly with the field for NP, from 0.12 K to 0.46 K. For IP, it is approximately constant with $\Delta T_{\mathrm{uc}} \approx 0.28$ K, and CP again shows a curved shape with a

minimum of 0.21 K at 30 mT.

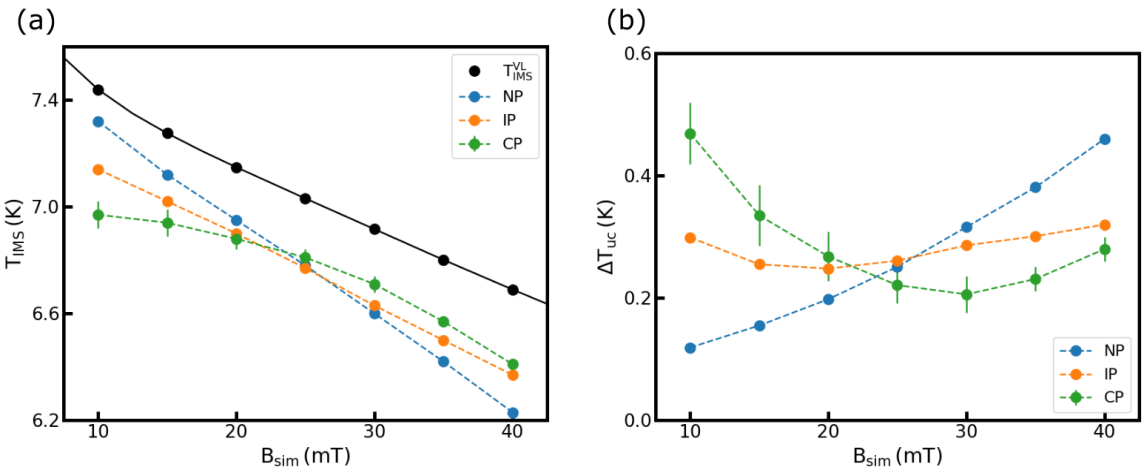

Figure 6.19: (a) Field dependence of the IMS transition temperature T_{IMS} for the cases of no pinning (NP), individual pinning (IP) and collective pinning (CP). Shown in black is the theoretical value according to $r_{\mathrm{min}}^{\mathrm{VL}}$. For NP and IP, the field dependence is linear, while the CP curve is bent. The lines cross each other at $B_{\mathrm{sim}} \approx 25\,\mathrm{mT}$, and there is no clear hierarchy of the transition temperatures between the pinning cases. (b) Temperature difference of the undercooling ΔT_{uc}. With increasing field, the effect increases for NP, is stagnant for IP and has a bent shape for CP. Again, the lines intersect at $B_{\mathrm{sim}} \approx 25\,\mathrm{mT}$. Error bars are only visible for CP due to the broadened transitions.

The correlation lengths ξ_{IMS} and ξ_{VL} are shown in figure (6.20). Qualitatively, the no pinning (NP) case can be well distinguished from both pinning cases (IP and CP). For NP, ξ_{VL} is almost constant over the field range at a value $\approx 12.0\,a_{\mathrm{VL}} \approx 2.25\,\mu\mathrm{m}$, while ξ_{IMS} is decreasing with increasing B_{sim} from $6.2\,\mu\mathrm{m}$ to $2.7\mu\mathrm{m}$. In contrast, in the presence of pinning, ξ_{VL} and ξ_{IMS} are increasing with B_{sim}. Regarding IP and CP, both parameters cross at $B_{\mathrm{sim}} \approx 30\,\mathrm{mT}$, with the IP parameters being higher for lower fields and the CP values being higher for larger fields. For IP, ξ_{VL} increases from $4.50\,a_{\mathrm{VL}} = 0.85\,\mu\mathrm{m}$ to $13.8\,a_{\mathrm{VL}} = 2.60\,\mu\mathrm{m}$, while ξ_{IMS} increases from $2.00\,\mu\mathrm{m}$ to $6.35\,\mu\mathrm{m}$. The change is slightly stronger for CP, with ξ_{VL} increasing from $2.40\,a_{\mathrm{VL}} = 0.45\,\mu\mathrm{m}$ to $17.5\,a_{\mathrm{VL}} = 3.30\,\mu\mathrm{m}$, and ξ_{IMS} increasing from $1.15\,\mu\mathrm{m}$ to $7.70\,\mu\mathrm{m}$. In both cases, the values at 35 mT and 40 mT are slightly unreliable, due to the large domains and the low IMS transition temperature.

In the absence of pinning centers (NP), the IMS is clearly defined by a field independent VL correlation length. However, our simulations are based on a perfect initial lattice, which is a somewhat unphysical case. The initial breakup of the VL and transition into the IMS is, therefore, predominantly relying on the thermal fluctuations in addition to the changing vortex-vortex interaction. Since they are, however, designed as a small corrective term, the impact on the emerging domain structure might be disproportionately strong in our simulations. In contrast, in the cases of individual pinning (IP) and collective pinning (CP), the pinning centers introduce defects in the

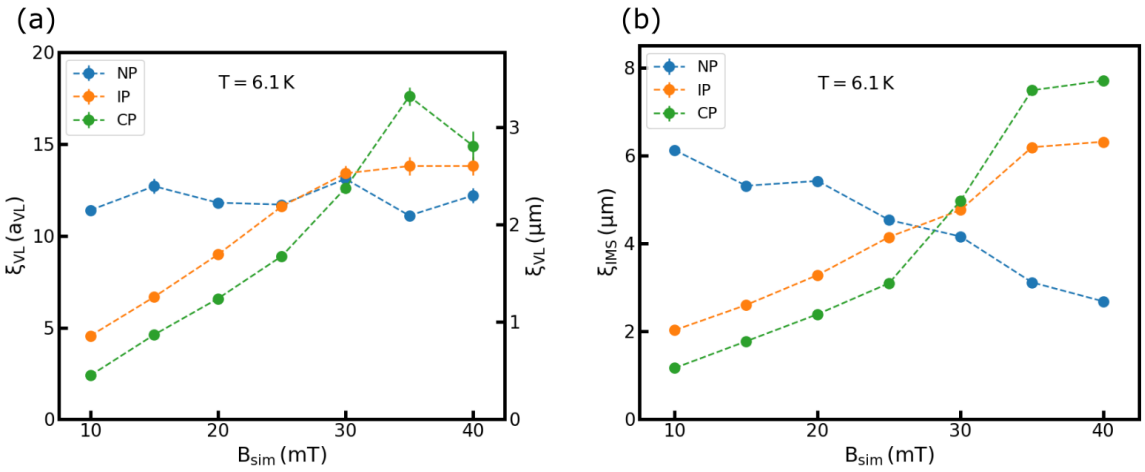

Figure 6.20: Field dependence of (a) the vortex lattice correlation length ξ_{VL} and (b) the IMS domain correlation length ξ_{IMS} at $T_{\mathrm{final}} = 6.1\,\mathrm{K}$ for the cases of no pinning (NP), individual pinning (IP) and collective pinning (CP). (a) ξ_{VL} is almost field independent for NP, while it is strongly increasing with the field for IP and CP. For IP, it levels off above 30 mT, while a kink towards higher correlation is seen at the same field for CP. Note that ξ_{VL} is given in units of a_{VL}, which is almost identical for all simulations. The right axis gives a scale in micrometers where $a_{\mathrm{VL}} = 188.5\,\mathrm{nm}$ has been assumed. (b) With increasing field, ξ_{IMS} is clearly decreasing for NP and increasing for IP and CP. Note that at high fields, the measured correlation lengths for IP and CP are close to the simulation size.

initial vortex lattice. These defects act as preferred breaking points of the VL and reduce the necessity of thermal fluctuations. The correlation length of the domains in these two cases is likely depending on the changing ratio of vortices to pinning centers. This ratio increases with increasing magnetic field, which fits the increasing $\xi_{\mathrm{VL}}(B)$ and $\xi_{\mathrm{IMS}}(B)$. We note, however, that the domain morphology changes from insular to laminar and highly connected with increasing field for all three studied cases. This change additionally affects the correlation length obtained from the simulations.

6.3 Summary

In this chapter, we have presented a series of systematic studies of the intermediate mixed state transition using two dimensional molecular dynamics simulations. The model superconductor was defined by a set of material parameters reminiscent of pure niobium, and the inter-vortex interaction was derived using the extended Ginzburg-Landau formalism. In addition, point-like pinning centers with a Gaussian interaction potential and a random distribution were used. All simulations were performed in a field cooling procedure, starting from a homogeneous hexagonal vortex lattice corresponding to the Shubnikov state. The number of vortices was kept constant throughout each simulation, emulating a perfect flux freezing scenario.

In the absence of pinning, all of our simulations have shown a transition from a homogeneous vortex lattice into the domain structure of the IMS. The transition has been primarily evaluated using the vortex lattice parameter a_{VL} and coherence length ξ_{VL} and the domain coherence length ξ_{IMS}. All three parameters were determined from the Fourier transforms of the real space vortex distributions and correspond to quantities measurable in neutron scattering experiments. The hallmarks of the IMS were a decrease of a_{VL} and ξ_{VL} below the IMS transition temperature T_{IMS} and non-zero ξ_{IMS}.

A prominent feature of the simulations is an undercooling of the initial vortex lattice. In comparison to the expected transition temperature T_{IMS} derived from the vortex interaction, the observed transition was at a lower temperature and associated with a significant drop of a_{VL}. The effect is owed to the initial perfect lattice configuration, where all vortex interactions cancel out and which is therefore a metastable state.

Our methodical studies concerned the general simulation procedure in terms of the temperature steps ΔT, number of steps per temperature S_{T} and vortex relaxation constant γ. We have found that these parameters mainly act as scaling parameters for the emerging IMS domain pattern. Either by increasing the number of simulation steps (using ΔT and S_{T}) or the mobility of the vortices (via γ), the domains tend toward larger structures.

For our further simulations, the methodical parameters were chosen to fit the following requirements: The domain size should be small enough to not be limited by the simulation area. At the same time, it should be as large as possible to observe the effect of pinning, which was expected to reduce the domain size. Finally, the simulation time had to be kept in mind.

The impact of pinning on the IMS transition was studied in dependence of the strength ν_{p} and density ρ_{p} of the pinning centers. On a large scale, three major regimes have been identified in the pinning parameters. For low ν_{p} and ρ_{p}, the simulation is effectively free of pinning, and no effect can be observed. If both parameters are high, the vortex configuration becomes chaotic with no remainders of an ordered vortex lattice. In between lies an extended region, where IMS domains emerge, but are affected by pinning. This region is characterized by a roughly constant value of $\nu_{\mathrm{p}} \times \rho_{\mathrm{p}}$, which we have observed over 5 orders of magnitude in ν_{p} and 4 orders of magnitude in ρ_{p}. Compared to pinning-free simulations, the IMS domains are smaller under the influence of pinning, with a tendency to decrease towards the chaotic regime. In the vortex lattice parameters $a_{\mathrm{VL}}\,(\mathrm{T})$ and $\xi_{\mathrm{VL}}\,(\mathrm{T})$, a smearing of the transition is observed. Depending on ρ_{p}, we can distinguish between two major cases of pinning. If the number of pinning sites is much lower than the number of vortices (approximately 10 % and lower), individual vortices are pinned. The rearrangement of vortices into the IMS domains is hindered by these immobile vortices which act as breaking points of the homogeneous lattice. In contrast, if there are equal or more pinning sites than vortices, the VL is pinned collectively. The pinning sites form a rough background potential and introduce slight deviations in the otherwise homogeneous lattice, which again facilitate the breakup.

The field dependence of the IMS transition and domain morphology has turned out to be strongly depending on the pinning properties. In the pinning-free case (NP), the domains are characterized by a field independent lattice correlation length ξ_{VL}. The domain correlation ξ_{IMS}, however, decreases with the magnetic field since the ratio of VL and Meissner domains is field dependent. In both pinning cases, individual pinning (IP) and collective pinning (CP), the VL correlation ξ_{VL} and the domain correlation ξ_{IMS} increase with the field. In addition, the redistribution process of the vortices seen in the lattice parameters a_{VL} and ξ_{VL} is distinct for each of the three cases. The prominent undercooling is affected by the magnetic field and pinning case as well. For IP and CP, the pinning characteristics appear to change qualitatively with the field, which is expected from the changing ratio of vortices to pinning centers with the magnetic field.

7 Comparison of experiments and simulations

In the presented work, we have studied the intermediate mixed state (IMS) in the intertype superconductor niobium from two different angles. On the one hand, a multiscale approach including four experimental techniques was used. The individual methods were chosen to access different features of the IMS, each on a different length scale: the bulk magnetic properties (VSM), the vortex lattice crystallography (SANS), the IMS domain morphology (VSANS) and the macroscopic domain distribution (NGI). On the other hand, two dimensional molecular dynamics (MD) simulations were performed. A novelty of these simulations was the description of the vortex interaction using the extended Ginzburg-Landau (EGL) formalism [13]. The results could be analyzed in a fashion similar to neutron scattering experiments, while simultaneously giving insight into the microscopic distribution of the single vortices and the real space domain morphology. The simulations were separated in a methodical part, focusing on the validation of the simulation procedure, and an experimental part, which addressed primarily the impact of pinning on the IMS. In this chapter, we will review and compare the major results of our experiments and simulations.

In the neutron experiments, the primary parameters describing the properties of the IMS are the vortex lattice constant a_{VL} and the correlation lengths of the vortex lattice ξ_{VL} and the IMS domains ξ_{IMS}. The simulations show the transition process directly, but for a quantitative evaluation and comparison to the experiments, equivalent quantities have been extracted from the Fourier transforms of the real space vortex distributions. In the following, we address a_{VL}, ξ_{VL} and ξ_{IMS} separately to highlight the accordances and disagreements between experiments and simulations.

Exemplary data of the **vortex lattice constant** a_{VL} is shown in figure (7.1). Panel (a) contains results from the SANS measurements performed on the medium purity sample MP-1 (cf. section (4.3), figure (4.2)). The simulation results shown in panel (b) are from the field dependent study featuring individual pinning (cf. section (6.2), figure (6.14)). In both cases, the number of vortices in the sample is constant over temperature due to a flux freezing transition in the experiment and a corresponding simulation procedure. In the Shubnikov state at high temperatures and fields, a_{VL} is constant over temperature. Here, the vortices are arranged in a homogeneous vortex lattice throughout the sample, which matches the external flux density. In the IMS, a_{VL} decreases below a field dependent transition temperature. All measurements in the IMS form a single field independent line $a_{\mathrm{IMS}}^{\mathrm{VL}}(T)$ (black line). In the simulations, the Shubnikov state is undercooled below the IMS line, which is approximately given by the theoretical value $a_{\mathrm{IMS}}^{\mathrm{VL}}(T)$ (black line) derived in EGL theory. At the IMS transition, the lattice constant shows a sudden drop towards the IMS line. Only at sufficiently low temperatures, the values of a_{VL} fall onto the same line for different fields.

In panel (c), all model curves for the IMS lattice parameter are compiled. For the experiments, the fitting curves $a_{\mathrm{IMS}}(T)$ are shown for all three samples (HP, MP, LP) (equation (4.1)). For the simulations, the optimal vortex lattice (VL) and two-vortex (vv) separations calculated in EGL theory are shown (cf. figure (5.3)). The drop in the EGL (VL) line at approximately 6 K marks the lattice instability, where the formation of multi-vortices is observed in the simulations. While the simulations were modeled to resemble real niobium, the match is not perfect. Compared to the measurements, the simulation lines are shifted to lower temperatures and lower a_{VL}. Additionally, the shape of the lines is similar, but not identical. A major difference between experiment and simulation is the dependence of the IMS line on the sample purity or the pinning properties. The experimental lines shift to higher lattice constants with decreasing sample purity. In contrast, all simulations with different pinning parameters follow the same IMS line, which is only defined by the parameters of EGL and the model superconductor (cf. figure (6.7)).

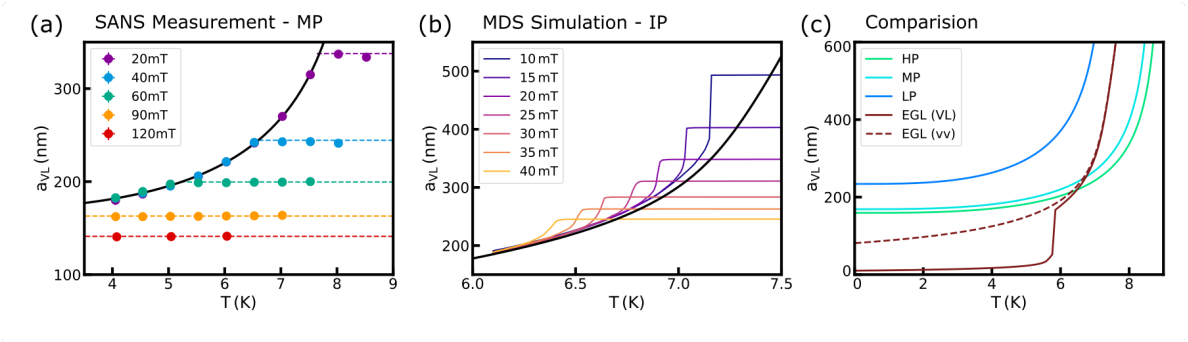

Figure 7.1: Comparison of the vortex lattice constant a_{VL} in experiment and simulation. (a) SANS measurements of the medium purity sample (MP-1). In all cases, where the IMS transition is observed, the lattice constant lies on a single line (black) defining the IMS. (b) Results of the simulations featuring individual pinning (IP), including the optimal vortex separation calculated in EGL theory (black). All curves show a significant undercooling and tend towards the theory curve at lower temperatures. (c) Comparison of the fitting curves of a_{VL} in the IMS of all real samples (HP, MP and LP) and the results of EGL for a vortex lattice (VL) and two vortices (vv). While the model lines for experiment and simulation are qualitatively similar, each real sample shows a different line, whereas all simulations are defined by the same curves, irrespective of pinning. The sharp drop of the EGL(VL) line just below 6 K marks the lattice instability, where multi-vortices begin to form.

In figure 7.2, results for a_{VL} from the simulations featuring collective pinning (CP) are shown. Panel (a) contains the full precision of the simulation, including all simulation steps. Panel (b) only shows a tenth of the data points and thereby resembles the precision of our SANS experiments. Included in both images are the theoretical IMS lines from EGL theory (in black (a) or gray (b)). Additionally, panel (b) shows a line for a_{IMS} as it would have been deducted in an experiment. It is obvious that this line deviates from theory. Additionally, there are no indications of a vortex lattice undercooling in the

experiment-like data. We note that for the other pinning cases (NP and IP) a similar treatment cannot conceal the undercooling, since it is too pronounced. However, the undercooled data points also complicate a clean definition of the IMS transition line. Primarily, the example of the collective pinning case shows that we might not see the true underlying IMS line in an experiment, but one distorted by pinning.

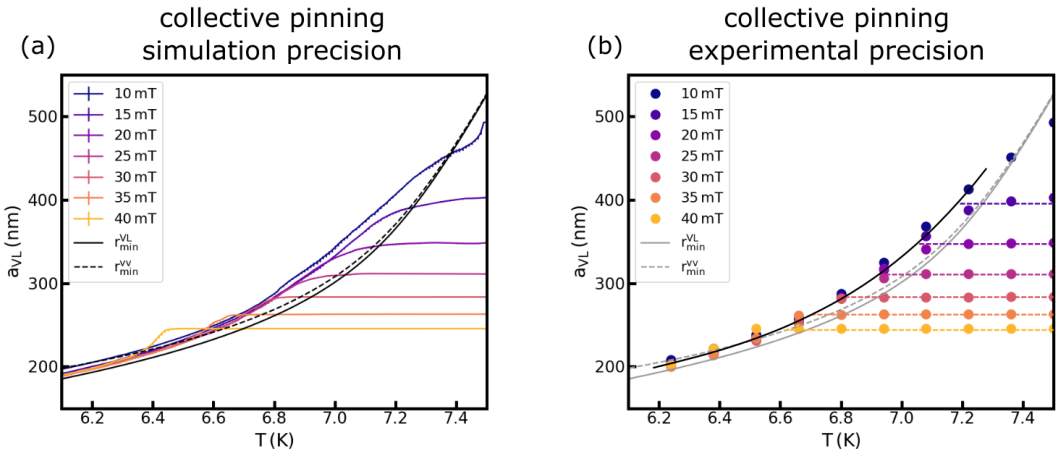

Figure 7.2: Vortex lattice constant a_{VL} of the simulation featuring collective pinning (CP). (a) complete results of the simulations, including all simulation steps. (b) reduced data set with a tenth of the original steps. Theory curves for the IMS line are shown in black (a) or gray (b). Panel (b) contains a line for a_{VL} (black) as it would have been deduced from an actual experiment. Note that the reduced precision shown in (b) does not allow to observe the broadened IMS transition of the simulations and the undercooling visible at large fields.

It is remarkable that the IMS is fundamentally described by a single line $a_{\mathrm{IMS}}(T)$, both in the experiments and in the simulations. From the simulations we know that this line defines an energetic optimum of the vortex separation, which is directly given by the inter-vortex interaction. While the IMS line is defined at all temperatures, the vortex rearrangement associated with the IMS can only be observed, if $a_{\mathrm{IMS}}(T)$ falls below the current vortex lattice constant. In our experiments and simulations, this condition is very well defined due to the prominent flux freezing. However, the measurements of HP-1, where the Meissner effect is observed, show the same behavior (cf. figure (4.2)). The discrepancies between experiments and simulations can be explained primarily by two factors. First is the undercooling, which obviously delays the IMS transition below the expected temperature and thereby affects the further progression of a_{VL}. In all simulations, the VL is initiated in a perfectly homogeneous state, which is furthermore stabilized by the fitting shape of the simulation area and the periodic boundaries. Even in the presence of pinning centers, the overall coherence of the lattice is typically not destroyed. Additionally, the initial breakup of the lattice is a statistical process which is in large parts mediated by the thermal fluctuations. The number of simulation steps might be insufficient for this process to unfold. Both effects increase the stability of the vortex lattice in the Shubnikov state, which we observe as the VL undercooling.

Second is the impact of pinning and the sample purity on the superconductor in addition to the actual pinning sites. Typically, the sample quality also affects superconducting parameters, such as the London penetration depth λ_{L}. These parameters, however, factor into the vortex interaction, which was neglected in our simulations. Additionally, EGL theory itself uses a set of model parameters which are depending on the superconductor's quality (cf. equation (2.7)). For the studies in this work, this dependence was neglected, because the correspondence between pinning parameters and other material parameters is not straightforward. Instead, we want to highlight that the mere presence of pinning centers does change the IMS transition process while the fundamental IMS line is not directly affected.

The **vortex lattice correlation length** ξ_{VL} is shown in figure (7.3) on the same examples as a_{VL} (for measurements, cf. section (4.3), figure (4.2) and for simulations, cf. section (6.2), figure (6.14)). The impact of the IMS on the VL correlation is a significant decrease, seen in experiment and simulation. In the measurements, $\xi_{\mathrm{VL}} \approx 7 - 8\, a_{\mathrm{VL}}$ in the Shubnikov state, which corresponds to approximately $1.5 - 2.5\,\mu$m, depending on the field. These values are very close to the resolution limit of the instrument with a direct beam width of $7.5 \cdot 10^{-4}/$Å, which corresponds to $0.8\,\mu$m. It is therefore likely that the lattice is more coherent than measured. Still, we observe a gradual decrease of the lattice correlation below the IMS transition temperature, down to a value of $\xi_{\mathrm{VL}} \approx 3 - 4\, a_{\mathrm{VL}}$ or $\approx 0.6 - 0.8\,\mu$m . The picture seen in the simulations is very similar, but much clearer due to the unlimited resolution. In the Shubnikov state, $\xi_{\mathrm{VL}} \approx 60 - 80\, a_{\mathrm{VL}}$ or $15 - 30\,\mu$m depending on the field. These values clearly resemble the size of the simulation area (cf. figure (6.13)). Compared to the measurements, the transition to the IMS is much more defined by a sharp drop of ξ_{VL} down to values of $5 - 15\, a_{\mathrm{VL}} \approx 1 - 3\,\mu$m. In the IMS, the lattice correlation slightly increases with decreasing temperature. Additionally, ξ_{VL} clearly increases with increasing magnetic field. This last feature is, however, depending on the pinning characteristics of the simulation (cf. figure (6.20)).

Due to the breakup of a homogeneous lattice into domains, the reduction of ξ_{VL} is natural. In large parts of the IMS, experiments and simulations show lattice correlations which are mostly constant over temperature in units of the changing lattice constant. This corresponds to a constant VL domain size in terms of vortices. Apparently, the VL domain morphology is defined close below the transition temperature. At lower temperatures, the domains merely contract according to $a_{\mathrm{IMS}}(T)$, but do not fracture further, recombine or otherwise change their size. The different behavior with a gradual reduction in experiment and a sharp drop in the simulations is for the most part connected to the undercooling seen in the simulations. At the IMS transition, ξ_{VL} abruptly changes, which introduces additional disorder into the vortex domain structure. We see that with decreasing temperature and thus increasing simulation time the lattice is slowly healing and the correlation increases. In the measurements, the change of a_{VL} is continuous, which may explain the smooth transition and gradually decreasing ξ_{VL}. In addition, the values obtained in experiment are limited by the resolution and integrated over a large sample volume. Both may have a smearing effect on the observed lattice correlation, in contrast to the high resolution, but very local results from the simulations. Similar to the vortex

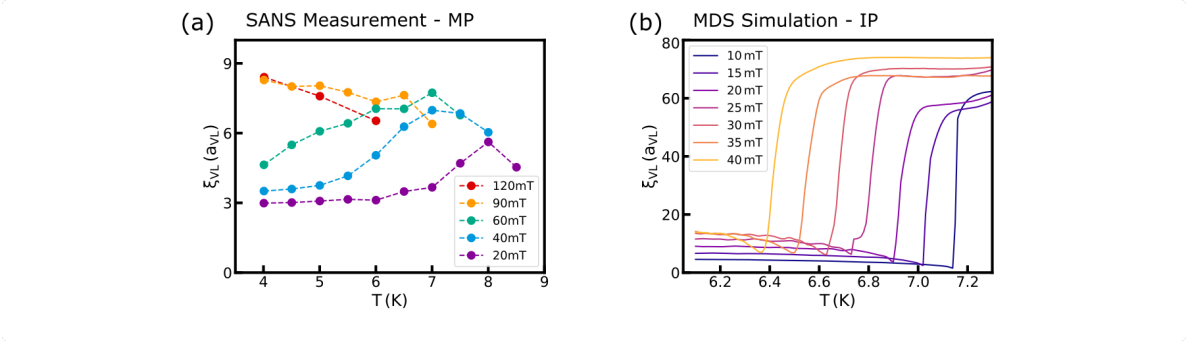

Figure 7.3: Comparison of the vortex lattice correlation length ξ_{VL} in experiment and simulation. (a) SANS measurements of the medium purity sample (MP-1). (b) Results of the simulations featuring individual pinning (IP). Both panels show a high correlation length in the Shubnikov state which drops to lower values in the IMS. The IMS transition is clearly defined by a sharp drop in the simulations compared to a small and gradual change in the experiment. Additionally, in the IMS the simulations show an increasing ξ_{VL} with the magnetic field, which is only slightly visible in the experiment.

lattice correlation, the correlation of vortices along the field direction ξ_{vortex} decreases in the IMS (cf. figure (4.5)). This effect indicates that the IMS domains are not homogeneous over the sample thickness, but have a three dimensional structure on the scale of $10\,\mu$m. Since our simulations are purely two dimensional, this effect can currently not be compared. It poses, however, an incentive to expand our simulations to three dimensions.

The **IMS domain morphology** is analyzed based on the VSANS scattering signal in our experiments. In the simulations, this corresponds mostly to the Fourier transforms of the vortex configurations at low q. Figure (7.4) shows data obtained from the medium purity sample MP-4 in a field of 40 mT (panel (a), cf. figure (4.8)) and data from the exemplary simulation with $B_{\text{sim}} = 30\,\text{mT}$ and no pinning sites (cf. section (5.3), figure (5.11)). The experimental data has an asymmetric peak, with its maximum at $\approx 7 \cdot 10^{-5}/\text{Å}$ very close to the resolution limit of $\approx 5 \cdot 10^{-5}/\text{Å}$. At higher q, the signal diminishes, following a power law with an exponent of approximately $3-4$. The VSANS signal emerges at 6.0 K, below the IMS transition. With decreasing temperature, the intensity increases while the signal shape stays intact. In the simulations, the Fourier transform has a double peak feature, apart from which it resembles the experimental data. Especially the temperature dependence is identical, with an emerging signal at 6.5 K below the IMS transition, which increases, but does not significantly change its shape while cooling down.

The stability of both signals over temperature is the most important result concerning the domain morphology. It indicates that the IMS domain structure is decided very close below the transition temperature and does not change significantly afterwards. This behavior also fits the constant lattice correlation ξ_{VL} in the IMS. The model function we have used to fit the data, of both experiment and simulation, was originally used in the context of spinodal decomposition (cf. equation (3.10)). In the spinodal scenario, a domain structure emerges from a homogeneous state, similarly to the domain formation

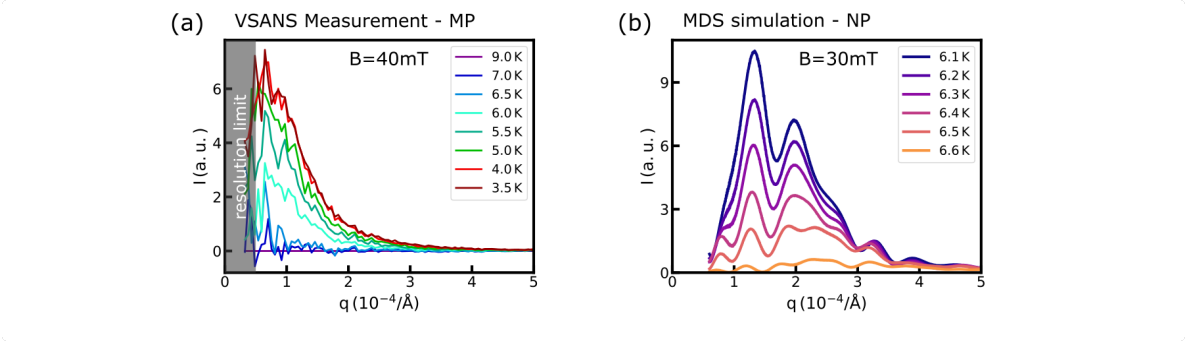

Figure 7.4: Comparison of the VSANS scattering signal / Fourier transform of the IMS domains in experiment and simulation. (a) VSANS measurements of the medium purity sample (MP-4). (b) Fourier transforms of the exemplary simulation featuring no pinning (NP). In both plots, the intensity increases with decreasing temperature, while the shape of the scattering signal stays approximately constant over temperature. Due to the limited instrument resolution, the VSANS measurement might be distorted. The strong oscillations visible in the simulation data are due to the limited simulation size.

observed in the IMS transition. Both cases differ, however, in the internal development of the domain structure. For a spinodal decomposition, the domains themselves have a constant shape throughout the unmixing process, and only the internal densities change. The IMS, however, clearly shows a changing size of the individual domains and only a constant scale of the morphology. Still, the two scenarios are close enough to allow a meaningful comparison. The quantitative evaluation of the domain morphology, expressed as the IMS correlation length ξ_{IMS}, is, however, limited in both experiment and simulation. In the measurements, the instrument resolution ($5 \cdot 10^{-5}$/Å, 13 μm) is very close to the measured correlation length ($7 \cdot 10^{-5}$/Å, 9 μm). It is therefore likely that the true domain morphology is larger than our result. The limitation of the simulation lies in the relatively small simulation size and therefore the low number of distinct domains. First, this means that the shape of these few domains is prevailing in the signal shape. In contrast, the experimental scattering signal is averaged over a huge number of domains and shows a statistical average. Second, the shape of the simulation size itself is clearly visible in the Fourier transform, as it is on the same scale as the domain size. In the example shown here, the double peak feature is actually an artefact stemming from the simulation area. Both effects increase the error of determining the true domain correlation length.

The **field dependence** of the IMS domain morphology has been addressed in the simulations in great detail, differentiating between three pinning scenarios (NP, IP, CP, cf. section (6.2.2)). In the experiments, however, the determination of the domain size was limited due to the resolution limits just addressed. Usable data of ξ_{IMS} has been obtained for two low purity (LP) samples in a previous study by Reimann et al [14]. The measurements were performed at the BT-5 VSANS beamline at the NIST Center for Neutron Research, using the samples LP-1 and a comparable sample LP-X with thickness 2 mm. The results are shown in figure (7.5) along with the results of our simulations. In the experiments (a), an increasing domain size with increasing external

field has been found. ξ_{IMS} has a value of $2 - 12\,\mu$m, which fits the estimates of our measurements of MP-4. The simulations (b) show two distinguishable field dependencies instead. In the absence of pinning (NP), the domain size decreases with increasing field. In contrast, the simulations including pinning (IP, CP) show an increasing dependence.

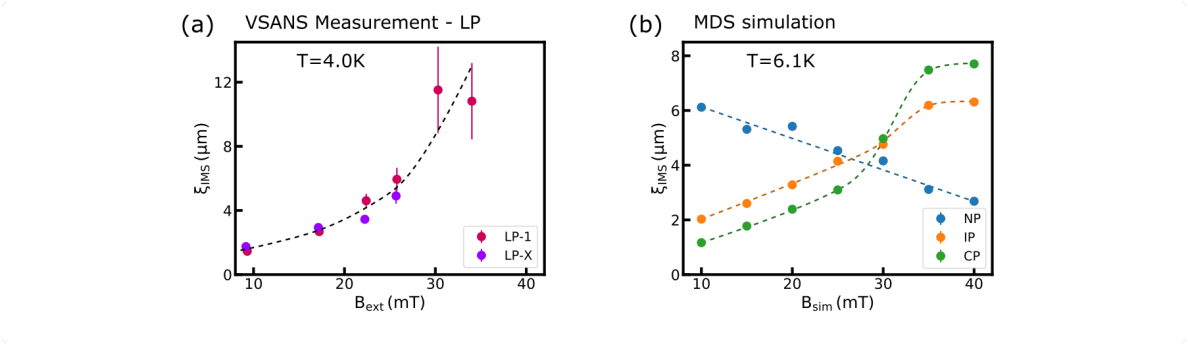

Figure 7.5: Comparison of the IMS domain correlation length ξ_{IMS} in experiment and simulation. (a) VSANS measurements of low purity samples from a previous study. LP-1 is the low purity sample used in this work and LP-X a similar sample with thickness 2 mm. For both samples, the domain size increases with increasing magnetic field. (b) Results of the field dependent simulations featuring three different pinning characteristics, no pinning (NP), individual pinning (IP) and collective pinning (CP). For NP, the domain size decreases with the field, while IP and CP show a growing domain size with increasing field. Both cases with pinning are comparable to the experimental data.

Between experiment and simulation, there is a clear match of the low purity (high pinning) sample and the pinning simulations (IP, CP). A clear assignment to either pinning case, however, cannot be done at this point. The increasing domain size is most likely connected to the decreasing ratio of pinning sites to vortices. We note, however, that the different pinning cases also show differences in the undercooling. It is possible that the distinction of the different pinning cases can be refined with improved simulation results.

In conclusion, the results of our experiments and our simulations are highly comparable. The most prominent feature is the uniquely defined $a_{\mathrm{IMS}}(T)$, which represents the microscopic properties of the inter-vortex interaction. In addition, several results indicate a domain morphology which is constant over temperature, but depending on the magnetic field. The main differences found between experiments and simulations were due to technical limitations of both approaches. In the experiments, a limited resolution of all neutron scattering techniques reduced the reliability of some quantities, especially the correlation lengths ξ_{VL} and ξ_{IMS}. The simulations are primarily limited by the two dimensional approach and the limited simulation size. Additionally, the potential of the underlying EGL model has not been fully exhausted, especially with regard to the impact of pinning and sample purity on the calculations.

As a closing statement, we want to repeat that the IMS is a highly fundamental phase in niobium and likely a defining feature in intertype superconductors. We have observed the formation of a vortex matter domain structure under vastly different circumstances. These include different purities, of both bulk and surface, sample shapes, a coexistence with either the Meissner effect or a flux freezing transition, and in field cooled, field heated and zero field cooled measurement. Especially, a remarkable stability against pinning was observed in the simulations over several orders of magnitude in both pinning parameters. While the IMS lattice parameter $a_{\mathrm{IMS}}(T)$ is defined at all temperatures, an actual transition into the IMS domain structure is only observed, if the current vortex density is above the one defined by a_{IMS}. How such a scenario is achieved is not crucial, but it is often connected to secondary effects of the sample shape and demagnetization or the pinning properties of a sample.

8 Outlook

Throughout this work, we have used a large variety of techniques to investigate the properties of the intermediate mixed state and have gained extensive insight into this intricate vortex matter state. In this final chapter, we present some of our plans for the future.

The **experimental** results of this work have shown that the resolution limitation of the neutron scattering techniques is deterring us from precisely determining the IMS domain morphology. In the SANS measurements of the vortex lattice, the correlation length ξ_{VL} is basically inaccessible in the Shubnikov state and imprecise in the IMS. Furthermore, the domain scattering signal measured with VSANS is likely truncated towards lower q. In a similar fashion, the DFI signal obtained with NGI is probably affected by the limited resolution. The different resolution in the experiments additionally reduces the quantitative comparability of the techniques. The scattering contrast of the IMS domains, e.g., is different in all three techniques due to the resolution. Increasing the resolution of a technique is, if possible, typically linked to a significant increase of the measurement time. At all three beamlines, we have used, the resolution can actually be increased, primarily by increasing the neutron wavelength or reducing the neutron source size, but it has to be determined if the effect is sufficient. Alternatively, the measurement technique can be changed in some cases. For samples, where the vortex lattice scattering has already been measured using SANS, single Bragg peaks can additionally be measured with VSANS. Using the higher resolution of VSANS, the lattice correlation ξ_{VL} can be determined more precisely. However, this also increases the measurement time significantly, because multiple experiments have to be performed. For the IMS morphology, a Bonse-Hart instrument can be used instead of a focusing VSANS setup, as it was done in the work by Reimann et al. [14]. However, even then, domain correlations beyond $10\,\mu$m are becoming difficult to resolve.

A novel approach is the quantitative use of the NGI to determine the domain structure. With an NGI, the autocorrelation function of a scattering system can be measured by changing the instrumental correlation length ξ_{NGI}. This is typically done by adjusting the neutron wavelength or the sample position, which is both restricted due to technical issues. In a first test, we have performed NGI measurements with ξ_{NGI} between $4\,\mu$m and $15\,\mu$m. The results are shown in figure (8.1). In order to cover a large range of ξ_{NGI}, we have measured at 5 different wavelengths (colored lines) and 4 sample positions (black dotted lines). The DFI value is different at each wavelength due to the λ_{N}-dependence of the macroscopic scattering contrast Σ. Over the full range of the measurements, we see a decreasing DFI value, which indicates a domain correlation beyond $15\,\mu$m. A problem arising during the evaluation was the scaling of Σ, which does not follow the usual λ_{N}^2 dependence on the neutron wavelength. Our current hypothesis is that this problem is connected to the neutron coherence volume, which also changes with λ_{N}.

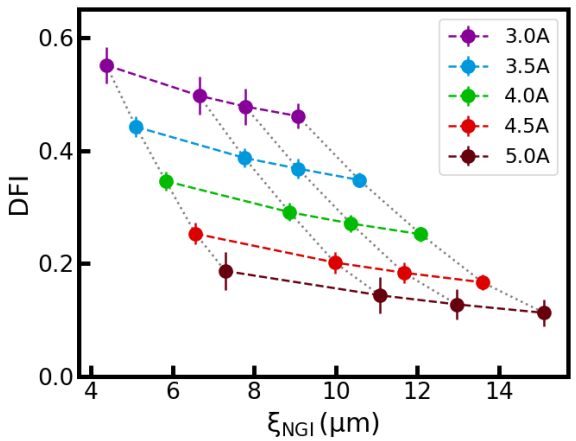

Figure 8.1: Preliminary results of quantitative NGI measurements of the sample MP-1. For the measurements, the correlation length of the instrument ξ_{NGI} has been changed using the wavelength (colored lines) and the sample position (black dotted lines). In the whole range between $4\,\mu$m and $15\,\mu$m, the DFI is decreasing, indicating a domain correlation beyond the accessible range.

Regarding the **simulations**, there are two major concerns for the validity. First is the two dimensional approach. The vortex correlation measured in SANS experiments has indicated that the IMS domain structure is, in fact, three dimensional. Furthermore, the correlation in field direction $\xi_{\mathrm{VL}} \approx 10\,\mu$m is comparable to the correlation perpendicular to the field $\xi_{\mathrm{IMS}} \approx 10\,\mu$m. In the three dimensional case, the elastic properties have a larger impact on the IMS transition, since the vortices have to be bent instead of being only moved. The problem with three dimensional simulations is, however, that vortices have to be simulated as extended string-like objects. This is typically done by sectioning the vortices into several parts, which increases the number of particles in the simulation and accordingly the simulation time. Our second concern is the undercooling of the vortex lattice below the theoretical transition line. The root of this effect lies probably in the insufficient simulation steps and in the perfect initial vortex lattice configuration. The number of simulation steps can be highly increased in order to test our first assumption. However, not every simulation can be performed with a highly increased simulation time. Instead, it might be viable to alter the time step adaption we use or to artificially increase the thermal fluctuations. Both measures are, however, physically questionable. Concerning the initial state of the simulations, a possible approach is to introduce small errors in the lattice by using randomly distributed pinning centers, which are removed prior to the cooldown procedure. Alternatively, a self assembly of the lattice from a random configuration could also work. As an additional point, the impact of pinning on the EGL model parameters and the model superconductor parameters used in the simulation should be reconsidered. We assume, however, that this problem is not that fundamental and reduces mainly to a scaling of the vortex interaction strength and range.

An **additional technique** we consider to include in our future studies of the IMS is muon spin rotation (MuSR). Using MuSR, the local magnetic field distribution in a superconducting sample can be measured. In a vortex lattice state, this can be used to determine the shape of the vortices (i.e. their magnetic field profile) or the degree of disorder in the lattice. For us, the motivation to use this technique is that MuSR is sensitive to all vortices in a sample. In contrast, the diffraction experiments performed with SANS only measure the ordered part, i.e. the vortex lattice. It is, however, our assumption that a part of the vortices may remain in disorder during the rearrangement of the IMS transition. In addition, the fraction of Meissner state domains can be directly measured by this technique, since they contain no magnetic field.

Figure (8.2) shows first measurements performed on sample MP-1 at the GPS beamline at the Paul-Scherrer institute (PSI). Panel (a) shows the temperature dependence of the local field distribution in an external field of 60 mT. At 8 K and 7 K the field distribution shows a curve typical for a well ordered vortex lattice. The curve is zero below a minimum field value, where it increases steeply to a maximum, after which it decreases more slowly up to a maximum field. The curves at both temperatures differ, due to the changing magnetic shape of the vortices, which is primarily defined by the temperature dependent superconducting length scales λ_{L} and ξ_{GL}. Below 5 K, in the IMS, several aspects of the field distribution change. Most obviously, a significant contribution at zero field emerges, which corresponds to the flux-free Meissner domains. Additionally, the field distribution corresponding to the vortices broadens and shifts to higher fields again. The former is due to the increasing disorder at the edges between VL domains and Meissner domains. The latter is an effect of the decreasing lattice constant in the IMS and the stronger overlap of the vortices. In panel (b), the volume fraction of the Meissner state is shown for two measurement series at 40 mT and 60 mT. The solid line included in the plot is a maximal value, calculated from our SANS measurements. Optimally, all vortices stay in a lattice configuration with increased vortex density, which is measured as vortex lattice constant and can be expressed as an internal flux density B_{IMS}. The fraction of vortex lattice domains is then given by the ratio of the initial flux density in the Shubnikov state, which corresponds to the external field B_{ext} and the internal B_{IMS}. Accordingly, the fraction of Meissner state domains is given as $1 - B_{\mathrm{ext}}/B_{\mathrm{IMS}}$. Obviously, the measured values are significantly reduced, at approximately 75 % and 50 % for both fields respectively. For a detailed analysis, however, the influence of domain edges on the field profile has to be taken into account. Hence, the actual value might be larger.

Finally, the pinning properties of our samples will be a major focus of our further work. While we know the bulk quality of our samples from magnetization and neutron activation measurements, the surface quality is not as well known. Especially for the MP samples, different combinations of grinding, polishing and etching have been used. A clear impact on the measurements has not been found, but the surface quality has also not been determined quantitatively. In the future, we plan to prepare a set of samples with well defined surface properties in order to study the effect. This will hopefully also answer the question, if surface pinning has to be considered in our simulations.

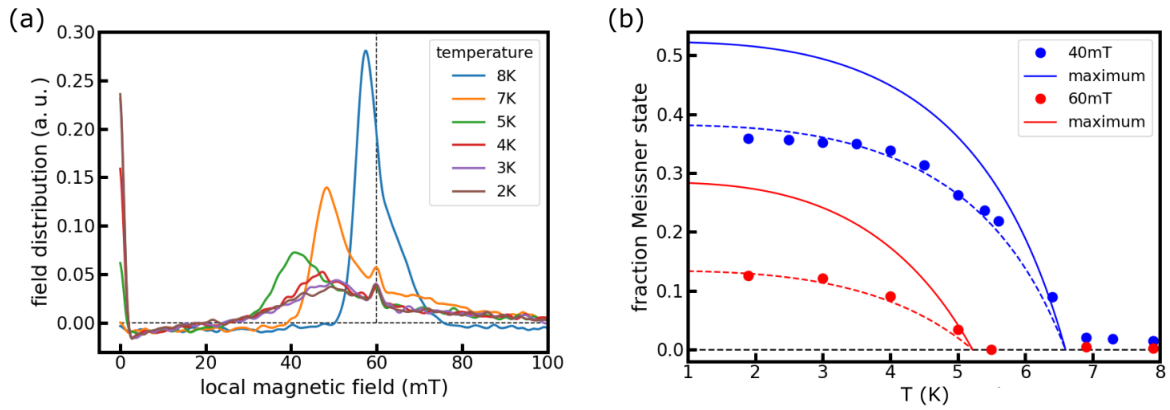

Figure 8.2: Preliminary results of MuSR data of the sample MP-1. (a) Temperature dependence of the local field distribution in an external field of 60 mT. At 8 K and 7 K, the clear shape of a homogeneous well ordered vortex lattice is visible. Below 5 K the broadening of the field distribution and an emerging contribution at 0 mT indicate the IMS. (b) Fraction of the flux-free Meissner state domains at 40 mT and 60 mT, extracted from the measured zero field contribution. The solid lines give an estimated upper limit of the Meissner domain fraction based on the vortex lattice constant measured in SANS.

Regarding the bulk quality of the samples, a defined preparation is not possible at the moment due to the difficulty in growing niobium single crystals. However, different thermal treatments could be used in order to improve or reduce the amount of defects in the crystal lattice.

A new approach currently in development is the depinning of the vortices using a driving current. Due to their magnetic properties, vortices interact with an electric current via the Lorentz force. Applying a sufficiently high current to a superconductor will induce a collective motion of the vortex matter perpendicular to the current. While in motion, the vortices effectively are in a pinning-free state. However, their movement and interaction with the current still create a situation fundamentally different from a pinning-free static vortex matter. First SANS images are shown in figure (8.3), measured on a medium purity sample similar to MP-4, in a current-free state (a) and under the influence of a driving current (b). The images show the same twofold hexagonal Bragg peaks as has been reported in this work (cf. figure (3.8)). Under the influence of a current, the peaks are somewhat smeared and their intensity is reduced, which is attributed to disorder of the lattice associated with the vortex movement. In the center of the image (white circle) around the direct beam (blacked out), the VSANS scattering signal from the IMS domains is visible. The scattering is isotropic in the current-free measurement (a), which agrees with the VSANS measurements presented in this work (cf. figure (3.4)). In contrast, panel (b) shows an elongated scattering signal along the current direction. This indicates that the domains are compressed in the direction of the current. This peculiar domain structure is the result of two interconnected currents: the electric driving current and the vortex current perpendicular to it, which has a few ramifications. Since the electric current cannot pass through Meissner state domains, there must exist

a connected vortex domain throughout the sample. Otherwise, the current would be limited to the surface of the sample. Additionally, the domain structure might redirect the current locally in order to flow around the Meissner domains. This, in turn would induce a vortex movement parallel to the net electric current. Furthermore, isolated vortex domains are stationary, as the current cannot flow through the surrounding Meissner domain. Taken together, the details of the domain morphology under the influence of a driving current and a potential dynamic behavior are a complex problem which will require extensive further investigations.

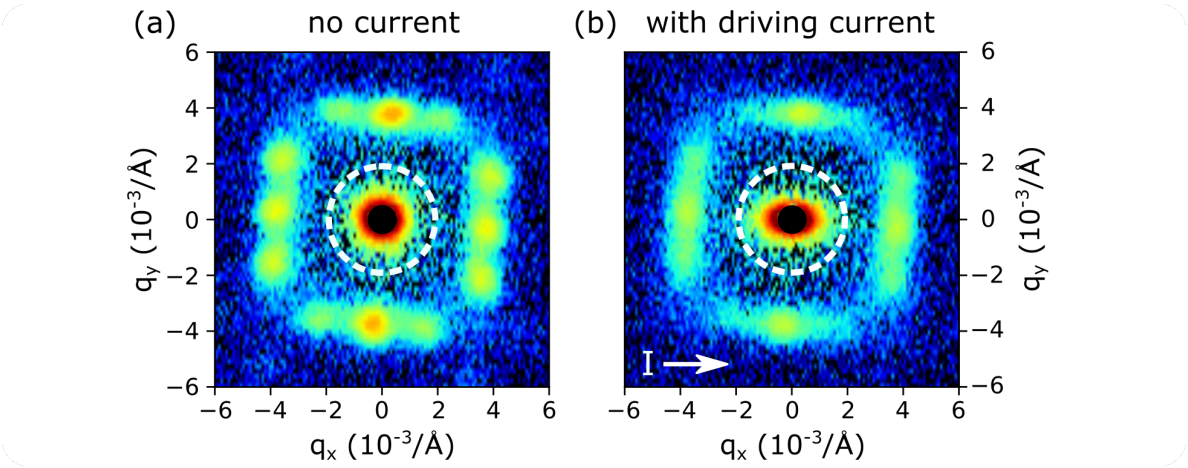

Figure 8.3: SANS images measured on a sample similar to MP-4 at 4 K in a field of 50 mT. Measurements were performed without (a) and with (b) an applied current. The Bragg peaks show a similar arrangement in both images, but are broader and have a reduced intensity in (b). Close to the direct beam (in the white circle) the scattering signal from the IMS domains is visible. Without a current, the scattering is isotropic. The driving current introduces an anisotropic scattering with higher scattering angles along the current direction.

List of Publications

- **Fabrication of gadolinium particle-based absorption gratings for neutron grating interferometry**
  A. Gustschin, T. Neuwirth, A. Backs, M. Schulz and F. Pfeiffer
  Rev. Sci. Instrum., 89(10):103702, 2018

- **Universal behavior of the intermediate mixed state domain formation in superconducting niobium**
  A. Backs, M. Schulz, V. Pipich, M. Kleinhans, P. Böni and S. Mühlbauer
  Phys. Rev. B, 100(6):1442, 2019

- **A high visibility Talbot-Lau neutron grating interferometer to investigate stress-induced magnetic degradation in electrical steel**
  T. Neuwirth, A. Backs, A. Gustschin, S. Vogt, F. Pfeiffer, P. Böni and M. Schulz
  Sci. Rep., 10(1):9, 2020

In preparation

- **Molecular dynamics simulations of the temperature-driven vortex clustering in intertype superconductors**
  A. Backs, A. Al-Falou, A. Vagov, P. Böni and S. Mühlbauer

- **Quantitative evaluation of neutron scattering close to the resolution limit using NGI and VSANS**
  A.Backs, T. Neuwirth, A. Gustschin, S. Mühlbauer, V. Pipich, P. Böni and M.Schulz

Acknowledgement / Danksagung

The results presented in this work would not have been possible without the help and support from many people. While all of them have my sincere gratitude, I would like to thank some of them in particular:

Prof. Peter Böni
Lieber Peter, vielen Dank, dass du es mir ermöglicht hast, diese spannende Forschungsarbeit durchzuführen, obwohl ich keinerlei Vorkenntnisse mit Neutronen oder Simulationen hatte. Du hast mir während der letzten Jahre alle Freiräume gelassen, die ich mir wünschen konnte, und warst dabei immer mit Rat und Unterstützung zur Stelle, wenn ich diese benötigt habe. Danke für dieses Vertrauen.

Sebastian Mühlbauer
Lieber Basti, danke dir für die Unmengen an Unterstützung, die du mir gegeben hast, angefangen bei Einführungen und Erklärungen zu Supraleitung, Magnetismus und Neutronenstreuung über Diskussionen und gemeinsame Messzeiten bis hin zur Korrektur meiner Arbeit. Die Zusammenarbeit in den letzten Jahre hat mir sehr viel Spaß gemacht.

Michael Schulz
Lieber Michi, vielen Dank, dass du mich in deiner Gruppe und sogar in deinem Büro aufgenommen hast. Durch dich habe ich mit dem NGI eine seltene, doch spannende Technik kennengelernt, die mir über die Jahre viel Spaß (und manchmal auch Frust) gebracht hat. Du hast mich mit meiner Arbeit und auch mit allen alltäglichen Problemchen am Institut immer unterstützt.

Abdel Al-Falou
Abdel, zusammen haben wir Neuland erforscht (zumindest für uns). Danke, dass du dich mit mir zusammen daran gewagt hast, den IMS zu simulieren, obwohl wir beide (und Basti) kaum Ahnung davon hatten. Ich hoffe, du hast daran ebenso viel Freude gefunden wie ich. Die Ergebnisse können sich auf jeden Fall sehen lassen.

Tommy Reimann
Danke dir, Tommy, dass du mich in die Welt von IMS und NGI eingeführt hast und damit den Weg für meine Arbeit deutlich geebnet hast. Eigentlich sollte ich auch deiner Dissertation hier einen eigenen Platz einräumen, die ich mittlerweile vermutlich genauso gut kenne wie du.

Tobias Neuwirth
Lieber Tobi, vielen Dank an dich für die Zusammenarbeit und Hilfe während der letzten Jahre. Die Diskussionen mit dir haben immer sehr viel Spaß gemacht und geholfen. Besonderer Dank auch für die überragende Verpflegung mit Kuchen und Kleingebäck.

Imaging - Gruppe & Mate (Kaffee) - Runde
Vielen Dank an das gesamte Team rund um ANTARES und NECTAR. Ich habe mich bei euch vom ersten Tag an immer willkommen und gut unterstützt gefühlt, was mir die Arbeit deutlich vereinfacht und jede Menge Spaß gebracht hat. Nicht zuletzt die Mittagspausen haben den Arbeitsalltag aufgelockert und mit reichlich Kuchen und Mate die Arbeitsmoral aufrechterhalten.

Alexei Vagov
Dear Alexei, thank you for reaching out to Basti and me. Your work on intertype superconductors and your explanations have deepened my understanding of the IMS considerably. Also thank you for providing me with your results, which allowed us to perform the simulations on a solid theoretical foundation.

Vitali Pipich
Dear Vitali, thank you for supporting me with the performance and analysis of several experiments at the KWS-3. Though, I have to admit that I still don't understand your software fully.

Markus Kleinhans
Markus, danke dir für die Durchführung der Magnetometrie-Messungen an deinem VSM.

Armin Kriele & Susanne Mayr
Vielen Dank für die Hilfe bei der Herstellung und Bearbeitung meiner Proben.

Chennan Wang & Roustem Khassanov
Thank you both for reaching out to me and helping me with the MuSR measurements at PSI. I am grateful that you introduced me to the world of Muons.

Familie, Freunde & Partner
Ganz herzlichen Dank an euch alle, dass ihr immer für mich da seid und mich unterstützt. Ohne den immensen Rückhalt, den ich bei euch finde, hätte ich den weiten und beschwerlichen Weg bis hierhin niemals durchgestanden. Ich hab euch lieb.

Bibliography

[1] G. R. Stewart. Unconventional superconductivity. *Advances in Physics*, 66(2): 75–196, 2017.

[2] V. L. Ginzburg and L. D. Landau. On the theory of superconductivity. *Zh. Eksp. Teor. Fiz.*, 20(3)(1064), 1950.

[3] R. P. Hübner. Magnetic Flux Structures in Superconductors. *Springer*, 2001.

[4] H. Träuble and U. Essmann. Die Beobachtung magnetischer Strukturen von Supraleitern zweiter Art. *Phys. Stat. Solidi B*, 20(1):95–111, 1967.

[5] N. V. Sarma. Transition from the flux lattice to the intermediate state structures in a lead-indium alloy. *Philos. Mag.*, 18(151):171–176, 1968.

[6] D. P. Almond, M. J. Lea, and E. R. Dobbs. Ultrasonic evidence against multiple energy gaps in superconducting niobium. *Phys. Rev. Lett.*, 29(12):764, 1972.

[7] V. Novotny and P. P. M. Meincke. Single superconducting energy gap in pure niobium. *J. Low Temp. Phys.*, 18(1-2):147–157, 1975.

[8] E.H. Brandt and U. Essmann. The flux-line lattice in type-II superconductors. *Phys. Stat. Solidi B*, 144(1):13–38, 1987.

[9] J. Auer and H. Ullmaier. Magnetic behavior of type-II superconductors with small Ginzburg-Landau parameters. *Phys. Rev. B*, 7(1):136, 1973.

[10] D. K. Christen, F. Tasset, S. Spooner, and H. A. Mook. Study of the intermediate mixed state of niobium by small-angle neutron scattering. *Phys. Rev. B*, 15(9): 4506, 1977.

[11] U. Klein. Microscopic calculations on the vortex state of type-II superconductors. *J. Low Temp. Phys.*, 69(1-2):1–37, 1987.

[12] E. H. Brandt. Microscopic theory of clean type-II superconductors in the entire field-temperature plane. *Phys. Stat. Solidi B*, 77(1):105–119, 1976.

[13] A. Vagov, A. A. Shanenko, M. V. Milošević, V. M. Axt, V. M. Vinokur, J. A. Aguiar, and F. M. Peeters. Superconductivity between standard types: Multiband versus single-band materials. *Phys. Rev. B*, 93(17):174503, 2016.

[14] T. Reimann, M. Schulz, D. F. R. Mildner, M. Bleuel, A. Brûlet, R. P. Harti, G. Benka, A. Bauer, P. Böni, and S. Mühlbauer. Domain formation in the type-II/1 superconductor niobium: Interplay of pinning, geometry, and attractive vortex-vortex interaction. *Phys. Rev. B*, 96(14):144506, 2017.

[15] C. Pfleiderer. Superconducting phases of f-electron compounds. *Rev. Mod. Phys.*, 81(4):1551, 2009.

[16] J. Bardeen, L. N. Cooper, and J. R. Schrieffer. Microscopic theory of superconductivity. *Phys. Rev.*, 106(1):162, 1957.

[17] G. W. Webb, F. Marsiglio, and J. E. Hirsch. Superconductivity in the elements, alloys and simple compounds. *Physica C*, 514:17–27, 2015.

[18] N. Karchev. Magnon exchange mechanism of ferromagnetic superconductivity. *Phys. Rev. B*, 67(5):054416, 2003.

[19] Y. Song, J. Van Dyke, I. K. Lum, B. D. White, S. Jang, D. Yazici, L. Shu, A. Schneidewind, P. Čermák, Y. Qiu, et al. Robust upward dispersion of the neutron spin resonance in the heavy fermion superconductor $Ce_{1-x}Yb_xCoIn_5$. *Nat. Commun.*, 7(1):1–10, 2016.

[20] S. Watanabe and K. Miyake. Coupled CDW and SDW fluctuations as an origin of anomalous properties of ferromagnetic superconductor UGe_2. *J. Phys. Soc. Japan*, 71(10):2489–2499, 2002.

[21] K. Fujita, M. H. Hamidian, S. D. Edkins, C. K. Kim, Y. Kohsaka, M. Azuma, M. Takano, H. Takagi, H. Eisaki, S. I. Uchida, et al. Direct phase-sensitive identification of a d-form factor density wave in underdoped cuprates. *Proc. Natl. Acad. Sci. USA*, 111(30):E3026–E3032, 2014.

[22] A. Greco and R. Zeyher. Isotope effect on the superconducting critical temperature of cuprates in the presence of charge order. *Supercond. Sci. Technol.*, 29(1):015002, 2015.

[23] T. R. Kirkpatrick, D. Belitz, T. Vojta, and R. Narayanan. Strong enhancement of superconducting T_c in ferromagnetic phases. *Phys. Rev. Lett.*, 87(12):127003, 2001.

[24] T. Moriya and K. Ueda. Antiferromagnetic spin fluctuation and superconductivity. *Rep. Prog. Phys.*, 66(8):1299, 2003.

[25] C. W. Chu, L. Z. Deng, and B. Lv. Hole-doped cuprate high temperature superconductors. *Physica C*, 514:290–313, 2015.

[26] Y. Maeno, H. Hashimoto, K. Yoshida, S. Nishizaki, T. Fujita, J. G. Bednorz, and F. Lichtenberg. Superconductivity in a layered perovskite without copper. *Nature*, 372(6506):532–534, 1994.

[27] G. R. Stewart, Z. Fisk, and J. O. Willis. Characterization of single crystals of CeCu2Si2. A source of new perspectives. *Phys. Rev. B*, 28(1):172, 1983.

[28] C. C. Tsuei and J. R. Kirtley. Pairing symmetry in cuprate superconductors. *Rev. Mod. Phys.*, 72(4):969, 2000.

[29] H. Hosono and K. Kuroki. Iron-based superconductors: Current status of materials and pairing mechanism. *Physica C*, 514:399–422, 2015.

[30] DM Lee and AJ Leggett. Superfluid ^{3}He - the early days. *J. Low Temp. Phys.*, 164(3-4):140–172, 2011.

[31] T. M. Rice and M. Sigrist. Sr_2RuO_4: an electronic analogue of 3He? *J. Phys. Cond. Matter*, 7(47):L643, 1995.

[32] D. Aoki, A. Huxley, E. Ressouche, D. Braithwaite, J. Flouquet, J. P. Brison, E. Lhotel, and C. Paulsen. Coexistence of superconductivity and ferromagnetism in URhGe. *Nature*, 413(6856):613–616, 2001.

[33] Y. Liu and Z. Mao. Unconventional superconductivity in Sr2RuO4. *Physica C*, 514:339–353, 2015.

[34] S. E. Brown. Organic superconductors: The Bechgaard salts and relatives. *Physica C*, 514:279–289, 2015.

[35] F. Kneidinger, E. Bauer, I. Zeiringer, P. Rogl, C. Blaas-Schenner, D. Reith, and R. Podloucky. Superconductivity in non-centrosymmetric materials. *Physica C*, 514:388–398, 2015.

[36] J. G. Bednorz and K. A. Müller. Perovskite-type oxides - The new approach to high-T_c superconductivity. *Rev. Mod. Phys.*, 60(3):585, 1988.

[37] S. Zhang, M. Tanaka, E. Watanabe, H. Zhu, K. Inumaru, and S. Yamanaka. Superconductivity of alkali metal intercalated TiNBr with α-type nitride layers. *Supercond. Sci. Technol.*, 26(12):122001, 2013.

[38] Y. Kasahara, K. Kuroki, S. Yamanaka, and Y. Taguchi. Unconventional superconductivity in electron-doped layered metal nitride halides MNX (M=Ti, Zr, Hf; X= Cl, Br, I). *Physica C*, 514:354–367, 2015.

[39] K. Takada, H. Sakurai, E. Takayama-Muromachi, F. Izumi, R. A. Dilanian, and T. Sasaki. Superconductivity in two-dimensional CoO_2 layers. *Nature*, 422(6927): 53–55, 2003.

[40] G. Q. Zheng, K. Matano, R. L. Meng, J. Cmaidalka, and C. W. Chu. Na content dependence of superconductivity and the spin correlations in $Na_xCoO_2 \cdot$ 1.3 H_2O. *J. Phys. Cond. Matter*, 18(5):L63, 2006.

[41] M. Tokumoto, K. Murata, H. Bando, H. Anzai, G. Saito, K. Kajimura, and T. Ishiguro. Ambient-pressure superconductivity at 8 K in the organic conductor β-(bedt-ttf) 2i3. *Solid State Commun.*, 54(12):1031–1034, 1985.

[42] F. Steglich and S. Wirth. Foundations of heavy-fermion superconductivity: lattice Kondo effect and Mott physics. *Rep. Prog. Phys.*, 79(8):084502, 2016.

[43] V. Moshchalkov, M. Menghini, T. Nishio, Q. H. Chen, A. V. Silhanek, V. H. Dao, L. F. Chibotaru, N. D. Zhigadlo, and J. Karpinski. Type-1.5 superconductivity. *Phys. Rev. Lett.*, 102(11):117001, 2009.

[44] P. K. Biswas, A. D. Hillier, R. P. Singh, N. Parzyk, G. Balakrishnan, M. R. Lees, C. D. Dewhurst, E. Morenzoni, and D. McK. Paul. Evidence of type-I and type-II superconductivity and their coexistence in ZrB12. *arXiv preprint arXiv:1910.09082*, 2019.

[45] Andrew Huxley. Neutron scattering from vortex lattices in superconductors. In *Vortices in Unconventional Superconductors and Superfluids*, pages 301–320. Springer, 2002.

[46] L. V. Shubnikov, V. I. Khotkevich, Y. D. Shepelev, and Y. N. Ryabinin. Magnetic properties of superconducting metals and alloys. *Zh. Eksp. Teor. Fiz*, 7:221–237, 1937.

[47] D. R. Aston, L. W. Dubeck, and F. Rothwarf. "Intermediate mixed" state of type-II superconductors. *Phys. Rev. B*, 3(7):2231, 1971.

[48] E.B. Bogomolnyi and A.I. Vainshtein. Stability of strings in gauge Abelian theory. *Sov. J. Nucl. Phys.*, 23(5), 1976.

[49] E. B. Bogomolny. Stability of classical solutions. *Sov. J. Nucl. Phys*, 24(449): 389–394.

[50] E. H. Brandt. The flux-line lattice in superconductors. *Rep. Prog. Phys.*, 58(11): 1465, 1995.

[51] H. R. Kerchner, D. K. Christen, and S. T. Sekula. Equilibrium properties of the fluxoid lattice in single-crystal niobium. I. Magnetization measurements. *Phys. Rev. B*, 21(1):86, 1980.

[52] R. Radebaugh and P. H. Keesom. Low-temperature thermodynamic properties of vanadium. II. Mixed state. *Phys. Rev.*, 149(1):217, 1966.

[53] S. Wolf, A. Vagov, A. A. Shanenko, V. M. Axt, and J. A. Aguiar. Vortex matter stabilized by many-body interactions. *Phys. Rev. B*, 96(14):144515, 2017.

[54] M. Franz, I. Affleck, and M. H. S. Amin. Theory of equilibrium flux lattices in unconventional superconductors. *Phys. Rev. Lett.*, 79(8):1555, 1997.

[55] A. A. Abrikosov. On the magnetic properties of superconductors of the second group. *Sov. Phys. JETP*, 5:1174–1182, 1957.

[56] S. Mühlbauer, C. Pfleiderer, P. Böni, M. Laver, E. M. Forgan, D. Fort, U. Keiderling, and G. Behr. Morphology of the superconducting vortex lattice in ultrapure niobium. *Phys. Rev. Lett*, 102(13):136408, 2009.

[57] U. Divakar, A. J. Drew, S. L. Lee, R. Gilardi, J. Mesot, F. Y. Ogrin, D. Charalambous, E. M. Forgan, G. I. Menon, N. Momono, M. Oda, C. D. Dehwurst, and C. Baines. Direct observation of the flux-line vortex glass phase in a type II superconductor. *Phys. Rev Lett.*, 92(23):237004, 2004.

[58] M. Laver, E. M. Forgan, A. B. Abrahamsen, C. Bowell, Th. Geue, and R. Cubitt. Uncovering flux line correlations in superconductors by reverse monte carlo refinement of neutron scattering data. *Phys. Rev. Lett.*, 100(10):107001, 2008.

[59] R. Toft-Petersen, A. B. Abrahamsen, S. Balog, L. Porcar, and M. Laver. Decomposing the Bragg glass and the peak effect in a type-II superconductor. *Nat. Commun.*, 9(1):901, 2018.

[60] R. Cubitt, E. M. Forgan, G. Yang, S. L. Lee, D. McK. Paul, H. A. Mook, M. Yethiraj, P. H. Kes, T. W. Li, A. A. Menovsky, et al. Direct observation of magnetic flux lattice melting and decomposition in the high-T_c superconductor $Bi_{2.15}Sr_{1.95}CaCu_2O_{8+x}$. *Nature*, 365(6445):407, 1993.

[61] W. Kwok, U. Welp, A. Glatz, A. E. Koshelev, K. J. Kihlstrom, and G. W. Crabtree. Vortices in high-performance high-temperature superconductors. *Rep. Prog. Phys.*, 79(11):116501, 2016.

[62] D. M. Gokhfeld. An extended critical state model: Asymmetric magnetization loops and field dependence of the critical current of superconductors. *Phys. Solid State*, 56(12):2380–2386, 2014.

[63] D. J. Thompson, M. S. M. Minhaj, L. E. Wenger, and J. T. Chen. Observation of paramagnetic Meissner effect in niobium disks. *Phys. Rev. Lett.*, 75(3):529, 1995.

[64] R. Prozorov. Equilibrium topology of the intermediate state in type-I superconductors of different shapes. *Phys. Rev. Lett.*, 98(25):257001, 2007.

[65] T. Reimann, S. Mühlbauer, M. Schulz, B. Betz, A. Kaestner, V. Pipich, P. Böni, and C. Grünzweig. Visualizing the morphology of vortex lattice domains in a bulk type-II superconductor. *Nat. Commun.*, 6:8813, 2015.

[66] J. D. Livingston and W. DeSorbo. Superconductivity, vol. 2, 1969.

[67] L. D. Landau. Theory of supraconductivity. *Zh. Eksp. Teor. Fiz.*, 7(371), 1937.

[68] R. N. Goren and M. Tinkham. Patterns of magnetic flux penetration in superconducting films. *J. Low Temp. Phys.*, 5(4):465–494, 1971.

[69] Ch. Jooss, R. Warthmann, A. Forkl, and H. Kronmüller. High-resolution magneto-optical imaging of critical currents in $YBa_2Cu_3O_{7-\delta}$ thin films. *Physica C*, 299 (3-4):215–230, 1998.

[70] L. Kramer. Thermodynamic behavior of type-II superconductors with small κ near the lower critical field. *Phys. Rev. B*, 3(11):3821, 1971.

[71] H. W. Weber, E. Seidl, M. Botlo, C. Laa, H. P. Wiesinger, and J. Rammer. Magnetization of low-κ superconductors-II. The lower critical field h_{c1}. *Physica C*, 161(3):287–293, 1989.

[72] C. M. Aegerter, H. Keller, S. L. Lee, C. Ager, F. Y. Ogrin, R. Cubitt, E. M. Forgan, W. J. Nutall, P. G. Kealey, S. H. Lloyd, et al. Transition from type-I to type-II superconducting behaviour with temperature observed by μSR and SANS. *arXiv:cond-mat/0305595v1*, 2003.

[73] A. Pautrat and A. Brulet. Temperature dependence of clusters with attracting vortices in superconducting niobium studied by neutron scattering. *J. Phys. Cond. Matter*, 26(23):232201, 2014.

[74] T. Reimann, S. Mühlbauer, M. Schulz, B. Betz, A. Kaestner, V. Pipich, P. Böni, and C. Grünzweig. Visualizing the morphology of vortex lattice domains in a bulk type-II superconductor. *Nat. Commun.*, 6:8813, 2015.

[75] A. Vagov, S. Wolf, M. D. Croitoru, and A. A. Shanenko. Universal flux patterns and their interchange in superconductors between types I and II. *Commun. Phys.*, 3(1):1–6, 2020.

[76] M. Silaev and E. Babaev. Microscopic theory of type-1.5 superconductivity in multiband systems. *Phys. Rev. B*, 84(9):094515, 2011.

[77] J. Y. Ge, J. Gutierrez, A. Lyashchenko, V. Filipov, J. Li, and V. V. Moshchalkov. Direct visualization of vortex pattern transition in ZrB 12 with Ginzburg-Landau parameter close to the dual point. *Phys. Rev. B*, 90(18):184511, 2014.

[78] R. Wiesendanger. Spin mapping at the nanoscale and atomic scale. *Rev. Mod. Phys.*, 81(4):1495, 2009.

[79] M. R. Koblischka and U. Hartmann. Recent advances in magnetic force microscopy. *Ultramicroscopy*, 97(1-4):103–112, 2003.

[80] A. Hubert and R. Schäfer. Magnetic Domains. *Springer, Berlin*, 255, 1998.

[81] A. Maisuradze, R. Khasanov, A. Shengelaya, and H. Keller. Comparison of different methods for analyzing μsr line shapes in the vortex state of type-II superconductors. *J. Phys. Cond. Matter*, 21(7):075701, 2009.

[82] T. T. Saraiva, A. Vagov, V. M. Axt, J. A. Aguiar, and A. A. Shanenko. Anisotropic superconductors between types I and II. *Phys. Rev. B*, 99(2):024515, 2019.

[83] I. Luk'yanchuk. Theory of superconductors with κ close to 1/2. *Phys. Rev. B*, 63 (17):174504, 2001.

[84] F. Mohamed, M. Troyer, G. Blatter, and I. Luk'yanchuk. Interaction of vortices in superconductors with κ close to $1/\sqrt{2}$. *Phys. Rev. B*, 65(22):224504, 2002.

[85] L. P. Gor'kov. Microscopic derivation of the Ginzburg-Landau equations in the theory of superconductivity. *Sov. Phys. JETP*, 9(6):1364–1367, 1959.

[86] E. Babaev, J. Carlström, M. Silaev, and M. Speight. *4. Type-1.5 superconductivity: From basic research to applications*. 01 2017. ISBN 9783110456806. doi: 10.1515/9783110456806-005.

[87] A. M. Campbell and J. E. Evetts. Flux vortices and transport currents in type II superconductors. *Advances in Physics*, 21(90):199–428, 1972.

[88] G. Antesberger and H. Ullmaier. Pinning of vortices in superconducting NbTa alloys due to normal conducting precipitates. *Philosophical Magazine*, 29(5): 1101–1124, 1974.

[89] D. D. Morrison and R. M. Rose. Controlled pinning in superconducting foils by surface microgrooves. *Phys. Rev. Lett.*, 25(6):356, 1970.

[90] H. J. Jensen, A. Brass, A. C. Shi, and A. J. Berlinsky. Simulations of the onset of diffusion in a flux-line lattice in a random potential. *Phys. Rev. B*, 41(10):6394, 1990.

[91] A. I. Larkin and Y. N. Ovchinnikov. Pinning in type II superconductors. *J. Low Temp. Phys.*, 34(3-4):409–428, 1979.

[92] C. P. Poole, H. A. Farach, R. J. Creswick, and R. Prozorov. Superconductivity. *Elsevier Science*, 29:30–31, 2010.

[93] E. H. Brandt. Geometric edge barrier in the Shubnikov phase of type-II superconductors. *Low Temp. Phys.*, 27(9):723–731, 2001.

[94] Co Po Bean. Magnetization of hard superconductors. *Phys. Rev. Lett.*, 8(6):250, 1962.

[95] A. Sanchez and C. Navau. Critical-current density from magnetization loops of finite high-T_c superconductors. *Supercond. Sci. Technol.*, 14(7):444, 2001.

[96] Ernst Helmut Brandt. Superconductor disks and cylinders in an axial magnetic field. I. flux penetration and magnetization curves. *Phys. Rev. B*, 58(10):6506, 1998.

[97] U. Krägeloh. Der zwischenzustand bei supraleitern zweiter art. *Phys. Stat. Solidi B*, 42(2):559–576, 1970.

[98] J. R. Clem, R. Prozorov, and Rinke J. Wijngaarden. Equilibrium intermediate-state patterns in a type-I superconducting slab in an arbitrarily oriented applied magnetic field. *Phys. Rev. B*, 88(10):104504, 2013.

[99] E. Zeldov, A. I. Larkin, V. B. Geshkenbein, M. Konczykowski, D. Majer, B. Khaykovich, V. M. Vinokur, and H. Shtrikman. Geometrical barriers in high-temperature superconductors. *Phys. Rev. Lett.*, 73(10):1428, 1994.

[100] E. H. Brandt. Irreversible magnetization of pin-free type-II superconductors. *Phys. Rev. B*, 60(17):11939, 1999.

[101] S. Foner. The vibrating sample magnetometer: Experiences of a volunteer. *J. Appl. Phys.*, 79(8):4740–4745, 1996.

[102] D. S. Sivia. *Elementary scattering theory: for X-ray and neutron users*. Oxford University Press, 2011.

[103] G. L. Squires. *Introduction to the theory of thermal neutron sattering*. Dover Publications Inc., 1978.

[104] S. Mühlbauer, D. Honecker, É. A. Périgo, F. Bergner, S. Disch, A. Heinemann, S. Erokhin, D. Berkov, C. Leighton, M. R. Eskildsen, et al. Magnetic small-angle neutron scattering. *Rev. Mod. Phys.*, 91(1):015004, 2019.

[105] P. H. van Cittert. Die wahrscheinliche Schwingungsverteilung in einer von einer Lichtquelle direkt oder mittels einer Linse beleuchteten Ebene. *Physica*, 1(1-6): 201–210, 1934.

[106] F. Zernike. The concept of degree of coherence and its application to optical problems. *Physica*, 5(8):785–795, 1938.

[107] J. Felber, R. Gähler, R. Golub, and K. Prechtel. Coherence volumes and neutron scattering. *Physica B*, 252(1-2):34–43, 1998.

[108] E. H. Brandt and M. P. Das. Attractive vortex interaction and the intermediate-mixed state of superconductors. *J. Supercond. Nov. Magn.*, 24(1-2):57–67, 2011.

[109] H. Furukawa. Dynamics-scaling theory for phase-separating unmixing mixtures: Growth rates of droplets and scaling properties of autocorrelation functions. *Physica A*, 123(2-3):497–515, 1984.

[110] J. Saroun. Evaluation of double-crystal SANS data influenced by multiple scattering. *J. Appl. Crystallogr.*, 33(3):824–828, 2000.

[111] V. Pipich and Z. Fu. KWS-3: Very small angle scattering diffractometer with focusing mirror. *JLSRF*, 1:31, 2015.

[112] M. Strobl. General solution for quantitative dark-field contrast imaging with grating interferometers. *Sci. Rep.*, 4:7243, 2014.

[113] F. Pfeiffer, C. Grünzweig, O. Bunk, G. Frei, E. Lehmann, and C. David. Neutron phase imaging and tomography. *Phys. Rev. Lett.*, 96(21):215505, 2006.

[114] C. Grünzweig, C. David, O. Bunk, M. Dierolf, G. Frei, G. Kühne, J. Kohlbrecher, R. Schäfer, P. Lejcek, H. M. R. Rønnow, et al. Neutron decoherence imaging for visualizing bulk magnetic domain structures. *Phys. Rev. Lett.*, 101(2):025504, 2008.

[115] T. Reimann, S. Mühlbauer, M. Horisberger, B. Betz, P. Böni, and M. Schulz. The new neutron grating interferometer at the ANTARES beamline: design, principles and applications. *J. Appl. Crystallogr.*, 49(5):1488–1500, 2016.

[116] M. Schulz and B. Schillinger. ANTARES: Cold neutron radiography and tomography facility. *JLSRF*, 1:17, 2015.

[117] J. S. Pedersen. Analysis of small-angle scattering data from colloids and polymer solutions: modeling and least-squares fitting. *Adv. Colloid Interface Sci.*, 70(0): 171–210, 1997.

[118] S. V. Grigoriev, A. V. Syromyatnikov, A. P. Chumakov, N. A. Grigoryeva, K. S. Napolskii, I. V. Roslyakov, A. A. Eliseev, A. V. Petukhov, and H. Eckerlebe. Nanostructures: Scattering beyond the Born approximation. *Phys. Rev. B*, 81(12): 125405, 2010.

[119] A. Heinemann and S. Mühlbauer. SANS-1: Small angle neutron scattering. *JLSRF*, 1:10, 2015.

[120] M. Laver, C. J. Bowell, E. M. Forgan, A. B. Abrahamsen, D. Fort, C. D. Dewhurst, S. Mühlbauer, D. K. Christen, J. Kohlbrecher, R. Cubitt, et al. Structure and degeneracy of vortex lattice domains in pure superconducting niobium: A small-angle neutron scattering study. *Phys. Rev. B*, 79(1):014518, 2009.

[121] P. Kneisel, G. Ciovati, P. Dhakal, K. Saito, W. Singer, X. Singer, and G. R. Myneni. Review of ingot niobium as a material for superconducting radiofrequency accelerating cavities. *Nucl. Instrum. Methods Phys. Res. A*, 774:133–150, 2015.

[122] Z. Revay. PGAA: Prompt gamma and in-beam neutron activation analysis facility. *JLSRF*, 1:20, 2015.

[123] B. Mühlschlegel. Die thermodynamischen Funktionen des Supraleiters. *Z. Phys.*, 155(3):313–327, 1959.

[124] J. Halbritter. On the penetration of the magnetic field into a superconductor. *Zeitschrift für Physik A*, 243(3):201–219, 1971.

[125] M. Nicodemi and H. J. Jensen. Creep of superconducting vortices in the limit of vanishing temperature: A fingerprint of off-equilibrium dynamics. *Phys. Rev. Lett.*, 86(19):4378, 2001.

[126] Y. Nonomura and X. Hu. Effects of point defects on the phase diagram of vortex states in high-T_c superconductors in the B$\|$c axis. *Phys. Rev. Lett.*, 86(22):5140, 2001.

[127] J. Smiseth, E. Smørgrav, E. Babaev, and A. Sudbø. Field- and temperature-induced topological phase transitions in the three-dimensional N-component London superconductor. *Phys. Rev. B*, 71(21):214509, 2005.

[128] D. S. Odintsov, I. A. Rudnev, and V. A. Kashurnikov. Vortex system dynamics and energy losses in a current-carrying 2D superconducting wafer. *J. Exp. Theo. Phys.*, 103(1):66–76, 2006.

[129] M. Pleimling and U. C. Täuber. Relaxation and glassy dynamics in disordered type-II superconductors. *Phys. Rev. B*, 84(17):174509, 2011.

[130] A. Brass and H. J. Jensen. Algorithm for computer simulations of flux-lattice melting in type-II superconductors. *Phys. Rev. B*, 39(13):9587, 1989.

[131] C. J. Olson, G. T. Zimanyi, A. B. Kolton, and N. Grønbech-Jensen. Static and dynamic coupling transitions of vortex lattices in disordered anisotropic superconductors. *Phys. Rev. Lett.*, 85(25):5416, 2000.

[132] J Wang, ZG Zhao, M Liu, DY Xing, and JM Dong. Possible inverse melting of vortex lattice in high-tc superconductors. *EPL*, 65(1):89, 2004.

[133] X. B. Xu, H. Fangohr, S. Y. Ding, F. Zhou, X. N. Xu, Z. H. Wang, M. Gu, D. Q. Shi, and S. X. Dou. Phase diagram of vortex matter of type-II superconductors. *Phys. Rev. B*, 83(1):014501, 2011.

[134] P. Paturi, M. Malmivirta, T. Hynninen, and H. Huhtinen. Angle dependent molecular dynamics simulation of flux pinning in YBCO superconductors with artificial pinning sites. *J. Phys. Cond. Matter*, 30(31):315902, 2018.

[135] G. Xu, B. Lian, P. Tang, X. L. Qi, and S. C. Zhang. Topological superconductivity on the surface of Fe-based superconductors. *Phys. Rev. Lett.*, 117(4):047001, 2016.

[136] Y. L. Liang, M. Khoshouei, G. Deganutti, A. Glukhova, C. Koole, T. S. Peat, M. Radjainia, J. M. Plitzko, W. Baumeister, L. J. Miller, et al. Cryo-EM structure of the active, G_s-protein complexed, human CGRP receptor. *Nature*, 561(7724): 492–497, 2018.

[137] K. G. Zhou, K. S. Vasu, C. T. Cherian, M. Neek-Amal, J. C. Zhang, H. Ghorbanfekr-Kalashami, K. Huang, O. P. Marshall, V. G. Kravets, J. Abraham, et al. Electrically controlled water permeation through graphene oxide membranes. *Nature*, 559 (7713):236–240, 2018.

[138] C. Yang, J. Chen, X. Ji, T. P. Pollard, X. Lü, C. J. Sun, S. Hou, Q. Liu, C. Liu, T. Qing, et al. Aqueous Li-ion battery enabled by halogen conversion-intercalation chemistry in graphite. *Nature*, 569(7755):245–250, 2019.

[139] J. Zhou, Y. Yang, Y. Yang, D. S. Kim, A. Yuan, X. Tian, C. Ophus, F. Sun, A. K. Schmid, M. Nathanson, et al. Observing crystal nucleation in four dimensions using atomic electron tomography. *Nature*, 570(7762):500–503, 2019.

[140] D. Frenkel and B. Smit. *Understanding molecular simulation: from algorithms to applications*, volume 1. Elsevier, 2001.

[141] A. R. Leach. *Molecular modelling: principles and applications*. Pearson education, 2001.

[142] J. S. Watkins and N. K. Wilkin. Extruding the vortex lattice: two reacting populations of dislocations. *EPL*, 126(1):16002, 2019.

[143] Y. Fily, E. Olive, and J. C. Soret. Driven flux-line lattices in the presence of weak random columnar disorder: Finite-temperature behavior and dynamical melting of moving Bose glass. *Phys. Rev. B*, 79(21):212504, 2009.

[144] E. H. Brandt. Fluctuation, melting, depinning, creep, and diffusion of the flux-line lattice in high-T_c superconductors. *Physica B*, 169(1-4):91–98, 1991.

[145] E. M. Forgan, S. J. Levett, P. G. Kealey, R. Cubitt, C. D. Dewhurst, and D. Fort. Intrinsic behavior of flux lines in pure niobium near the upper critical field. *Phys. Rev. Lett.*, 88(16):167003, 2002.

[146] C. J. Bowell, R. J. Lycett, M. Laver, C. D. Dewhurst, R. Cubitt, and E. M. Forgan. Absence of vortex lattice melting in a high-purity Nb superconductor. *Phys. Rev. B*, 82(14):144508, 2010.

[147] L. Landau. The intermediate state of supraconductors. *Nature*, 141(3572):688–688, 1938.

[148] A. Hubert. Zur Theorie der zweiphasigen Domänenstrukturen in Supraleitern und Ferromagneten. *Phys. Stat. Solidi B*, 24(2):669–682, 1967.

[149] S. Yoon, H. Dai, J. Liu, and C. M. Lieber. Surface pinning as a determinant of the bulk flux-line lattice structure in copper oxide superconductors. *Science*, 265 (5169):215–218, 1994.

[150] R. B. Flippen, T. R. Askew, J. a. Fendrich, and C. J. van der Beek. Surface flux pinning in $YBa_2Cu_3O_{7-\delta}$. *Phys. Rev. B*, 52(14), 1995.

[151] V. F. Rusakov, V. V. Chabanenko, A. Nabiałek, and O. M. Chumak. Oscillations of a single Abrikosov vortex in hard type-II superconductors. *J. Low Temp. Phys.*, 43(6):670–682, 2017.

[152] B. Rosenblum and M. Cardona. Evidence for normal regions at low temperatures in the superconducting mixed state. *Phys. Rev. Lett.*, 12(24):657, 1964.

[153] Y. B. Kim, C. F. Hempstead, and A. R. Strnad. Flux-flow resistance in type-II superconductors. *Phys. Rev.*, 139:A1163–A1172, Aug 1965. doi: 10.1103/PhysRev.139.A1163. URL `https://link.aps.org/doi/10.1103/PhysRev.139.A1163`.

[154] J. Bardeen and M. J. Stephen. Theory of the motion of vortices in superconductors. *Phys. Rev.*, 140:A1197–A1207, Nov 1965. doi: 10.1103/PhysRev.140.A1197. URL `https://link.aps.org/doi/10.1103/PhysRev.140.A1197`.

[155] C. J. Olson, C. Reichhardt, and F. Nori. Nonequilibrium dynamic phase diagram for vortex lattices. *Phys. Rev. Lett.*, 81(17):3757, 1998.

[156] Alejandro B. Kolton, Daniel Domínguez, and Niels Grønbech-Jensen. Hall noise and transverse freezing in driven vortex lattices. *Phys. Rev. Lett.*, 83(15):3061, 1999.

[157] X. B. Xu, Y. Liu, H. Fangohr, L. Zhang, S. Y. Ding, Z. H. Wang, S. L. Liu, G. J. Wu, and H. M. Shao. Metastable behavior of vortex matter in the electronic transport processes of homogenous superconductors. *Phys. Rev. B*, 73(21):214521, 2006.

[158] X. B. Xu, H. Fangohr, Z. H. Wang, M. Gu, S. L. Liu, D. Q. Shi, and S. X. Dou. Vortex dynamics for low-κ type-II superconductors. *Phys. Rev. B*, 84(1):014515, 2011.

[159] C. Reichhardt, J. Drocco, C. J. O. Reichhardt, and A. R. Bishop. The effect of pinning on vortex states with attractive and repulsive interactions. *Physica C*, 479:15–18, 2012.

[160] R. Labusch. Elasticity effects in type-II superconductors. *Phys. Rev.*, 170(2):470, 1968.

[161] A. Houghton, R. A. Pelcovits, and A. Sudbø. Flux lattice melting in high-T_c superconductors. *Phys. Rev. B*, 40(10):6763, 1989.

[162] S. P. Brown, D. Charalambous, E. C. Jones, E. M. Forgan, P. G. Kealey, A. Erb, and J. Kohlbrecher. Triangular to square flux lattice phase transition in $YBa_2Cu_3O_7$. *Phys. Rev. Lett.*, 92(6):067004, 2004.

[163] A. D. Huxley, M. A. Measson, K. Izawa, C. D. Dewhurst, R. Cubitt, B. Grenier, H. Sugawara, J. Flouquet, Y. Matsuda, and H. Sato. Flux-line lattice distortion in $PrOs_4Sb_12$. *Phys. Rev. Lett.*, 93(18):187005, 2004.

[164] E. H. Brandt. Computer simulation of vortex pinning in type II superconductors. II. Random point pins. *J. Low Temp. Phys.*, 53(1-2):71–152, 1983.

[165] B. Mutaftschiev. *The atomistic nature of crystal growth*, volume 43. Springer Science & Business Media, 2013.